University of Bath

PHD

Optimum efficiency control of the CTX powertrain

Guebeli, Markus

Award date:
1993

Awarding institution:
University of Bath

Link to publication

General rights
Copyright and moral rights for the publications made accessible in the public portal are retained by the authors and/or other copyright owners and it is a condition of accessing publications that users recognise and abide by the legal requirements associated with these rights.

- Users may download and print one copy of any publication from the public portal for the purpose of private study or research.
- You may not further distribute the material or use it for any profit-making activity or commercial gain
- You may freely distribute the URL identifying the publication in the public portal ?

Take down policy
If you believe that this document breaches copyright please contact us providing details, and we will remove access to the work immediately and investigate your claim.

Download date: 13. May. 2019

OPTIMUM EFFICIENCY CONTROL OF THE CTX POWERTRAIN

submitted by Markus Guebeli
for the degree of PhD
of the University of Bath
1993

COPYRIGHT

Attention is drawn to the fact that the copyright of this thesis rests with its author. This copy of the thesis has been supplied on condition that anyone who consults it is understood to recognise that its copyright rests with its author and that no quotation from the thesis and no information derived from it may be published without the prior written consent of the author.

This thesis may be made available for consultation within the University Library and may be photocopied or lent to other libraries for the purposes of consultation.

UMI Number: U071068

All rights reserved

INFORMATION TO ALL USERS
The quality of this reproduction is dependent upon the quality of the copy submitted.

In the unlikely event that the author did not send a complete manuscript
and there are missing pages, these will be noted. Also, if material had to be removed,
a note will indicate the deletion.

UMI U071068
Published by ProQuest LLC 2013. Copyright in the Dissertation held by the Author.
Microform Edition © ProQuest LLC.
All rights reserved. This work is protected against
unauthorized copying under Title 17, United States Code.

ProQuest LLC
789 East Eisenhower Parkway
P.O. Box 1346
Ann Arbor, MI 48106-1346

UNIVERSITY OF BATH
LIBRARY
31 29 SEP 1994
Ph.D.
5085144

SUMMARY

This study investigates the improvement in performance that can be gained by controlling the CTX transmission electro-hydraulically.

A simplified viscous shear theory has been used to describe the transmission of power through the belt-pulley system. This has enabled the incorporation of an analytical transmission efficiency optimisation strategy into a pump discharge control scheme in which only pulley speed and displacement are measured.

The optimum efficiency scheme was implemented on a dynamic powertrain test rig in conjunction with a strict engine Ideal Operating Line strategy. The design of suitable control laws was assisted by dynamic simulation of the CVT powertrain.

Poor dynamic performance compared with the hydro-mechanically controlled version prompted the development of a robust multivariable controller that maximised the rate of change of transmission ratio in transient operation and ensured optimum efficiency in steady state operation.

ACKNOWLEDGEMENTS

Many people contributed to the work presented. First, I would like to thank my supervisors Prof. Cliff Burrows and Nick Vaughan for supporting the CTX project. Nick helped greatly improve this thesis. He took over my supervision from Robert Dorey who initially started the project. Ford Motor Company provided the CTX transmission.

I am indebted to John Micklem for supplying me with the viscous shear stress model. His and Torquil Ross-Martin's valuable criticism decisively influenced the quality of this work.

Alan Jefferis built the whole rig. He was never tired of preparing the CTX for the next test and was *always* available when something went wrong.

I am grateful to the Bath*fp* team. Will Richards and Derek Tilley shared their profound knowledge in computer simulation and hydraulics with me. Derek advised Alan and me to commission the dynamometer and solved the crises I encountered when designing the controllers.

CONTENT

LIST OF FIGURES AND TABLES

FIGURES

TABLES

CONVENTIONS

Italic font is used for emphasis and variable names.

CAPITAL LETTERS are used for abbreviations such as CTX. A short definition of these terms is given in the glossary.

Units. Apart from a few exceptions common in engineering SI-units were used. The used non-SI-units are

rpm	revolution per minute (rotational speed)
mph	miles per hour (velocity)
km/h	kilometres per hour (velocity)
kPa	kilopascal (pressure)
bar	(pressure)
L/min	litre per minute (hydraulic flow)

Cross references. Examples demonstrate the usage of section, figure and equation reference:

5.2	is a reference to section 5.2.,
Figure 2.13	designates Figure 2.13, and
(6.34)	refers to equation (6.34).

Figures are listed at the end of each chapter.

NOMENCLATURE

The nomenclature is separated into four sections: Variable Speed Unit (VSU), Engine, Powertrain and Control. This enables the use of familiar symbols when describing the physical processes that were based on viscous shear theory for the VSU, on thermodynamics for the engine and dynamics for the powertrain. Within this framework it should be understood that the same symbol might describe two different quantities, such as T typically means *temperature* in thermodynamics but *torque* in dynamics. Each of the four sections is divided into logical sub-sections. The numerical values of constants are given in brackets.

1. Variable Speed Unit (VSU)

1. Subscripts

p	Primary pulley
s	Secondary pulley

2. Variables

Most variables can take on subscripts p or s for reference to primary or secondary pulley.

α	Angle between the straight belt line and the pulley centre connection
β	Angle of lap on a pulley
η	Viscosity of oil between segments and pulley
η/k_t	Viscous shear parameter
τ	Shear stress in oil film
C	Compression of the belt
C_C	Compression in the straight path of the belt
F	Pulley clamping force
G	Radial shear force
P_L	VSU power loss
R	Active belt radius (radius of circular arc defined by the rocking edge of segments)
R_{pi}, R_{po}, R_{si}, R_{so}	In- and outgoing belt radii as defined in equation (5.35)
T	Pulley torque resulting from viscous shear stress
T_l	Torque loss reflected to primary pulley
T_{p+}	Primary pulley torque (sum of primary viscous shear torque and torque loss)
U	Tension in the bands
k	Scaling factor for incoming and outgoing radii for torque loss model
k_t	Oil film thickness constant
n	Pulley speed

p Hydraulic cylinder pressure
s Slip
t Oil film thickness between segments and pulley
v_L Longitudinal belt velocity
v_R Radial belt velocity

3. Geometrical Substitution Variables
A_c Radial component of the sliding contact area of a segment
h Uniform radial belt thickness
p_1, p_2 Compensated radius for the torque loss computation
q Compensated radius for the longitudinal viscous relation (can take subscript p or s)
r Number of segments engaged (can take subscript p or s)

4. Empirical Constants
υ_P Hydraulic pump efficiency (0.6)
c_{V0} Constant coefficient for viscous shear parameter (6 N/m^2)
c_{V1} Linear coefficient for viscous shear parameter (-80 N/m^3)
d_p Diameter of lumped primary orifice model (3.5 mm for hydro-mechanical, 1.3 mm for electro-hydraulic unit)
d_s Diameter of lumped secondary orifice model (3.0 mm for hydro-mechanical, 2.1 mm for electro-hydraulic unit)
k_t Torque loss constant ($0.25*10^{-4}$)

5. Dimensions
Θ Half the pulley wedge angle (11°)
A_p Primary actuator area ($1.9792*10^{-2}$ m^2)
A_s Secondary actuator area ($0.9719*10^{-2}$ m^2)
D Hydraulic pump displacement of the standard hydro-mechanical unit ($9.72*10^{-6}$ m^3/rev)
L Belt length (0.6486 m)
R_{pMin} Minimum primary radius (0.0288 m)
R_{sMin} Minimum secondary radius (0.032 m)
X Pulley centre distance (0.155 m)
b Segment thickness at most inner part (0.0015 m)
c Radial length of segment side (0.0046 m)
m Mass of belt per unit length (1.3462 kg)
s Segment thickness at rocking edge (0.002184 m)
Number of belt segments (297)

2. Engine

1. Subscripts

0	Ambient
m	Manifold

2. Variables

η_{vol}	Volumetric efficiency
ϕ	Throttle angle
ρ_m	Specific weight of air in manifold
A_{th}	Throttle open area
T	Temperature
T_E	Engine torque
V_{swept}	Swept volume
c_D	Throttle discharge coefficient
$c_D A_{th}$	Effective butterfly flow coefficient
$c_D^* A_{th}^*$	Effective flow coefficient (sum of butterfly flow coefficient and leakage flow coefficient.
dm_C/dt	Cylinder air mass flow
dm_{th}/dt	Throttle air mass flow
f_η	Interpolation function of tabulated volumetric efficiency map (Appendix A)
f_T	Interpolation function of tabulated torque map (Appendix A)
h_{th}	Enthalpy of air flowing through throttle valve
h_c	Enthalpy of air flowing into cylinder
m	Air mass
n_E	Engine speed
p	Pressure
u_m	Internal energy of air in manifold

3. Empirical Constants

γ	Ratio of specific heats (1.41)
R	Specific gas constant (280 J/kgK)
$c_{\phi 0}$	Constant coefficient for throttle discharge coefficient computation (0.478)
$c_{\phi 1}$	Linear coefficient for throttle discharge coefficient computation (0.696)
$c_{\phi 0}$	Exponential coefficient for throttle discharge coefficient computation (0.121)
$c_L A_L$	Leakage flow coefficient (8e-6 m^2)
c_p	Specific heat of air at constant pressure (1000 J/kgK)
c_v	Specific heat of air at constant volume (720 J/kgK)
g_η	Linear volumetric efficiency map extrapolation coefficient (1.7 %/kPa)
g_T	Linear torque map extrapolation coefficient (1.4 Nm/kPa)

4. Dimensions

ϕ_0	Throttle angle at which throttle nominally closed (5°)
D	Throttle bore diameter (34 mm)
V_m	Manifold Volume (0.004 m^3)
d	Throttle bar diameter (7.3 mm)

3. Powertrain

1. Variables

α Engine throttle angle
γ Road gradient
η_F Final drive efficiency
F_T Tyre force
F_d Driving resistance force
F_r Rolling resistance force
T_A Axle torque
T_C Clutch loss torque
T_E Delivered engine torque
T_T Torque between engine and transmission
n_D Differential output speed
n_E Engine speed
n_T Tyre speed
n_p CTX input speed (with engaged clutch equal to engine speed)
n_s Secondary pulley speed (equal to final drive input speed)
v_0 Head wind velocity
v_C Car speed
v_p Input voltage to primary valve
v_s Input voltage to secondary valve

2. Empirical Constants

c_{C0} Constant clutch loss coefficient (2.04 Nm)
c_{C1} Linear clutch loss coefficient (-4.25e-3 Nms/rad)
c_{C2} Quadratic clutch loss coefficient (1.03e-5 Nms^2/rad^2)
c_{F0} Final drive idling torque (zero efficiency point) (2.5 Nm)
c_{Fm} Maximum final drive efficiency (0.96)
c_{Fq} Final drive steepness coefficient (5.0 Nm)

3. Lumped Parameters

J_E Engine inertia (0.16 kgm^2)
J_D Differential inertia (0.6 kgm^2)
J_W Wheel and axle inertia (6.56 kgm^2)
c_A Axle damping constant (6670 Nm/rad)
f Coefficient of rolling resistance (0.015)
k_A Axle spring constant (98 Nms/rad)
m^* Generalised car mass (915 kg)
r_T Compensated wheel radius (0.27 m)

4. Dimensions

A Vehicle cross section (1.95 m^2)
R_F Final drive reduction ratio (5.671)
c_D Aerodynamic drag coefficient (0.35)
m Car mass (825 kg)

5. Physical Constants

ρ	Density of air (1.202 kg/m^3)
g	Acceleration due to gravity (9.81 m/s^2)

4. Control

$\sigma(A)$	Singular value of a matrix A
A	State matrix
B	Input matrix
C	Output matrix
D	Direct output matrix
$F_{FF}(s)$	Feed froward transfer function
$G_{IOL}(s)$	Transfer function of the IOL controller
$G_{OE}(s)$	Transfer function of the OE controller
H_∞	*H-Infinity* norm:

$$\|G\|_\infty \triangleq \sup_\omega \bar{\sigma}(G(j\omega))$$

K_{FF}	Feed forward gain
K_I	Integral gain
K_P	Proportional gain
K_S	Slip warp gain
$S(s)$	Sensitivity
$T(s)$	Complementeary sensitivity
$W_1(s)$	Disturbance attenuation function
$W_3(s)$	Limit for the largest anticipated plant disturbance
e_s	Slip error
e_{ss}	Steady state error
u	Input vector
x	State vector
y	Output vector

1. INTRODUCTION

The use of a continuously variable transmission (CVT) in an automobile allows the engine to operate along its ideal operating line (IOL). This strategy runs the engine at its most efficient operating point for a demanded engine power yielding minimum fuel consumption. The CTX transmission (inspired by *C*ontinuously variable *T*ransa*X*le, Figure 1.1) is a Van Doorne designed CVT developed by Ford in the mid-eighties for automotive use. It has been built into the Fiesta range since 1987 and more recently into Escort and Orion models but the performance of cars fitted with the CTX did not fulfil the expectations with respect to fuel consumption. This study investigates the potential of the CTX powertrain and methods to optimise its consumption.

Figure 1.1 shows a cross section of the CTX (courtesy of Ford Motor Company Ltd, detailed description in Chapter 3), an automatic transmission for transverse engine mounting in front wheel drive cars with a maximum engine capacity of 1.6 L. The variable speed unit (VSU) is a Van Doorne design with the metal thrust belt (Hendriks, 1988). The clamping forces at both pulleys which determine the transmission ratio are controlled hydraulically. One of the forces can be set arbitrarily leaving the other to adjust the transmission ratio. This process is governed by an hydro-mechanical control unit that lacks the flexibility of an electronic powertrain controller. Its replacement by a computer controlled electro-hydraulic unit resulted in the concept that stimulated the research in this work.

1.1. Objectives

The objectives of this thesis fall into three categories: improving power transmission efficiency of the VSU, reducing fuel consumption of the CTX powertrain and investigating the advantages of an overall CVT powertrain controller. These objectives may be rephrased in the form of a series of questions:

Power transmission efficiency of the VSU. How can operating conditions within the transmission be adjusted to optimise the power transmission efficiency of the Van Doorne VSU?

Fuel consumption of the CTX powertrain. What improvements compared with the hydro-mechanical control unit are realisable through a strict implementation of the ideal operating line (IOL) strategy? Are there any limitations with respect to the dynamic response within this framework?

Overall powertrain controller. How can the transient response of a CVT powertrain be improved by means of an overall powertrain controller?

1.2. Scope of the study

The overall aim of this project is the achievement of a lower fuel consumption for a CTX powertrain. Mathematical modelling of such a system allowed an investigation by computer simulation to design and assess improvements. The validity of this model has been demonstrated by comparison with results from a sophisticated experimental rig constructed to provide vehicle emulation (Figure 1.2, description see chapter 2). The simulated results demonstrate the improvements in fuel consumption obtained. However, experimental confirmation fell outside the scope of this study principally because adequate fuel flow measurement facilities were not available.

1.3. Recent Developments in Automobile CVTs

The arrival of a reliable VSU design and advances in connection with micro computers and their application in engineering problems have strongly influenced the development of CVT powertrains for automobile applications.

1.3.1. CVTs in Production

Horowitz (1980) showed that *metal traction V-belt type VSUs* (see definition of traction type VSU in Beachley, 1980) are the only design to offer efficient and practical (power density, mechanical complexity) CVT motoring. The developments in the past decade have proven his statement although the optimistic overall efficiencies of 96% have not yet been realised. The only exception to the metal V-belt design in the development of automobile CVTs is the Perbury CVT, Stubbs 1980. The Perbury CVT is a toroidal design now developed by Torotrak (Lambert, 1988) and has been installed in test vehicles but never put into production. Recent work by Nissan (Nakano, 1990 and Machida, 1990) have revived the design and show promising results. However, the world's only supplier of VSU for production cars is Van Doorne with its metal thrust belt design. In the eighties Ford strenuously developed the CTX. The first prototypes showed promising results (Stockton, 1984, Eggert, 1984, Hahne, 1984); by 1987 the CTX was in production (Röper, 1987, Dittrich, 1988, Kalkert, 1988). The same CVT is on offer by Fiat (Howard, 1992). Subaru independently developed a CVT based on the Van Doorne VSU and equipped it with electronic control (Sakai, 1988, Narumi, 1990). The Subaru CVT differs from the CTX in having a magnetic powder clutch and uses a pair of conventional synchromesh gears as a means of forward/reverse change-over mechanism.

The mechanical production process to achieve a reliable product seems to have been overcome by Van Doorne (Hendriks, 1988 and 1993). The metal V-belt VSU unit has a life expectancy equal to that of the car. The fact that the Perbury design has not made it into production suggests that problems (dynamic characteristics, reliability, efficient manufacturing) for this design have not yet been solved.

The metal V-belt CVT is a proven design commercially available from four major manufacturers (Fiat, Ford, Rover, Subaru). Although not loved by the superficial press (Howard, 1992) it is beginning to become a commercial success. According to Autocar & Motor (1992) 6% of total 1992 Fiesta sales were CTX cars and that share is increasing.

1.3.2. Control of CVT Powertrains

The control of the CVT powertrain is essential because it defines the means to implement the initial goal to decrease the fuel consumption. Guo (1988) shows that, unfortunately, vehicle performance and fuel economy have opposing requirements. This, together with the necessary realisation of all safety aspects, further complicate the control task. From an early stage these requirements pointed to an electronic control to give the necessary flexibility to implement the complex control tasks. Eggert (1984) introduced the CTX transmission and mentioned the potential for improvements with an electronic controller. The mass production of such a controller at that time was too costly and thus ruled out. Subaru with the ECVT (Sakai, 1988) has introduced the first electronically controlled CVT. Gieles (1989) reports on an electronically controlled prototype CVT for a Volvo 440 and concludes that electronic control can improve efficiency while maintaining vehicle performance. Hendriks (1993) from Van Doorne also introduces an electronically controlled CVT. He projects the efficiency to increase by an average of 15% (Hendrik's Figure 10) as compared to hydro-mechanically controlled transmissions. Seidel (1992) and Narumi (1990) predict that the application of complex control algorithms (adaptive control and fuzzy control, respectively) will further improve the compromise between consumption and transient performance.

1.4. Unsolved Problems

Previous theoretical studies have forecast the undisputable success of CVT powertrains. Why has the practical implementation proven to be more complicated than initially assumed?

1.4.1. Consumption and Driveability

The consumption of cars equipped with Van Doorne based CVTs is reported to be comparable to cars with conventional 5 speed manual gearboxes, Kalkert (1988), Abromeit (1985). Theoretically, the consumption of a CVT should be considerably better. Engels and Main (1985) report on work on the experimental study ELTEC. They mention the difficulties one faces to achieve comfortable and safe driving, i.e. driveability, with a CVT car and confess that the reduction of consumption can only be tackled in a second development stage. Electronic control is an essential tool to carry this out because it offers the needed flexibility.

1.4.2. Transient Behaviour and Driveability

A CVT powertrain suffers from the principal disadvantage that considerably increased axle torque can only be achieved by increasing the engine speed. This is due to the consumption optimising schedule imposed onto the engine which results in typical high torque/low speed operation. During the engine speed transient, power is used to accelerate the engine and only after a higher engine speed is reached can the power be transmitted to the axle. This results in the typical lag in transient response (Guo, 1988). This lag is inherent to a CVT system and only a smaller engine inertia can actively reduce it. However, it is important *how* the transition of engine speed is conducted because this has severe consequences on the driveability, i.e. the acceleration impression the driver experiences. No procedure has been defined that specifies a suitable transition of operating points in connection with enhanced driveability.

1.4.3. Efficiency Control

The metal V-belt CVT uses a hydraulic system to ensure correct operation. The discharge pressure of the pump contributes directly as a power loss, and additionally

influences the efficiency of power transmission through the VSU. Electronic line pressure control has been expressed by many as an essential procedure to actively control the efficiency of the transmission (Seidel, 1992, Schwab, 1990, Narumi, 1990). Gieles (1989) forecasts an improvement in consumption of 1% per bar lower line pressure. Bonthron (1985) has shown that the efficiency of a Van Doorne VSU based CVT does not decrease when changing the ratio. However, no suitable scheme to control the line pressure has emerged, yet.

1.5. Research Steps

The published material comes solely from the promoters of the CTX themselves and can hardly be regarded as objective. Thus, a clarification of the performance of the transmission in terms of efficiency and the ability regarding the ratio adjustment is desirable. Additionally, having established the necessity for electronic control three steps could be identified to achieve the overall goal of the project:

1. assess of the performance of the CTX,
2. find ways to adjust the line pressure to optimise efficiency, and
3. implement electronic control and exploit the advantages with respect to overall powertrain control.

1.6. Organisation of the Document

The remainder of this thesis is divided into eight chapters and four appendices:

Chapter 1

Has introduced the objectives of this study, reviewed the situation before the research and formulated the research needs.

Chapter 2

Explains the design and construction of the purpose built test rig.

Chapter 3

Describes the CTX in detail and assesses the performance with the standard

control unit. The method to gain enhanced control is introduced: The hydro-mechanical (HM) control unit is replaced with an electro-hydraulic (EH) unit.

Chapter 4

Presents the theoretical analysis of the CTX powertrain. Particular attention is given to the power transmission phenomenon between the belt and the pulleys.

Chapter 5

Validates the models with experimental data. This yields reliable mathematical descriptions.

Chapter 6

Investigates optimum efficiency and IOL control strategies. Classical controller design leads to stable feedback systems that are implemented on the rig. The calculated potential fuel savings are presented. Disadvantages from a dynamic point of view are identified.

Chapter 7

Uses numerical simulation to define new multivariable control strategies that optimise the transient performance of the CTX powertrain to overcome dynamic problems.

Chapter 8

Summarises the results and discusses the new findings.

Chapter 9

Presents the conclusions.

Appendix A

Contains the paper "Maximum transmission efficiency of a steel belt continuously variable transmission" by Guebeli, Micklem and Burrows (1992).

Appendix B

Gives details of steady state engine maps.

Appendices C

Explains the linear model gained through the linearisation of the dynamic simulation at a representative operating point.

Appendix D

Lists the linear systems used for the design and the control of the H_∞ controller in Chapter 8.

Glossary

Explains the abbreviations (CAPITAL LETTERS) used throughout the document.

References

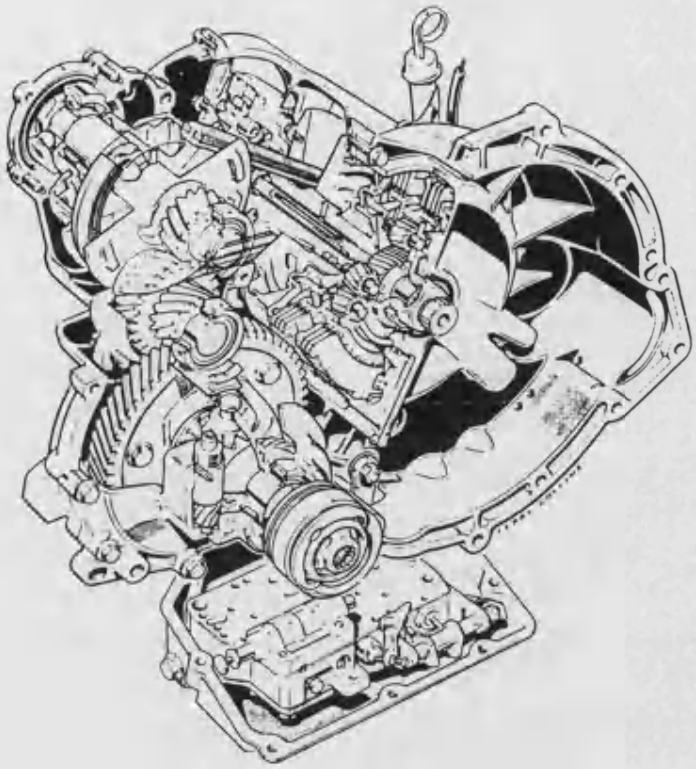

Figure 1.1 Section of the CTX transmission. The hydraulic control unit adjusts the pressures in the pulley cylinders and thus the transmission ratio.

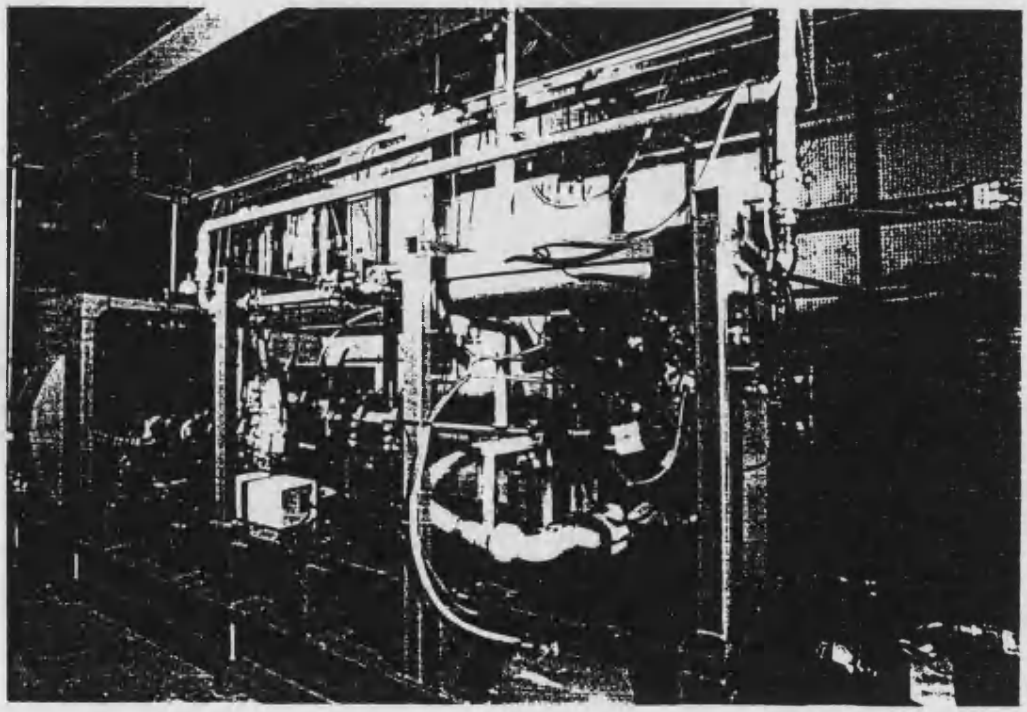

Figure 1.2 Photograph of the dynamic powertrain test rig

2. THE TEST RIG

This chapter introduces the CTX powertrain test bed. The rig was built to satisfy two needs. First, the study had to be supported by experimental data. The acquisition of experimental data enabled the validation of the mathematical models. Secondly, the developed control strategies had to be tested on a representative scale. The dynamic interaction between the powertrain and the vehicle plays an important role and, thus, had to be emulated on the test bed.

Section 2.1 gives an overview of the rig. The design and implementation of the hydrostatic dynamometer are explained in 2.2. The instrumentation is described in 2.3; the acquisition of CTX data is of particular importance. Details of the hardware of the control loops are listed in 2.4.

2.1. The Powertrain Test Bed

Figure 2.1 shows a sketch to scale of the test bed. The three main components *engine*, *CTX transmission* and *dynamometer* (flywheel and hydraulic pump) are connected through torque and speed transducer units. The long shaft between the engine and the CTX was necessary to isolate radial engine movements allowing the CTX to be rigidly connected to the frame. The differential of the transmission is locked which enables the power transmission to one axle. The flywheel and the hydraulic pump run at nominal car wheel speed.

The electronic signal processing is schematically shown in Figure 2.2. Two separate control computers are in charge of the dynamometer and the CTX powertrain, respectively. The signal conditioning and the signal amplifiers are the interfaces between the rig and the control computers. All conditioned signals are available for data acquisition for which an additional computer was employed.

2.2. The Hydrostatic Dynamometer

The dynamometer for steady state and transient testing of the CTX powertrain was purpose built. Based on previous work within the department an hydrostatic unit was chosen. This section describes design considerations, the implementation and the employed control strategy.

2.2.1. Operating Modes

The dynamometer provides steady state and dynamic powertrain testing and these form the basis of three modes (*steady state constant speed*, *steady state constant torque* and *car emulation*) for control of the dynamometer.

Steady state operation enables the mapping of the powertrain typically used for efficiency evaluation. The dynamometer can be run in either *constant speed* or *constant torque* mode. Zero steady state error is ensured for both. The whole operating envelope of the CTX powertrain is covered. This includes uphill driving for up to 30% gradient and over-run operation that typically occur for 10% downhill driving which specifies the motoring capabilities.

Car emulation. This mode enables the transient operation of the powertrain typically occurring in real life. The powertrain's reaction to driver demand or changing road gradient is tested in circumstances close to a real application. The dynamometer emulates the car inertia, aerodynamic drag and other phenomena including a braking term. A real-time simulation provides the basis to do this.

Figure 2.3 explains the dynamometer's operation for the three modes (*constant speed*, *constant torque* and *car emulation*). The scheme was implemented in a real-time program containing also the digital speed and swivel controllers (see below). The switches in Figure 2.3 were thus actuated through software. In speed and torque mode the dynamometer controls its speed and absorbed torque, respectively (*external speed*

demand, external torque demand). In car emulation mode the dynamometer behaves like a car. *Road gradient* and *brake signal* can be applied through the real-time software. The brake signal can be provided externally.

2.2.2. The Design

The dynamometer comprises of a flywheel representing the inertia of a Ford Fiesta sized vehicle and an hydrostatic loading system.

FLYWHEEL

For operation in car emulation mode the dynamometer has to emulate the car's inertia. Although Guebeli and Dorey (1990) proposed a control scheme for stable inertia emulation it was decided to have a real inertia in the form of a flywheel. The kinetic energy of the car and the wheels are represented (which relates to an inertia of 66.7 kgm^2).

HYDROSTATIC LOADING SYSTEM

An hydrostatic loading system with high transient capabilities was derived in Guebeli (1990). A similar, but dynamically improved, system was built. The heart of the system is a servo-poppet valve assembly which restricts the pump outflow thus converting the absorbed power into heat. The heat is dissipated by a cooler and no power recovery takes place. In order to satisfy the wide operating range a variable displacement hydraulic pump unit was chosen. The specified motoring capabilities (over-run operation) made a full flow boost pump necessary.

2.2.3. The Hydraulic Circuit

The hydraulic circuit is shown in Figure 2.4. The absorbed torque is controlled by adjusting the swivel angle and the discharge pressure of the loading pump. The swivel adjustment uses a proportional valve and an equal area actuator. The loading system

comprising of a servo valve, orifice, poppet valve and safety relief valve has been assembled in a manifold, optimising the transient capabilities. The pressure drop across the orifice is determined by the flow through it which can be adjusted by the servo valve. This pressure is applied to the back face of the poppet valve which, in turn, sets the loading pump discharge pressure.

2.2.4. Control

Swivel adjustment. The displacement of the loading pump has to be adjusted so that it does not draw more than the delivered flow from the boost pump at any speed. This prevents cavitation at high loading pump speeds that could damage the components. Assuming no volumetric losses a demanded swivel angle can be computed as a function of the loading pump speed such that the loading pump flow is constant. This corresponds to a power limit (Figure 2.5). The swivel demand can be used as a schedule for a closed loop swivel angle position control as shown in Figure 2.5.

Discharge pressure adjustment. Rapid changes of torque on the loading pump are achieved by control of the discharge pressure. Considerations in the light of car emulation determine this adjustment. The principal equations of motion for the emulated car and the real life dynamometer are

Car emulation	Dynamometer	(2.1)
$J_C\dot{\omega}_C = T_P - T_L$	$J_D\dot{\omega}_D = T_P - T_{Pump}$	

where subscripts C, D and P correspond to car, dynamometer and powertrain, respectively. T_L is the load acting on the car and consists of tyre resistance, aerodynamic drag, the road gradient and the optional braking torque. It can be computed as a function of the car speed ω_C. For a successful emulation $\omega_D = \omega_C$ is the target. Assuming for simplicity $J_D = J_C$ it is obvious that T_{Pump} must be equal to T_L, the load acting on the car. This means that if T_{Pump} were adjusted to be T_L at any time car emulation would be achieved. This would make a torque transducer between the

flywheel and the pump necessary to obtain the required accuracy. However, if $J_D = J_C$ is not assumed, car emulation has to be accomplished through speed feedback control: If T_P is measured and T_L computed the theoretical car speed (ω_C) can be determined through numerical integration of the above left hand side equation. This process is pictured in Figure 2.6 where T_p relates to the *Measured Torque*, T_L to the *Demanded Torque* and the computed ω_C to the *Demanded Pump Speed*, respectively. The demanded pump speed can be used for reference in a speed control loop (see Figure 2.6). The elimination of T_P in the two equations above and assuming successful car emulation, i.e. $\omega_D = \omega_C = \omega$, leads to

$$T_{Pump} = T_L + \dot{\omega}\left(J_C - J_D\right) \tag{2.2}$$

$|J_C - J_D|$ plays a crucial role for successful car emulation and has to be as small as possible to minimise dynamic requirements on T_{Pump}. Additionally, a small J_D increases the dynamics in ω_D that further spiral the dynamic requirements (equation (2.1) right hand side). The accuracy at which the pump torque can be controlled within a speed feedback loop as in Figure 2.6 is crucial for car emulation. This will be evaluated later.

An analogue PI controller (Figure 2.5) was satisfactory for the swivel control loop. For the speed control loop (Figure 2.6) a more sophisticated digital PID implementation was necessary. The anti-windup implementation was essential, because the dynamometer can easily be operated in saturation (e.g. very hard braking). Details of the controller design can be seen in Guebeli (1990). The interaction of the two loops could not be established in theory to a satisfactory accuracy. Therefore, it was imperative that the controllers could be tuned on-line. A trapezoidal integration method (Tustin) is used for the numerical integration process (computation of the demanded pump speed).

2.2.5. Performance

Steady state. Figure 2.7 shows the operating envelope in the familiar speed-torque diagram. This envelope has to contain the steady operating points of the powertrain which are dominated by its peak axle torque and peak engine power. The largest transmission ratio of 13.6 ("first" gear) results in a peak axle torque of 1142 Nm. With a maximum transmission efficiency of 97% the dynamometer just covers the maximum axle torque. Peak power of the engine is 38 kW. This compares to the power limit of 48 kW (1100 Nm at 420 rpm) of the dynamometer and is well within the limit. Note that the decreasing torque capability at high speeds goes hand in hand with the power limit of the powertrain. A safety margin not to draw more than 60% of the theoretical boost flow was implemented. This restricted the power limit (Figure 2.5) and resulted in the dark area envelope in Figure 2.7. The lighter shaded area extends to the theoretical operating envelope limited by component dimensions.

Car Emulation Performance. The finite bandwidth of the speed controller and the pressure control system (although very high, at approximately 100 rad/s, Ghaffarzadeh et al, 1992) and the integration in the car inertia model impose a limit on the dynamic performance. This can be demonstrated by examination of the torque response of the dynamometer alone. The transmission was disconnected (i.e. break between flywheel and CTX, Figure 2.1). Figures 2.8 and 2.9 show experimental data acquired in torque mode operation with increasing torque step demands and the resulting dynamometer speed. The effective torque applied by the dynamometer can be observed by the speed behaviour and the discharge pressure. Having no external load the dynamometer, and thus the flywheel, should decelerate linearly (constant torque acting on inertia, dotted line). The dashed line is the measured speed that should coincide with the dotted line. The pump discharge pressure is proportional to the absorbed torque and should thus correspond to the torque demand (solid line). Figures 2.8 and 2.9 differ in the initial dynamometer speed and the demanded torque step.

In Figure 2.8 the initial speed is 970 rpm where the swivel angle is automatically adjusted to about 50%. The peak-time, T_p, and damping ratio, ζ, of the discharge

pressure signal (about 0.75 seconds and 0.7, respectively) suggest a bandwidth of about

$$\omega_n = \frac{\pi}{T_p\sqrt{1-\zeta^2}} = 5.87 \text{ rad/s} \qquad (2.3)$$

At 2.5 seconds the pressure signal decreases. This is due to the action of the swivel controller that increases the swivel caused by the reducing speed. The torque absorption can only be observed from the speed behaviour. After an initially expected lag the torque absorption is too high and from 3 seconds onwards corresponds to the demand. In the period between 1.5 and 2.5 seconds the dynamometer decelerates too much. The speed error is acceptable.

In Figure 2.9 the initial speed is only 400 rpm where the swivel angle is at 100%. The pressure signal suggests an increased bandwidth of about 12 rad/s. No interaction between the swivel and the speed controller take place because the swivel controller remains inactive. The accumulated speed error is larger than in Figure 2.8 but still tolerable.

2.3. Instrumentation

The measurement of physical quantities served two purposes. The performance of the CTX had to be determined and the mathematical models (numerical applications of extensive analysis) had to be validated with experimental data. Secondly, some physical quantities were needed for feedback systems. (dynamometer, 2.2; and CTX powertrain control, 6.2 and 6.3). This section explains the measurement techniques (transducer types, signal conditioning) and elaborates on their accuracy and limitations to the possible interpretation.

2.3.1. Measured Quantities

Table 2.1 Measured Quantities

	CTX	Dynamometer	Engine
Speed	input (n_E) primary pulley (n_p) belt (v_L) output (n_s)	←	←
Torque	input (T_p) output (T_s)	←	←
Pressure	primary (p_p) secondary (p_s) clutch (p_c)	boost (p_b) loading (p_l) control (p_c)	
Displacement	primary radius (R_p) secondary radius (R_s)	swivel angle (δ)	throttle angle (α)

← means measurement on the left applies.

Table 2.1 lists all measured quantities grouped into *CTX*, *Dynamometer* and *Engine*. The symbol used for each variable is shown in brackets.

2.3.2. Measurement Technique

Speed. A frequency to voltage technique was applied. Magnetic pick-offs with toothed wheels supplied pulses that were conditioned in an in-house built Frequency to Voltage ("F to V") card (Guebeli, 1989). The achievable accuracy is within 0.1% of the maximum measurement. The narrow speed band (apart from the dynamometer speed) favoured the applied technique.

Torque. Strain gauge type torque transducers were used. An in-house DC-amplifier evaluated the change in bridge resistance.

Pressure. Strain gauge pressure transducers in connection with the in-house DC-amplifiers were employed.

Displacement. LVDTs (linear variable displacement transducers) were used for high precision demands (primary and secondary radius). For looser specifications (swivel angle and throttle angle) ordinary potentiometers were employed.

2.3.3. The instrumentation of the CTX

Figure 2.10 shows a photograph of the CTX with its instrumentation. The engine drives from the right through the CTX input torque transducer. The dynamometer is on the left, driven by the CTX via the CTX output torque transducer. Toothed discs for speed measurements are recognisable at the torque transducer units. Two out of three pressure transducers are identifiable. They are mounted on the CTX casing. Two probes manufactured from aluminium are used to determine the active radii of the thrust belt around its circular path on the pulleys. This measurement was crucial in *truly determining the slip.* To the auther's knowledge this has not been carried out by others. The secondary pulley probe is recognisable on top of the CTX. A cross section of this device explains its operation (Figure 2.11). The linearly guided spring loaded rod pushes a roller assembly onto the endless band packs of the belt. LVDTs (not shown in Figure 2.11) measure the displacement. The probe is mounted parallel to the fixed pulley surface. Magnetic pick-offs can be incorporated to measure the belt speed (see Micklem et al, 1991).

2.3.4. Some Thoughts on Accuracy

In CVT transmission work one is confronted with the measurement of two sensitive quantities: efficiency and slip.

$$\eta = \frac{n_s T_s}{n_p T_p} \quad , \quad s = 1 - \frac{n_s R_s}{n_p R_p} \tag{2.4}$$

Both of these quantities rely on post computation of measured quantities in the form of the ratio of two products. The maximum error of the slip s with respect to errors

in speed and radii measurement is

$$\left|\frac{\delta s}{s}\right| \leq \left|\frac{\partial s}{\partial n_s}\frac{\delta n_s}{s}\right| + \left|\frac{\partial s}{\partial n_p}\frac{\delta n_p}{s}\right| + \left|\frac{\partial s}{\partial R_s}\frac{\delta R_s}{s}\right| + \left|\frac{\partial s}{\partial R_p}\frac{\delta R_p}{s}\right| \qquad (2.5)$$

$s^* = s - 1$ is introduced to evaluate the relative error (no division by zero; s^* is the geometrical transmission ratio but this has no significance here.). Noting that $\delta s = \delta s^*$, equation (2.5) can be re-arranged

$$\left|\frac{\delta s}{s^*}\right| \leq \left|\frac{\delta n_s}{n_s}\right| + \left|\frac{\delta n_p}{n_p}\right| + \left|\frac{\delta R_s}{R_s}\right| + \left|\frac{\delta R_p}{R_p}\right| \qquad (2.6)$$

A 1% accuracy in every measured channel would accumulate to an overall accuracy of 4%. This amount of inaccuracy is not tolerable for the efficiency and slip, since slip values and improvements in efficiency in the order of this magnitude are expected to be measured.

For the work presented in this thesis all possible measures were taken to minimise the accumulated inaccuracies for slip and efficiency measurements. This applied particularly to the pre-filtering before the digital data acquisition in order to prevent aliasing effects. All averaging work was carried out numerically and was always the last step in the evaluation. These measures decreased the probability of worst case inaccuracies. However, it goes without saying that these thoughts have to be carried in mind when interpreting slip and efficiency values. An accuracy within 0.5% for these values is the most optimistic one can assume.

2.3.5. Hydraulic Valve Amplifiers

All mechanical power sources for control purposes are hydraulic. The command signal must be interpreted and transmitted to the valve by means of an amplifier. Table 2.2 summarises the amplifiers used, and the variables in brackets correspond to the

Table 2.2 Hydraulic valve amplifiers and their command and controlled variables

	Hydraulic Valve Amplifier	Used to control
CTX	primary actuator valve (v_p) secondary actuator valve (v_s)	primary pressure (p_p) secondary pressure (p_s)
Dynamometer	servo-poppet valve (v_c) proportional valve (v_δ)	pump discharge pressure (p_c) swivel position (δ)
Engine	throttle valve (v_α)	throttle position (α)

command variables.

2.4. Control Loop Hardware

Two sophisticated digital control tasks were mastered on the rig. The real time car emulation (see 2.2) and the CTX powertrain controller (see 7.) are based on two separate control computer-analogue/digital interface units. This section describes their hardware topology. Apart from these advanced digital controller, ordinary analogue PI controllers were used for hydraulic position control of engine throttle and pump swivel angle.

2.4.1. The DSP32C System

The system comprises of a DSP32C digital signal processor from AT&T with corresponding A/D input and D/A output boards. A fast A/D converter and a separate data bus offered speed performance far in excess of that required. Program development and communication were carried out through a PC. The programming language was DSP32C Assembler. The system was used to control the dynamometer.

2.4.2. The T800 System

This is a transputer system from Intel tailored to meet the requirements for digital closed-loop control. A separate analogue input/output board with its own data link was part of this tailoring. Programs were developed in parallel C. This way the multitasking capabilities of the transputer could be used advantageously for the powertrain control tasks. Communication took place through a PC where all the data management was accomplished.

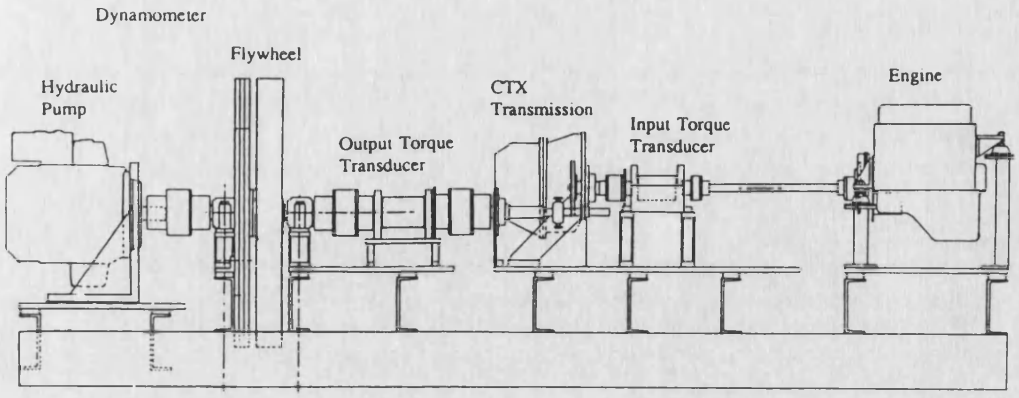

Figure 2.1 CVT powertrain test bed. Scaled sketch

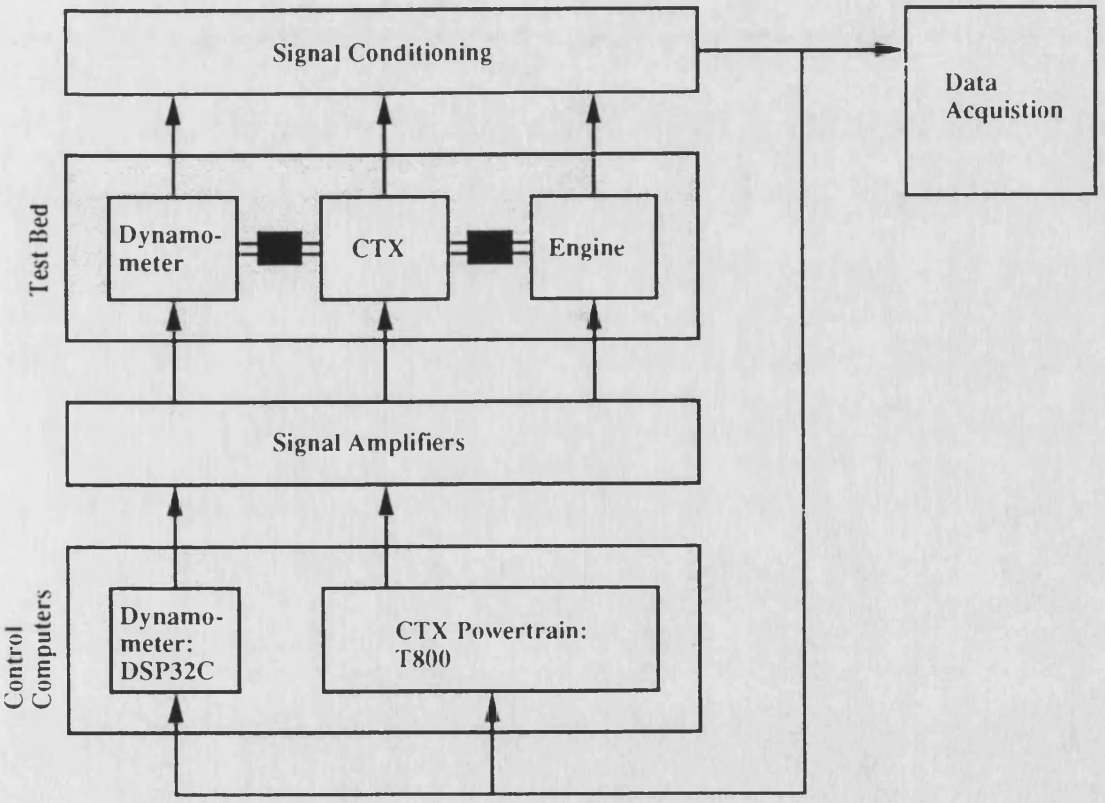

Figure 2.2 Instrumentation of the powertrain test bed

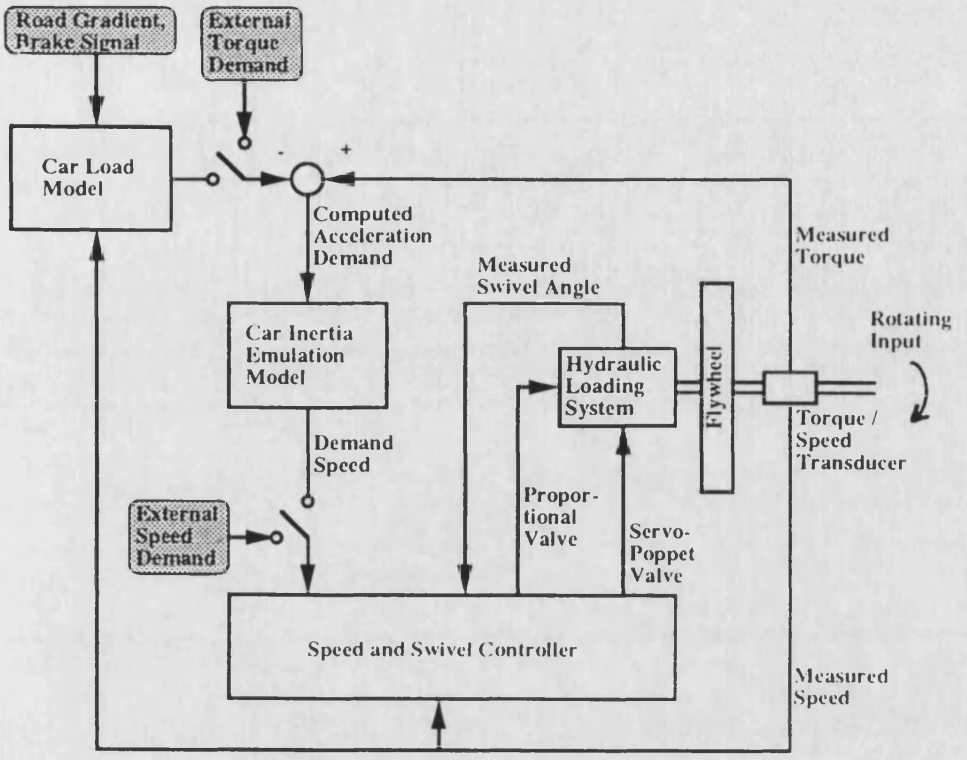

Figure 2.3 Dynamometer operating modes. The switches determine the modes *constant speed* (Ext. Speed Demand), *constant torque* (Ext. Torque Demand) or *car emulation* (Road Gradient, Brake Signal).

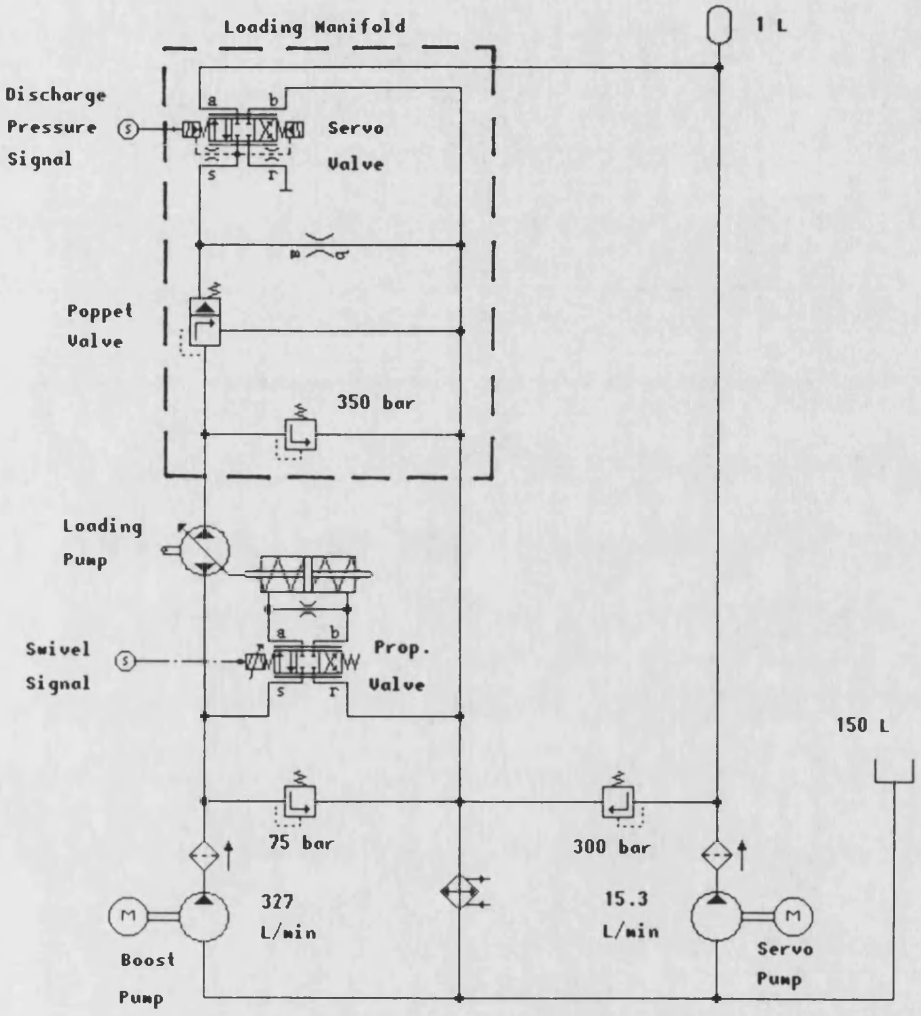

Figure 2.4 Hydraulic circuit of the dynamometer. The loading manifold houses all components to accurately control the discharge pressure of the loading pump.

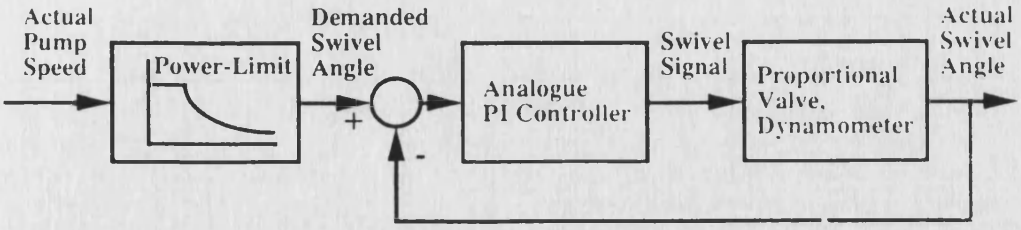

Figure 2.5 Swivel angle control scheme. The flow limitation of the full flow boost pump inflicts a power limitation on the circuit.

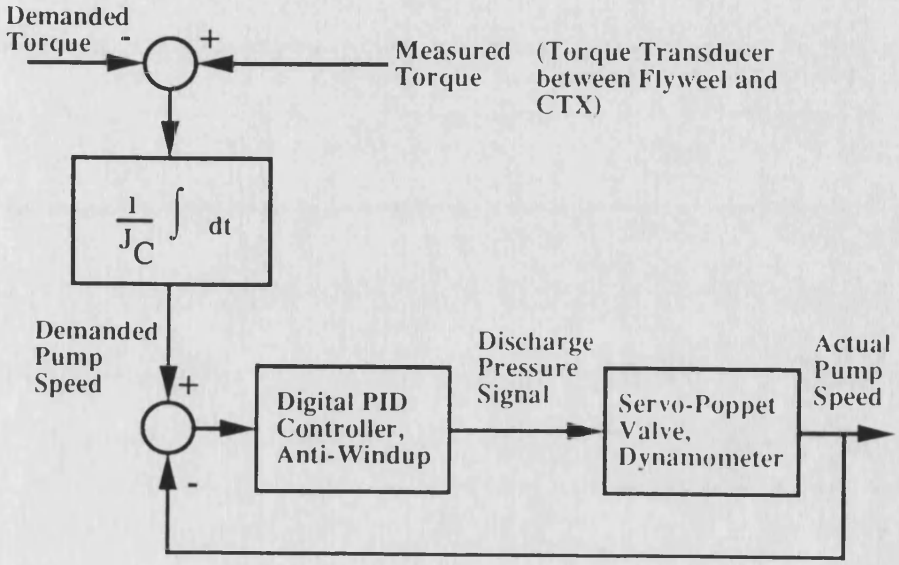

Figure 2.6 Discharge pressure control scheme. The discharge pressure adjusted by the servo-poppet valve controls the speed of the dynamometer.

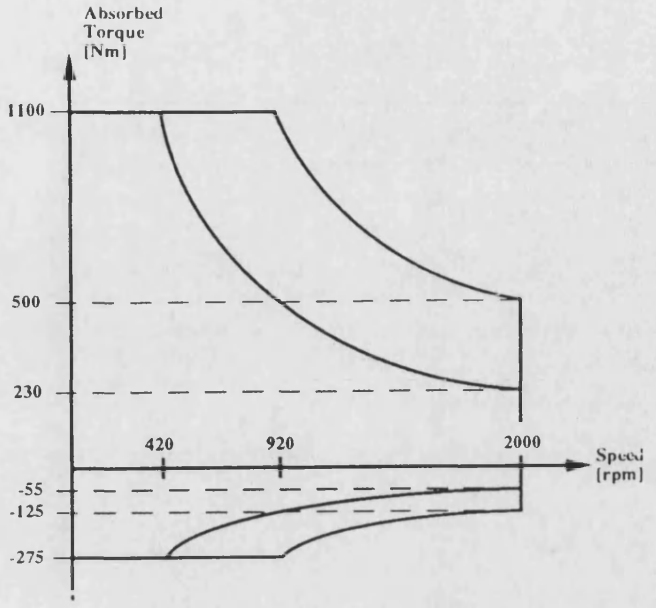

Figure 2.7 Dynamometer operating envelope. The dark area is the implemented envelope (safety margin, see text); the brighter area pictures the maximum possible operating envelope.

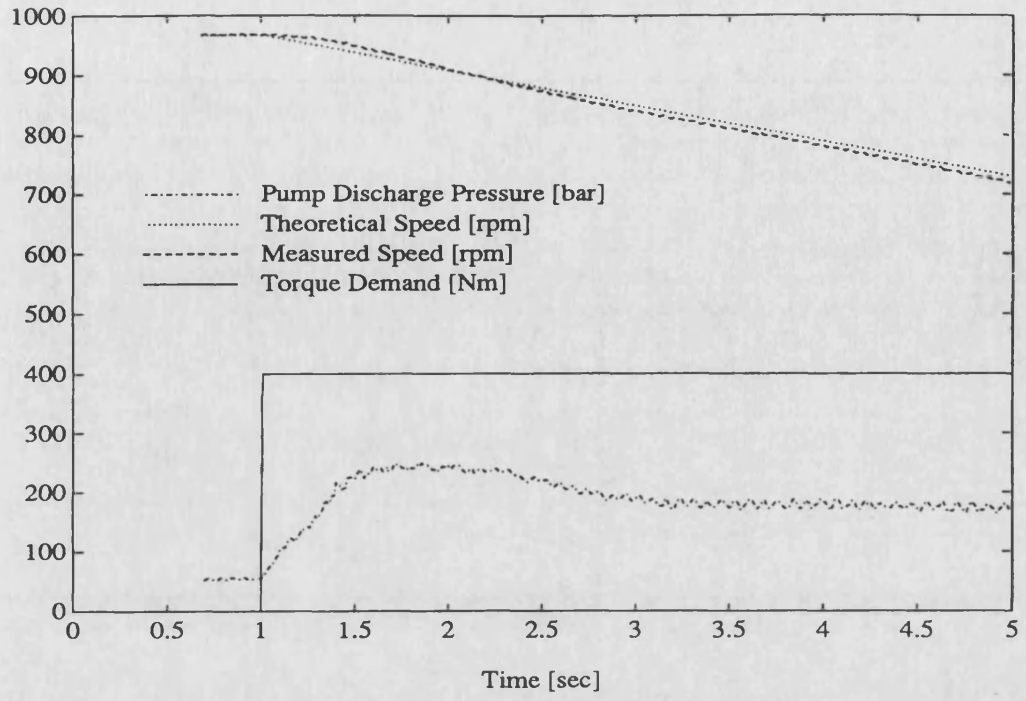

Figure 2.8 Experimental data for torque step demand. The discharge pressure is proportional to the absorbed torque.

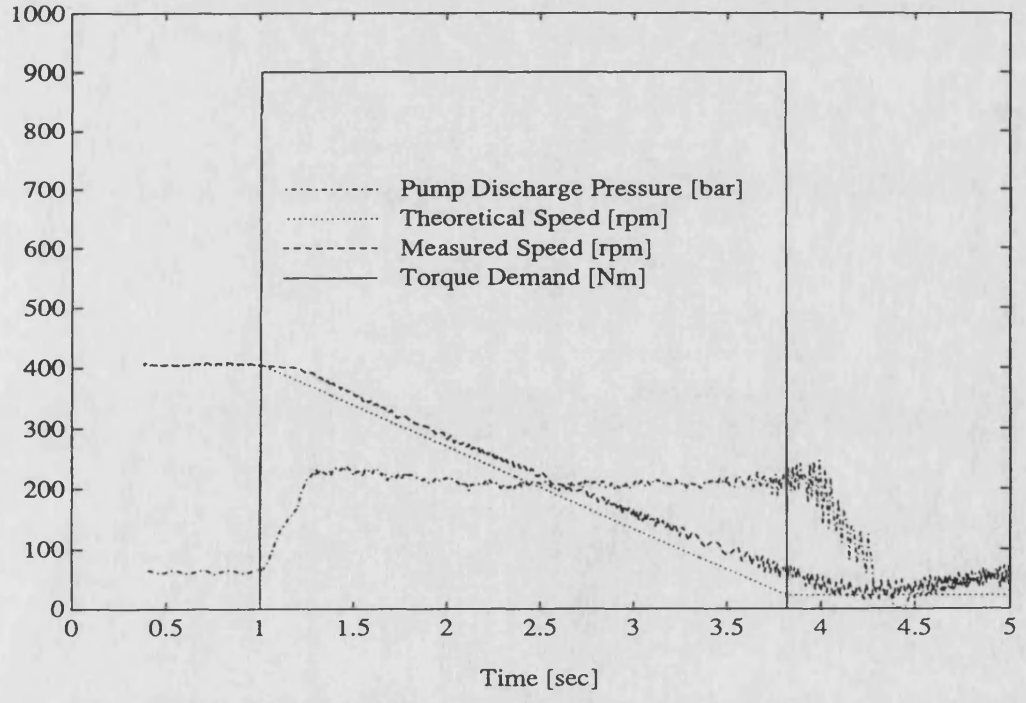

Figure 2.9 Experimental data for torque step demand. The discharge pressure is proportional to the absorbed torque.

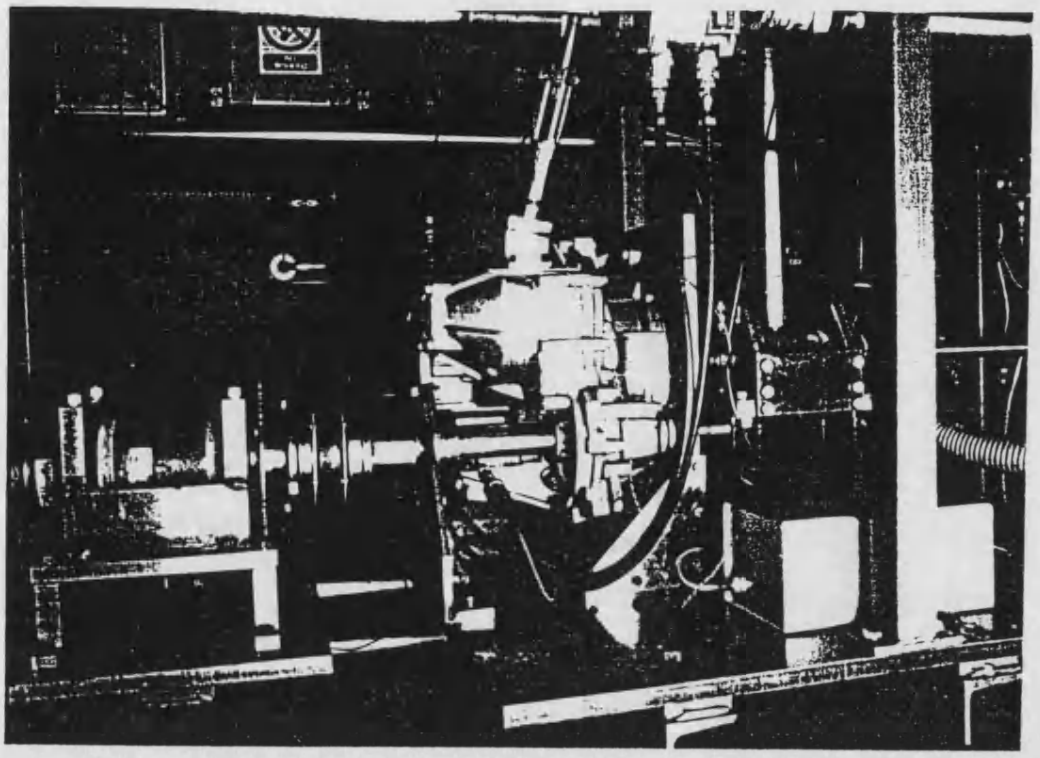

Figure 2.10 Photograph of the CTX instrumentation. The engine is driving from the right.

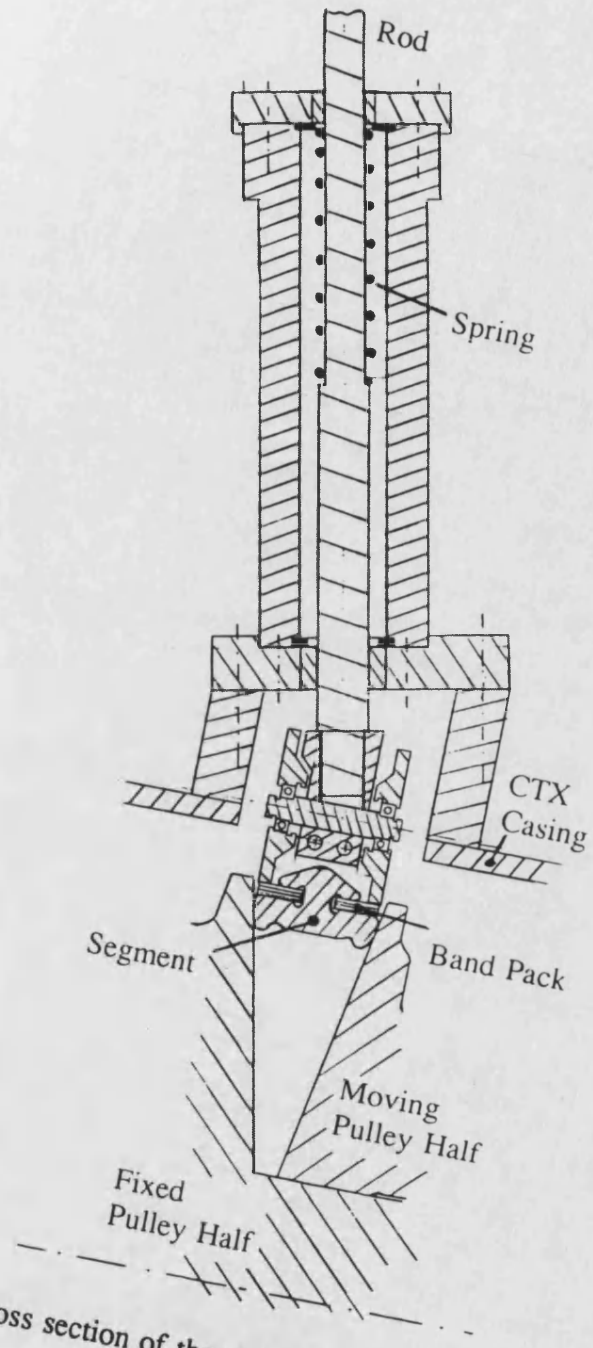

Figure 2.11 Cross section of the active radius measurement transducer

3. THE CTX

A detailed knowledge of the transmission components is essential to support the theoretical analysis and is thus acquired in this chapter. Initial and improved performance have to be compared to judge the success. The assessment of the original CTX in steady state and transient operation is the first step to achieve this. The improved performance is obtained by use of intelligent control strategies implemented on computers. This imposes the application of electro-hydraulic valves which, in turn, will enable the analysis of the CTX to be independent of the employed hydro-mechanical control unit.

Section 3.1 introduces the CTX in detail. The performance measurements of the CTX in its original state are presented in 3.2; steady state efficiency of the transmission, as well as the transient performance and the fuel consumption of the CVT powertrain are determined. Section 3.3 explains the alterations in the hydraulic circuit. Industrial, electronically operated valves in conjunction with computer control replace the hydro-mechanical control unit.

3.1. Operation

Figure 3.1 shows a cross section of the CTX (drawing courtesy of Ford Motor Company Ltd). A metal thrust belt runs between two vee-pulleys. Their axial clamping forces are controlled by hydraulic valves (mounted in the control valve manifold) and cylinders. Corresponding axial movement of the vee-pulleys results in different active radii at which the belt acts, and thus in variable transmission ratio. Two wet plate clutches and an epicyclic gear train provide automatic take-up from rest in forward or reverse gear. A reduction drive feeds the power to the incorporated differential and, subsequently, to the wheels.

VSU

Belt. Figure 3.2 (Figure 3 from Hendriks, 1988) shows the metal thrust belt. The belt consists of 297 thrust segments that are guided along circular paths around the pulleys and straight lines between them by two sets of 10 endless steel bands. This enables power to be transmitted by compression rather than tension. The belt is the performance limiting unit in the transmission. Its rating limits the maximum torque 150 Nm which was the basis for the design of the other components such as the clutch and the final drive. However, an improved 250 Nm belt is currently being developed at Van Doorne (Hendriks, 1993) which can be incorporated in an uprated transmission.

Segment. Figure 3.3 shows a segment. Contact between two neighbouring segments is made through the rocking edge.

AUXILIARY UNITS

Clutch. Figure 3.4 (courtesy of Ford Motor Company Ltd) demonstrates the operation of the clutch assembly. The engine shaft is directly connected to the carrier of the epicyclic gear set. The reverse clutch locks the outer gear. Engagement leads to the direction of rotation depicted by the arrows in Figure 3.4. The forward clutch connects the planet carrier with the sun gear, thus locking up the planetary gear set. It is important to note that the engaging of either clutch results in relative motion of the clutch plates of the other. Although the plates are not pressurised viscous drag takes place in them.

Hydraulic System. The hydraulic power is supplied through a pump running at engine speed (11 in Figure 3.1). All valves are incorporated in the control manifold. The primary and clutch actuators are connected through the pipes running internally in the input shaft (see Figure 3.1). The primary and secondary actuator areas are chosen such that operation is guaranteed with the secondary pressure always greater than the primary one. A pressure relief valve adjusts the pump pressure and thus the secondary pressure. The primary pressure is adjusted using a flow control valve, effectively acting as pressure reducing valve (Röper and Simon, 1987).

Final gear set / differential. Two meshing pairs make up the combined transmission ratio of 5.671.

CONTROL

Transmission ratio and clutch control assembly. The control manifold (10, Figure 3.1) is an implementation of the powertrain controller. The actuation of the clutch, the transmission ratio and system pressure adjustment are supervised according to the driver's demand. Additionally fulfilling safety requirements it is evident that the design of the manifold is very complex. Figure 3.5 demonstrates this. It shows a photograph of the control unit disconnected from the CTX housing. The two ground faces are bolted together with a metal gasket in the middle. Dozens of individual springs, orifices and spool-sleeve assemblies make up the 12 valves that operate the clutch and VSU actuators (Röper et al, 1987). The factors taken into account which modify the control action include the throttle position, the engine and the primary pulley speed and the transmission ratio, as well as the position of the manual selector.

Control Strategy. Three major control tasks are administrated: the clutch, the system pressure and the ratio adjustment.

- The clutch is only disengaged at very low car speeds enabling stopping with the engine running.
- The system pressure is controlled to guarantee safe operating conditions in the belt pulley system. An active belt radius feedback signal is used to compensate the system pressure for overrun conditions. This way the wasted power is limited.
- The transmission ratio is adjusted according to the driver's demand. The fed-in throttle position indicates this, whereupon the controller modulates the engine load by adjusting the primary pressure and, consequently the transmission ratio. The engine is operated close to a specified operating line (Röper, 1989).

TRANSMISSION FLUID

The transmission fluid provides lubrication (belt/pulley and gears). Additionally, it is the hydraulic power medium for the axial cylinders of the vee-pulleys and serves as cooling liquid. An externally installed cooler acts as heat exchanger.

3.2. Performance

The efficiency and the performance of the CTX in its initial configuration are assessed. The performance is expressed as a calculated fuel consumption for the steady state and the rate of change of transmission ratio dynamically. The disappointing efficiency of the transmission prompted further investigations leading ultimately to the control strategy described in Chapter 6.

3.2.1. Efficiency of the CTX

Figure 3.6 shows the measured overall steady state efficiency of the CTX. The dynamometer was operated in constant speed mode while the engine torque was set by means of adjusting the engine throttle angle. The hydro-mechanical controller adjusted the operating conditions, i.e. hydraulic pressures, and thus engine speed. The efficiency peaks at under 90%. At extreme operating conditions the efficiency is below 50%. This, predominantly, takes place at low engine torques and suggests a relatively large power loss at this condition.

The efficiency map comprises effects from power train control and the efficiency of the transmission. The first point determines the engine speed and torque that influence the efficiency through the auxiliary units; the latter is considered in more detail.

Slip. A direct loss of efficiency is caused by the slip in the VSU. Figure 3.7 shows the measured slip values for the data presented in Figure 3.6. Note that Figure 3.7 is rotated by +90° about the vertical axis to enable a better view of the surface. Between

5% and 7% of the transmitted power lost at low car speeds is due to the slip of the VSU.

Hydraulic supply. The lowest efficiencies in Figure 3.6 at low engine torques indicate the presence of substantial losses at these operating conditions. Apart from the low efficiency of the gears in the final drive the hydraulic pump consumes a large amount of power. Figure 3.8 shows the pump losses for the same data. A constant efficiency of 0.6 was assumed for the hydraulic pump (4.2.3). Figure 3.8 is rotated a further +90° about the vertical axis as compared to 3.7.

INTERPRETATION

The efficiency of the CTX is disappointingly low. This particularly applies to low engine torque conditions. A series of power losses are encountered, namely through the clutch, the VSU including the hydraulic pump and the final gear set, and dominate at small throughput power reducing the efficiency considerably. Figures 3.7 and 3.8 confirm the large influence of the adjusted operating conditions in the VSU. This prompted the detailed study of the VSU leading to an optimum efficiency control (6.2).

3.2.2. Fuel Consumption of the CTX Powertrain

The adjusted engine speed for the steady state test in the previous section is pictured in Figure 3.9. The hydro-mechanical control unit is the implementation of the proposed ideal operating line strategy outlined in 3.1 and Röper (1989). The adjustment of the engine speed should lead to minimum consumption. Figure 3.10 shows the average fuel flow for the previous data. Data from Appendix B were taken to interpolate the presented data. The engine speed and the delivered torque determined the operating condition and hence the fuel flow.

INTERPRETATION

The fuel flow data from Figure 3.10 will later be taken to compare the performance of the improved controller (Chapter 6). The typical measurement to quantify the performance of a powertrain is usually the consumption per mileage (or the reciprocal respectively). This application would have involved the operation of the powertrain through a standard driving cycle and was outside the scope of this study.

3.2.3. Transient Behaviour of the CTX Powertrain

A CVT allows the engine to be operated in its most efficient operating conditions. This results in operating points typically described by low speed / high torque. Additional power has to be developed on the driver's command to accelerate the car. This can only be done by increasing the engine speed since power output is near maximum for the actual engine speed (high torque). Thus, the ability to change the transmission ratio quickly plays an important role. This section investigates this for the hydro-mechanical control unit.

The transient test in response to a driver's step increase is investigated. Figure 3.11 shows the CTX powertrains's response to throttle step demands to 20°, 40°, 60° and 90°. The steady initial car speed is in each case about 11 m/s (25 mph). The dynamometer was operated in car emulation mode. Data for acceleration from stand still are presented in Guebeli (1992, Appendix A). The actuation of the clutch can be observed in there.

INTERPRETATION

Transient capability. The rate of change of transmission ratio is excellent (see bottom graph) giving only a small lag time until the engine speed increases.

The Operating line strategy has not been correctly implemented, as can be seen from the second graph (increasing engine speed). The operating line relates a throttle angle to an engine speed and the control system should ensure that this speed is maintained.

The second graph in Figure 3.11 shows that although the throttle angle has been kept constant after the induced step the engine speed varies. The hydro-mechanical implementation - bearing in mind all requirements for safety, as well as the additional control of the clutch and lubrication - imposes obvious limits.

3.3. Electro-Hydraulic Circuit

The hydro-mechanical control unit lacks the flexibility needed to provide data to analyse the VSU and to implement enhanced control strategies. External control over the clamping forces improves these shortcomings.

The developed electro-hydraulic circuit enables the adjustment of both clamping forces. Additional tasks managed by the hydro-mechanical control unit, such as clutch control and lubrication, are implemented on a separate system. This leads to a much wanted simplification. Some characteristics of the hydro-mechanical system are first examined.

Given dimensions. The areas of the primary and secondary actuators are given. These would be the main design factors and their adoption needs justification. This is in spite of the fact that it is not feasible to alter them. The absolute size of one area can be chosen in accordance with the planned operating pressure. The ratio between the two areas is crucial. Simple equilibrium considerations lead to

$$\frac{F_p}{\beta_p} = \frac{F_s}{\beta_s} \tag{3.1}$$

where β is the angle of lap around one pulley. Taking the given ratio $A_p/A_s = 2.04$ into account and considering the two extreme cases of minimum and maximum primary radius gives

$$R_{p,\min} = 28.8 \text{ mm:} \qquad p_p = p_s \frac{A_s}{A_p} \frac{\beta_p}{\beta_s}\bigg|_{R_p = R_{p,\min}} = p_s \cdot 0.33$$

$$R_{p,\max} = 72.6 \text{ mm:} \qquad p_p = p_s \frac{A_s}{A_p} \frac{\beta_p}{\beta_s}\bigg|_{R_p = R_{p,\max}} = p_s \cdot 0.7 \tag{3.2}$$

where β_p/β_s is a function of the primary radius, R_p, and can be computed using equations (4.3) and (4.4). This means that for

$$p_s \cdot 0.33 \leq p_p \leq p_s \cdot 0.7 \tag{3.3}$$

the whole ratio range can be adjusted and thus the secondary pressure can always be greater than the primary.

Limits of rate of change of transmission ratio. Röper (1987) formulated the flow requirements to satisfy the pre-specified rate of change of transmission ratio. The installed pump is the one specified by him. He notes correctly that the ratio changes only when corresponding pressures on the primary and secondary cylinder act. Therefore, there exists a pressure dictated limit of the rate of change. Based on Becker's theory (1987) Röper determines minimum secondary pressures to guarantee the wanted rate of change. The new theory developed in chapter 5 contradicts his statements.

Within this framework it is understood that the secondary area was chosen smaller than the primary. This led to equation (3.3) and thus an implementation where the secondary pressure is equal to the pump discharge pressure (see 3.1). This, in turn, gave the controller the freedom to set the secondary pressure independent of the primary in an event of ratio change towards first gear which is the most desired characteristic.

Hydraulic circuit. Figure 3.12 shows the altered hydraulic circuit to externally adjust the clamping forces of the VSU. Equation (3.3) guarantees that all operating conditions can be achieved having the secondary pressure always greater or equal to the primary one. This results in a straight forward pressure relief - pressure reduction assembly. Both electronically controlled valves are industrial off-the shelf types. The external pump supplies a constant flow rate equivalent to the internal one at 5000 rpm. The internal pump is disabled.

Implementation. Vickers valves were chosen.

Primary valve:	KFDGV-3-02C20N-Z-M-U1-H7-20 proportional directional control valve, single-stage design with spool position feedback 20 L/min at Δp = 5 bar, bandwidth 50 Hz
Secondary valve:	CGEV-6BK-3-U-H-10 two-stage pressure relief valve, electronic proportional control rated for 200 L/min, 70 bar maximum pressure, typical rise time 0.15 s

In terms of industrial hydraulics extremely low operating pressures had to be achieved (see Chapter 6). Careful considerations prevented the build-up of a too high back pressure.

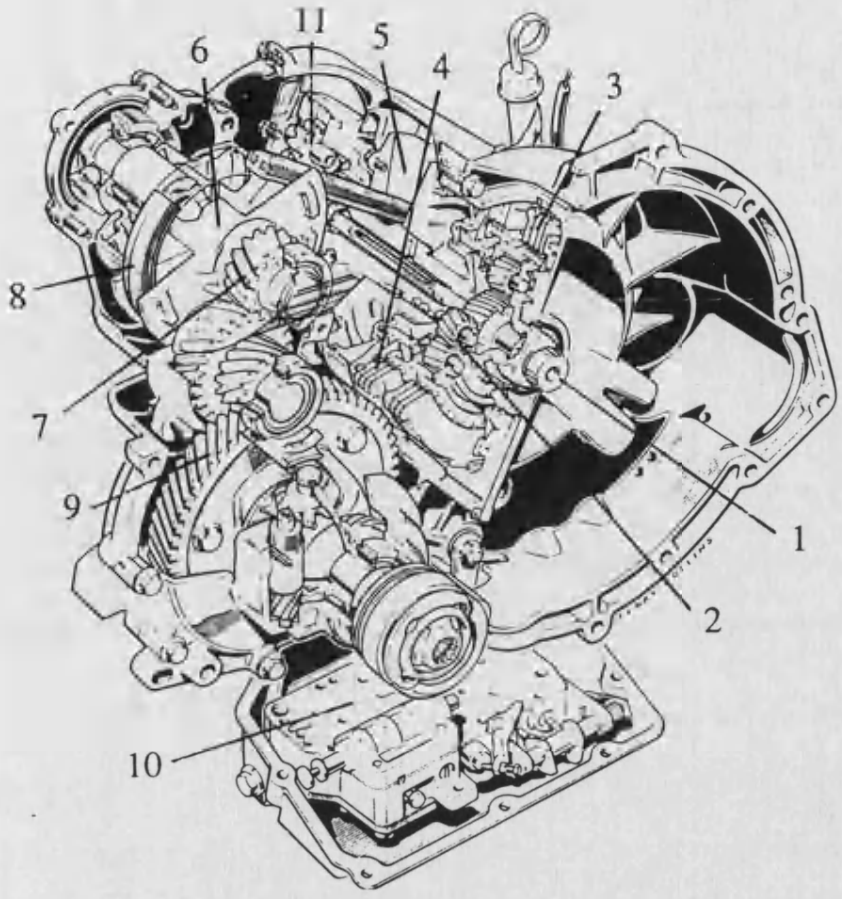

1:	Input Shaft	2:	Planetary Gear Set
3:	Reverse Clutch	4:	Forward Clutch
5:	Primary Pulley	6:	Secondary Pulley
7:	Reduction Drive	8:	Metal Thrust Belt
9:	Final Drive, Differential	10:	Control Valve Manifold
11:	Hydraulic Pump		

Figure 3.1 Cross section of the CTX (courtesy of Ford Motor Company Ltd)

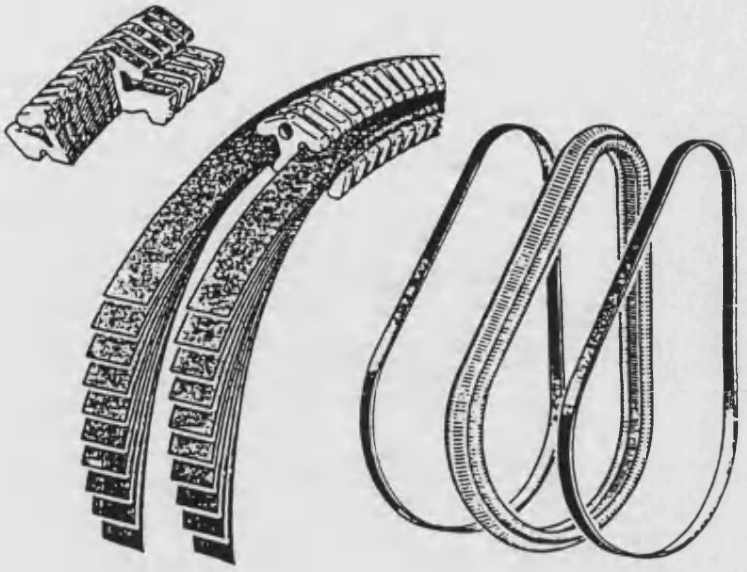

Figure 3.2 The Van Doorne belt. The thrust segments are hold together by two packs of endless bands.

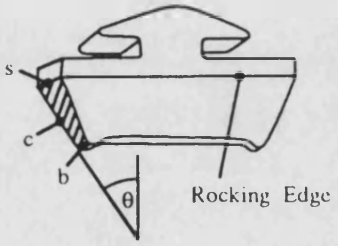

Figure 3.3 Belt segment. The sliding contact area is marked.

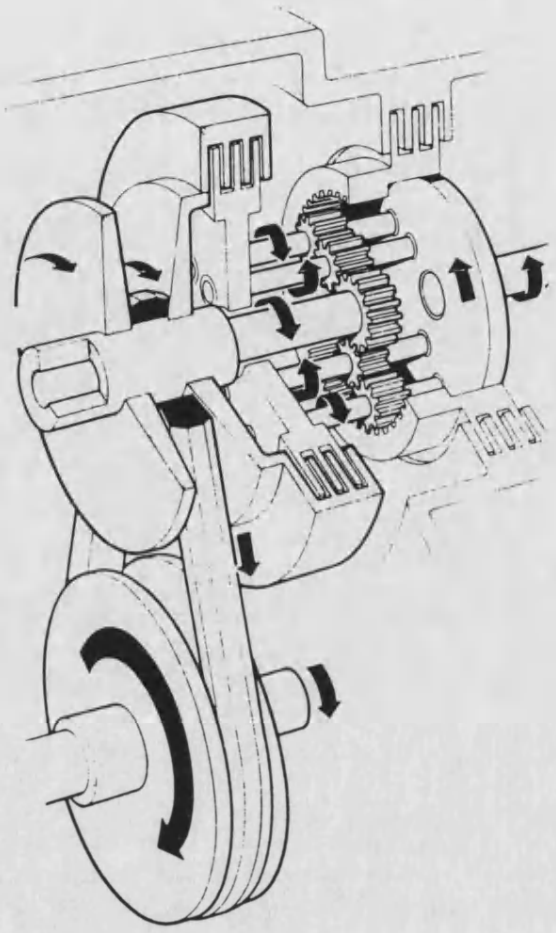

Figure 3.4 Forward and reverse clutch with planetary gear set. The direction of the arrows symbolises reverse driving. The reverse clutch locks the outer gear.

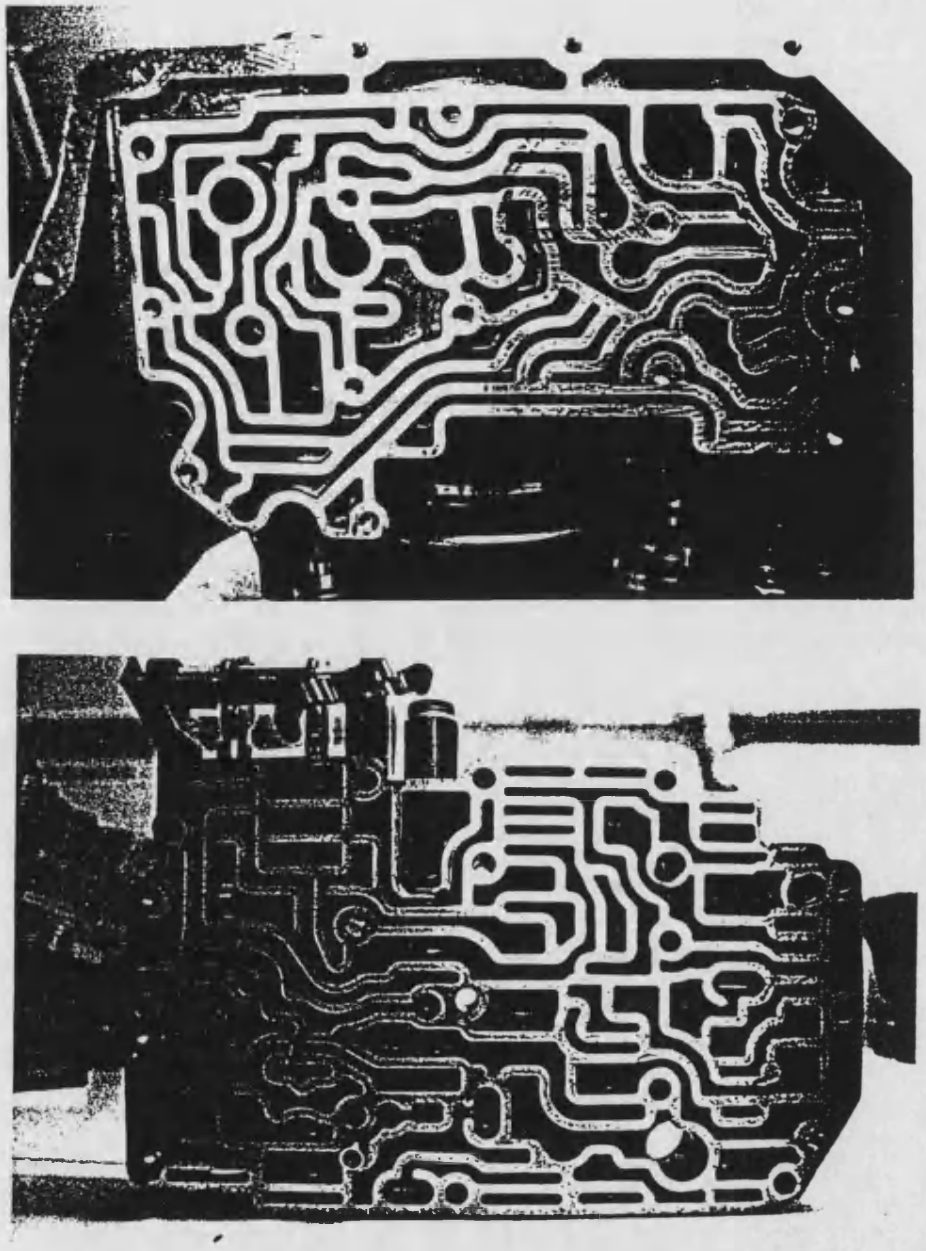

Figure 3.5 Interface between control manifold and CTX casing. The control manifold (below) houses all valves. The two faces are bolted together "sandwiching" a gasket plate.

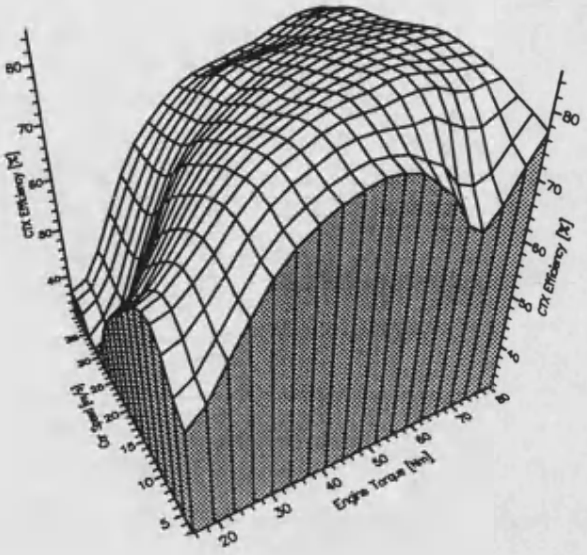

Figure 3.6 Steady state efficiency of the hydro-mechanically controlled CTX. The efficiency peaks just under 90% for high engine torque and moderate car speed.

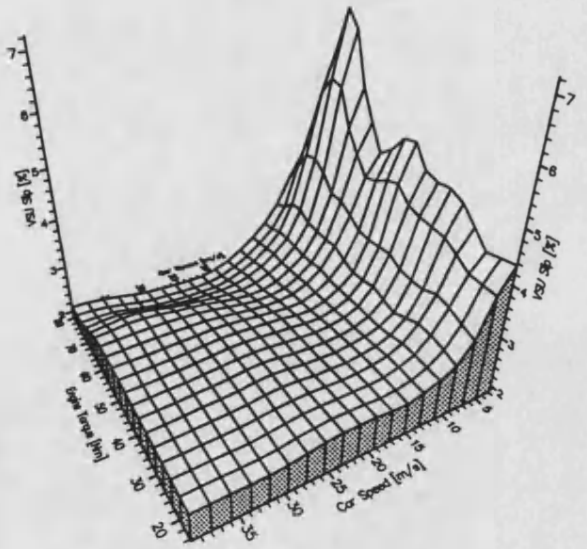

Figure 3.7 Measured steady state VSU slip. At low car speeds the slip increases with engine torque, whereas at high car speeds the slip reduces.

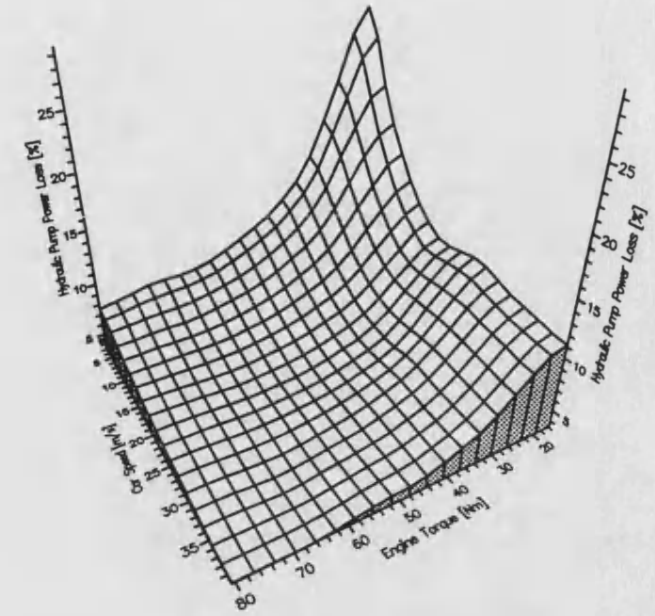

Figure 3.8 Hydraulic pump power loss in percent of input power. The consumed power by the pump at low engine torque is considerable.

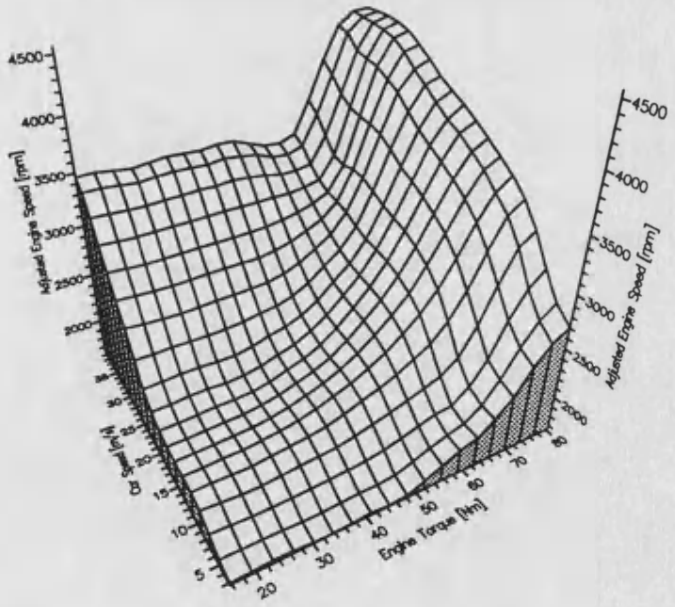

Figure 3.9 Adjusted engine speed by the hydro-mechanical control unit. The controller attempts to adjust low speed / high torque engine conditions. This leads to good consumption values.

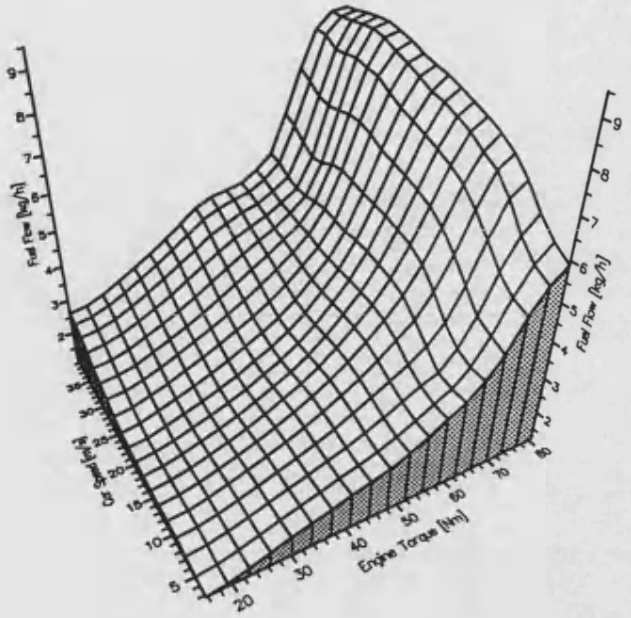

Figure 3.10 Average steady state fuel flow. The engine operating point adjusted by the hydro-mechanical control unit determines the fuel flow.

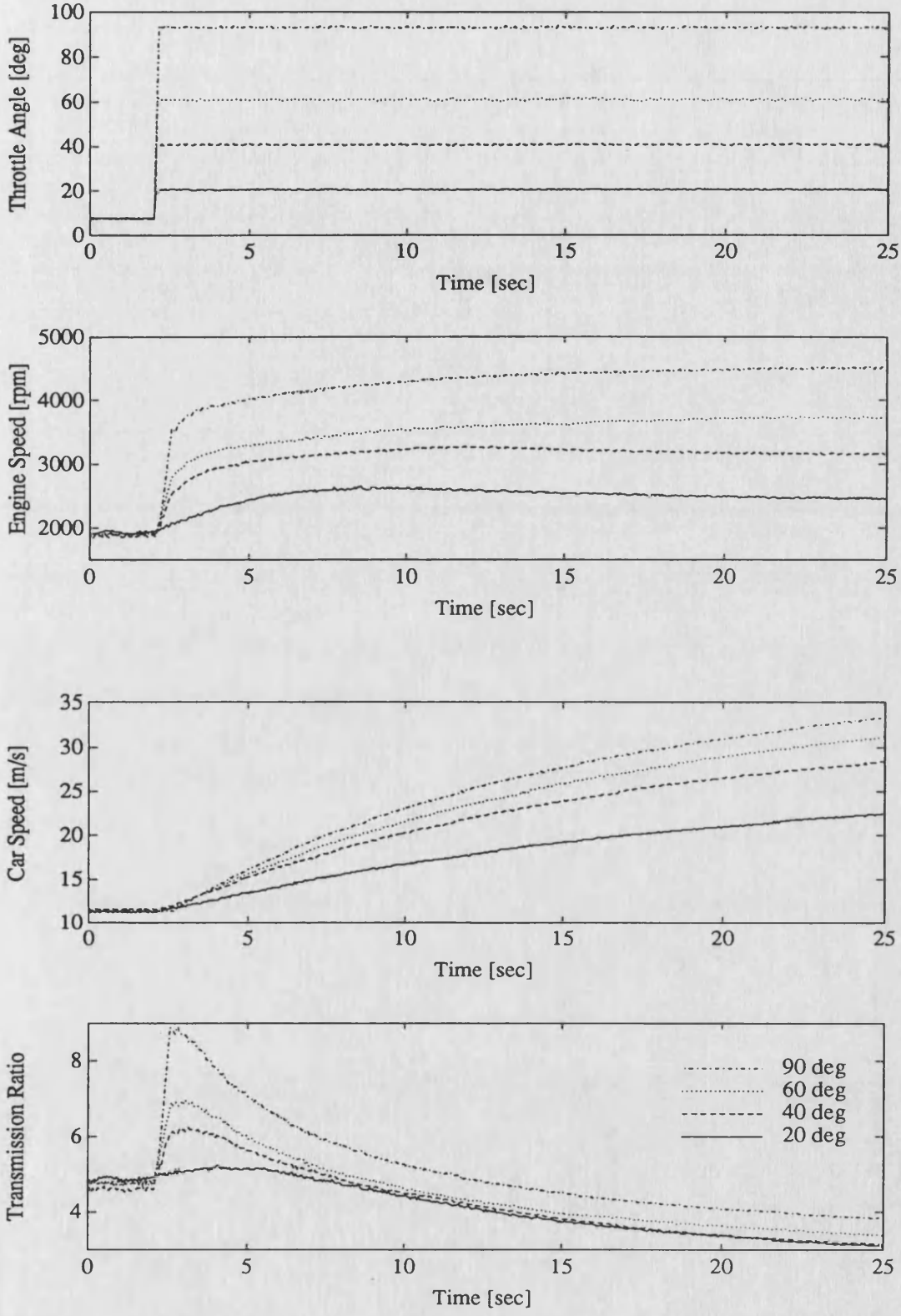

Figure 3.11 Response of CTX powertrain on throttle step demands. The rate of change of transmission ratio is considerable; the implementation of the ideal operating line leaves much to be desired.

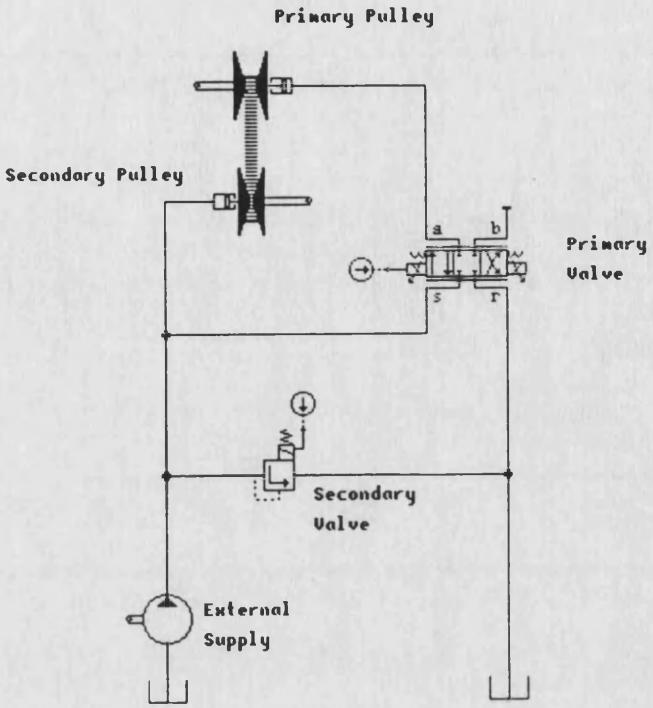

Figure 3.12 Electro-hydraulic circuit. The secondary pressure controlled through a pressure relief valve; the primary is set by a flow valve, in this configuration acting as a pressure reducing valve.

4. MATHEMATICAL MODELLING OF THE POWERTRAIN COMPONENTS

This chapter describes the physical modelling of the powertrain components. These component models describe the engine, transmission and vehicle characteristics. The transmission model is sub-divided into the Van Doorne VSU and then the additional components to give the Ford CTX unit. The aim is an accurate and, at the same time, easily structured system that enables the subsequent analysis. The validation of the chosen structures and the determination of system specific constants are presented in chapter 5. The subsequent chapters use the validated models to synthesize new, improved designs.

The model of the VSU based on a viscous shear power transmission phenomenon is presented in 4.1. Section 4.2 looks at the CTX transmission. Power losses accumulated in different subcomponents (clutch, final drive/differential) are modelled accurately. Section 4.3 presents methods to model an internal combustion engine. Models of the wheel-road interaction and the car are developed in 4.4.

Significance of individual models. The analysis of the mathematical models assists the tackling of two issues: the efficiency optimisation of the CTX and the transient capabilities of the powertrain. The pursuit of these issues forced the development of two novel models used along-side already existing ideas. These were the models of the belt-pulley system (section 4.1) and the engine (section 4.3). Original theoretical work that led to these two models is presented in this chapter. Generalised models gained from published material included the final drive/differential and the hydraulic pump. Models of hydraulic components were offered by Bath*fp* (Chapter 5), and are not described here.

Powertrain dynamics terminology. Figure 4.1 shows the free-body diagrams of the mechanical components of the CTX powertrain clarifying the nomenclature.

Inertias. The inertia of the primary pulley is lumped into the engine inertia, J_E; the inertia of the secondary pulley is lumped into the final drive inertia, J_D. The only included belt inertia forces are those due to centripetal accelerations of the belt.

4.1.1. Viscous Shear Stress Model

Micklem (1991) introduced the viscous shear stress approach. He recognised that correct values for the slip are obtainable with this approach. Results gained from using a Coulomb friction phenomenon (Becker, 1987) used an unrealistic stiffness of the belt to fit the slip data.

Nature of the phenomenon. The presence of an oil film between belt and pulleys in conjunction with high pressures in these films is responsible for the effect. When an oil film is virtually squeezed out metallic surfaces are protected by additive molecules contained in the oil. The thin layers (several molecules thick) behave in a viscous manner with a corresponding viscosity very much greater than that of the bulk of the oil.

Preliminary explanations introduce the assumptions and establish the kinematics and relations in the oil film. Equations of motion are formulated for one pulley only. They are evaluated in radial and in longitudinal belt directions. Subsequently, the equations are interpreted for both pulleys. Their combination leads to the viscous shear stress model.

ASSUMPTIONS

Assumption S1: Shear stress in the oil film. The power is transferred between the pulleys and the belt by means of a viscous shear stress (Micklem et al, 1991)

$$\tau = \eta \frac{v_{rel}}{t} \tag{4.1}$$

where v_{rel} is the relative velocity between the two sliding members and η is an

4.1. The Van Doorne VSU

Of all power transmission components within the considered CVT powertrain the *Van Doorne Variable Speed Unit* is the least understood and, in terms of efficiency control, the most influential. This is due to the arbitrary setting of one clamping force determining the operating conditions (e.g. slip).

The presented model consists of two parts and is based on Micklem's (1990, 1991) ideas. The *viscous shear stress model* (4.1.1) defines the distinct load-slip relationship of the VSU. Micklem (1991) showed that models based on a Coulomb friction phenomenon (Becker, 1987, Gerbert, 1984, Sun, 1988) did not determine measured slips satisfactorily. This prompted the development of the viscous shear theory. Experimental slip measurements confirmed the theory but showed at the same time that further losses were encountered. These further losses are described by the second part of the model: the *torque loss model* (4.1.2). This model accounts for the necessary work to force the belt out and into the vee-pulleys which has a negative influence on the efficiency.

THE SIMPLIFIED SYSTEM

Ideal system. The structural characteristics of the belt pulley system are assumed to be ideal, i.e. no deformation under any load takes place. The belt moves in a circular path when engaged with a pulley.

Uniform belt structure. Figure 4.2 shows the segments guided around the pulleys by the bands. The contact between them is the rocking edge (Figure 3.3) which defines the *active radius*. Gaps between the segments occurring in the slack bit of the belt have been shown to have no influence on the performance. They are "used" up when they enter the driving pulley again. This is due to the faster travelling of the bands. The segments are under compression around the pulleys and along the compressed belt, and therefore, the belt can be treated as a *uniform structure*. Additionally, the shear connection between the bands and the segments is assumed negligible.

empirical parameter.

Assumption S2: The thickness of the oil film is assumed to be

$$t = \frac{k_t}{p_{mean}} \tag{4.2}$$

where p_{mean} is the mean oil pressure and k_t is an empirical parameter.

The physical process describing the thickness of the oil film must be of elasto-hydro-dynamic (EHD) nature. Within the EHD theory the thickness of the oil film depends much more on the relative velocity of the sliding members (i.e. the slip) than on the pressure in the oil film. This is accounted for by considering the ratio k_t/η dependent on the active primary radius, R_p, which is a crude measure for the slip (5.1.1). This term is defined as the *viscous shear parameter* and results from inserting (4.2) in (4.1). The approximation immensely simplifies the subsequent analysis.

BELT

The active radius is defined to the rocking edge of the segments (Figure 3.3).

Kinematics. Figure 4.3 shows the idealised belt geometry. R_p and R_s are related through the kinematic constraint

$$L = R_p\beta_p + R_s\beta_s + 2\sqrt{X^2 - (R_s - R_p)^2} \tag{4.3}$$

where

$$\begin{aligned} &\beta_p = \pi - 2\alpha\,, \quad \beta_s = \pi + 2\alpha \\ &\sin\alpha = \frac{R_s - R_p}{X} \end{aligned} \tag{4.4}$$

For v_{Rp} and v_{Rs} holds

$$v_{Rs} = - v_{Rp} \frac{\beta_p}{\beta_s} \quad \text{with:} \quad v_{Rs} = \dot{R}_s \qquad v_{Rp} = \dot{R}_p \tag{4.5}$$

Segment. The sides *s*, *b* and *c* in Figure 3.3 are used to designate the contact area between the segment and the pulley. Although the belt is assumed uniform the contact area plays an important role in the determination of the characteristics.

THICKNESS OF THE OIL FILM

The mean pressure in the oil film is

$$p_{mean} = \frac{\dfrac{F}{\cos\Theta}}{\dfrac{c(s+b)}{2}\,\dfrac{R\beta}{s}} \tag{4.6}$$

The numerator is the perpendicular force component (Figure 3.4, $\delta N \cos\Theta = \delta F$), whereas the denominator is the contact area between the pulley and the belt consisting of the number of engaged individual segment areas (Figure 4.3, sliding contact area). The effect of the radial viscous shear force is neglected (see later *RADIAL EVALUATION*). Introducing

$$A_c = \frac{1}{2} c \cos\Theta (s + b) \tag{4.7}$$

as the radial component of the segment's sliding contact area, and

$$r = \frac{R\beta}{s} \tag{4.8}$$

as the number of engaged segments and substituting p_{mean} in (4.2) (Assumption S2) gives

$$t = rA_c \frac{k_t}{F} \tag{4.9}$$

This equation describes the relation between the clamping force and the oil film thickness.

RADIAL EVALUATION

Figure 4.4 shows the belt pulley free body diagram of a thin element of a sector angle $\delta\gamma$. All forces influencing the motion of the belt in radial direction are drawn. The belt is treated as a continuum; respective corrections to uniformly distribute the sliding contact area have to be made. The radial equation of motion for the belt and the axial equation of motion for the pulley half are formulated. δG is the radial component of the shear force and needs some explanation first.

In the limit as δ tends to zero δx tends to dx. Therefore, the equations of motion are formulated in terms of the infinitesimal operator d.

Radial shear force component dG. The viscous shear stress (Assumption S1, equation (4.1)) in radial pulley face direction multiplied by the corresponding area gives the force dG.

$$dG = \eta \frac{\frac{v_R}{\cos\Theta}}{t} dA \tag{4.10}$$

The contact area of a segment has to be considered when determining dA. The average radial thickness of the contact area of the belt is the segment area divided by the segment thickness s.

$$dA = R d\gamma \frac{A_{Segment}}{s} \quad , \quad A_{Segment} = \frac{c(s+b)}{2} \tag{4.11}$$

where $Rd\gamma$ corresponds to the infinitesimal width of the belt sector. Combining

equations (4.10) and (4.11) gives

$$dG = \eta \frac{v_R}{t} \frac{Rc(s+b)}{2s\cos\Theta} d\gamma \tag{4.12}$$

Radial contribution of U and C. The tension U and the compression C affect the belt in the radial direction.

$$dU_{radial} = 2U \sin\frac{d\gamma}{2} \tag{4.13}$$

It holds ($d\gamma$ is infinitesimal)

$$\sin\frac{d\gamma}{2} = \frac{d\gamma}{2} \tag{4.14}$$

and thus

$$dU_{radial} = 2U\frac{d\gamma}{2} = U\,d\gamma \tag{4.15}$$

The same calculations apply to C. According to the simplifications and assumptions, the compression builds up uniformly (or decreases) during engagement in the two pulley halves. C_C is the compression in the straight compressed belt part.

$$dC_{radial} = C_C \frac{\gamma}{\beta} d\gamma \tag{4.16}$$

Radial equation of motion for belt. The sum of the radial forces acting on the belt inwards and outwards must be equal. The centripetal force is included.

$$U\,d\gamma + 2\,dG\cos\Theta = C_C\frac{\gamma}{\beta}d\gamma + 2\,dN\sin\Theta + \frac{v_L^2}{R}\,m\,d\gamma\,R \tag{4.17}$$

Axial equation of motion for pulley half.

$$dN\cos\Theta + dG\sin\Theta = dF \tag{4.18}$$

Eliminating dN from the two above equations and combining the dG terms gives

$$U\,d\gamma - C_C\frac{\gamma}{\beta}d\gamma - 2\,dF\tan\Theta + 2\eta\frac{v_R}{t}\frac{R(s+b)c}{2s\cos^2\Theta}d\gamma - v_L^2\,m d\gamma = 0 \tag{4.19}$$

The substitution

$$h = \frac{(s+b)c}{2s\cos^2\Theta} \tag{4.20}$$

is introduced. The *integration from 0 to* β of equation (4.19) gives ($dF = Fd\gamma/\beta$, uniform distribution)

$$U - \frac{C_C}{2} - \frac{F\,2\tan\Theta}{\beta} + 2\eta\frac{v_R R}{t}h - v_L^2\,m = 0 \tag{4.21}$$

LONGITUDINAL EVALUATION

The longitudinal evaluation of the equation of motion yields the viscous shear relation connecting the transmitted torque with the slip speed. The transmitted torque determines the compression in the straight path of the belt.

Torque from viscous shear stress. The only tangential force acting on the belt is the viscous shear force. The application of the viscous shear principle (Assumption S1) yields a relation between the applied pulley torque and the slip speed. Taking the arrangement in Figure 4.5, the torque transmitted through the oil film is

$$T = 2\,r\int_{x=R-c\cos\Theta}^{R} x\,dF_{Shear} \tag{4.22}$$

where the integral can be understood as the torque resulting from one segment area. r is the number of engaged segments. dF_{Shear} is expanded using equation (4.1) (Assumption S1)

$$dF_{Shear} = \frac{\eta}{t}\left(nx - \frac{v_L}{R}x\right)dA \tag{4.23}$$

where the expression in the bracket corresponds to the relative speed between the segment and the pulley (nx is the pulley speed at radius x, $(v_L / R)\,x$ is the segment speed at radius x). dA is the infinitesimal area marked in Figure 4.5 and can be expressed as a function of x

$$dA = \left(\frac{b-s}{c\cos\Theta}(R-x) + s\right)\frac{dx}{\cos\Theta} \tag{4.24}$$

Inserting (4.23) and (4.24) in (4.22) yields

$$T = 2r\frac{\eta}{t}\left(n - \frac{v_L}{R}\right)\int_{R-c\cos\Theta}^{R} x^2\left(\frac{b-s}{c\cos\Theta}(R-x) + s\right)\frac{dx}{\cos\Theta} \tag{4.25}$$

Making the substitution

$$\begin{aligned} q &= 2\int_{R-c\cos\Theta}^{R} x^2\left(\frac{b-s}{c\cos\Theta}(R-x) + s\right)\frac{dx}{\cos\Theta} \\ &= c(s+b)R^2 - \frac{2}{3}c^2\cos\Theta(s+2b)R + \frac{1}{6}c^3\cos^2\Theta(s+3b) \end{aligned} \tag{4.26}$$

gives

$$T = \frac{\eta}{t}\left(n - \frac{v_L}{R}\right)rq \tag{4.27}$$

Compression on straight path of belt. Only the transmitted torque through the oil film influences the compression in the belt. This is due to the idealised structure of the belt.

$$C_C = \frac{T_p}{R_p} = -\frac{T_s}{R_s} \tag{4.28}$$

THE VISCOUS SHEAR STRESS MODEL

The application of the above equations to the primary and secondary pulley yields the model equations describing the power transmission through the belt-pulley system.

Radial. The interaction between the two clamping forces tensions the belt and, in turn, determines the radial dynamics of the belt. Equation (4.21) can be applied to both pulleys yielding

$$\frac{2\tan\Theta F_p}{\beta_p} - 2\eta h\frac{v_{Rp}R_p}{t_p} = \frac{2\tan\Theta F_s}{\beta_s} - 2\eta h\frac{v_{Rs}R_s}{t_s} \tag{4.29}$$

Equations (4.5) and (4.9) are used to extract the radial belt equation (elimination of v_{Rs}, t_p and t_s)

$$\dot{R}_p = \frac{\tan\Theta A_c k_t}{h\eta s}\,\frac{F_p - \frac{\beta_p}{\beta_s}F_s}{F_p + F_s} \tag{4.30}$$

An important conclusion from this equation is the evaluation in steady state. In steady state dR_p/dt must be zero. This leads to

$$F_p = \frac{\beta_p}{\beta_s}F_s \tag{4.31}$$

This equation will be important in chapters 5 and 6.

Longitudinal. The longitudinal belt problem characterises the relation between the input and output speeds and transmitted torques. This follows directly from equation (4.28).

$$T_p = -T_s \frac{R_p}{R_s} \tag{4.32}$$

Equation (4.27) can be applied to the primary and secondary pulley. These two equations can be used to eliminate the longitudinal belt speed, v_L. Using (4.9) to substitute for the oil film thickness leads to

$$n_p = \frac{R_s}{R_p} n_s - \frac{A_c k_t}{\eta} \left(\frac{R_s T_s}{R_p q_s F_s} + \frac{R_p T_s}{R_s q_p F_p} \right) \tag{4.33}$$

Equations (4.30) and (4.33) both contain the ratio of the empirical parameters k_t/η. As discussed above this ratio is assumed linearly dependent on the primary radius with an equation of the form

$$\frac{k_t}{\eta} = c_{V0} + c_{V1} R_p \tag{4.34}$$

The constants c_{V0} and c_{V1} will be determined in chapter 5.

4.1.2. Torque Loss Model

Micklem (1993) complemented the viscous shear model by an additional torque loss from the necessary work to force the belt out and into the vee-pulleys. Viscous shear considerations enabled the introduction of the torque loss. The Coulomb friction approach (Becker, 1987, Gerbert, 1984, Sun, 1988) could not explain any other power loss than slip.

Nature of the phenomenon. The viscous shear stress forces have to be overcome to remove segments from the circular path between the two pulley halves onto the straight line and to insert them again. The necessary work is wasted and is formulated as a torque loss. This is intuitive. When driving the belt pulley assembly with no load a torque must be exerted onto the driving pulley to keep it going. This torque corresponds to the loss torque.

ASSUMPTIONS

Assumption T1: In- and outgoing radii. A radial force has to be acting to bring the segments out of the circular path onto the straight line (point (1), Figure 4.6). This is only possible by "kinking" the belt, nominally reducing the primary outlet radius. Similar effects at inlet are responsible for the increased secondary inlet radius. The following relations are assumed

$$\begin{aligned} R_{po} &= k_p R_p & R_{pi} &= \frac{R_p}{k_p} \\ R_{so} &= k_s R_s & R_{si} &= \frac{R_s}{k_s} \end{aligned} \qquad (4.35)$$

Assumption T2: Relation between radial force and clamping force. The radial force necessary to tear a segment out of the circular path is assumed to be proportional to the acting clamping force on that segment.

$$F_{radial} = const \frac{F}{\frac{R\beta}{s}} \qquad (4.36)$$

MODEL - REALITY

A simplified model is assumed to quantify the torque loss in an approximate manner. The presence of the kink in the compression path is only hypothetical. In reality the

compressed straight belt behaves like a rigid beam. The forcing of this part of the belt from a circular path makes moments necessary that counteract the transmitted torque.

TORQUE BALANCE

Formulating the torque balance at the secondary pulley in Figure 4.6 gives

$$CR_{si} = T_s + U(R_{si} - R_{so}) \tag{4.37}$$

Using equation (4.35) (Assumption T1), formulating the torque balance for the primary pulley and then using the above equation to eliminate C gives

$$T_{p+} = T_s k_p k_s \frac{R_p}{R_s} + UR_p k_p \left(\frac{1}{k_p^2} - k_s^2 \right) \tag{4.38}$$

where T_{p+} consists of the transmitted viscous shear torque and the torque loss T_l that is sought.

$$T_{p+} = T_p + T_l \tag{4.39}$$

Assuming the viscous torque relation (4.32) (Note that the negative sign in that equation does not apply here, since the acting and not the transmitted torque is considered.) equations (4.38) and (4.39) can be used to determine the torque loss.

$$T_l = Uk_p R_p \left(\frac{1}{k_p^2} - k_s^2 \right) - T_s \frac{R_p}{R_s} (1 - k_p k_s) \tag{4.40}$$

DETERMINE k_p AND k_s

Assumption T2 is used to relate k_p to R_p and k_s to R_s, respectively. The subscripts can be omitted, since the same relations at either pulley are valid. Figure 4.7 visualises Assumption T2; from equation (4.36) it follows

$$F_{radial} = (U - C)\sin\delta = \text{const}\,\frac{F}{\frac{R\beta}{s}} \tag{4.41}$$

The relation between k and R can only be established for the special case $T_s = 0$ for which the compression C becomes negligible. Recalling from (4.21) that for this case

$$U = \frac{F\ 2\tan\Theta}{\beta} \tag{4.42}$$

holds, where the belt velocity is neglected. Combining the two previous equations leads to (note that $C = 0$)

$$\sin\delta = \text{const}\,\frac{1}{R} \tag{4.43}$$

Recalling from Figure 4.7 and taking equation (4.35) (Assumption T1) into account yields

$$\cos\delta = \frac{R_o}{R} = k \tag{4.44}$$

Adding the squares of equations (4.43) and (4.44) leads to

$$R^2\left(1 - k^2\right) = k_l \tag{4.45}$$

where k_l is a constant to be determined experimentally (see chapter 5).

THE TORQUE LOSS MODEL

The geometrical substitutions p_1 and p_2 are introduced. They use (4.45) to eliminate k_p and k_s from (4.40).

$$p_1 = R_p \sqrt{1 - \frac{k_l}{R_p^2}} \left(\frac{R_p^2}{R_p^2 - k_l} - \frac{R_s^2 - k_l}{R_s^2} \right) \tag{4.46}$$

$$p_2 = \frac{R_p}{R_s} \sqrt{\left(1 - \frac{k_l}{R_p^2}\right)\left(1 - \frac{k_l}{R_s^2}\right)} \tag{4.47}$$

They simplify the torque loss model. Equation (4.21) is used to express U in (4.40). The effect of the radial shear force is neglected. It follows

$$T_l = p_1 \left(\frac{2 \tan\Theta F_p}{\beta_p} + \frac{T_p}{2R_p} + v_L^2 m \right) + p_2 T_s \tag{4.48}$$

For later application in chapter 6 it is important to note that the centripetal term can be approximated by neglecting the slip. This means that v_L can be replaced by either $R_p n_p$ or $R_s n_s$.

4.2. The Components of the CTX

This section describes models for the other components within the CTX transmission previously described in chapter 4 (auxiliary units). Particular emphasis is placed on modelling power loss.

4.2.1. Clutch

Although not slipping during normal driving the clutch assembly (clutches and epicyclic gear set) consumes some power. The power loss can be explained with the idling of the epicyclic gear set causing viscous drag. This effect takes also place

within the reverse clutch plates. Viscous friction would normally suggest a linear function of speed. However, experimental results proved a quadratic function of speed.

$$T_C = c_{C0} + c_{C1} n_p + c_{C2} n_p^2 \tag{4.49}$$

The loss model is validated in chapter 6 where the constants c_{C0}, c_{C1} and c_{C2} are determined, too. It will be shown that the influence of the clutch plate pressure can be neglected.

4.2.2. Final Drive

The final drive consists principally of two gear sets. The differential action is locked in rig operation and its influence can be neglected in straight driving. The observations concentrate on the final drive gear sets. The gearing gives a transmission ratio of R_F = 5.671 and the speed relation

$$n_D = \frac{n_s}{R_F} \tag{4.50}$$

where n_D is the differential output speed and n_s is the secondary pulley speed. Van Dongen (1982) investigated the efficiency characteristics of transaxles. The final gear assembly has the same layout as a standard manual transaxle in a transverse engine arrangement. Van Dongen's paper presents experimental measurements; an analysis of the physical processes leading to power losses is deliberately omitted. The presented model attempts to fit his results. The efficiency of a manual transaxle consisting of two gears can be approximated by

$$\eta_F = c_{Fm} \left(1 - e^{-\frac{T_{in} - c_{F0}}{c_{Fq}}} \right) \tag{4.51}$$

where T_{in} is the driving input torque. c_{Fm} determines the maximum efficiency point, c_{F0} the zero efficiency point and c_{Fq} the steepness (see Figure 5.16). According to Van Dongen's data the speed dependency plays a negligible role and can be neglected.

The inertias of the secondary pulley, the final drive and the differential are lumped into the final drive inertia J_D. Newton's second law gives

$$J_D \frac{dn_D}{dt} = \eta_F T_e R_F - T_A \tag{4.52}$$

where T_A is the axle torque (4.4).

4.2.3. Hydraulic Pump

The absorbed power of the hydraulic pump has to be determined. The efficiency of hydraulic pumps, although very important in every application, is not well documented. McCandlish and Dorey (1984) based their work on Wilson who, back in 1948, published some very useful experiments. They anticipate the efficiency of a gear pump used in the operating range of the CTX to vary between 0.5 and 0.7. There is no detailed performance map available for the unit. Under these circumstances an approximation to a constant value $\eta_P = 0.6$ is justifiable. This value was used to produce the data in Figure 3.8 and may seem low. However, the pump is not an industrial product and the manufacturing and assembly specifications hinder a more optimistic value.

4.3. The Engine Model

An important aspect of this research is the exploitation of engine efficiency (consumption). A CVT is a means to match engine and transmission, optimising the engine efficiency (Stockton, 1984). An accurate model of an engine is essential to predict the dynamic interactions.

4.3.1. Approach

The engine behaviour is modelled to satisfy the requirements of powertrain simulation work and has limitations for other applications.

Requirements. Two similar important features should be incorporated. First, the engine model should yield accurate consumption and emission values. Secondly, dynamics should be represented sufficiently to investigate the interactions between engine and transmission.

Approach. A combined dynamic/instantaneous approach was chosen. Accurate consumption and emission values are achieved by making use of comprehensive steady state data. This is the instantaneous part of the model. It replaces the physical and chemical dynamics of the combustion process determining the production of power. It is called instantaneous because the manifold pressure and the actual engine speed determine instantaneously the consumption, emission, etc. The dynamics are represented by the thermodynamic events in the inlet manifold. A physically inspired mathematical description determines the state of some engine parameters dynamically. This, in turn, makes the instantaneous model quasi-dynamic.

Justification. Measured steady state data substitute the *difficult and sometimes inaccurate computations* representing the detailed combustion process. Engine management systems (EMS) ensure defined operating conditions and thus a true representation. Engine transients are greatly determined by the inlet manifold characteristics (Sogawa et al, 1989, Finlay et al, 1987). A physical model determining the dynamics in that manifold is thus a good approach.

Schematic engine model. The engine model consists of four submodels, Figure 4.8. The model of the throttle valve (1) represents the throttling of the intake air mass flow and is explained in 4.3.2. In ordinary operating points up to 90% of the total pressure drop will take place here (Heywood, 1988). The energy balance of the throttle air mass flow and the cylinder air mass flow determines the manifold pressure p_m (2). The

corresponding thermodynamic relations are defined in 4.3.3. The produced torque and the actual cylinder air mass flow are computed as a function of the actual manifold pressure and engine speed (3). Additional outputs of this submodel are the fuel consumption and the resulting exhaust gases. A lumped model of the engine inertia (4) yields the engine speed through the difference between the engine and load torques. Submodels (3) and (4) are explained in 4.3.4.

Limitations. The developed model is based on an averaged steady flow analysis. The periodic variations of parameters due to the volume flow rate variation during each cylinder filling are neglected. Thus, the cyclic production of power due to piston movement and individual combustion is not represented. This also applies to other operating transients not covered by steady state data maps (humidity of the air, etc.).

4.3.2. Throttle Valve

This model determines the air mass flow as a function of the pressure difference over the butterfly valve (p_0 - p_m in Figure 4.8) and its opening, ϕ. The mass flow rate (dm_{th}/dt) is computed from orifice equations for compressible flow. The throttle open area is a function of the active throttle angle. It is assumed that the discharge coefficient depends on throttle opening and is determined experimentally.

Orifice equations for compressible flow. The orifice equations for compressible flow yield the mass flow rate depending on the upstream and downstream pressure and the opening of the butterfly valve. When the velocity of the mass flow at the minimum area (vena contracta) reaches the velocity of sound the condition is called choked or critical flow. In this case the pressure at the vena contracta is related to the stagnation pressure, p_{crit}.

$$p_{crit} = p_0 \left(\frac{2}{\gamma+1}\right)^{\frac{\gamma}{\gamma-1}} = 0.53\ p_0 \qquad (4.53)$$

$$\text{with } \gamma = \frac{c_p}{c_v} = 1.39$$

For pressure ratios across the throttle less than the critical value, i.e. for $p_m > p_{crit} = 0.53\ p_0$, the mass flow rate is given by (it is assumed that the downstream pressure is equal to the pressure at the vena contracta, i.e. no pressure recovery occurs)

$$\dot{m}_{th} = \frac{c_D^* \dot{A}_{th}^* p_0}{\sqrt{RT_0}} \left(\frac{p_m}{p_0}\right)^{\frac{1}{\gamma}} \left(\frac{2\gamma}{\gamma-1}\left(1 - \left(\frac{p_m}{p_0}\right)^{\frac{\gamma-1}{\gamma}}\right)\right)^{\frac{1}{2}} \qquad (4.54)$$

For pressure ratios greater than the critical value, i.e. for $p_m \leq p_{crit}$, when the flow at the throttle plate is choked

$$\dot{m}_{th} = \frac{c_D^* A_{th}^* p_0}{\sqrt{RT_0}} \gamma^{\frac{1}{2}} \left(\frac{2}{\gamma+1}\right)^{\frac{\gamma+1}{2(\gamma-1)}} \qquad (4.55)$$

p_0 and T_0 are the upstream total pressure and temperature. The product $c_D^* A_{th}^*$ is the effective flow coefficient (see below).

Effective flow coefficient. The effective flow coefficient accounts for the effective flow area and the frictional losses. Pilot lines within the carburettor build a leakage path. The leakage path is modelled as a fixed orifice whose flow coefficient ($c_L A_L$) is determined experimentally. The leakage flow is combined with the butterfly flow to give the effective flow coefficient.

$$c_D^* A_{th}^* = c_D A_{th} + c_L A_L \qquad (4.56)$$

c_D and $c_L A_L$ are determined by validation with experimental values (5.3.1).

Throttle plate open area. The throttle plate open area A_{th} is computed as a function of the throttle angle α. The throttle plate shaft affects the open area sufficiently to be included in the analysis. A throttle angle of 5° corresponds to a completely closed throttle. Nevertheless, some leakage takes place ($c_L A_L$). The throttle plate open area is (Harrington, 1970)

$$A_{th} = \frac{D^2\pi}{4}\left(1 - \frac{\cos\phi}{\cos\phi_0}\right) + \frac{d}{2\cos\phi}\sqrt{D^2\cos^2\phi - d^2\cos^2\phi_0} + \frac{D^2\cos\phi}{2\cos\phi_0}\arcsin\left(\frac{d\cos\phi_0}{D\cos\phi}\right) - \frac{d}{2}\sqrt{D^2 - d^2} - \arcsin\left(\frac{d}{D}\right) \tag{4.57}$$

Throttle discharge coefficient. The discharge coefficient is assumed to be a function of the throttle opening and can be approximated by

$$c_D(\phi) = c_{\phi 1} e^{-c_{\phi q}\phi} + c_{\phi 0} \tag{4.58}$$

where $c_{\phi 0}$, $c_{\phi 1}$ and $c_{\phi q}$ are constants. This is an empirical relation and is validated later in 5.3.1.

4.3.3. Manifold

The thermodynamic properties used to determine the conditions in the manifold are the throttling process, the energy and continuity equation and the state equation. It has been assumed that the presence of fuel does not affect the air flow rate. Additionally, steady state flow rates are assumed. The air is treated as ideal gas with constant specific heats.

The thermodynamics aspects of the throttling process have not been considered above and are included as part of the manifold model. The throttling process is an adiabatic steady-flow process. It is essentially irreversible and is a means of reducing the pressure by intentionally introducing friction into the pipe. Rogers and Mayhew (1967) state that in a throttling process with low-speed flow (typically for a carburettor) the kinetic energy difference between inlet and outlet is negligible. Heat transfer can be neglected. Also, no work crosses the boundary. This reduces the steady flow energy equation to

$$h_{in} = h_{out} \tag{4.59}$$

When applied to the throttle manifold assembly, Figure 4.8,

$$T_m = T_0 \tag{4.60}$$

Energy equation. Based on the insight from the throttling process the steady flow energy equation of the manifold is (Finlay, 1987)

$$\frac{dT_m}{dt} = \frac{1}{m_m c_v}\left[h_{th}\frac{dm_{th}}{dt} - h_c\frac{dm_c}{dt} - u_m\frac{dm_m}{dt}\right]$$

$$h_{th} = c_p T_0 \tag{4.61}$$

$$h_c = c_p T_m$$

$$u_m = c_v T_m$$

The balance of incoming and outgoing enthalpy and the change in internal energy determine the rate of change of temperature. The effect of the fuel vaporisation, which would lead to an additional term (cooling influence), and heat transfer across the manifold boundaries are neglected.

Mass continuity equation. The rate of change of mass in the manifold is given by continuity

$$\frac{dm_m}{dt} = \frac{dm_{th}}{dt} - \frac{dm_c}{dt} \tag{4.62}$$

The fuel mass is neglected.

State equation. Assuming ideal gas the state equation gives

$$p_m = \frac{m_m R T_m}{V_m} \tag{4.63}$$

4.3.4. Engine Mechanism

This section describes submodels (3) and (4) from Figure 4.8. The combustion and kinematic processes yielding kinetic energy is assumed to be averaged and represented by experimental data. Steady state engine data is used to calculate the engine torque produced depending on manifold pressure and actual engine speed as shown in Figure 4.9. Figure 4.10 shows the similar function for the volumetric efficiency. The presented data is extracted from Appendix B. Interpolation transformed the tabulated function into a continuous grid. A continuous spline interpolation routine is used to yield the continuous relationship

$$T_E = f_T(n_E, p_m) \quad , \quad \eta_{vol} = f_\eta(n_E, p_m) \tag{4.64}$$

Cylinder air flow. The cylinder air flow is computed on the basis of the volumetric efficiency of the engine.

$$\frac{dm_c}{dt} = \eta_{vol} V_{swept} \rho_m \tag{4.65}$$

Consumption. Maps can be incorporated in a similar way, e.g. to give consumed fuel. Figure 4.13 shows the consumption map extracted from the data in Appendix B. The integration of this map function

$$m_F = \int f_F(n_E, p_m)dt \tag{4.66}$$

gives the fuel mass used.

Emission. The same thoughts would be used to incorporate emission data. However, this is not included within this study.

Engine inertia. The inertia of the engine and the primary pulley and clutch is treated as a lumped parameter. The application of Newton's second law leads to

$$J_E \frac{dn_E}{dt} = T_E - T_T \tag{4.67}$$

4.3.5. Extrapolation of Map Data

It is important to realise that the experimental map data can only be used for interpolation. To ensure correct operation of the model for powertrain analysis new modelling ideas are developed to cater for any argument values that require extrapolation. This involves predominantly operating conditions where the engine is used to brake the vehicle. A separation into engine speed and manifold pressure dependency simplifies the model description.

Engine speed. Figure 4.11 depicts the manifold pressure dependency of the three dimensional maps f_T and f_η. Extrapolation for pressures smaller than the minimum map manifold pressure ($p_{m,min}$) assumes a constant linear gradient (g). g_T and g_η are determined in chapter 5.

Manifold pressure. Figure 4.12 shows the engine speed dependency of the three dimensional maps f_T and f_η. The adopted model assumes that the boundary values at $n_{E,min}$ and $n_{E,max}$ are representative for extrapolation (constant extrapolation).

4.4. Driveline and Vehicle

A model of the driveline and vehicle was needed for two simulations. First as the basis for the real time simulation necessary to control the dynamometer on the rig. Secondly as part of the overall system simulation.

The model divides into three parts. The *driveline compliance* represents the dynamic effects of the flexible shafts and the longitudinal tyre stiffness. It acts between the differential and the *generalised car mass* resulting in the distinct second order system response of the car. The *tyre model* includes rolling resistance and a compensated rolling radius.

Driveline compliance. The model of the driveline compliance is not included in the real time simulation for car emulation. This is due to the limited bandwidth of the torque absorbtion of the dynamometer. The limited bandwidth is similar to the bandwidth of the second order system resulting from a spring/damper-generalised car mass unit (about 15 rad/s, although the damping ratio is too large). Thus, the spring/damper effect takes place on the rig already and does not need to be included. The spring/damper model for the dynamic simulation generates the torque

$$T_A = k_A \int (n_D - n_T)\, dt + c_A (n_D - n_T) \tag{4.68}$$

where n_D is the differential output speed and n_T the tyre speed. c_A and k_A are determined in to give similar response to the dynamometer (Chapter 5).

Tyre. A simplified tyre model is all that is necessary. The compensated radius (r_T) is

assumed constant, about 3% smaller than the no load radius.

$$v_C = r_T n_T \quad , \qquad F_T = \frac{T_A}{r_T} \tag{4.69}$$

The power loss associated with the deformation is modelled as a force loss

$$F_r = fmg \tag{4.70}$$

where F_r is the rolling resistance. f is the coefficient of rolling resistance and is a function of car speed. However, in the case of radial-ply tyres f can be approximated by a constant to an accuracy band of 10% (Bosch, 1986) and thus, the constant value was used.

The generalised car mass (m^*) consists of the car mass (m) and a referred component for the inertia of the driveline and wheels (J_W)

$$m^* = m + \frac{J_w}{r_T^2} \tag{4.71}$$

The driving resistance consists of aerodynamic drag and climbing resistance. The head wind (v_0) is incorporated, too.

$$F_d = \frac{1}{2} c_D \rho A (v_C + v_0)^2 + mg \sin\gamma \tag{4.72}$$

Newton's second law gives

$$m^* \dot{v}_C = F_T - F_r - F_d \tag{4.73}$$

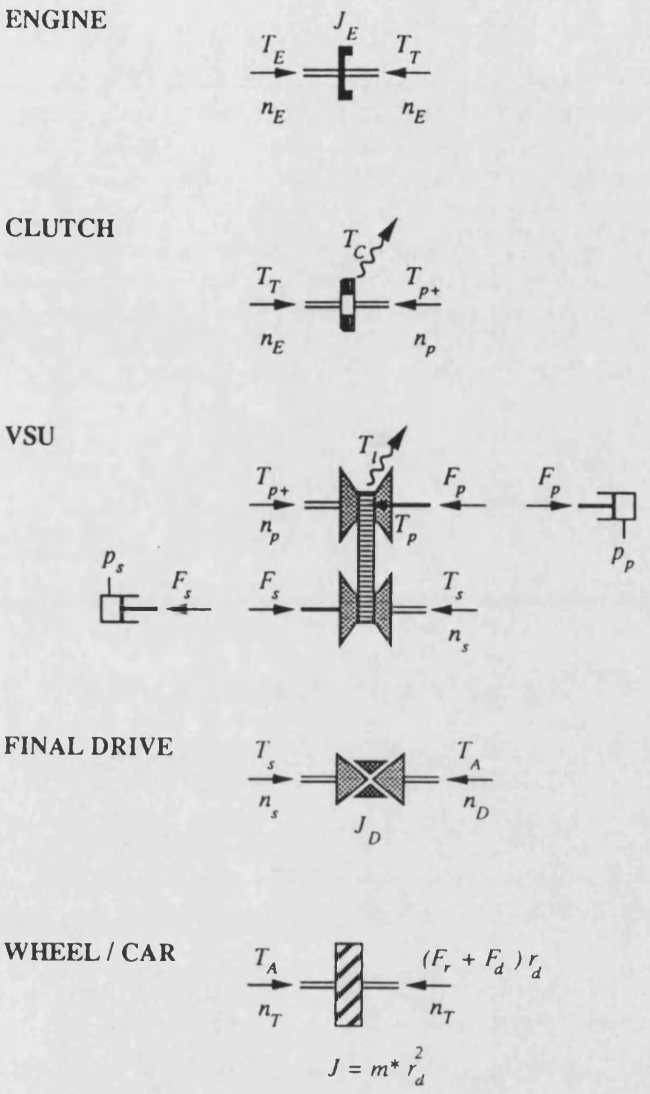

Figure 4.1 Free-body diagram of CTX powertrain components

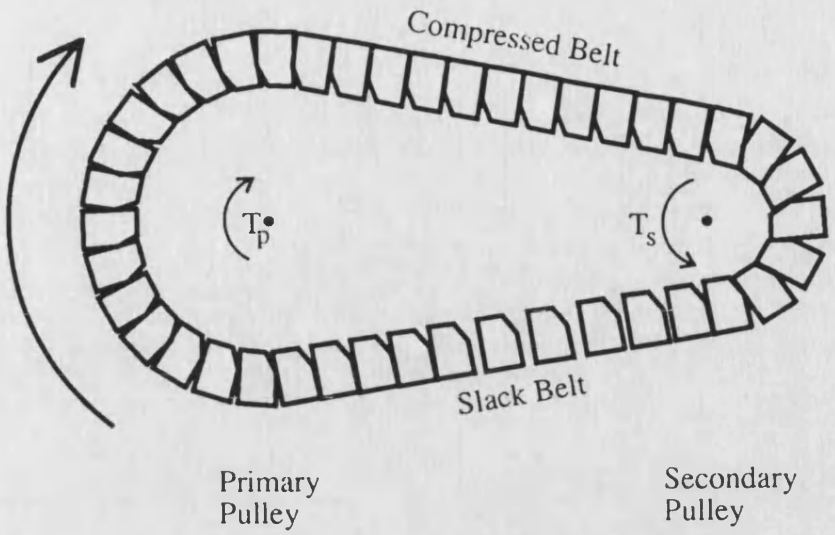

Figure 4.2 Belt segments rounding the pulleys. The gaps in the slack path are used up by the time they enter the primary pulley again.

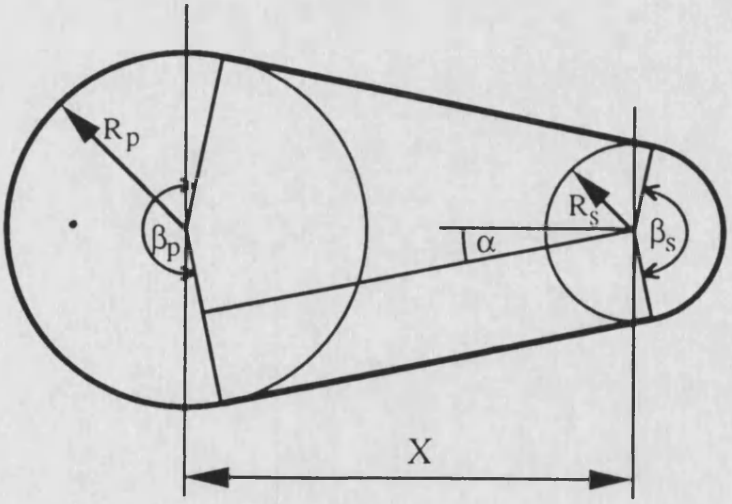

Figure 4.3 Belt Geometry. Fixed belt length and pulley centre distance determine the relation between primary and secondary radius.

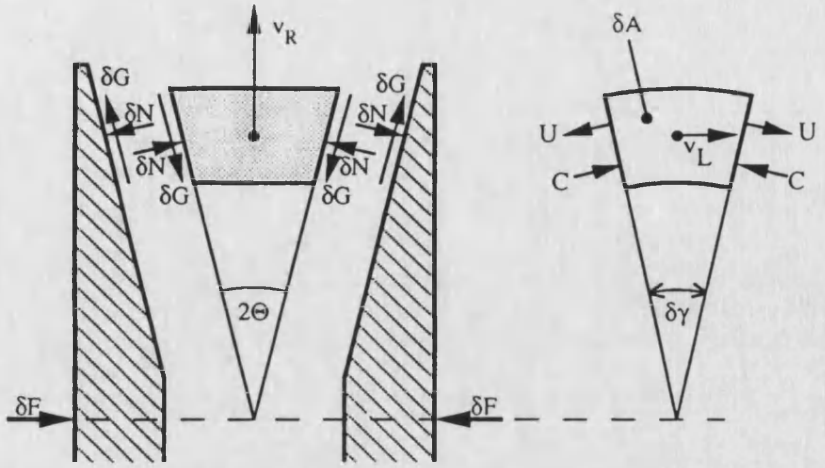

Figure 4.4 Belt pulley free body diagram. δG is the radial viscous shear force component.

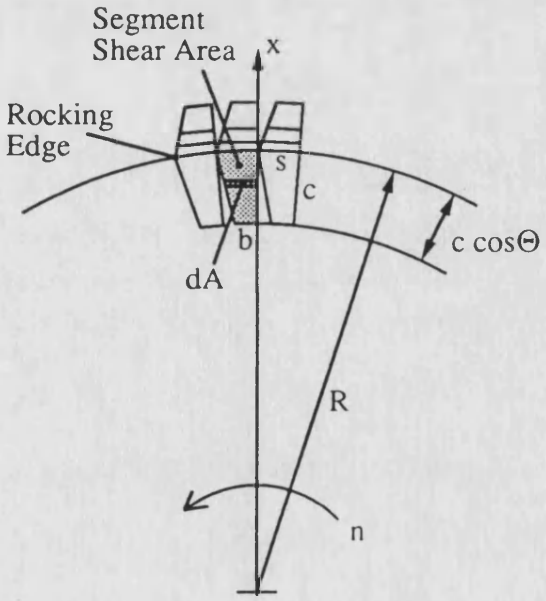

Figure 4.5 Viscous shear area of a segment

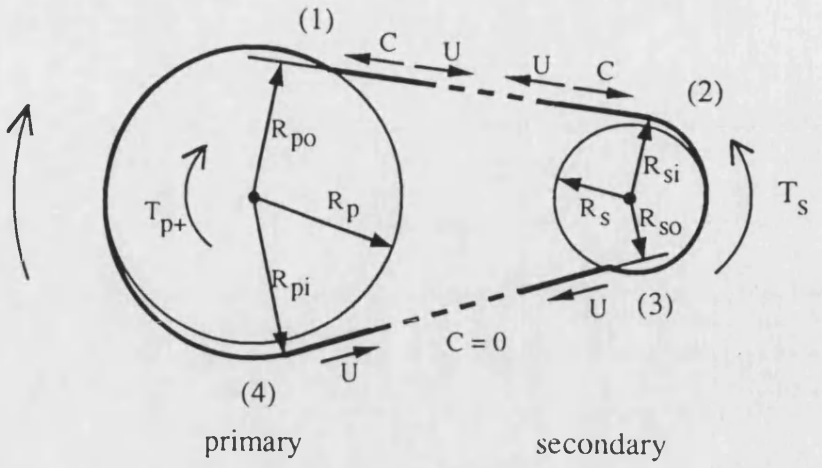

Figure 4.6 Torque loss free body diagram

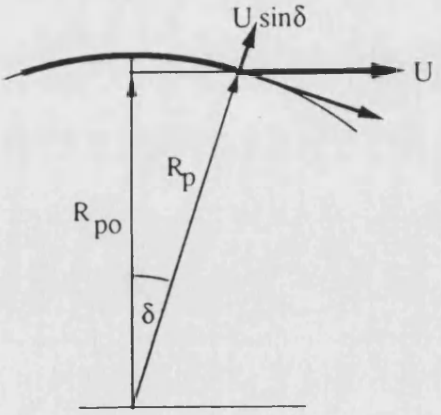

Figure 4.7 "Kink" model. The radial component of the band tension *U* tears the segment out of the circular path.

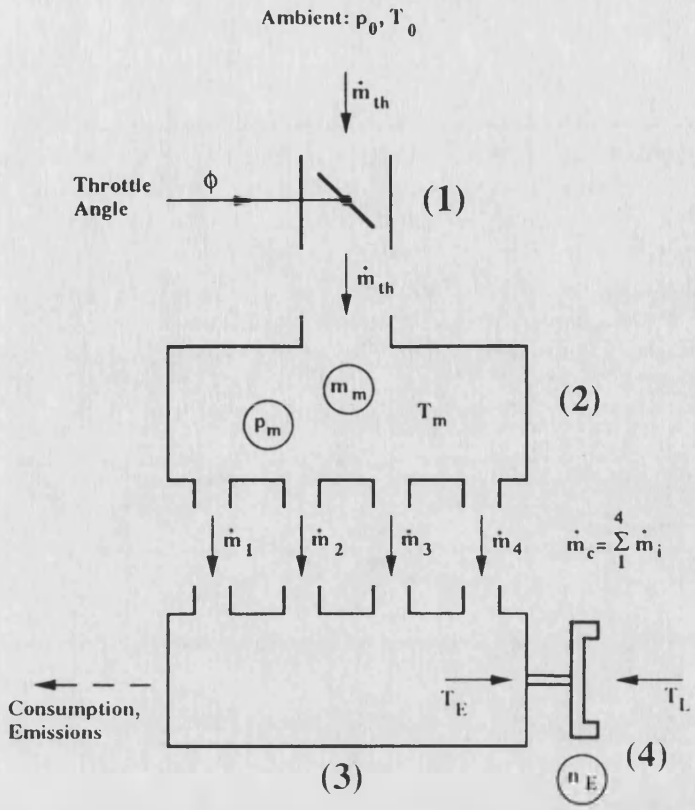

Figure 4.8 Schematic engine model. States are encircled and are determined by the throttle angle (ϕ) and engine load (T_L).

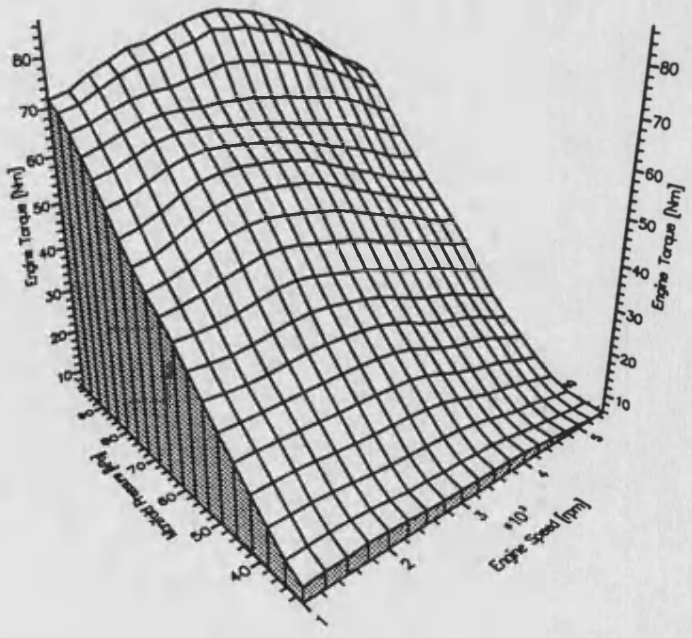

Figure 4.9 Visualised torque map

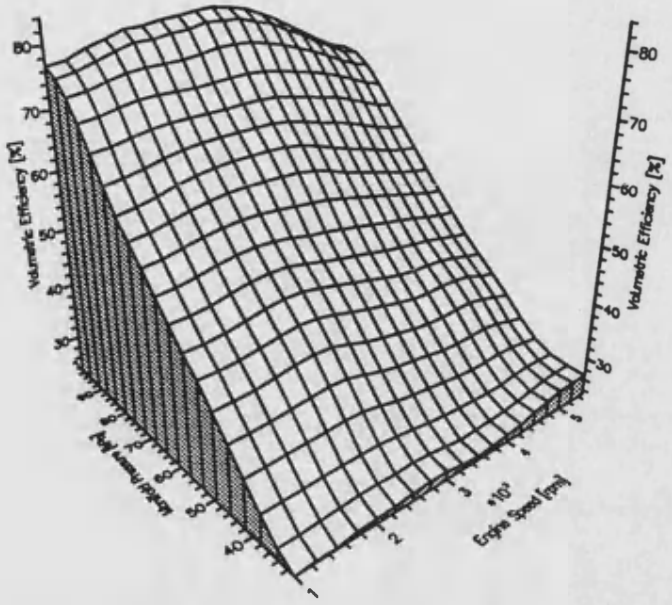

Figure 4.10 Visualised volumetric efficiency map

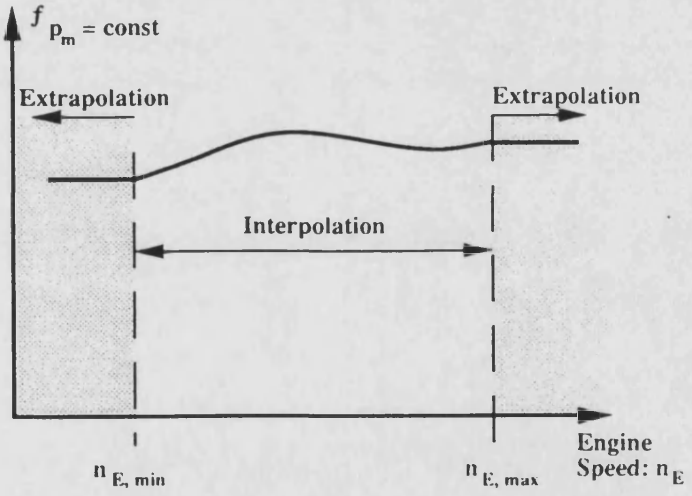

Figure 4.11 Interpolation and extrapolation for constant manifold pressure p_m

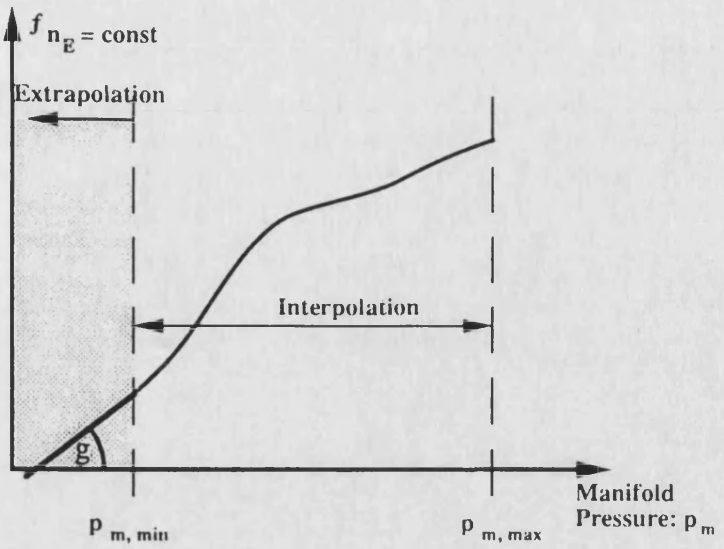

Figure 4.12 Interpolation and extrapolation for constant engine speed n_E

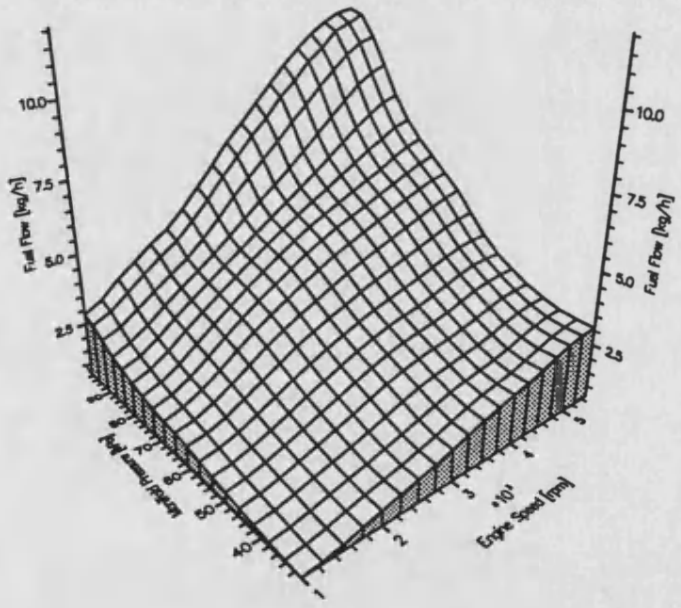

Figure 4.13 Visualisation of fuel flow map

5. VALIDATION

This chapter validates the mathematical models derived in the previous chapter. The modelling approaches are justified and modelling constants are determined.

Sections 1 to 3 in this chapter are organised to correspond with the ones in chapter 4. Section 5.1 presents the validation of the VSU model; 5.2 compares theory and measurement of the components of the CTX; the engine model is validated in 5.3. Section 5.4 validates the VSU with the electro-hydraulic control circuit.

HOW WAS THE VALIDATION CONDUCTED?

Experimental data acquired through a series of specific tests were used to validate the components of the CTX powertrain. Table 5.1 presents these tests. Although not reflected by the order in this chapter they were carried out in the displayed sequential order.

CAR LOAD MODEL

The validation of the car load model is an exception to the above. c_A and k_A (equation (4.68)) are chosen to give corresponding dynamic responses from the numerical simulation and the test bed emulation. The pressure response in Figure 2.8 and 2.9 (and thus the torque absorbtion) suggests a representative bandwidth of about 10 rad/s (between 6 and 12 rad/s, page 31 ff.) with a damping ratio of 0.7. Taking into account the generalised car mass reflected into an inertia it follows

$$k_A = \omega_0^2 \, m^* r_T^2 = 6670 \, \frac{\text{Nm}}{\text{rad}} \tag{5.1}$$

and

$$c_A = 2 \zeta \omega_0 \, m^* r_T^2 = 1200 \, \frac{\text{Nm s}}{\text{rad}} \tag{5.2}$$

Representative figures for a Ford Fiesta sized vehicle would be $\omega_0 = 15$ rad/s and $\zeta = 0.3$. A response with these parameters cannot be achieved by the dynamometer, and

Table 5.1 Series of tests for the sequential validation of submodels

Validated Component	Applied Test [1]	Determined Constants
engine, butterfly valve	- [2]	$c_{\phi 1}$, $c_{\phi q}$, $c_{\phi 0}$, $c_L A_L$
engine dynamics	engine-CTX decoupled, throttle step demand	J_E, V_m, g_η, g_T
clutch / CTX input losses	no VSU belt, steady state	c_{C0}, c_{C1}, c_{C2}
differential / final drive	- [3]	c_{Fm}, c_{Fq}, c_{F0}
VSU, speed / slip	spacer at primary pulley, steady state	c_{V0}, c_{V1}
VSU, torque loss	spacer at primary pulley, steady state	k_l
VSU, radial dynamics	standard hydro-mechanical control unit, transient test	d_p, d_s [5]
VSU, electro-hydraulics	CTX-dyno decoupled, primary valve step demand	d_p, d_s [5]
car load	- [4]	c_A, k_A

[1] Unless otherwise stated and where applicable, external electro-hydraulic control was used to adjust the pulley actuator pressures.
[2] Data from the steady state map (Appendix B) was taken.
[3] Experimental data from van Dongen (1982) validated the model.
[4] The car load model was not validated. c_A and k_A were chosen to give similar dynamic responses of the emulation on the test bed and the numerical simulation.
[5] *dp* and *ds* will be introduced in 5.1.2

is not attempted in the numerical simulation.

NUMERICAL SIMULATION

Dynamic simulation. The equations of the models from chapter 4 build a set of ordinary differential equations (ODE). Bath*fp* (see below) is a numerical solver for this type of problem and was used for the implementation. Many models in chapter 4 are formulated for steady state use. Examples are the torque loss and the longitudinal

viscous shear model of the VSU and the engine mechanism model. These models are implemented as *instantaneous models* within Bath*fp*. The interaction of these models with the dynamic models represents the whole dynamic simulation.

Bathfp. Bath*fp* is a numerical simulation environment developed at the Fluid Power Centre within the School of Mechanical Engineering. Three main characteristics of the programme led to its application. First, models of hydraulic components are available within the package (*fp* stands for *fluid power*). They are robust implementations at no cost and were useful for the incorporation of hydraulics in cooperation with the VSU. Second, a highly developed numerical integration method is used. This ensures short run-times and, above all, numerically accurate solutions. Third, Bath*fp* forces a clear structure of the models to be implemented. Exact definitions of the interfaces of the models (units, states, etc.) assisted the conceptual definition of the problem and ensured the future applicability.

5.1. The Van Doorne VSU

The *viscous shear stress* phenomenon determines the speed relation and radial dynamics. These two aspects are validated in 5.1.1. The torque loss phenomenon explains the additional torque loss not covered by the viscous shear stress model and is compared with measured data in 5.1.2.

Constant radius test. The steady state data were recorded at constant radii, i.e. a mechanical end stop at the primary pulley determined the geometrical transmission ratio. This enabled the variation of the secondary pressure, and thus of the conditions in the oil film, while keeping the same belt geometry. The secondary clamping force was determined through the pressure in the secondary hydraulic actuator.

$$F_s = p_s A_s \tag{5.3}$$

The primary clamping force was not measured but deduced using (4.31) (evaluation of the radial belt equation (4.30) in steady state):

$$F_p = \frac{\beta_p}{\beta_s} F_s \tag{5.4}$$

5.1.1. Speed Relation of Viscous Shear Model

The speed relation (4.33) determines the computed slip of the VSU. It is compared with the measured slip gained from the constant radius (steady state) tests. Equations (4.31) and (4.32) can substitute F_p and T_s in the viscous speed relation (4.33) to give

$$n_p = \frac{R_s}{R_p} n_s + \frac{T_p}{F_s} \frac{A_c k_t}{\eta} \left[\frac{R_s^2}{R_p^2 q_s} + \frac{\beta_s}{\beta_p q_p} \right] \tag{5.5}$$

Then, the relation between the primary and secondary speed depends on the ratio T_p/F_s (and additionally on the belt geometry). The quantity T/F will be called the *viscous shear power density*. Bearing in mind that the slip is

$$s = 1 - \frac{n_s R_s}{n_p R_p} \tag{5.6}$$

which can be re-written

$$n_p = n_s \frac{R_s}{R_p} + s\, n_p \tag{5.7}$$

and comparing this formula with the modified speed relation (5.5) it becomes evident that the slip s must depend on the ratio T_p/F_s, too. This fact epitomises the viscous shear approach and has immense importance for the understanding of the Van Doorne VSU. The presented data displays the slip in function of T_p/p_s, p_s being proportional to F_s (equation (5.3)).

Figure 5.1 shows measured and computed slip data as a function of T_p/p_s for the fixed primary radius (R_p) of 0.029 m. The three sub-plots present data for different secondary speed (n_s). The straight lines are the first order least square approximation to the measured and computed data points. The slip was computed knowing the secondary power (speed and torque), the secondary force (or pressure) and the primary radius (T_s, n_s, F_s and R_p), equations (4.29) through (4.31); the measured slip was deduced from measured primary and secondary speeds and radii (n_p, n_s, R_p and R_s), equation (5.6), and henceforth this quantity is referred to as the measured slip . Figures 5.2 through 5.4 show the corresponding data for primary radii of R_p = 0.0392 m, R_p = 0.05 m and R_p = 0.0703 m.

The measured slip relied on measured speeds and radii. This made the quantity of the slip very sensitive to any inaccuracies (2.3.4) and resulted in a few cases of negative slips. These particular measurements are wrong but have to be interpreted in the light of an estimated likely error of 0.5%. However, the coherence of the overall data is convincing such that this minor abnormality is not important.

Each computed slip value (star in Figures 5.1 to 5.4) should correspond to the measured slip value (cross in Figures 5.1 to 5.4). This resulted in the fact that the computed data points do not lie on straight lines. The reason for the deviation of the computed points to the first order approximation being smaller is that the numerical amplification of the inaccuracies in the slip determination is smaller for the computed slip. For this case, n_p and R_s are computed as functions of n_s and R_p (T_s and F_s that are responsible for the deviation in first place) and thus no measurement noise in form of a ratio of two measured quantities is introduced in the slip computation (2.3.4).

INTERPRETATION

Correspondence of measured and computed data. By and large measured and computed data correspond satisfactorily. In terms of relative error they are comparable to the results presented by Becker (1987) although his data does not cover the whole operating range. In Figures 5.2 and 5.3 a speed dependency is present. This is an effect not explainable with the theory proposed and requires further study.

Previously published data (Becker, 1987) deduced the measured slip from a speed difference relative to the no-load case. The measurement of the radii have enabled the *true determination* of the slip. To the author's knowledge, such data had not been published before. The values of the measured slips, especially at small primary radii, are a magnitude higher than the ones measured by Becker. Whether Becker's slip determination or his worries about exceeding the imagined minimum clamping forces (Coulomb friction model) resulted in his data is an open question. Apart from Becker's data no other slip measurements could be found.

Viscous shear stress behaviour. The measured slips are linearly dependent on the ratio T_p/p_s (at fixed speed and radius). This corresponds to the slip interpretation used (see above equations (5.5) and (5.7)) and thus fully justifies the viscous shear stress approach. The viscous shear parameter k_t/η was assumed to vary with the primary radius R_p. The determined values for the four cases (Figure 5.1 to 5.4) are plotted in Figure 5.5 against the primary radius. A linear fit is a good approximation, yielding

$$\frac{k_t}{\eta} = c_{V0} + c_{V1} R_p \tag{5.8}$$

with

$$\begin{aligned} c_{V0} &= 6 \frac{\mathrm{N}}{\mathrm{m}^2} \\ c_{V1} &= -80 \frac{\mathrm{N}}{\mathrm{m}^3} \end{aligned} \tag{5.9}$$

Dependency of slip on primary radius. Figures 5.1 through 5.4 show that the slip depends inversely - apart from other factors - on the primary radius. This means that the primary radius is a first approximation to the relative velocity between the belt and the pulley. EHD theory (Assumption S2, Chapter 4) suggested that the thickness of the oil film depends on the slip speed. Hence, the inverse of the primary radius is an approximate measure for this dependency.

5.1.2. Radial Dynamics of Viscous Shear Model

The radial dynamics model was investigated using the data of Figure 3.11 where the CTX was operated in its original state. A step change in throttle demand is initiated at time 2 seconds. The hydro-mechanical control unit responds quickly by changing the transmission ratio. The adjusted primary and secondary pressures are used to validate the radial model (equation (4.30)). Both pressures are shown for the case of the 90 deg throttle step in Figure 5.6. The combination of the pressures resulted in a change of primary radius as shown in Figure 5.7 (solid line). In this Figure computed data is plotted as well. During the computations it became evident that the measured pressures outside the CTX casing were not the ones acting in the cylinders. High flows through the long and winding pipe work in the CTX casing produced a substantial pressure drop. The introduction of orifices modelling the hydraulic resistance through the pipe work resulted in the computed data. Orifice diameters of d_p = 3.5 mm and d_s = 3 mm with a flow discharge coefficient of 0.8 led to the dashed line in Figure 5.7.

The computed data in Figure 5.7 (dashed line) is adequate for the dynamics but there is a steady state error which cannot be explained with the simple viscous shear stress model. A more realistic treatment of the belt (equation of motion for the belt instead of only allowing for the centripetal forces) could result in a different steady state solution. However, a steady state correction has been introduced which leads to a better comparison of measured and computed data (dotted line in Figure 5.7); a scaling factor in the β_p/β_s term of equation (4.30) has been added. A value of 1.22 (as compared to 1) resulted in the presented data. The initial increase of the dashed line is due to the initial condition. The scaling factor influences the dynamics to a certain extent, but as the orifice model dominates for the faster dynamics this is not important. Figure 5.8 shows the steady state corrected data for different throttle step demands of 40°, 60° and 90° repeated from Figure 3.11.

INTERPRETATION

The initial change of R_p is in very good agreement with the measurement. This supports a good dynamic representation by the flow limiting orifice model and the radial shear formula for large rate of change of R_p. For low hydraulic flows and thus smaller rate of changes in R_p the radial shear formula is dominant and uncovers the shortcomings of the simplified treatment (see above). This questions the validity of the steady state interpretation of equation (4.30) (i.e. equation (5.4)) that will be used extensively in Chapters 6 and 7. However, as was shown in the validation of the slip data of the viscous shear model in 5.1.1 this inaccuracy has no influence on the overall accuracy of the viscous shear approach.

5.1.3. Torque Loss Model

The validation of the torque loss model is conducted in two stages. No load data (T_A = 0) yielded a ball-park figure for the constant k_l. The subsequent comparison of computed and measured load data validated the model and further tuned k_l.

Figure 5.9 shows no load data for R_p = 0.05 m. This primary radius was the closest operating condition with equal primary and secondary radius. The CTX output shaft was disconnected. The necessary torque to drive the transmission is then the measured torque loss depicted in Figure 5.9 (allowing for clutch losses, 5.2.1). A value of the constant k_l of $0.3 \cdot 10^{-4}$ gave the computed data. Although not shown this value tied in well with no load data acquired at different constant radii.

Figure 5.10 shows torque loss data for a constant primary radius of 0.029 m. Measured and computed torque loss data are plotted against the secondary pressure for three representative secondary pulley speeds (n_s). For a particular secondary pressure and speed, five values of torque (for some cases only 4) were used to cover the operating range. The straight lines are first order least square approximations to the measured and computed data. Figures 5.11 through 5.13 present essentially the same data as Figure 5.10 but for primary radii of R_p = 0.0392 m, R_p = 0.05 m and R_p

= 0.0703 m. The torque loss constant k_l was re-defined to $0.25 \cdot 10^{-4}$ for Figures 5.10 through 5.13. The measured torque loss was deduced form torque and radius measurements.

INTERPRETATION

The correspondence of measured and computed data is satisfactory. Major discrepancies only occur for the largest primary radius (extreme overdrive). The deviation of measured data points increases with the primary radius. This suggests the dependency on primary radius which is not represented correctly by the model (see Figure 5.14, Primary Torque Component).

Dependency on primary radius. Considerable power is consumed for large primary radii. Thus, it is very important to adjust small secondary pressures in overdrive. Figure 5.14 shows the term-wise evaluation of the torque loss formula; losses due to the transmitted torque, the system pressure and the primary speed are presented as a function of the primary radius. A large value wedges the segments harder into the pulley halves where upon additional power is wasted by removing them. The primary speed dependency is somewhat surprising. However, large primary pulley speeds and large primary torques are impossible, since this would correspond to an excessive car speed.

5.2. The Components of the CTX

Recorded data for the clutch losses and published data for the final drive are used to determine the model specific constants.

5.2.1. Clutch Assembly

The belt was removed from the CTX to establish the performance of the clutch assembly. The design of the clutch with a forward and a reverse multi plate wet clutch

is prone to consume some power. The no belt test confirmed this. The hydraulic pump was disconnected; the secondary and the clutch pressure were modulated using the electro-hydraulic control circuit.

Clutch pressure dependency. It was found that a change in clutch pressure hardly influenced the power consumption and was thus not necessary to incorporate into the loss model. Maximum changes of 10% due to clutch pressure changes were measured.

Secondary pressure dependency. The influence of the secondary pressure on the no belt power consumption was negligible.

Speed influence. Figure 5.15 shows the clutch torque loss as a function of the engine speed. The proposed model (quadratic function of speed, equation (4.49)) was fitted in a least square sense to the measured data. This process determined the constants c_{C0}, c_{C1} and c_{C2} from equation (4.49)

$$\begin{aligned} c_{C0} &= 2.04 \text{ Nm} \\ c_{C1} &= -4.25 * 10^{-3} \frac{\text{Nm s}}{\text{rad}} \\ c_{C2} &= 1.03 * 10^{-5} \frac{\text{Nm s}^2}{\text{rad}^2} \end{aligned} \tag{5.10}$$

The initial drop of the clutch loss torque with increasing speed is not important because the consumed power increases steadily with the used formula.

5.2.2. Final Drive

The efficiency of a manual transaxle consisting of two gear sets and a transmission ratio of 5.01 is plotted in Van Dongen's paper (1982). The CTX final drive ratio of

5.671 is comparable and, thus, Van Dongen's data is directly relevant. The speed dependency is negligible. The efficiency can be approximated by an exponential law in function of the input torque (4.51). Figure 5.16 compares Van Dongen's and the modelled efficiency. The values of the constants c_{Fm}, c_{F0} and c_{Fq} were determined by visual comparison of Van Dongen's and the modelled efficiencies.

5.3. The Engine

The application of steady state data maps makes the validation of steady state behaviour redundant. The validity of the dynamics is investigated.

5.3.1. Discharge Coefficient

The butterfly valve flow model assumed that the discharge coefficient depends on the valve opening. Engine data from Appendix B was used to extract a pressure-flow relation for the butterfly valve. The mass continuity condition (4.62) ensures that, in steady state, the cylinder air mass flow and the butterfly air mass flow are equal. (4.65) was used to compute the measured cylinder air mass flow, that is equal to the butterfly flow (4.62). This data, together with the butterfly model (equations (4.53) through (4.57)), determined the measured experimental discharge coefficient. This is shown in Figure 5.17 where the experimental discharge coefficient is plotted against throttle opening. Based on a representative leakage whole of 1.8 mm a leakage flow coefficient ($c_L A_L$) of $8 \cdot 10^{-6}$ m^2 was used.

The constants of the exponential model (4.58) were determined by fitting the exponential function to the measured data in a least squares error sense. This resulted in the determination of $c_{\phi 0}$, $c_{\phi 1}$ and $c_{\phi q}$.

$$c_{\phi 1} = 0.696 \ , \quad c_{\phi q} = 0.121 \ , \quad c_{\phi 0} = 0.478 \tag{5.11}$$

INTERPRETATION

The correspondence between the measured and the computed data is acceptable. The deviation in the experimental data suggests the dependency of the discharge coefficient on other parameters (e.g. air mass flow) than only the throttle valve opening.

5.3.2. Engine Dynamics

The dynamic torque production with respect to changes in throttle angle is validated.

Experiment. The layout of the rig made it difficult to acquire suitable dynamic data. Any load on the engine had to be applied through the CTX; not knowing the dynamic characteristics of the CTX it was impossible to use such measurements. The only experiment possible was a no load test, i.e. no coupling between the engine and the CTX. Step demands in the throttle position resulted in speed changes of the engine. The same test could be simulated and was thus chosen. Figure 5.18 shows measured and computed data.

Acceleration. The most influential factor determining the acceleration behaviour is the lumped engine inertia, J_E. A value of 1.6 kgm^2 was satisfactory. The volume of the manifold is similarly important. A ball park figure was available and applied (V_m = 0.004 m^3).

Deceleration. This phase was used to determine the coefficients of the extrapolation models (f_η and f_E). Gradient values of

$$g_\eta = 1.7 \frac{\%}{\text{kPa}} \quad , \text{ and } \quad g_T = 1.4 \frac{\text{Nm}}{\text{kPa}} \tag{5.12}$$

resulted in the data displayed in Figure 5.18.

INTERPRETATION

The presented data proves the satisfactory dynamic representation by the model. Further simulation data demonstrate the dynamic torque production of the engine that was aimed to be modelled.

Dynamic behaviour of manifold model. Figure 5.19 shows the dynamic behaviour of the manifold model during simulation. The engine is kept at constant speed. A change in throttle angle is induced. Four different steps in throttle angle demonstrate the engine's behaviour. The size of the throttle step clearly influences the response time in the development of torque. This is due to the lag of the manifold pressure signal. The change in manifold air temperature during the transient seems to be high but was not investigated further. As explained earlier (4.3.3 *Throttling*) it is perfectly acceptable that the temperature in the manifold is equal to ambient temperature at steady state.

5.4. Electro-Hydraulic Circuit

The dynamic validation of the CTX with electro-hydraulic control is essential for two reasons. First, linearised models can be obtained and can be used for the design of feedback control systems. Second, the dynamic non-linear simulation with the identified controller can be used to investigate the performance over the whole operating range.

Valve dynamics. The primary and secondary valves (Figure 3.12) were represented through standard Bath*fp* models. The primary valve used a sophisticated database model (accurate pressure/spool displacement/flow data). A linear second order system (ω_0 = 50 Hz, ζ = 1.0) modelled the dynamics. The secondary valve is assumed to behave like a first order linear system. A steady state test was carried out to determine the pressure gain, Figure 5.20. The maximum pressure gain is about 14 bar/V (gradient between 1 V and 2 V secondary voltage). The time constant (τ) determined by the manufacturer was 0.034 s (The specified rise time T_R is 170 ms, $T_R = 5\ \tau$).

Hydraulic restriction. The hydraulic pipe work to each of the pulley cylinders was modelled as one lumped orifice acting at the cylinder entry. The diameters of the orifices are important for the dynamics but were validated against ratio change data where steady state flow limitations due to the hydraulic resistance is dominant. The comparison of measured and computed data is presented in Figure 5.21. The engine was run at constant throttle angle and drove the CTX under no load. Step inputs to the primary valve resulted in the presented data. The engine speed was about 1500 rpm, the secondary pressure was constant at 16 bar. Orifice radii of d_p = 1.3 mm for the primary and d_s = 2.1 mm for the secondary cylinder were chosen for the data presented in Figure 5.21 (with a discharge coefficient of 0.8). The further restriction as compared to the standard CTX hydraulics (5.1.1 RADIAL DYNAMICS, orifice diameters of 3.5 mm and 3.0 mm, respectively) resulted from longer pipe lines due to the external construction of the electro-hydraulic valve block.

INTERPRETATION

The gradients (i.e. dR_p/dt) correspond satisfactorily. The discrepancies in the third plot result from an integrating action and are not important. A side-product of the simulation is the insight into the primary and secondary cylinder flows in comparison with the maximum pump flow. Figure 5.22 displays the primary and secondary actuator flows for the ±10 V primary voltage step change. The external pump delivery was in the order of 42 L/min against a maximum cylinder flow of 7 L/min. This shows clearly that the rate of change of the transmission ratio is limited by the hydraulic pressure drop in the actuator lines. The internally employed pump would deliver about 12 L/min at the test speed. This highlights another factor of the design that has to take the pressure drop due to the restrictions in the primary and secondary pressure lines into account.

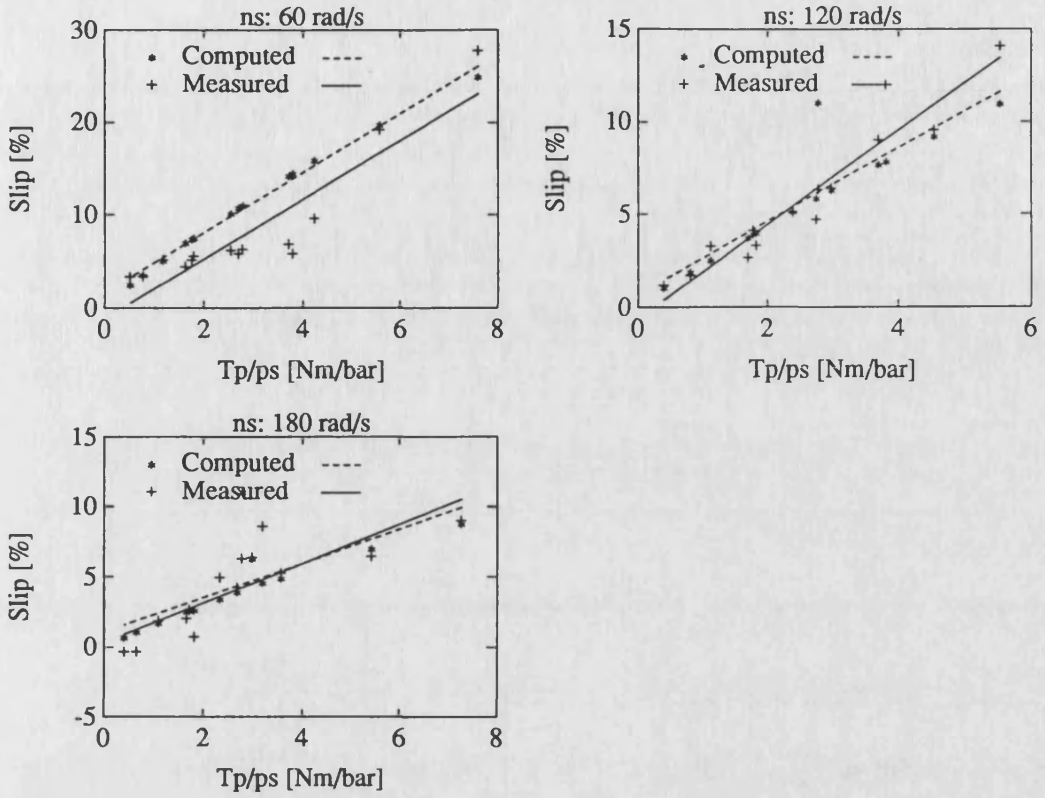

Figure 5.1 Measured and computed slip for R_p = 0.029 m

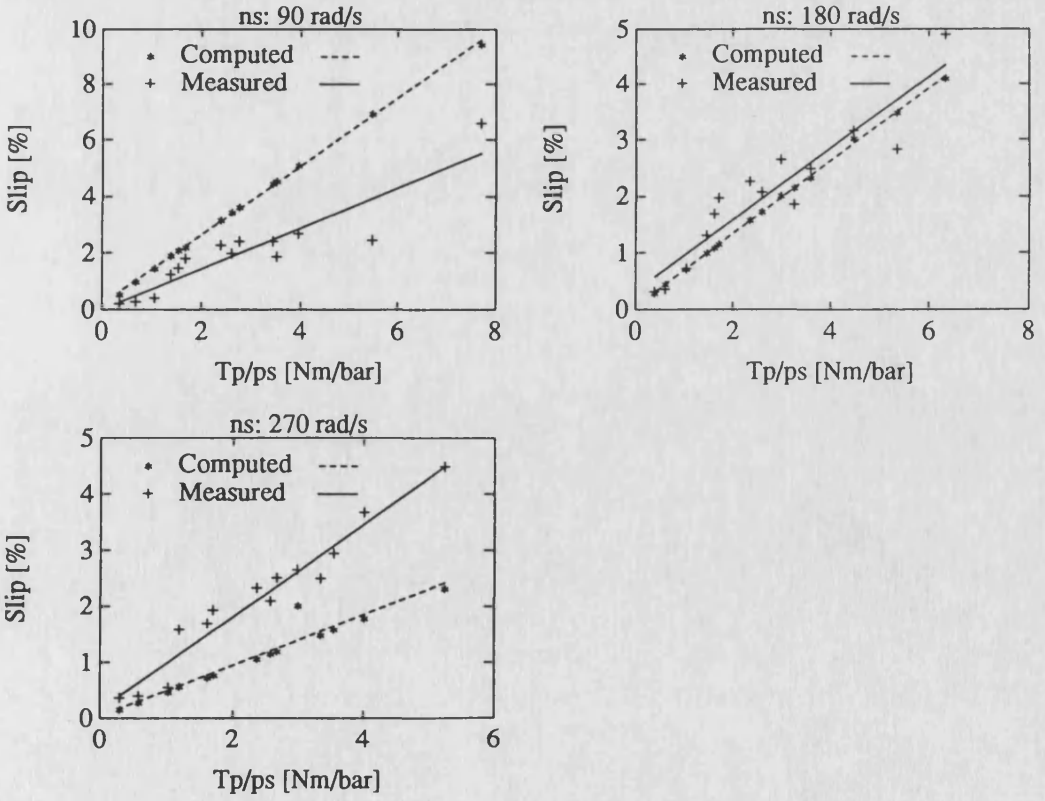

Figure 5.2 Measured and computed slip for R_p = 0.0392 m

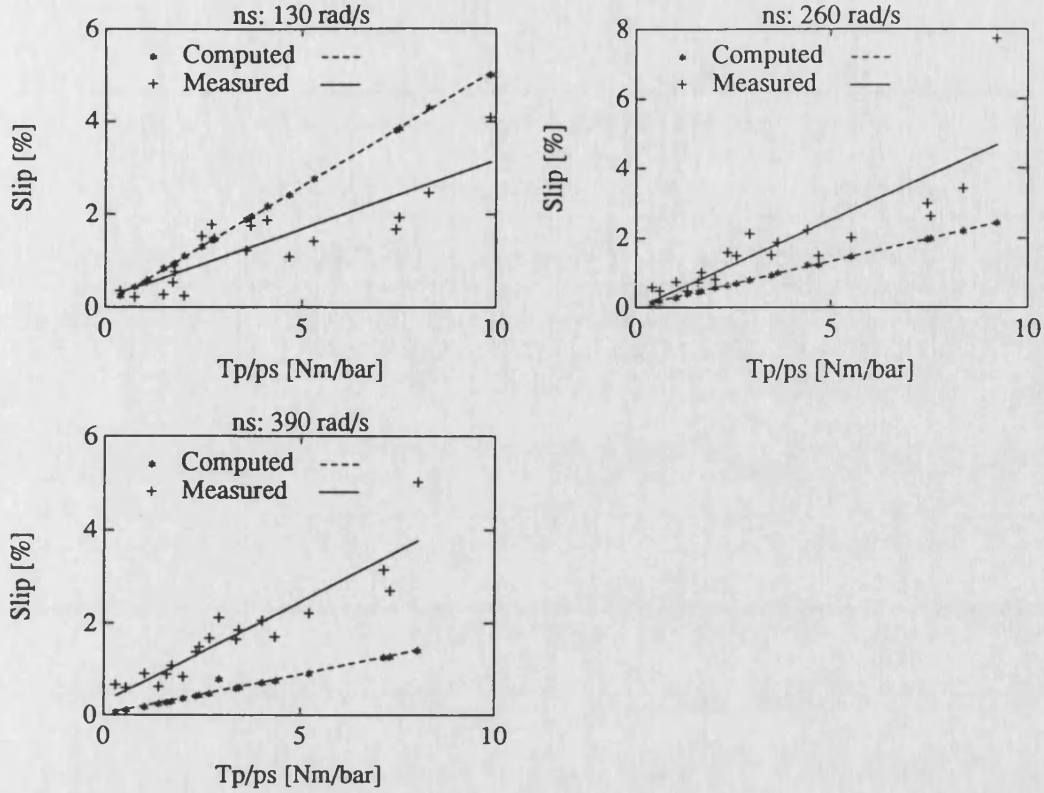

Figure 5.3 Measured and computed slip for R_p = 0.05 m

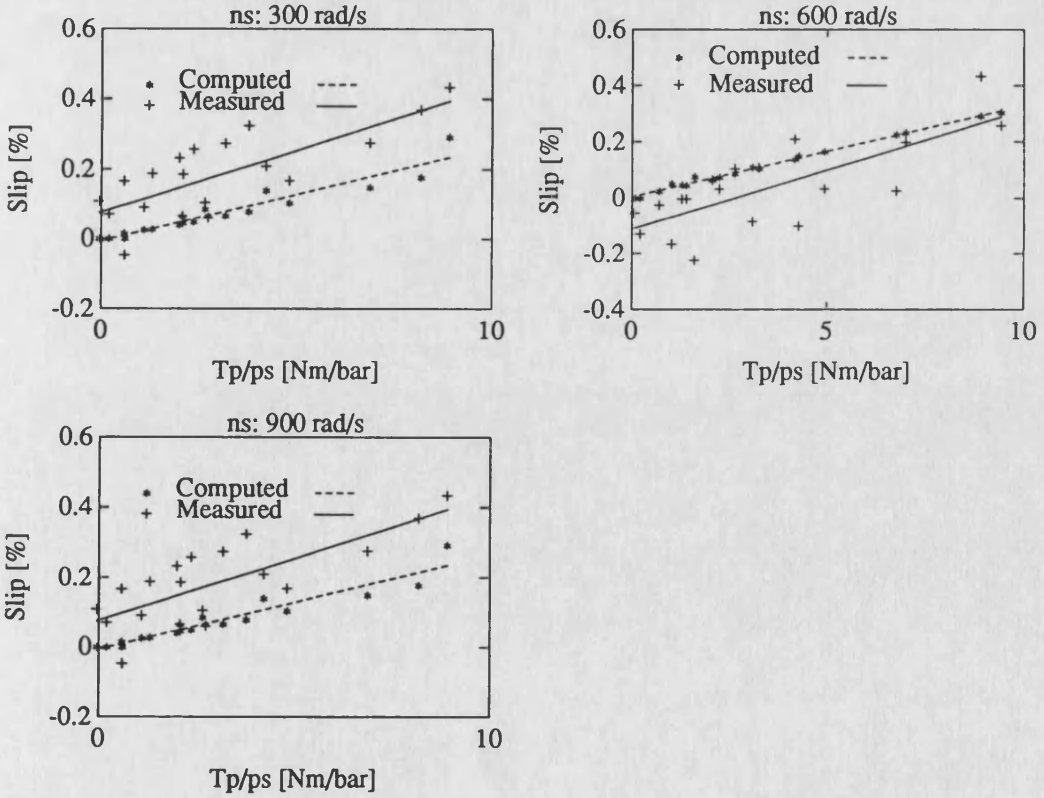

Figure 5.4 Measured and computed slip for R_p = 0.0703 m

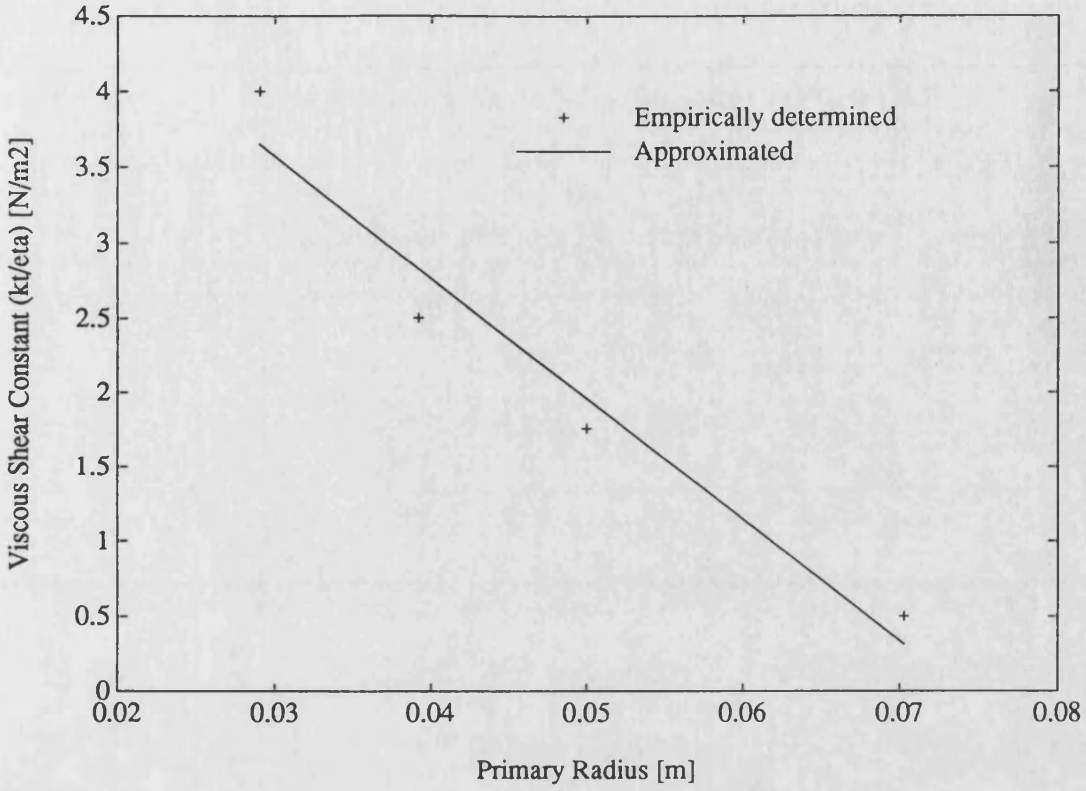

Figure 5.5 Viscous shear parameter as a function of primary radius

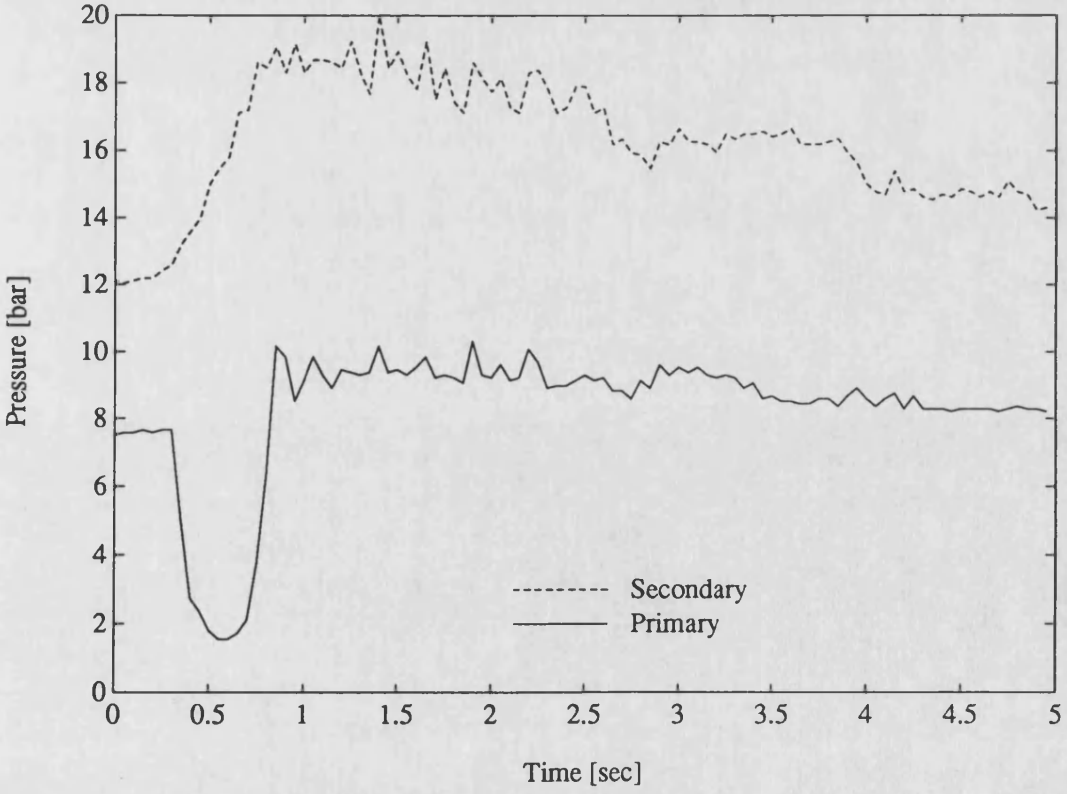

Figure 5.6 Measured primary and secondary pressure for the 90° throttle step of Figure 3.11

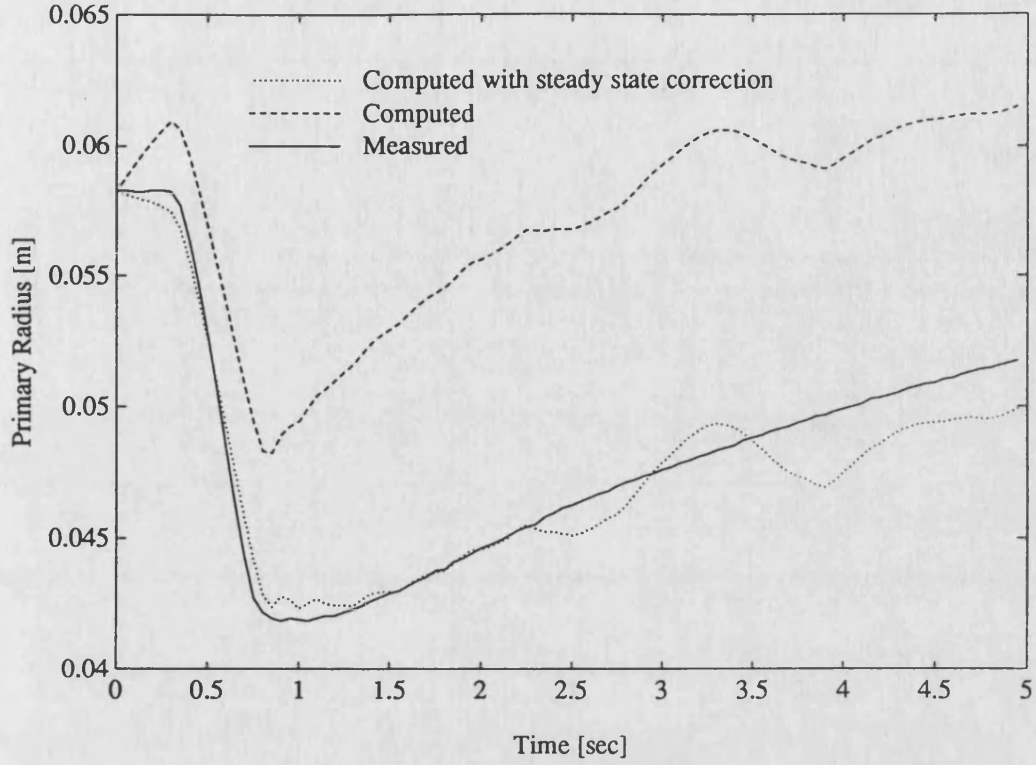

Figure 5.7 Measured and computed primary radius for the 90° throttle step

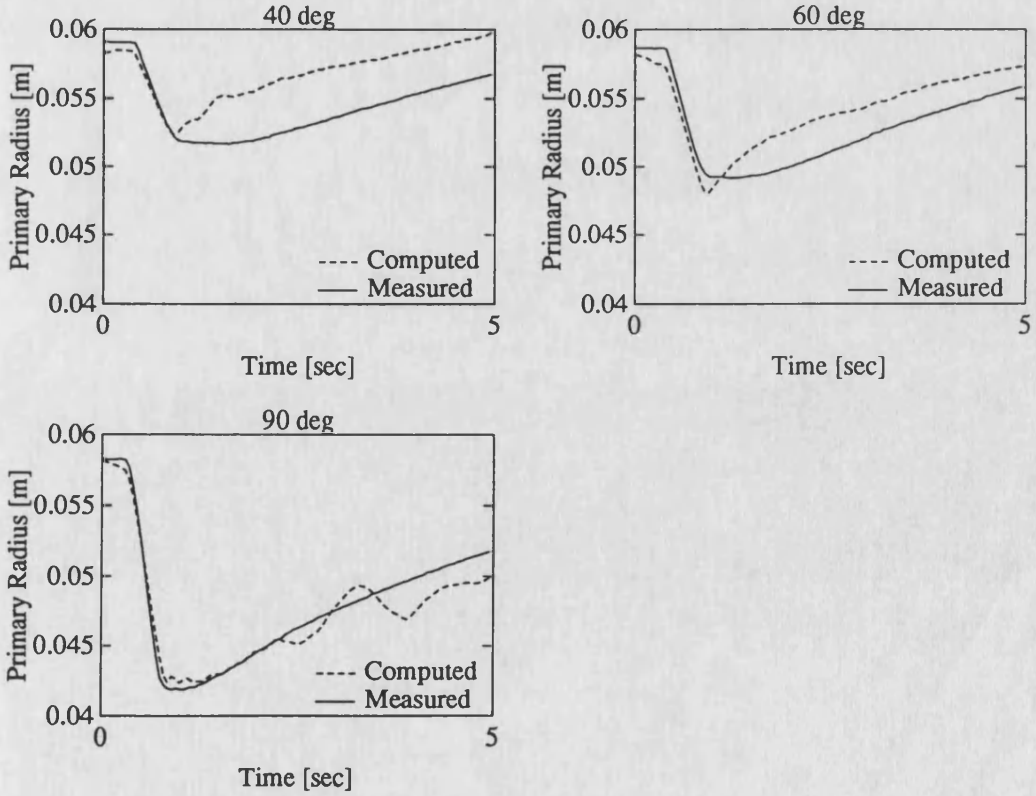

Figure 5.8 Primary radius for different throttle step demands

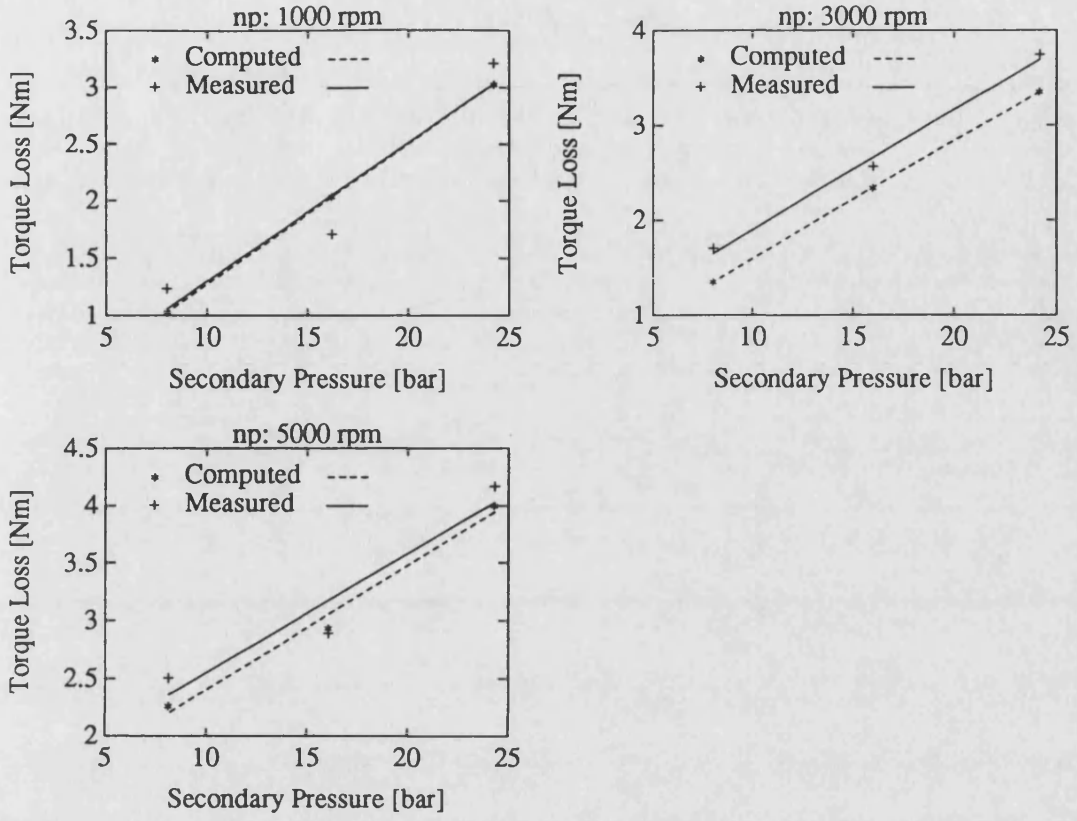

Figure 5.9 Measured and computed no load torque loss for R_p = 0.05 m.

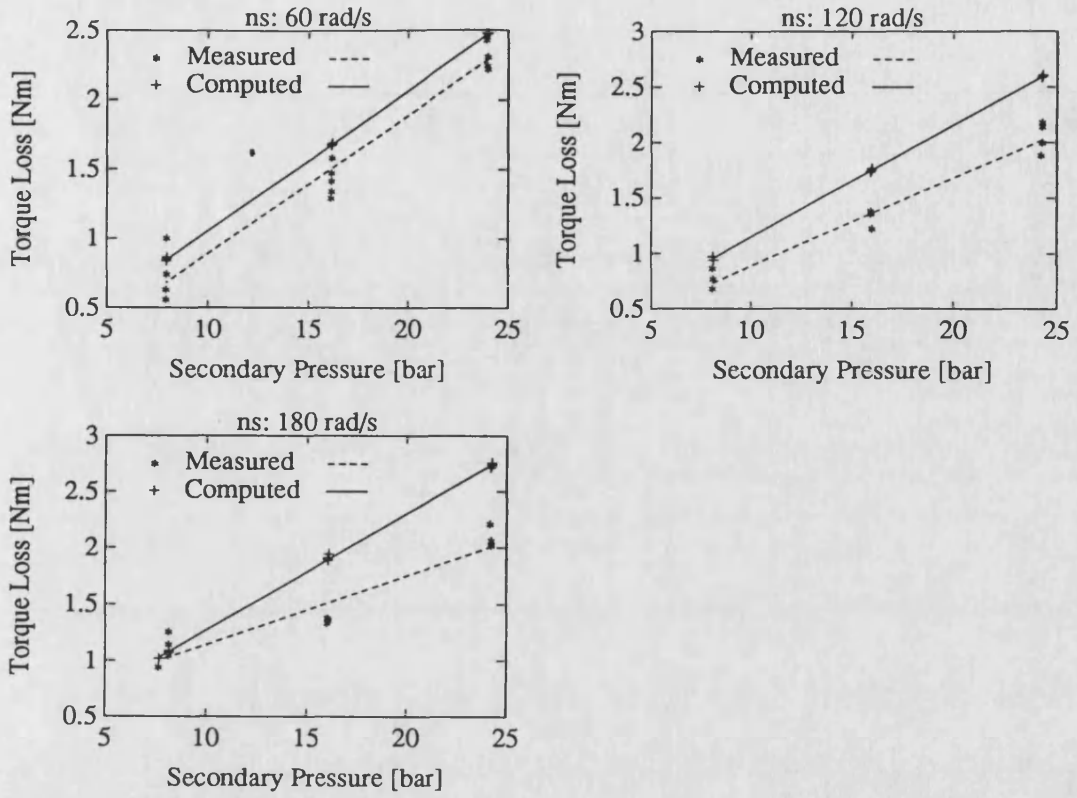

Figure 5.10 Measured and computed torque loss for R_p = 0.029 m

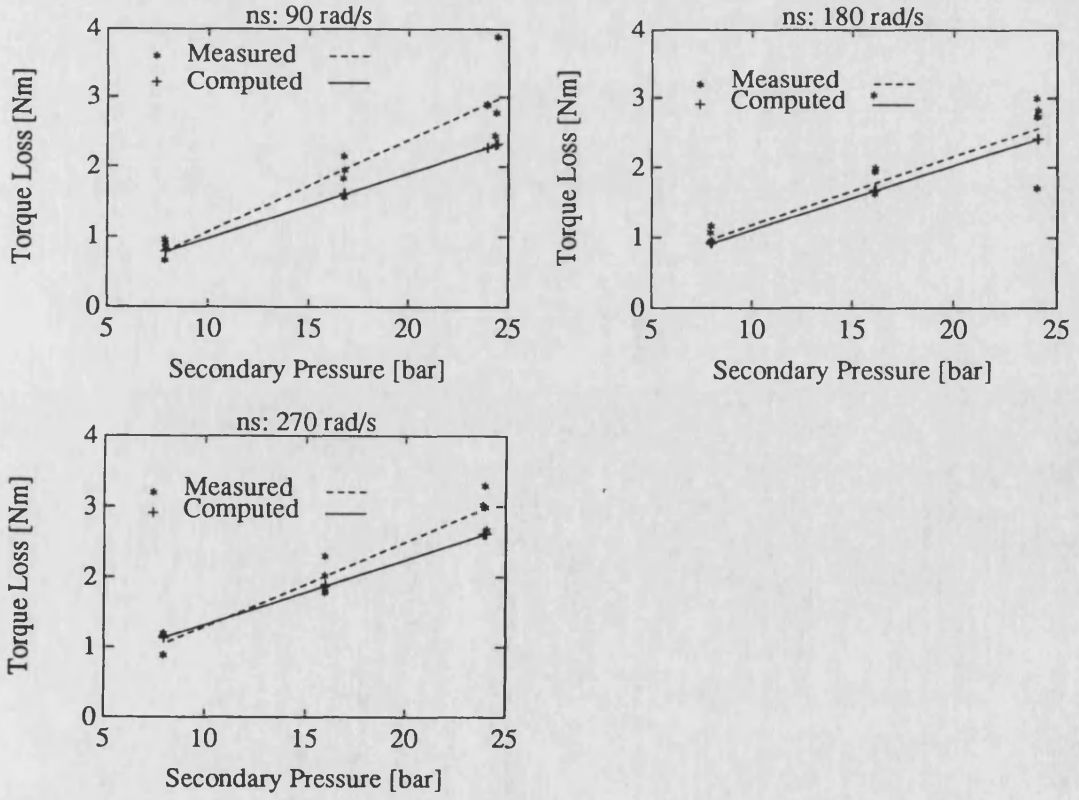

Figure 5.11 Measured and computed torque loss for R_p = 0.0392 m

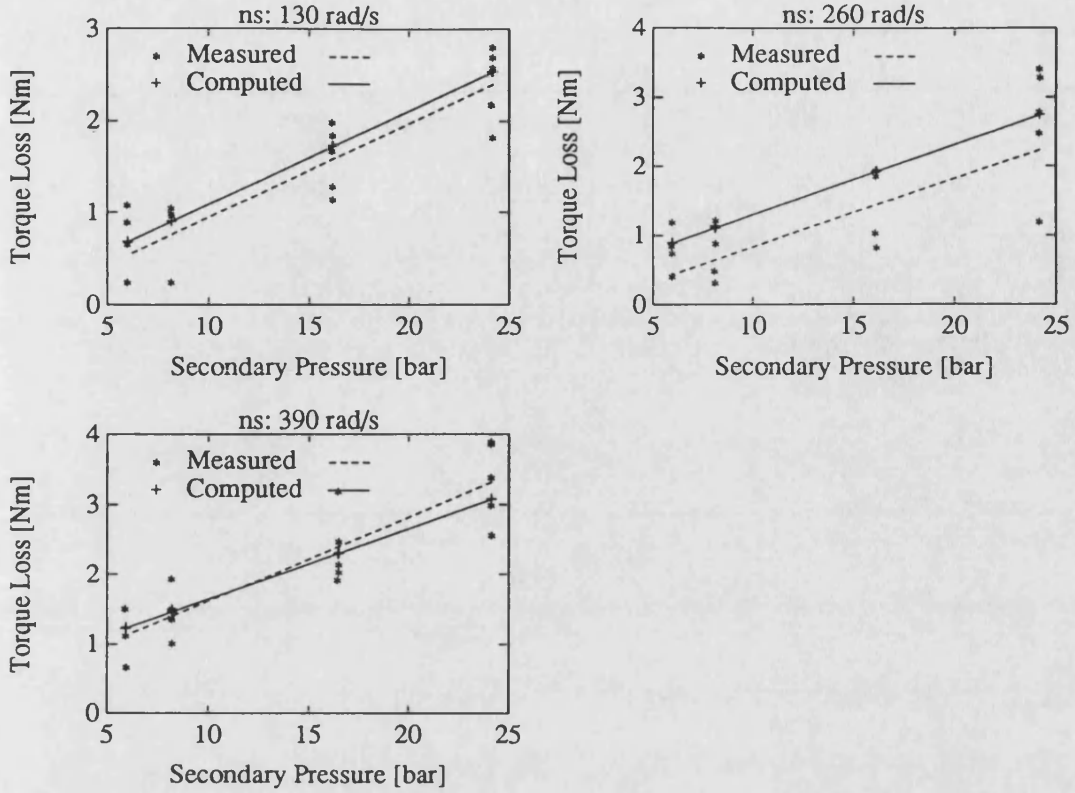

Figure 5.12 Measured and computed torque loss for R_p = 0.05 m

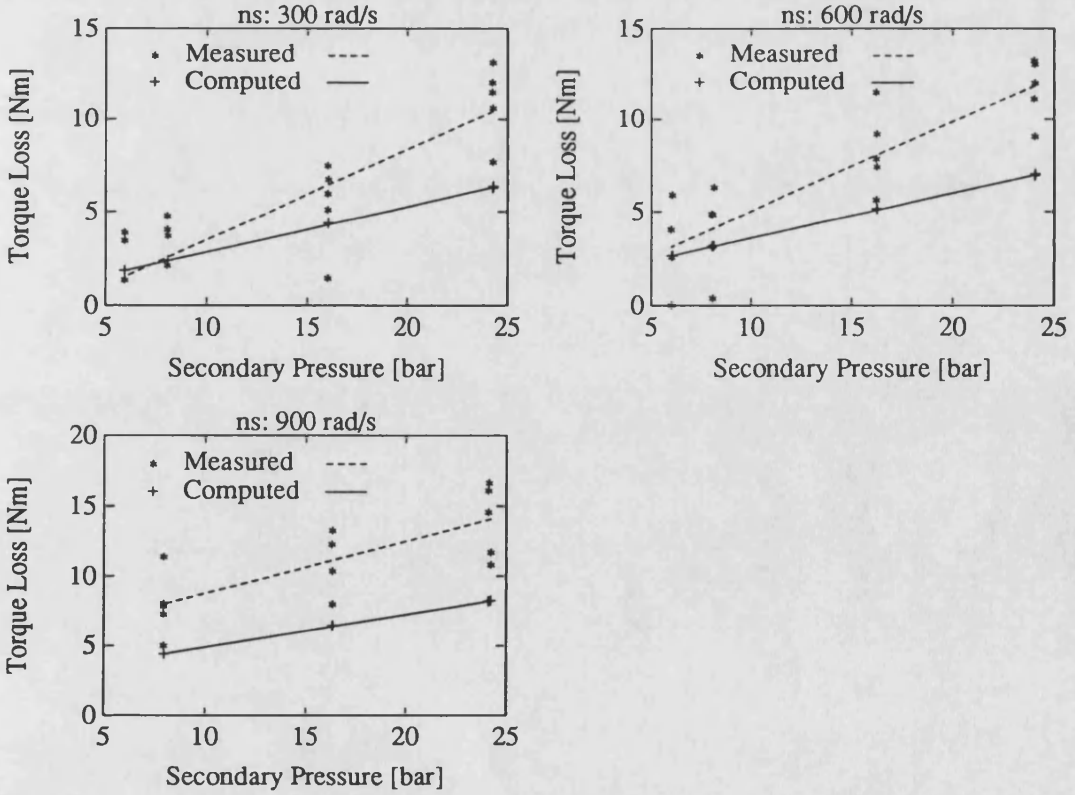

Figure 5.13 Measured and computed torque loss for R_p = 0.0703 m

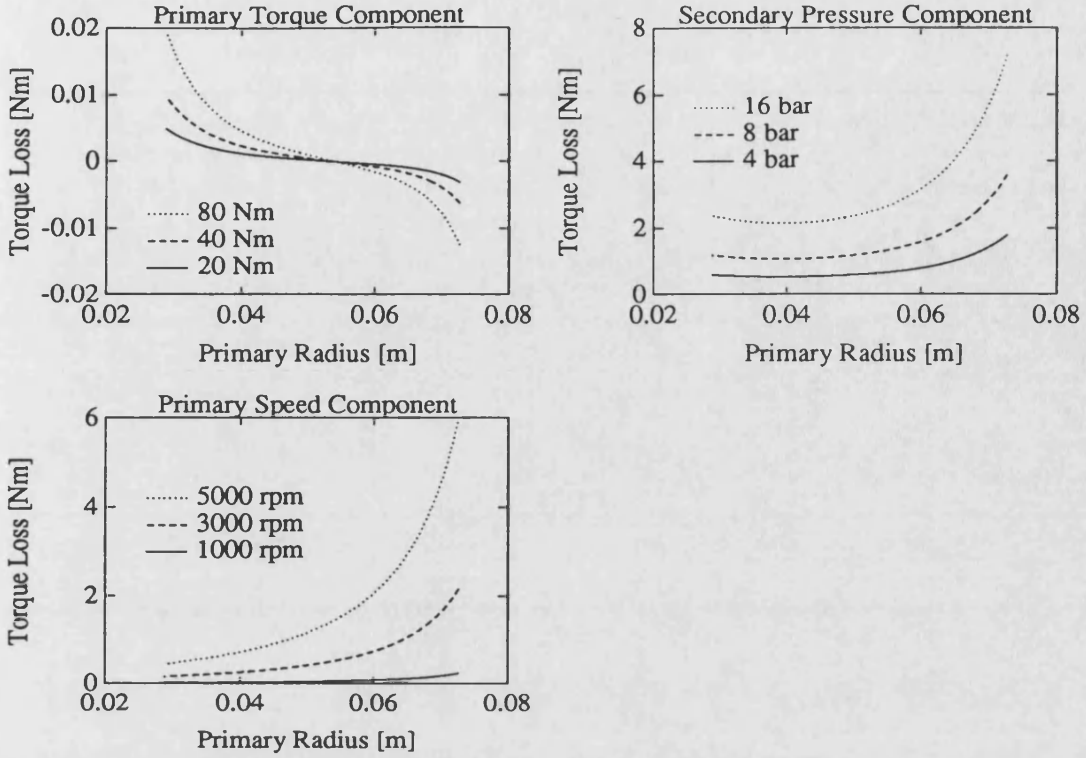

Figure 5.14 Influence of different torque loss components. The torque component is two magnitudes smaller than the others.

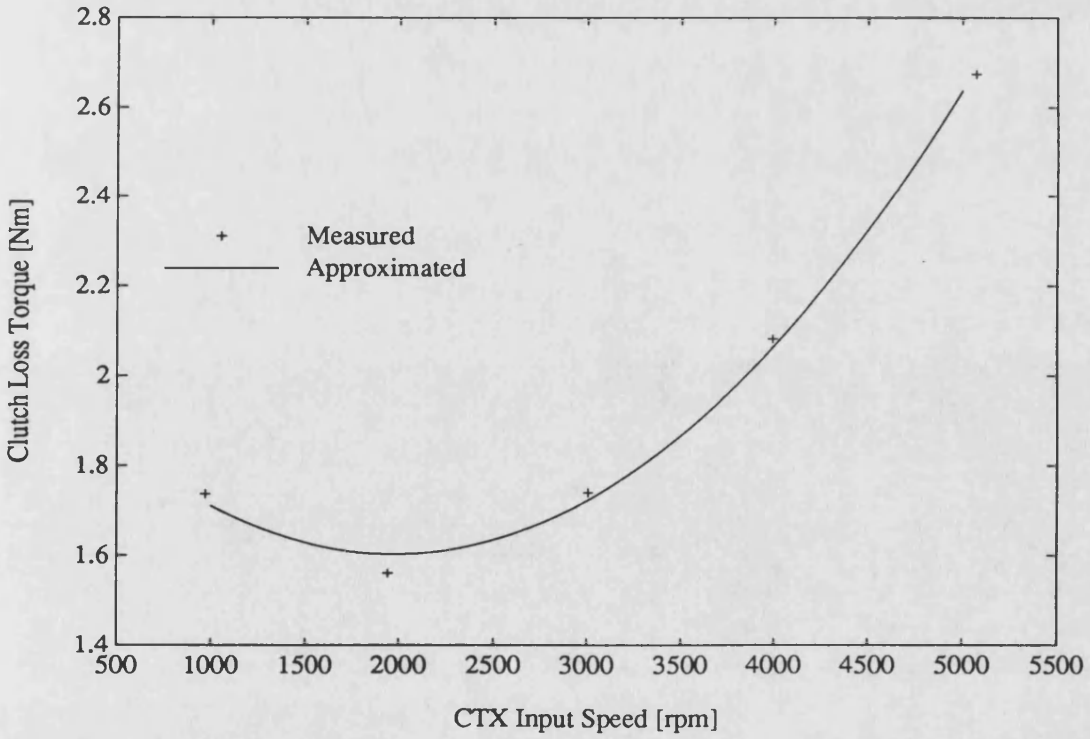

Figure 5.15 Measured and computed clutch torque loss as a function of CTX input speed. A quadratic relation is recognisable.

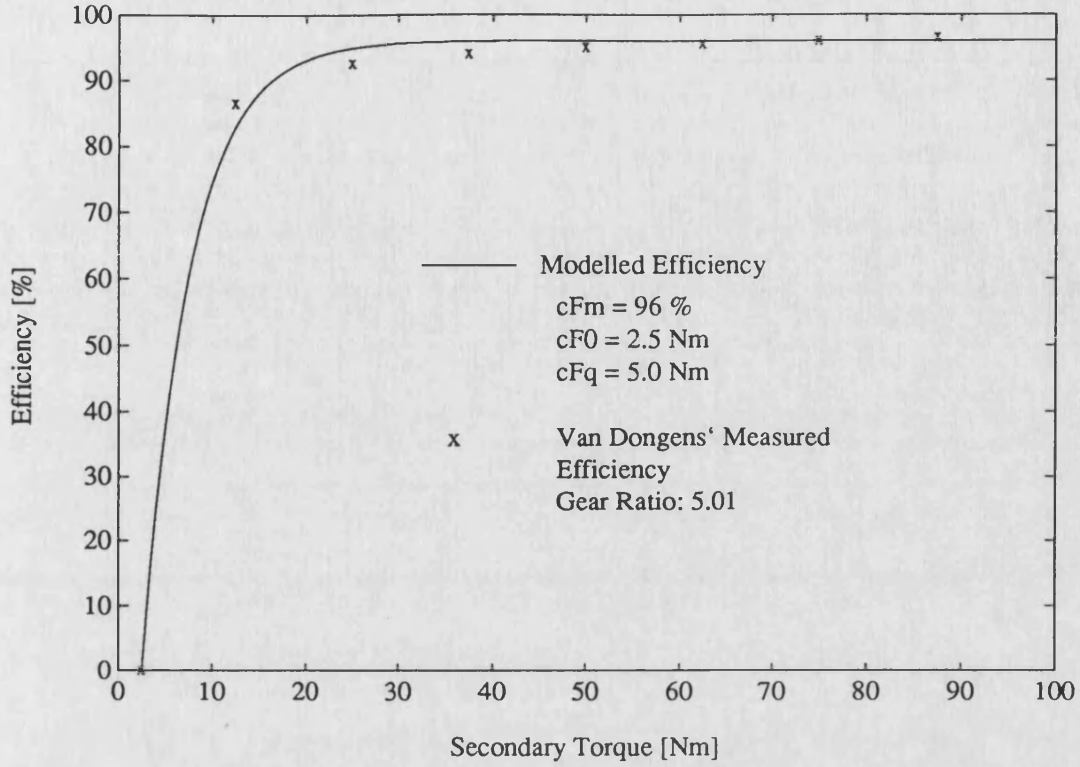

Figure 5.16 Comparison of van Dongen's and modelled final drive efficiency

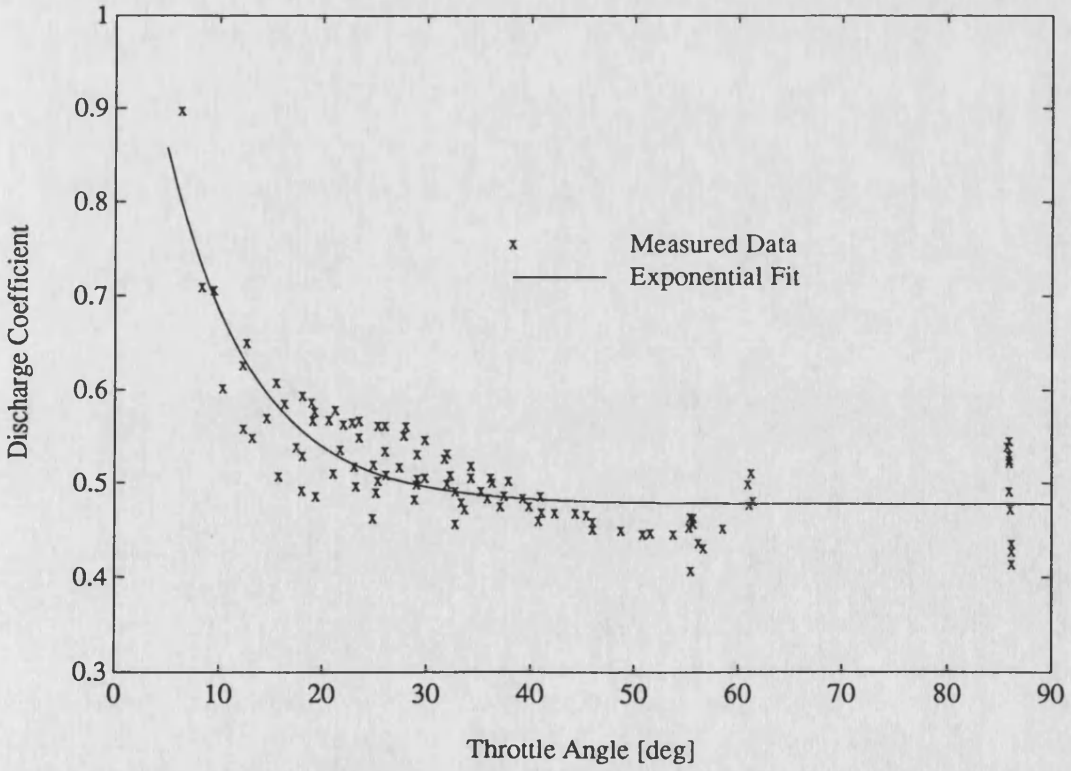

Figure 5.17 Measured and approximated discharge coefficient. The exponential fit resulted from a least square error approximation.

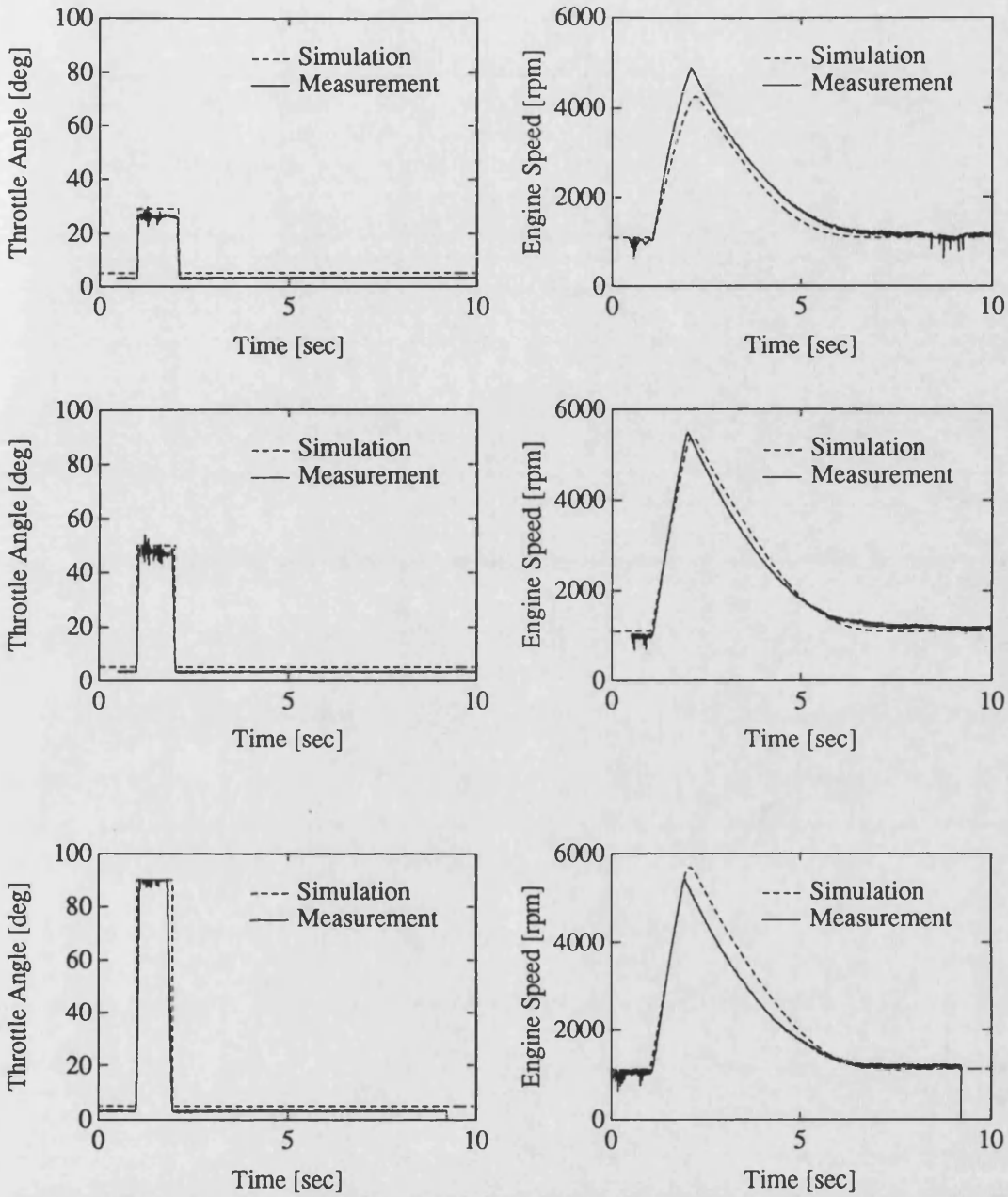

Figure 5.18 Engine validation data. A step change in throttle angle is applied; no load acts on the engine.

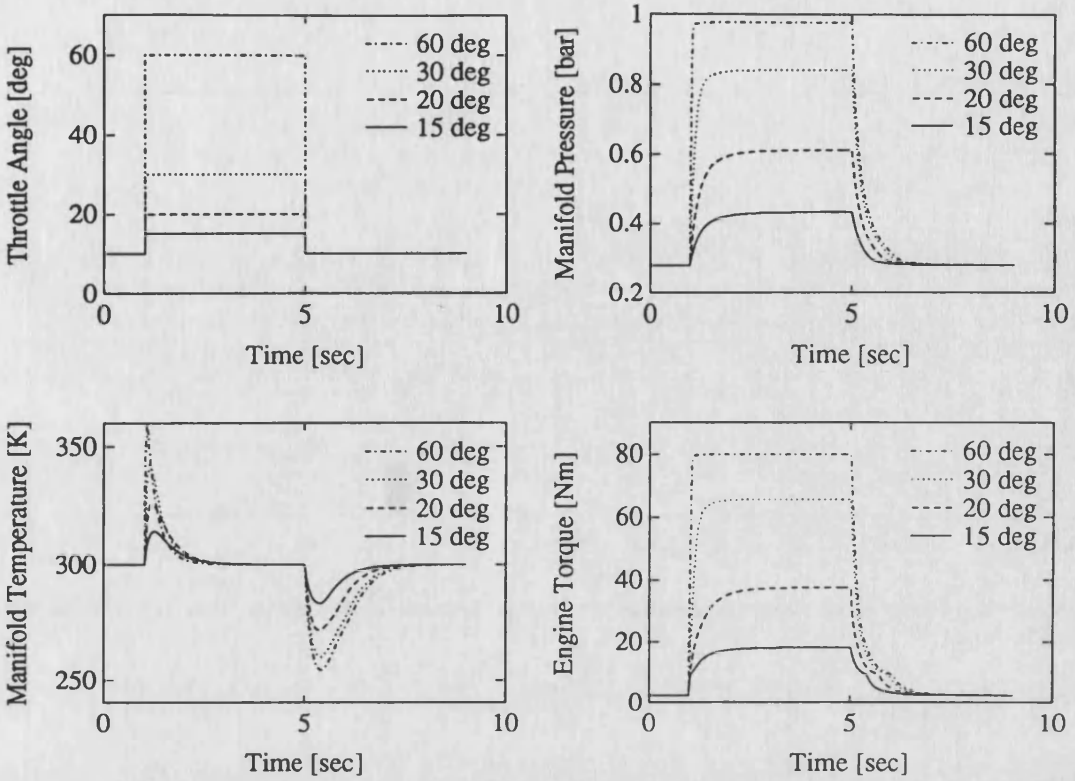

Figure 5.19 Dynamic simulation data. The engine speed was set constant to 2000 rpm; i.e. the inertia model was not used to compute the engine speed dynamically.

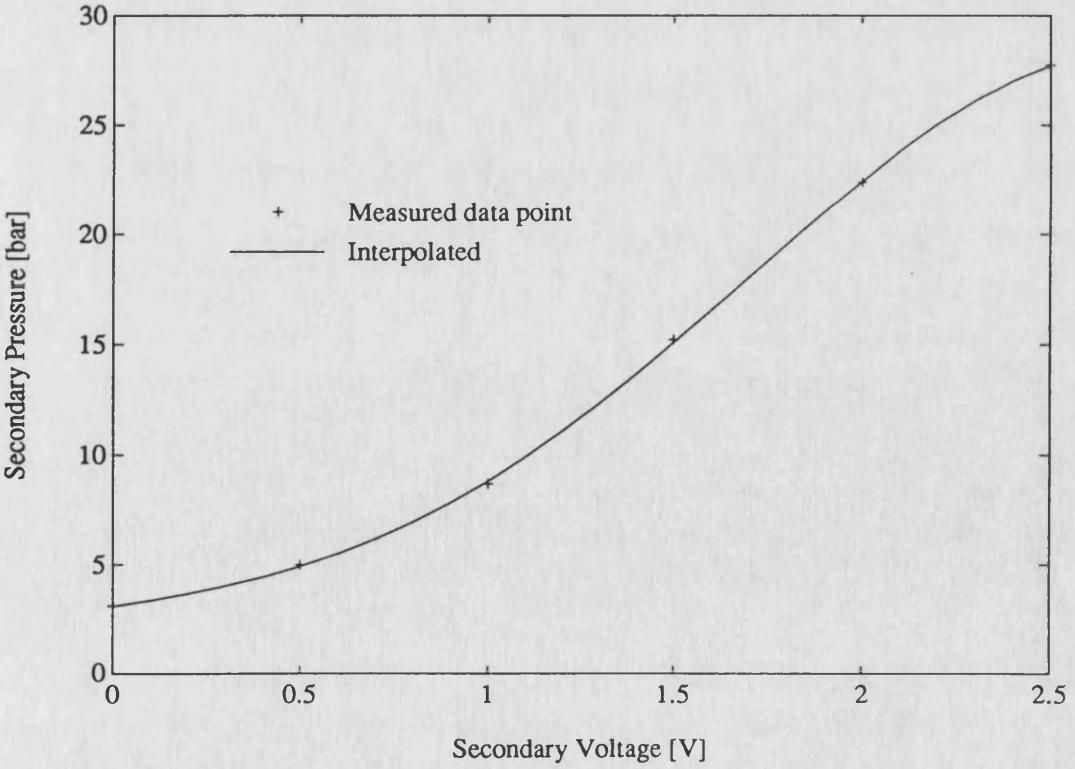

Figure 5.20 Measured secondary pressure as a function of the secondary voltage

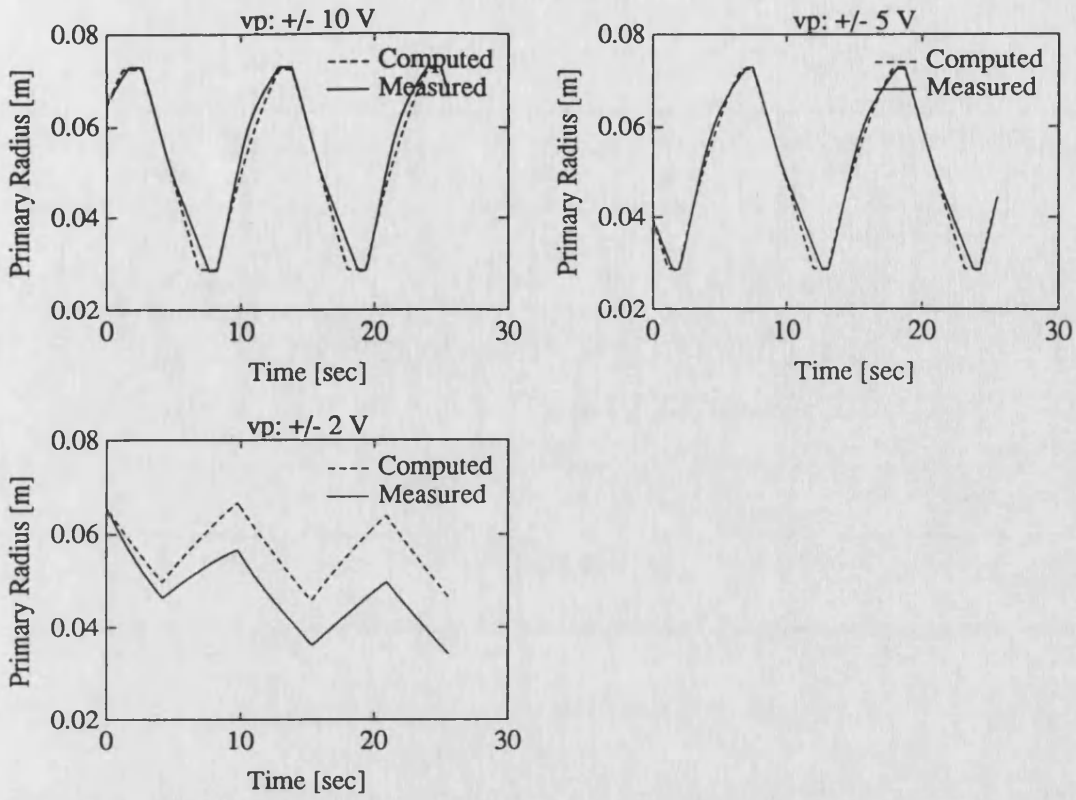

Figure 5.21 Measured and computed changes in primary radius using the electro-hydraulic control

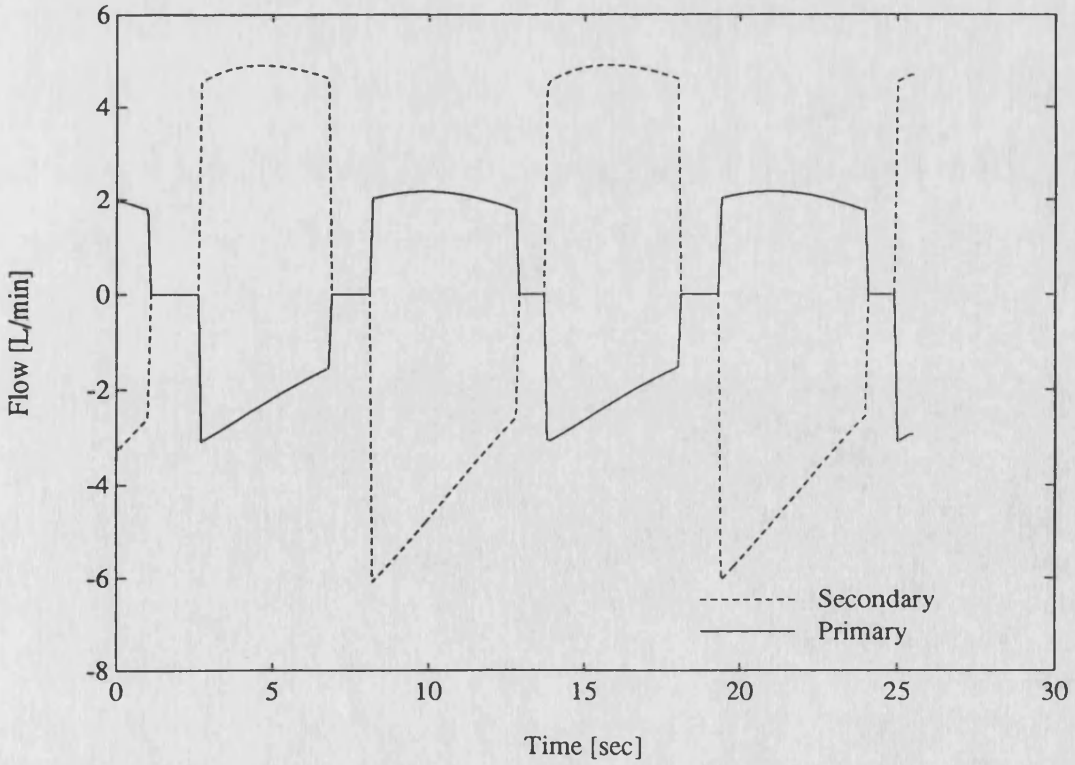

Figure 5.22 Primary and secondary actuator flow for v_p ±10 V primary voltage step

6. OPTIMUM EFFICIENCY OF THE CTX POWERTRAIN

This chapter focuses the information accumulated in the previous two chapters in line with the objectives outlined in Chapter 1. Fuel consumption can be improved in two ways. First, operating procedures that maximise the power transmission efficiency of the VSU are implemented. This results in closed loop control of the VSU slip. Secondly, a strict IOL powertrain control strategy is realised and any resulting disadvantages with respect to transient response are investigated.

The concept of optimum efficiency control of the VSU is explained in 6.1. Considerations for the overall CTX powertrain control strategy are given in 6.2. Sections 6.3 and 6.4 elaborate on these ideas yielding a controller and its implementation. The performance of the new system is evaluated and compared with the initial system in 6.5. 6.6 summarises the results.

An optimum efficiency (OE) and an IOL controller are designed. Simple proportional and integral laws are used to drive the primary and secondary valve. This enables easy on-line tuning. A more sophisticated method is pursued in Chapter 7 where a robust multivariable feedback controller is designed.

6.1. Optimum Efficiency Control of the VSU

The secondary pressure is controlled by means of the secondary valve to achieve maximum transmission efficiency of the VSU in steady state.

6.1.1. The Optimisation Problem

Three loss components hamper the power transmission efficiency of the VSU. These are losses due to *viscous shear (slip)*, the *torque loss* and the *hydraulic pump*. Thus, the secondary pressure has to be determined at which the sum of the power losses is

minimised.

CONVENTIONS

Independent variable. In the steady state, the secondary force is proportional to the secondary pressure (equation (5.1)) and is used as independent variable.

Belt geometry. The belt kinematics determine one active radius if the other is given (equations (4.5) and (4.6)). The notation $R_{\cdot}$ (*R subscript dot*) is used to designate this.

ASSUMPTIONS

Quasi steady state operation is assumed. Small changes in secondary pulley force have no influence on the belt geometry and the output power. It could be equally well assumed that the input power is not affected by the secondary force. The choice of the output side, at this stage, is arbitrary. However, it will be advantageous in 6.1.3 where it allows an elegant control strategy to be developed. Hence n_s, T_s and $R_{\cdot}$ are assumed intermittently fixed. Additionally, equation (4.33) holds which fixes the ratio of the primary and secondary pressures.

Constant. Intermittently fixed variables (n_s, T_s and $R_{\cdot}$) go into the computation as constants.

SOLUTION

The sum of the power losses in terms of the components shear loss, torque loss and pump loss may be expressed as

$$P_L = \left(n_p T_p + n_s T_s\right) + n_s \frac{R_s}{R_p} T_l + \frac{D_p}{A_s \nu} F_s n_p \qquad (6.1)$$

The "+" sign in the shear loss component results from the sign convention. The correct power loss due to the torque loss would be $n_p T_l$. For reasons of subsequent analytical simplification n_p is approximated by

$$n_p \approx n_s \frac{R_s}{R_p} \tag{6.2}$$

in which the slip is neglected.

Equations (4.31) through (4.33) are used to express equation (6.1) as a function of F_s, n_s and $R_.$.

$$\begin{aligned} P_L = & \left[n_s \frac{R_s}{R_p} - \frac{A_c k_t}{\eta} \left(\frac{R_s T_s}{R_p q_s F_s} + \frac{R_p \beta_s T_s}{q_p R_s \beta_p F_s} \right) \right] \left[- T_s \frac{R_p}{R_s} + \frac{D_p}{A_s \nu} F_s \right] \\ & + n_s T_s + n_s \frac{R_s}{R_p} Q \left[\frac{2 \tan \Theta F_s}{\beta_s} - \frac{T_s}{2R_s} + v_L^2 m \right] \end{aligned} \tag{6.3}$$

This can be re-arranged to give

$$P_{loss} = A_0 + A_1 F_s + A_2 \frac{1}{F_s} \tag{6.4}$$

where

$$\begin{aligned} A_0 = & -n_s T_s - T_s \frac{D_p A_c k_t}{\eta A_s \nu} \left[\frac{R_s}{R_p q_s} + \frac{R_p \beta_s}{q_p R_s \beta_p} \right] + n_s T_s + \\ & n_s \frac{R_s}{R_p} \left[p_1 \left[- \frac{T_s}{2R_s} + v_L^2 m \right] + p_2 T_s \right] \\ A_1 = & \, n_s \frac{R_s}{R_p} \frac{D_p}{A_s \nu} + n_s \frac{R_s}{R_p} p_1 \frac{2 \tan \Theta}{\beta_s} \\ A_2 = & \, T_s^2 \frac{A_c k_t}{\eta} \frac{R_p}{R_s} \left[\frac{R_s}{R_p q_s} + \frac{R_p \beta_s}{q_p R_s \beta_p} \right] \end{aligned} \tag{6.5}$$

A_1 and A_2 only depend on n_s, T_s and $R_.$ and are thus constant (see Assumption). A_0 depends additionally on v_L which neglecting slip can be approximated by

$$v_L \approx n_s R_s \tag{6.6}$$

Therefore, A_0 is also constant.

The minimum of equation (6.4) has to be determined. The easy structure of (6.4) simplifies this task considerably. P_L is an odd function in F_s with two extremes, a local minimum for $F_s > 0$ and a local maximum for $F_s < 0$. Physically, only positive F_s are realisable. Hence, setting the differential with respect to F_s to zero results in the determination of the sought minimum.

$$\frac{d}{dF_s}\left[A_0 + A_1 F_s + A_2 \frac{1}{F_s}\right] = 0 \tag{6.7}$$

Bearing in mind that A_0 through A_2 are constants this simplifies to

$$A_1 + A_2 \frac{1}{F_s^2} = 0 \tag{6.8}$$

Hence, if

$$F_s = F_{s,opt} = \pm\sqrt{\frac{A_2}{A_1}} \tag{6.9}$$

the sum of the power losses is minimum. Note that F_s has to be positive and thus no ambiguity occurs. Inserting for A_1 and A_2 from (6.5) into (6.9) leads to

$$F_{s,opt} = \pm\frac{T_s}{\sqrt{n_s}}\frac{R_p}{R_s}\sqrt{\frac{\frac{A_c k_t}{\eta}\left[\frac{R_s}{R_p q_s} + \frac{R_p \beta_s}{q_p R_s \beta_p}\right]}{\left[\frac{D_p}{A_s v} + p_1 \frac{2\tan\Theta}{\beta_s}\right]}} \tag{6.10}$$

This is the *efficiency optimising law*. The function in R_r in the square root is always positive which ensures always a real solution.

NUMERICAL EXAMPLE

The components and the sum of the power losses in equation (6.3) are plotted in Figure 6.1 against the secondary pressure for a typical operating condition. (6.10) leads to $F_{s,\,opt}$ = 3710 N which corresponds to an optimum secondary pressure ($p_{s,\,opt}$) of 3.82 bar. This compares to a value of 3.85 bar as read from the graph. The difference results from the used approximation and is, as expected, negligible. The efficiency for this operating condition is 95% and compares with an efficiency of 93% for a secondary pressure of 10 bar which is a condition typically set by the standard hydro-mechanical control unit.

6.1.2. Numerical Interpretation

The efficiency optimising law is evaluated over the whole operating range of the VSU.

OPTIMUM SECONDARY PRESSURE

The optimum secondary pressure that is proportional to $F_{s,opt}$ from (6.10) depends on the throughput power (n_s and T_s) and the belt geometry (R_r). Figure 6.2 illustrates the relation between the optimum secondary pressure and the throughput power for a given primary radius R_p = 0.0288 m. The power is expressed in terms of the input power into the CTX (n_p and T_p). This enables a consistent presentation for different radii which can be seen in Figures 6.3 through 6.5 for primary radii of R_p = 0.0434 m, R_p = 0.058 m and R_p = 0.0726 m.

The optimum secondary pressure is very small for large primary radius. This is due to the dependency of the torque and pump loss on the secondary pressure, especially at large primary radius and high speeds (see Figures 5.14 and 6.1). There are two further points about operation at R_p = 0.0726 m.

1. *A secondary pressure smaller than 1 bar (gauge)* would give the necessary clamping force with the existing secondary actuator area. Pressures of such small magnitudes are difficult to adjust because often the build-up of back pressure caused by the pressure drop over the cooler and the pipe work exceeds these values. A smaller secondary actuator area would require higher pressures and is thus a factor to improve the design. This is evaluated in Chapter 8.

2. *Viscous shear power density* T_p/p_s. The viscous shear model has been validated for values of T_p/p_s up to about 10 (see 5.1.1, Figures 5.1 to 5.4). The low secondary pressures in Figure 6.5 suggest values of T_p/p_s of about 80. This seriously stretches the range of the viscous shear model and uncovers doubts about validity. When the fixed radius tests were carried out the importance of acquiring data for T_p/p_s greater than 10 was not recognised and has not been investigated. However, as will be seen later, the electro-hydraulic control circuit was not able to adjust secondary pressures that were smaller than 4 bar.

VSU OVERALL EFFICIENCY

The corresponding efficiencies for the operating conditions in Figures 6.2 through 6.5 are shown in Figures 6.6 through 6.9. The efficiency optimising law is fulfilled and thus the presented data is the optimum efficiency of the Van Doorne VSU.

The optimum VSU efficiency for medium radii is reassuring. The efficiency values for maximum radii must be interpreted carefully, since excessive values of T_p/p_s are questionable because of the doubts over the viscous shear model validity.

OPTIMUM SLIP

The slip at which the efficiency is maximum is called the *optimum slip*. The slip is proportional to the viscous shear power density T_p/p_s, equations (5.5) to (5.7), and this ratio is determined by the efficiency optimising law. This means that for given speed and belt radius, the optimum slip is constant and, thus, independent of the primary

torque. Figure 6.10 shows the adjusted optimum slips for operating conditions that correspond to the previous data (Figures 6.2 to 6.5 and 6.6 to 6.9, respectively).

The optimum slip for large primary radii is below 1% although only very small clamping forces are employed. The optimum clamping forces for small primary radii are similar to the ones set by the hydro-mechanical control unit and thus, the optimum slips for small primary radius R_p compare to the ones measured in Figure 5.1.

6.1.3. Control Strategy

Two control schemes that incorporate the efficiency optimising law are developed in this section. The difference lies in the feedback variables used. The secondary voltage, v_s in Figure 6.11, is used to adjust optimum efficiency conditions.

PRESSURE FEEDBACK

Figure 6.11 shows the direct incorporation of the efficiency optimising law (6.10) into a closed-loop control scheme. $p_{s,opt}$, the proportional value to $F_{s,opt}$, is used as a demand for the closed-loop pressure control (the actual secondary pressure, $p_{s,act}$, is measured). This means that all variables on the right of equation (6.10) have to be known at run time (i.e. n_s, T_s and R). The error signal between the demanded and the actual secondary pressure is fed into the controller *G(s)* to be designed in 6.4. The secondary speed and the radius can be measured, whereas it would not be possible on a mass production scale to measure the secondary torque. However, the engine torque can be estimated from an engine management system and the secondary torque could be computed using models presented in this study. This increases the complexity of the powertrain control computer at the benefit of having a robust control loop.

SPEED FEEDBACK

The optimising law (6.10) can easily be rearranged using equation (4.32)

$$\frac{\pm T_p}{F_{s,opt}} = \sqrt{n_s} \sqrt{\frac{\frac{D_p}{A_s \nu} + p_1 \frac{2\tan\Theta}{\beta_s}}{\frac{A_c k_t}{\eta}\left[\frac{R_s}{R_p q_s} + \frac{R_p \beta_s}{q_p R_s \beta_p}\right]}} \tag{6.11}$$

Replacing T_p/F_s in equation (5.4) with $T_p/F_{s,opt}$ of equation (6.11) leads to the computation of an optimum primary speed, $n_{p,opt}$.

$$n_{p,opt} = \frac{R_s}{R_p} n_s + \sqrt{n_s} \frac{R_s}{R_p} \sqrt{\left[\frac{D_p}{A_s \nu} + Q \frac{2\tan\Theta}{\beta_s}\right] \frac{A_c k_t}{\eta}\left[\frac{R_s}{R_p q_s} + \frac{R_p \beta_s}{q_p R_s \beta_p}\right]} \tag{6.12}$$

$$= \frac{R_s}{R_p} n_s + \sqrt{n_s}\, f_{opt}(R)$$

The square root is a function in R and is abbreviated with $f_{opt}(R)$. (6.12) can be used in a speed feedback layout as shown in Figure 6.12, where $n_{p,opt}$ is compared with the actual primary speed n_p. The difference between the two will be referred to as the *slip error*. Again, the controller *G(s)* is going to be designed in 6.4. The study of (6.12) shows that only the secondary speed, n_s, and the belt geometry have to be known to compute the reference value, $n_{p,opt}$. The basis to do this lies in the efficiency optimising law and the application of the modelled speed relation (VSU Slip Model, Figure 6.12). Contrary to the pressure feedback scheme this strategy works autonomously which means it does not require any knowledge of the torque throughput. This enables the adjustment of optimum operating conditions independent of engine characteristic and would thus extend the application to others than only automobile use. Additionally, the measurement of the secondary pressure is not necessary. However, comparing (6.12) with (5.7) it becomes apparent that the second term on the right hand side in (6.12) relates to the slip that has to be adjusted to

ensure optimum efficiency. This needs further consideration.

Determination of slip for the speed feedback control scheme. The slip error (Figure 6.13: input to the controller *G(s)*) disappears for correct operation.

$$n_p - n_{p,opt} \doteq 0 \tag{6.13}$$

Inserting (6.12) gives

$$n_p - \frac{R_s}{R_p} n_s - \sqrt{n_s}\, f_{opt}(R_.) \doteq 0 \tag{6.14}$$

where all values on the left side are measured. Comparing this equation with (5.7) gives

$$s_{opt} = \frac{\sqrt{n_s^m}\, f_{opt}(R_.^m)}{n_p^m} \tag{6.15}$$

This means that a successful control action must determine the slip of the VSU. If this is not done correctly equation (6.13) will not be satisfied and thus the correct optimum secondary pressure will not be adjusted. The sensitivity of the measured slip to any inaccuracies in determining n_p, n_s or $R_.$ is expressed by the maximum error.

$$\begin{aligned} \left|\frac{\delta s_{opt}}{s_{opt}}\right| &= \left|\frac{\partial s_{opt}}{\partial n_s}\frac{\delta n_s}{s_{opt}}\right| + \left|\frac{\partial s_{opt}}{\partial n_p}\frac{\delta n_p}{s_{opt}}\right| + \left|\frac{\partial s_{opt}}{\partial R_.}\frac{\delta R_.}{s_{opt}}\right| \\ &= \frac{1}{2}\left|\frac{\delta n_s}{n_s}\right| + \left|\frac{\delta n_p}{n_p}\right| + \left|\frac{f'_{opt}(R_.)}{f_{opt}(R_.)}\right| |\delta R| \end{aligned} \tag{6.16}$$

The third component of the sum is evaluated graphically in Figure 6.13. The function f_{opt} is evaluated numerically for values of R_p, top left graph. f_{opt} is approximated by a 4th order polynomial function in a least square error sense, top right graph. This

yielded the function f_{appr} which was used to compute the partial differentiation of f_{opt}. The bottom left graph illustrates this, $f'_{opt}(R_p) \approx f'_{appr}(R_p) = \partial f_{appr}(R_p)/\partial R_p$. The factor of the third term on the right hand side of equation (6.16), $f'_{opt}(R_p)/f_{opt}(R_p)$, is plotted in the bottom right graph using again the approximation $f'_{opt}(R_p) \approx f'_{appr}(R_p)$.

The error of the speed measurement is about 0.1%. An error of 0.1 mm in the primary radius (due to measurement error or even irregular belt kinematics, such as wave action on straight paths) could result in a 1% deviation ($f'_{opt}(R_p)/f_{opt}(R_p) \approx 100$ at R_p = 0.07 m). This brings the total maximum error to about 1.15% compared to optimum slips of below 1% for large primary radii (Figure 6.10). Unfortunately the sensitivity increases the inaccuracy of the slip determination with increasing primary radii (bottom right graph in Figure 6.13) while the absolute value of the optimum slip decreases with increasing primary radii. Hence, it will be difficult to operate successfully at large primary radii. However, the principle of operation rather than a mature technical application is established in this work.

6.1.4. Choice of Control Strategy

The speed feedback strategy is pursued here since the autonomous structure is such an attractive alternative. Table 6.1 summarises the advantages and disadvantages of the two control schemes. The autonomous implementation outweighs the robustness aspect of the pressure feedback strategy. It reduces the number of required variables to be measured and widens up the strategy for other applications. The disadvantage of the speed feedback scheme is the determination of the slip that will make the control task particularly difficult at large primary radii (see above).

Table 6.1 Comparison of the pressure and the speed feedback control schemes

Control Scheme	Advantage	Disadvantage
pressure feedback	robust	pressure measurement, torque information [1]
speed feedback	autonomous	determination of slip (on-line)

[1] The torque is not measurable on a production scale. This could be inferred from an engine management system.

6.2. IOL Control of the CTX Powertrain

This section explains the embedding of the IOL-strategy into the powertrain control scheme. The implementation uses the primary pressure (transmission ratio) to adjust the engine speed.

6.2.1. The IOL for the Ford Engine

The IOL (Ideal Operating Line) specifies the most efficient steady state operation of the engine and is defined by the engine speed and the delivered torque. This determines other variables, such as fuel flow or throttle angle. In fact each line in the data presented in Appendix B corresponds to one operating point. Figure 6.14 visualises the specific consumption data from Appendix B. Lines of constant specific consumption are plotted against speed and torque, as well as the IOL. The IOL determines the delivered torque for a particular speed, and equally well the throttle angle for this particular speed. Figure 6.15 shows the relation between speed and throttle angle defined by the IOL.

6.2.2. Control Strategy

The CTX powertrain control strategy ensures that the engine is operated along its IOL. The driver demands power by means of the throttle position. The IOL determines the speed at which the engine should run which is adjusted by the controller (see Figure 6.15). Figure 6.16 shows the control scheme. The primary pressure is set by means of the primary valve command, v_p, which adjusts the transmission ratio. This changes the load on the engine transferring the engine operating point to the one defined by the IOL. *G(s)* is the controller to be designed in 6.4.

For a conventional manual transmission powertrain the engine power is directly proportional to the power delivered to the axle. This is not the case in the dynamic sense for a CVT powertrain where, initially, excess engine power is used to adjust the new engine operating point (in an IOL strategy excess power is realised by increasing the speed). After having reached the new engine speed the excess power is available at the axle. This describes the often reported transient lag of CVT powertrains.

6.3. Controller Design and Implementation

This section explains the design of the optimum efficiency (OE) and the IOL controller. The controllers *G(s)* in Figures 6.12 and 6.16 are going to be designed. The control loops are assumed independent, i.e. no interaction between the two is taken into account. A more sophisticated approach allowing for dynamic interaction of the command signals is described in Chapter 7.

6.3.1. Process and Specifications

Input-output system. Figure C.1 in Appendix C shows the Bath*fp* icon representation of the CTX powertrain system. Inputs 1 and 2 are the primary and the secondary valve commands v_p and v_s. The only output considered for this design is the engine speed.

Output 2 is only used in Chapter 7. The throttle angle is considered here as a disturbance input. The primary valve driver features a deadband compensator that is included in the simulation. The hydraulic secondary valve model is instantaneous; the dynamics are represented by the first order lag. An additional relief valve was used to set the maximum system pressure. This is modelled by the limit model at the input to the first order lag.

Linear plant. The open loop Bath*fp* simulation was used to drive the system to a representative operating point where a numerical evaluation led to the Jacobian matrix and thus to a linear model description. Appendix C lists the linear plant model used for the control system design. A worst case operating point was chosen: the engine run at about 3200 rpm with 40° throttle angle (steepest torque gradient); the VSU transmission ratio was about 1 (R_p = 0.0531 m); the corresponding car speed 15 m/s; the secondary pressure was 10 bar, the primary 5.3 bar.

System specification. The specification of the closed loop system can be separated into three points.

1. Controller structure. The simplest controller structure to enable on-line tuning of the control parameters has to be found.

2. Dynamics. The bandwidth of the plant should not suffer too much in closed-loop operation.

3. Steady state error. A "small" (see later 6.3.2) steady state error following step input is permitted in the ideal operating line (IOL) loop. No steady state error on step input is permitted for the optimum efficiency (OE) loop.

6.3.2. Design

Controller structure. The two controllers *G(s)* from Figures 6.12 and 6.16 are designed. The command signal v_s is used to close the OE loop, v_p is used to close the IOL loop. It is important to note that the dynamic computation ensures the convergence of the reference values for n_E and n_p which are equal for engaged clutch.

Digital implementation. The controller is designed as a continuous system and subsequently transformed into discrete form for implementation (6.5).

An Independent loop closing design method was used. Having two inputs and two objectives (OE and IOL) that control the same output requires careful consideration to be given to select the first loop. The two inputs v_p and v_s set the pulley cylinder pressures p_p and p_s. v_s directly influences both p_s and p_p, whereas v_p only changes p_p. Hence, the v_p-command loop (IOL loop) has to be closed first.

IOL LOOP

Figure 6.17 shows the open loop Bode plot for the extracted SISO system with input v_p and output n_E from Appendix C. The steady state phase of 180° means that a negative gain will be required. Considering this, the system is of type 0. A proportional controller with gain K_P results in a finite steady state error to a step input. The Bode plot in Figure 6.17 indicates that a proportional gain, K_P, of about 2 can be expected to give robust closed loop behaviour (gain margin = 20 dB, phase margin = 70°). This means that the steady state error e_{ss} due to a unit step input would become $1/(2 \cdot 60\text{dB}) = 0.5 \cdot 10^{-3}$ rad/s. This steady state error is acceptable and thus the proportional controller is satisfactory. A root locus evaluation gives a gain K_P = -2.7 to give a dominant damping ratio of 0.7. Figure 6.18 shows the unit step response of the closed loop linear system; the steady state error nearly disappears.

OPTIMUM EFFICIENCY LOOP

Figure 6.19 shows the open loop Bode plot for the extracted SISO system with input v_s and output n_E having the IOL loop closed with the controller designed above. Again, a negative input was used and the system is of type 0. Zero closed loop steady state error is required. This means that the controller has to include a pole at zero to make the steady state error disappear. The simplest of controllers with this structure is an integrator K_I/s. The Bode plot shows that the bandwidth of the plant will fall to about 20 rad/s. The root locus investigation leads to a gain K_I = -1.95 to give a dominant damping ratio of 0.6. Figure 6.20 shows the step response and the corresponding influence of the step disturbances. Due to the higher bandwidth of the

v_p input the disturbance rejection is small.

6.4. Implementation

The numerical simulation in Bath*fp* assisted with the implementation in two ways. First, the closed loop behaviour of the designed controller interacting with the non linear system was assessed. Secondly, the dynamic response was investigated and improved with additional measures.

One of the main concerns of the OE speed feedback scheme was that in reponse to a rapid throttle change the secondary pressure would build up too slowly which would cause high slips. The investigation in the simulation proved that this was not a problem. Note that the dynamic engine model was essential to verify this behaviour in simulation.

6.4.1. Controller Gains

The Bath*fp* simulation showed that the designed controller gains resulted in the expected behaviour. However, the controller gains were selected disregarding any interactions. The simulation showed that the designed closed loop damping ratios of 0.7 resulted in too low stability margins, especially when discontinuous inputs were applied. Thus the gains were reduced by 40% (K_P = -1.6 and K_I = -1.2), which corresponds to dominant damping ratios of 0.51 and 0.6, respectively, for the linear system. The stability was largely independent of the operating point.

6.4.2. Transient Response

Antiwindup. The minimum adjustable secondary pressure on the rig was about 3 bar, due to the build-up of back pressure. The OE strategy leads to pressures smaller than

that which results in a windup of the integrator. The given open loop characteristic of the secondary valve (Figure 5.20) was used as a saturation indicator. Secondary valve command signals outside the 0.2 and 2.2 V band correspond to saturation and thus the integration was stopped when the command signal went outside this band.

Transmission ratio. The simulation showed that rapid changes in transmission ratio required higher magnitude of the secondary pressure. Unfortunately, the chosen control strategy adjusted small secondary pressures (for optimum steady state efficiency). The transient performance was improved by adding a feed forward term from the throttle angle. A second order Chebyshev bandpass filter with the pass band between 1 Hz and 10 Hz was implemented. The pass band was determined by a method of trial and error. A gain of K_{FF} = 0.2 proved adequate.

6.4.3. Digital Implementation

Figure 6.21 shows the overall continuous controller that was to be implemented on the T800 transputer system. The reference signals n_{EJOL} and $n_{e,OE}$ were computed using the principles explained in 6.2 and 6.3.

Tustin's method was used to convert the continuous description into discrete form. A *sampling time of 10 ms* was chosen. This figure resulted from an early decision and it is appreciated that this was a compromise which might have detrimentally affected the faster IOL loop. However, careful signal conditioning including *antialiasing* resulted in a stable predictable system. All sampled signal were 50 Hz low pass filtered. The possibility to tune the controller gains on-line proved very useful. The zero order holds and the low sampling frequency introduced additional phase shift and, in order to maintain stability, the gains had to be decreased further. The recorded data to be presented in 6.4.4 used gains K_P = -1.25, K_I = -0.95 and K_{FF} = 0.1.

6.4.4. Results from the Rig

This section compares measurement and simulation results. The basis of comparison was the response with a throttle step demand to 60° carried out on the rig and in the Bath*fp* simulation. The initial car speed was about 11 m/s for both cases. Figures 6.22 through 6.25 show the results. Measured and computed data are displayed in each plot. The controller gains were identical.

The simulation and the test on the rig used different algorithms to compute the demanded engine speed based on the IOL. This resulted in a difference in demanded engine speed and thus different steady state engine speeds (n_E, Figure 6.22). Both signals have steady state errors. This is due to the acceleration of the vehicle which can be interpreted as an acting disturbance. From this point of view it should have been realised that an integrator is needed to make this error smaller. The computed and measured primary and secondary pressures (p_p, Figure 6.22 and p_s, Figure 6.23) diverge during the interval 2 to 4 seconds. The displayed measured pressures were recorded from the pressure transducers that were mounted outside the CTX casing. The computed pressures correspond to the line pressures, i.e. the pressures at the supply side of the orifice model. The pressure drop over the pipework into the cylinders which is significant during the high flow phase between 2 and 4 seconds created the difference. Figure 6.26 shows the computed actuator pressure. This signal follows the recorded secondary pressure better although differences are still present. This is partly due to the pressure drop between the transducer and the actuator and partly due to the difference in controller action. The CTX input torque (T_t, Figure 6.24) differs considerably in steady state. This could have been due to a mismatch of the engine map data and the actual performance of the engine used. This torque difference is mainly responsible for the difference in car speed (v_C, Figure 6.24).

The correspondence of the computed and measured slip and efficiency is remarkable. The large noise component for data from 1 to 4 seconds is due to the very small CTX output torque that is needed to drive the car at a constant steady speed of 11 m/s.

6.5. Performance

This section compares the performance of the electro-hydraulically (EH), optimum efficiency controlled CTX with the hydro-mechanical (HM) controlled one. It directly relates to section 3.2.

6.5.1. Efficiency

Guebeli (1992, Appendix A) showed that a gain in power transmission efficiency of 2% over the standard control unit is typical for full load operating range when the optimising law is ensured. The mathematical model is used to demonstrate the efficiency improvement over the whole operating range. CTX input power data that produced Figure 3.6 were taken to compute the efficiency according to the optimum efficiency law. The improvement against the data in Figure 3.6 is plotted in Figure 6.27 and 6.28. Both Figures carry the same information; Figure 6.27 visualises the gain in three dimensions, 6.28 in two dimensions.

The efficiency of the HM controlled CTX could only be established with the overall powertrain control enabled. This made it impossible to measure the improvement in efficiency because that would have meant to operate the EH controlled CTX in exactly the same operating point (input speed, input torque and transmission ratio) which was not carried out.

INTERPRETATION

The improvement in efficiency at high torques (50 to 80 Nm) is relevant since the powertrain controller adjusts to use these operating conditions. The efficiency improvement of about 5% cannot be directly extrapolated onto consumption values and has to be compared with the measured efficiency presented in Figure 3.6 (80% efficiency is typical). The peak efficiency improvement of about 20 % is in the low speed low torque range and has thus no relevance.

6.5.2. Fuel Consumption

The same steady state test as in 3.2.2 was carried out to determine the calculated fuel consumption improvement of the EH version. Measured data from the rig were taken to calculate the fuel flow. Figures 6.29 and 6.30 show the % change as compared to Figure 3.10. Again, Figure 6.29 in three dimensions and 6.30 in two dimensions displaying the same information.

INTERPRETATION

The line along the maximum improvement corresponds more or less with steady state level driving operating line. For this condition the true implementation of the IOL brings gains in the order of about 20%. For other operating points gains are about 10% but some losses were recorded. These occur at high torque low car speed conditions. This again is a consequence from the true implementation of the IOL. The engine speed adjusted by the HM controller was considerably higher, which produced more power and consumed more fuel. Unfortunately, the gain in power does not enter in the issue considered.

Note, that it is very difficult to give credit to either the OE or the IOL scheme for the improvement. Also, the presented steady state gains cannot be extrapolated onto fuel savings for a driving cycle which was not assessed.

6.5.3. Transient Behaviour

The same transient test as in 3.2.3 was repeated with the new controller. Throttle steps of 40°, 60° and 90° were applied with an initial car speed of 11 m/s, Figure 6.31. The irregularity in the 40° case at time 7 seconds is due to an instability in a control loop that has not been investigated further.

The slope at which the engine speed increases is the same for all three step inputs (and also the transmission ratio). This suggests a saturation of the flow to and from the pulley cylinders. This was recognised earlier when a larger secondary pressure resulted in faster ratio changes.

INTERPRETATION

Figure 6.32 shows the 90° throttle step changes of Figures 3.11 and 6.31, respectively. The true implementation for the IOL strategy can be seen by the engine speed plots. The engine speed climbs from 1400 to 5000 rpm against a change from 2000 rpm to about 4000 rpm. The car speed of the EH version clearly lags the HM case. The initial ratio change is much larger for the EH case which explains the lag. The increased engine power accelerates the car only marginally faster such that at time 25 seconds the initial speed gap is re-instated. This is disappointing. It was expected that the acceleration was much better having the engine running at its peak power point. However this was not investigated further.

6.6. Summary

The developed control strategies improved the steady state operation considerably. Typical gains of 5% in transmission efficiency and about 10% in fuel consumption were calculated. However, the transient behaviour of the powertrain in connection with optimum strategies has suffered compared to the HM controlled CTX. There are two reasons that explain this. First, the chosen IOL imposes very low engine speed for constant steady state driving at moderate car speeds. The request to increase the car speed can only be dealt with by increasing the engine speed considerably. Secondly, the rate of change of transmission ratio is clearly limited. This is due to increased hydraulic resistance that hinders high flows to and from the pulley cylinders.

In the light of the achieved improvements a strict IOL strategy is worthwhile pursuing. An improvement in transient transmission ratio control is thus the ultimate key for further progression.

The correspondence of the overall system behaviour (Figures 6.22 to 6.25) confirms the good system representation by the simulation. Particularly the slip and efficiency data in Figure 6.25 substantiate the validity of the computer simulation. This builds the basis for Chapter 7 where only simulation is used.

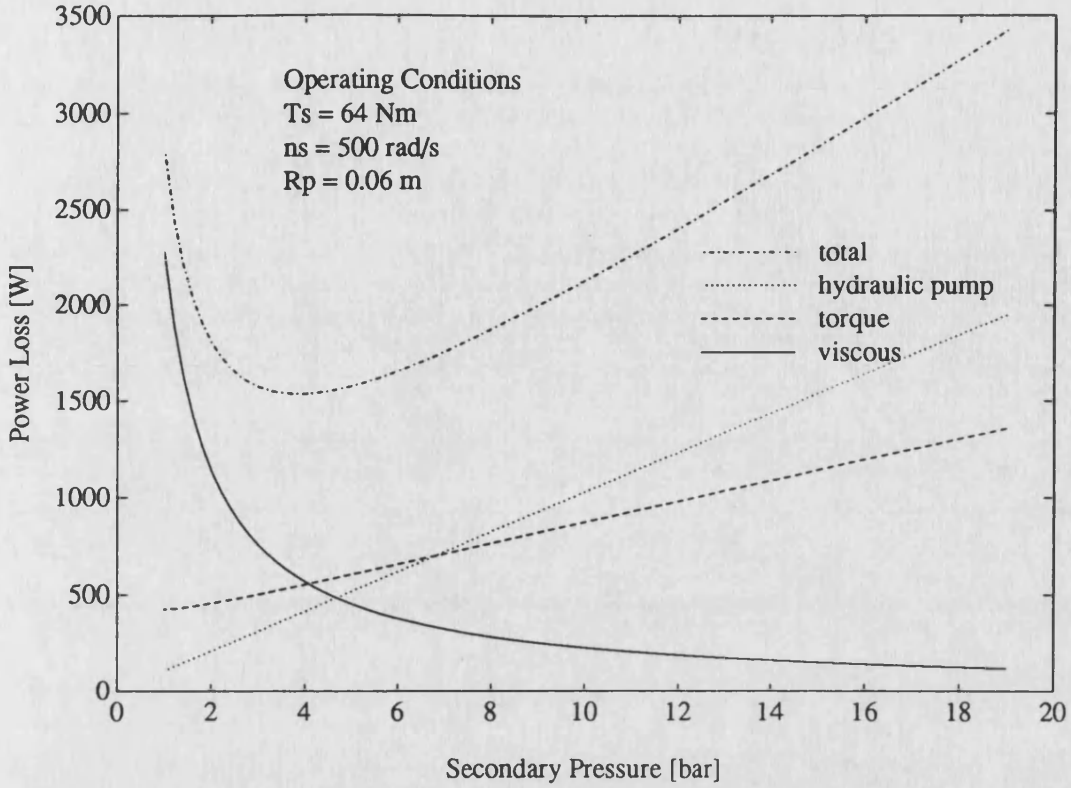

Figure 6.1 Power losses for a typical operating condition. The minimum of the sum of the power losses (total) is at p_s = 3.85 bar.

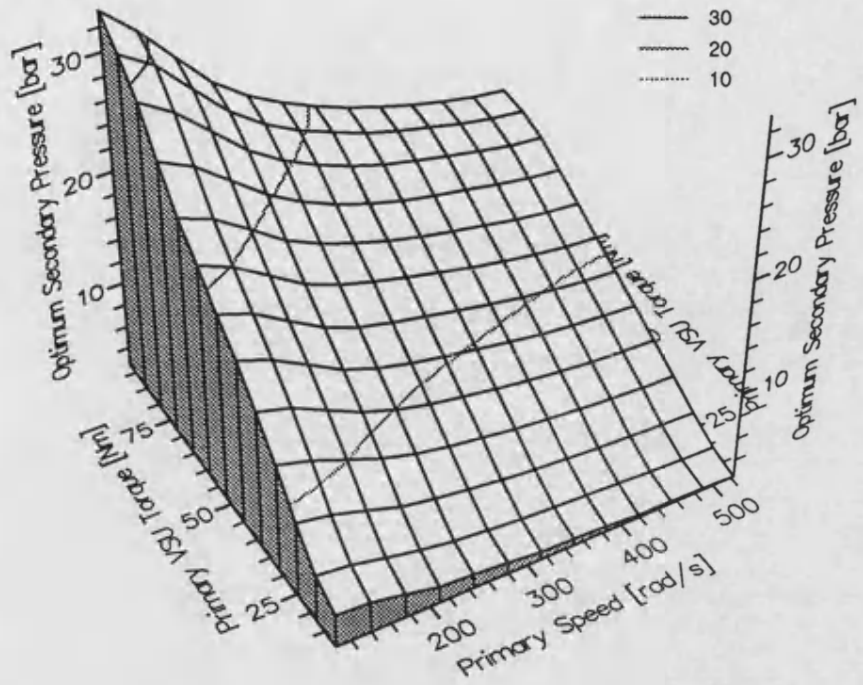

Figure 6.2 Efficiency optimum secondary pressure for R_p = 0.0288 m

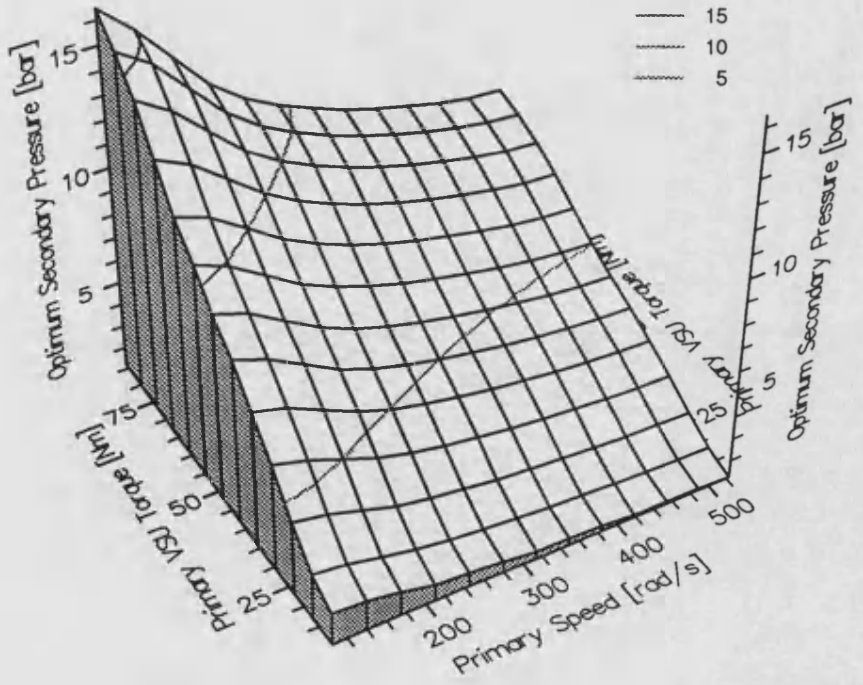

Figure 6.3 Efficiency optimum secondary pressure for R_p = 0.0434 m

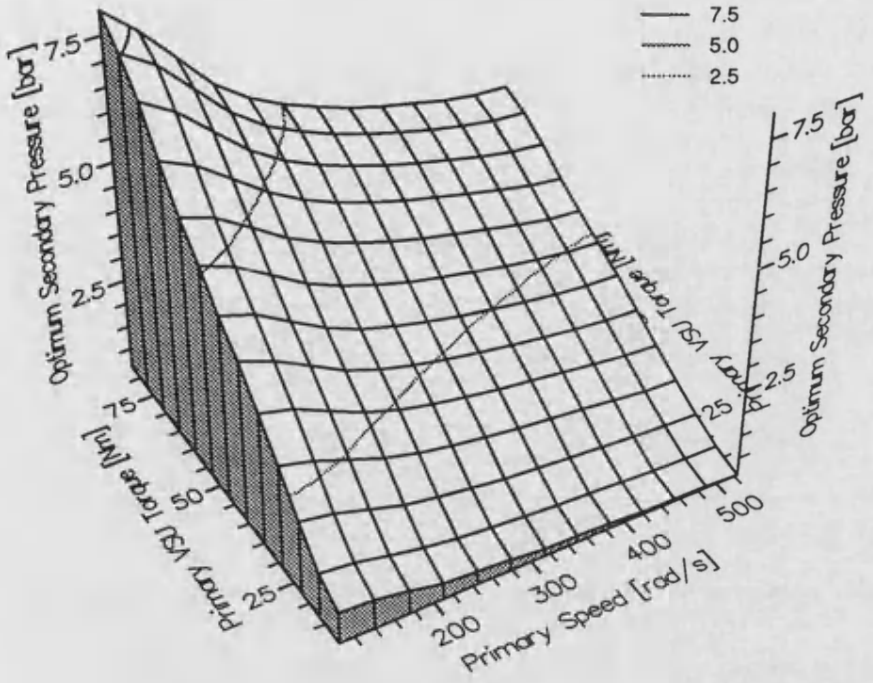

Figure 6.4 Efficiency optimum secondary pressure for R_p = 0.058 m

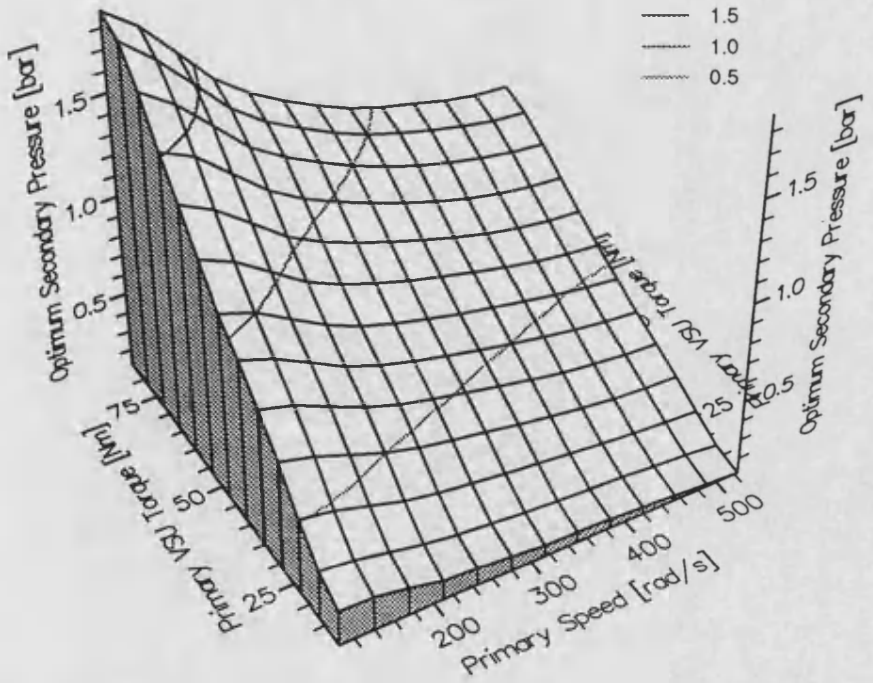

Figure 6.5 Efficiency optimum secondary pressure for R_p = 0.0726 m

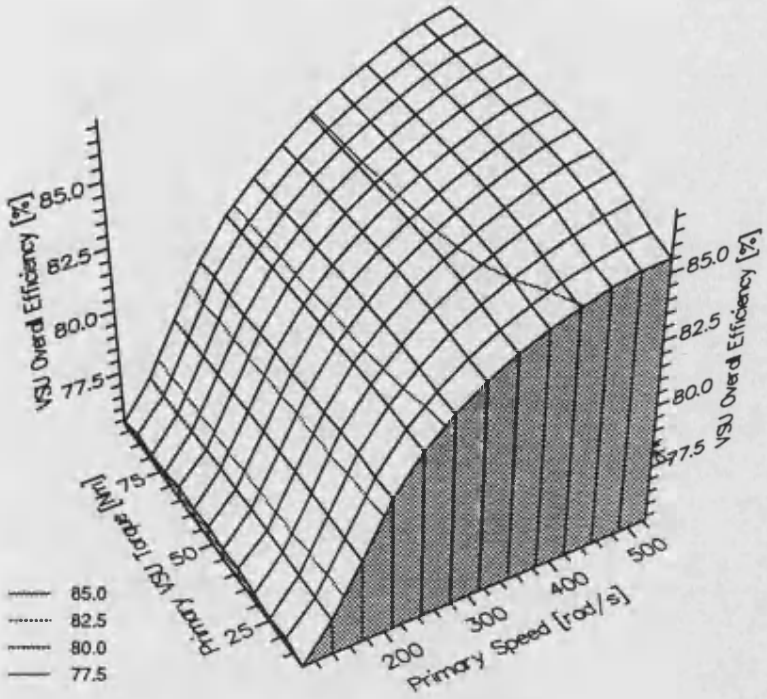

Figure 6.6 VSU optimum efficiency for R_p = 0.0288 m

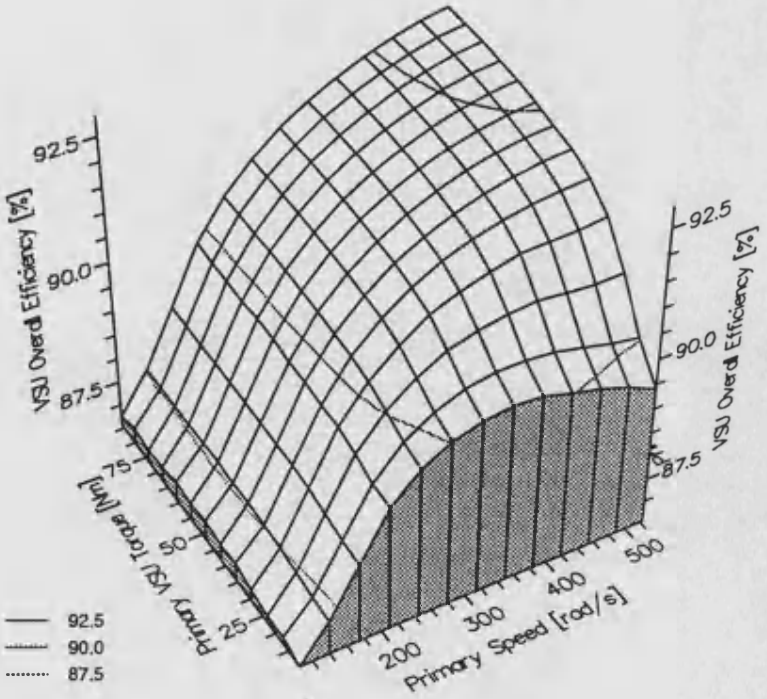

Figure 6.7 VSU optimum efficiency for R_p = 0.0434 m

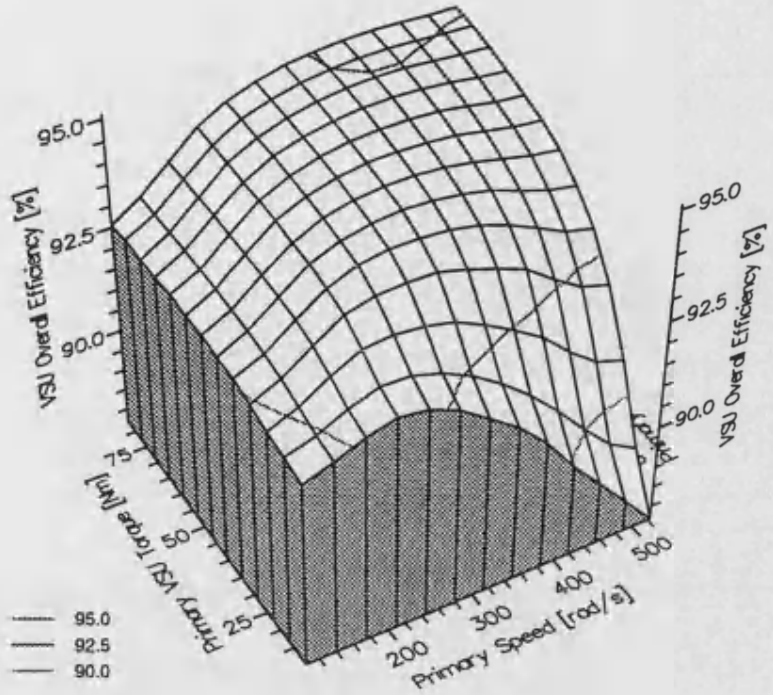

Figure 6.8 VSU optimum efficiency for R_p = 0.058 m

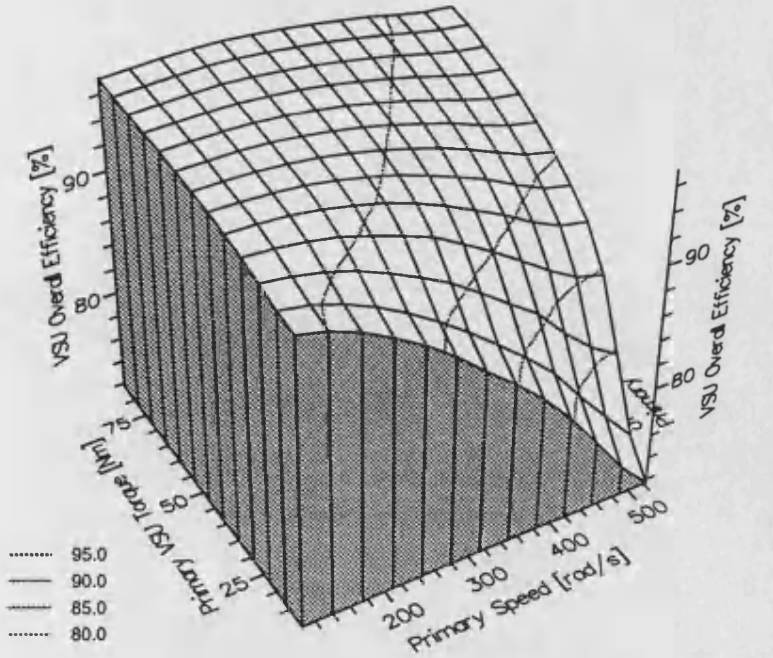

Figure 6.9 VSU optimum efficiency for R_p = 0.0726 m

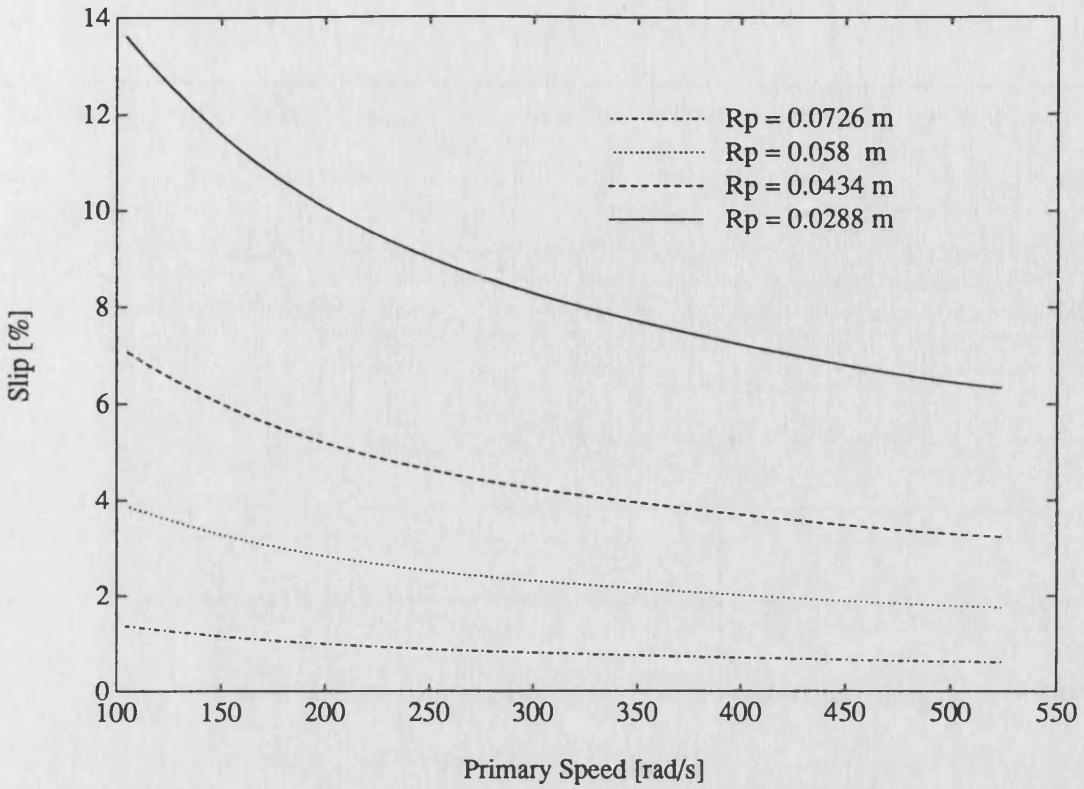

Figure 6.10 Efficiency optimum slips. The slip that leads to optimum transmission efficiency is independent of the transmitted torque. The secondary pressure is set accordingly to do this.

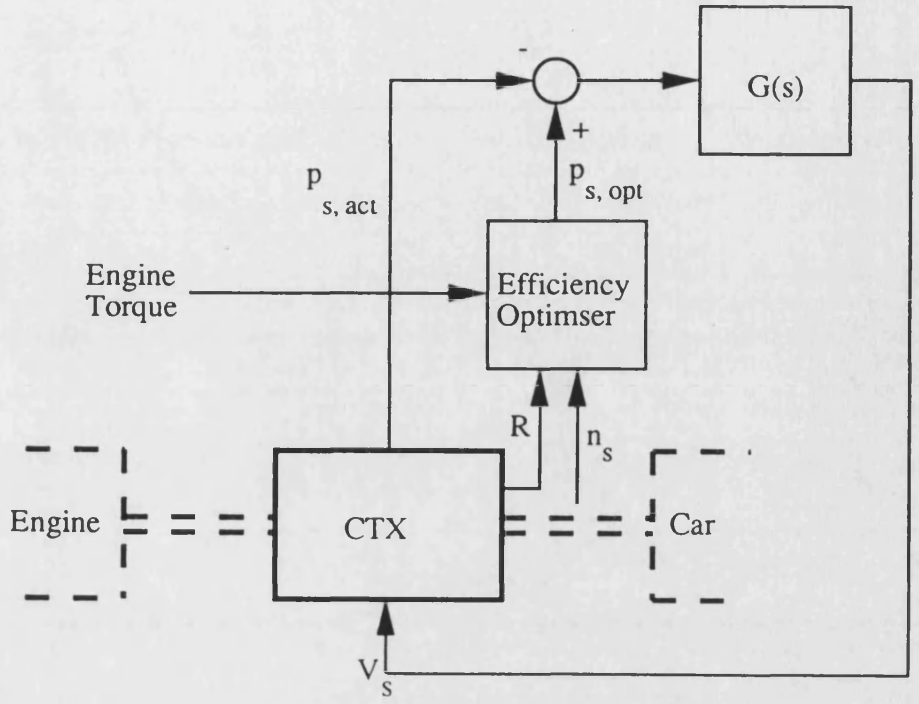

Figure 6.11 Pressure feedback strategy for optimum transmission efficiency control

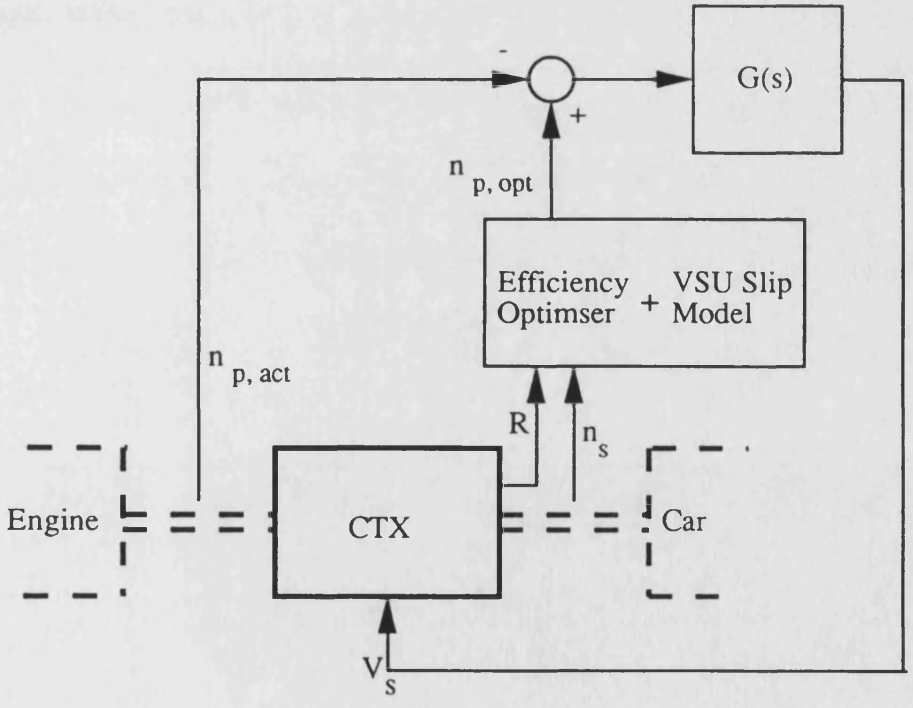

Figure 6.12 Speed feedback scheme for optimum transmission efficiency control

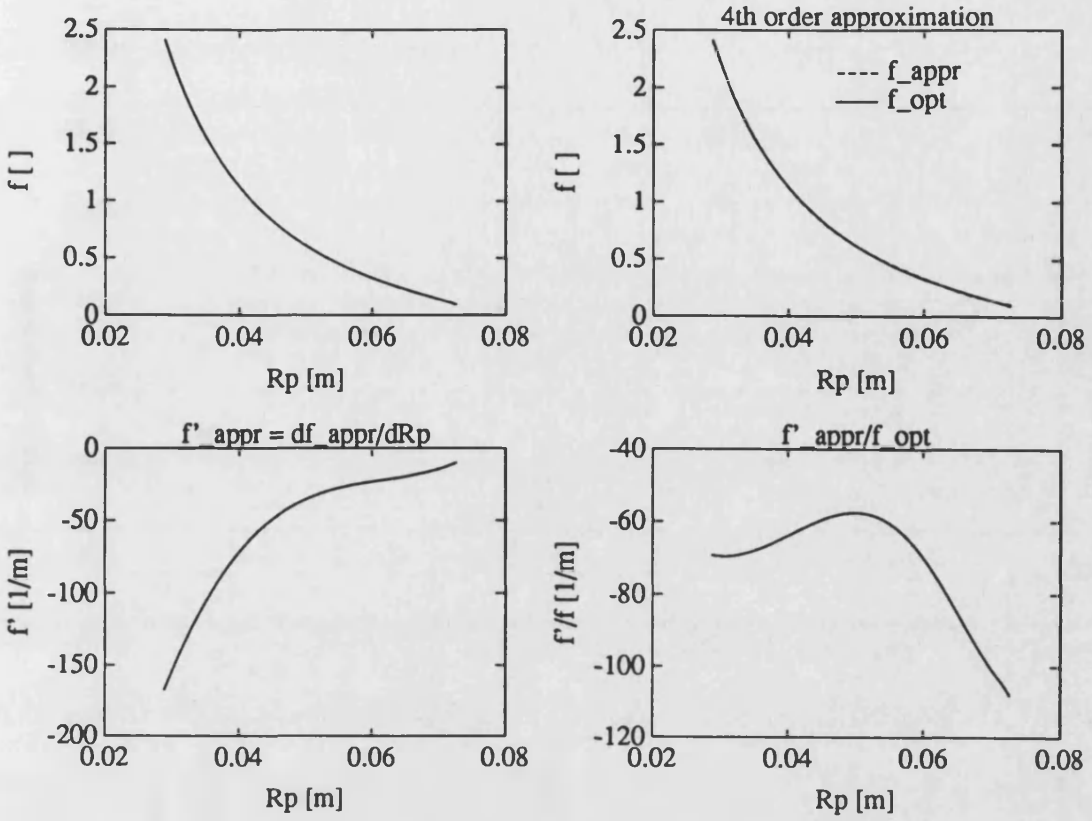

Figure 6.13 Graphical evaluation of the partial derivative of $f_{opt}(R_p)$

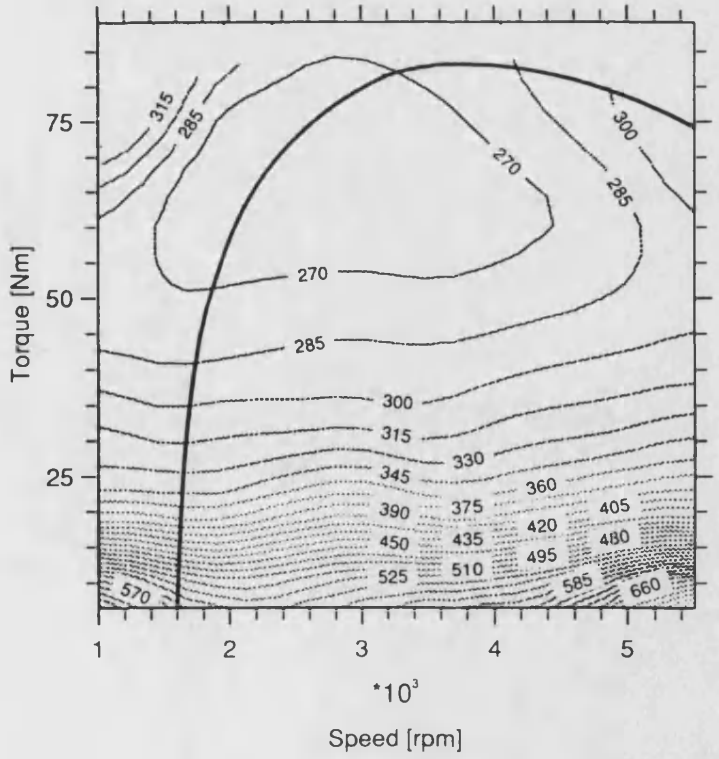

Figure 6.14 Specific consumption map and IOL of the Ford engine. The IOL relates speed and torque for increasing power.

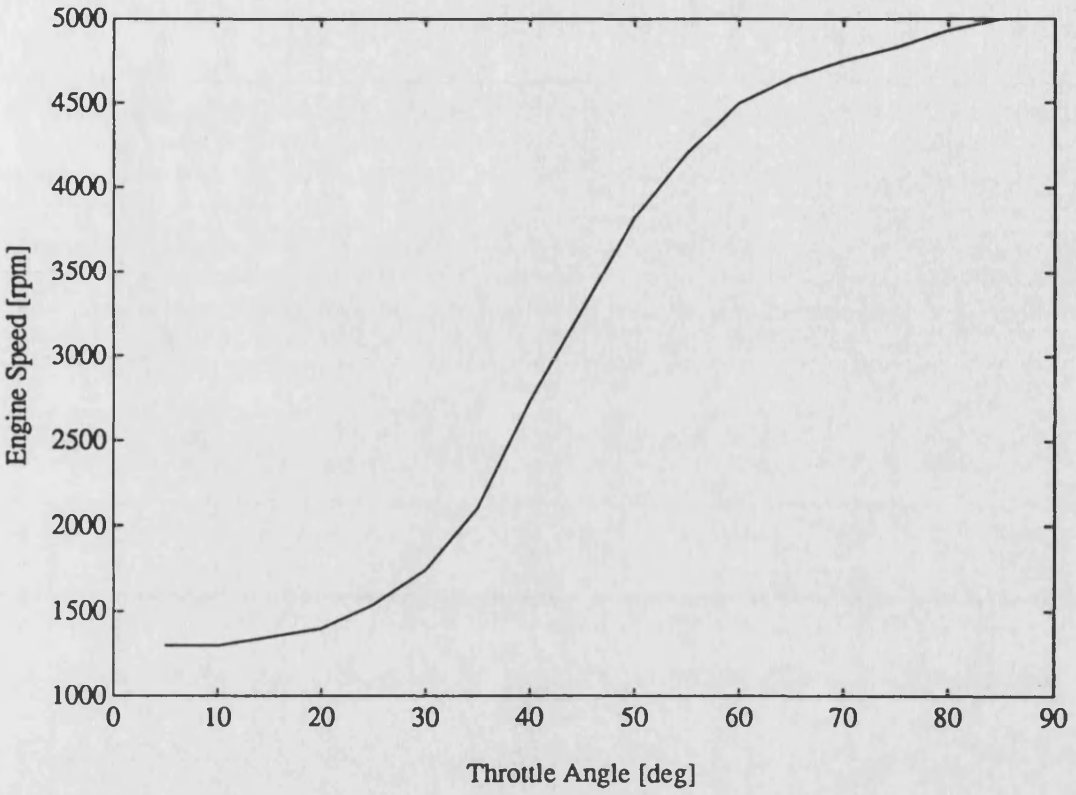

Figure 6.15 Relation between throttle angle and engine speed defined by the IOL

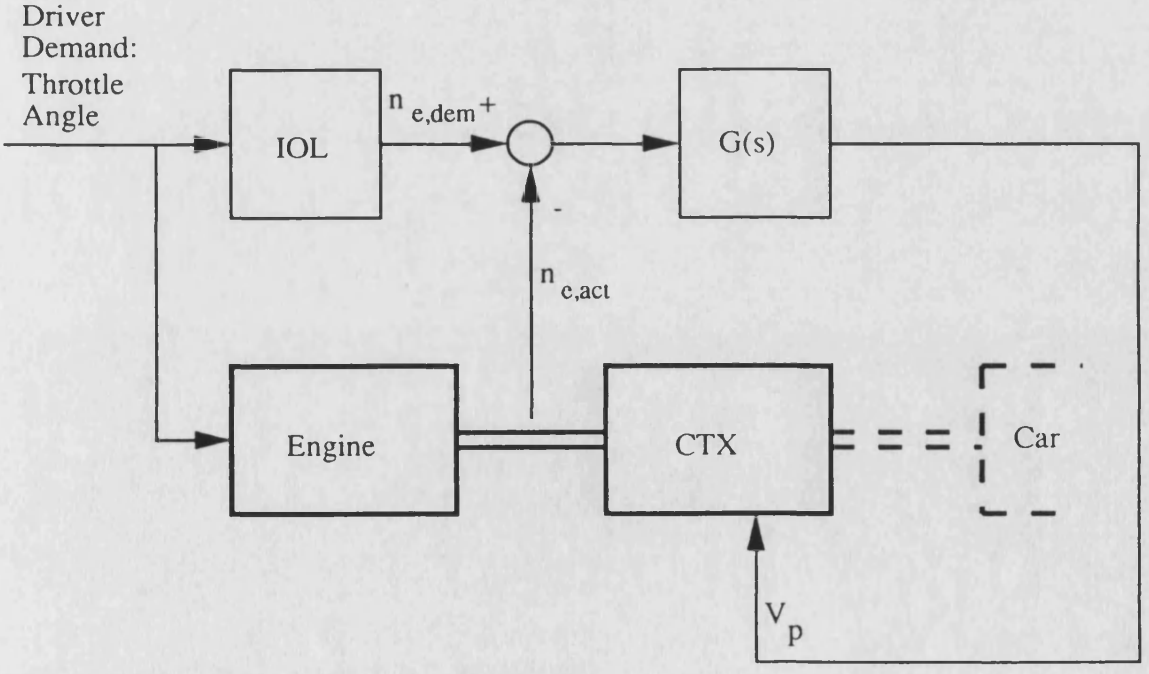

Figure 6.16 Engine torque control scheme

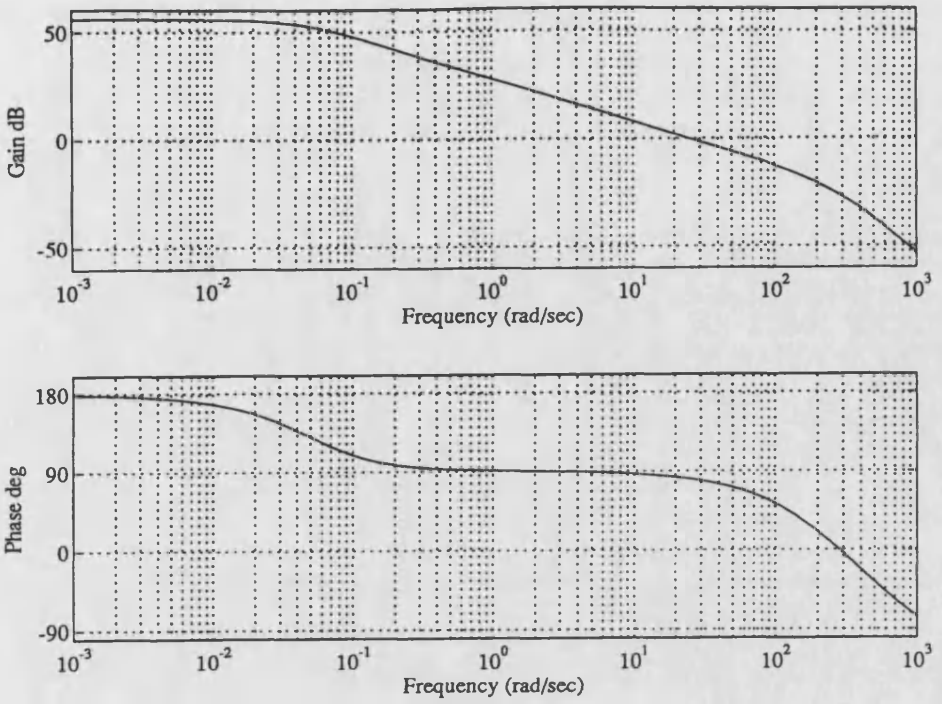

Figure 6.17 Bode plot for input v_p to output n_E

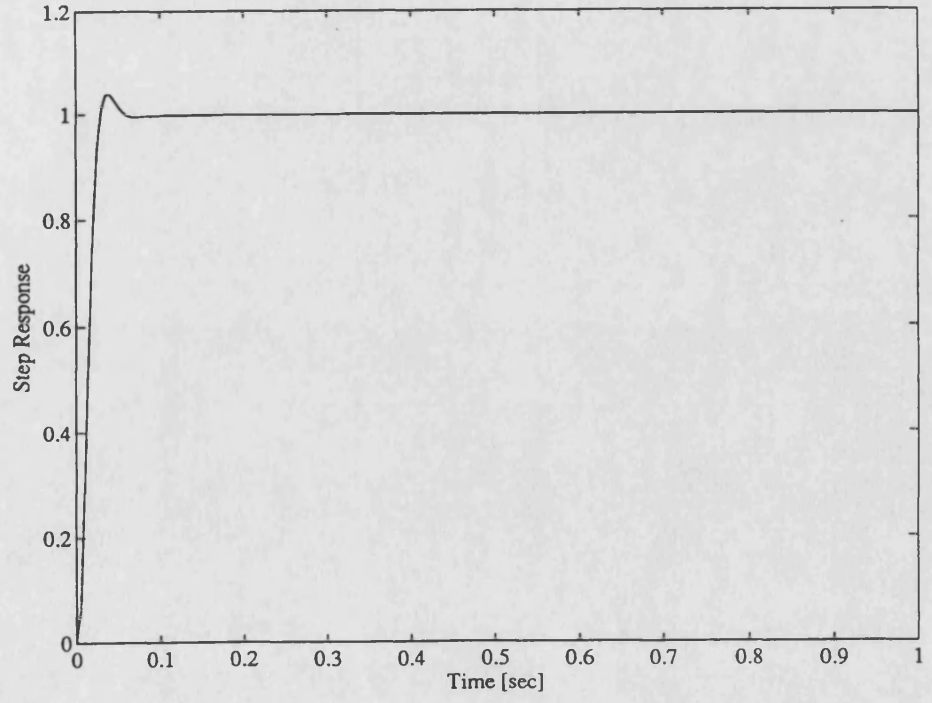

Figure 6.18 Step response with closed IOL loop

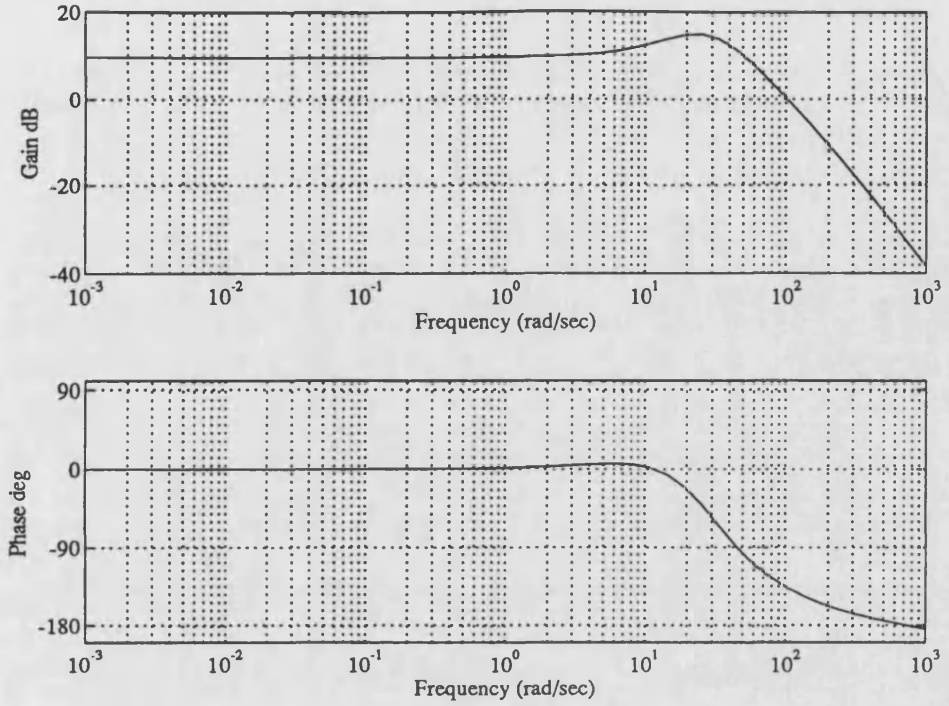

Figure 6.19 Bode plot from input v_s to output n_E with closed IOL loop

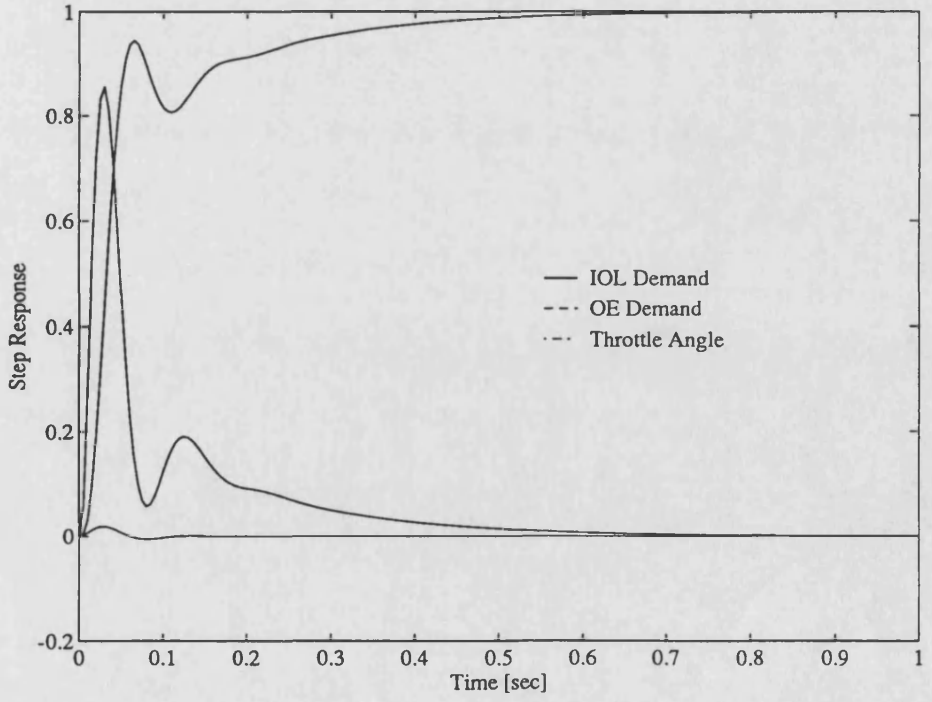

Figure 6.20 Response or step on v_s with closed IOL and OE loops

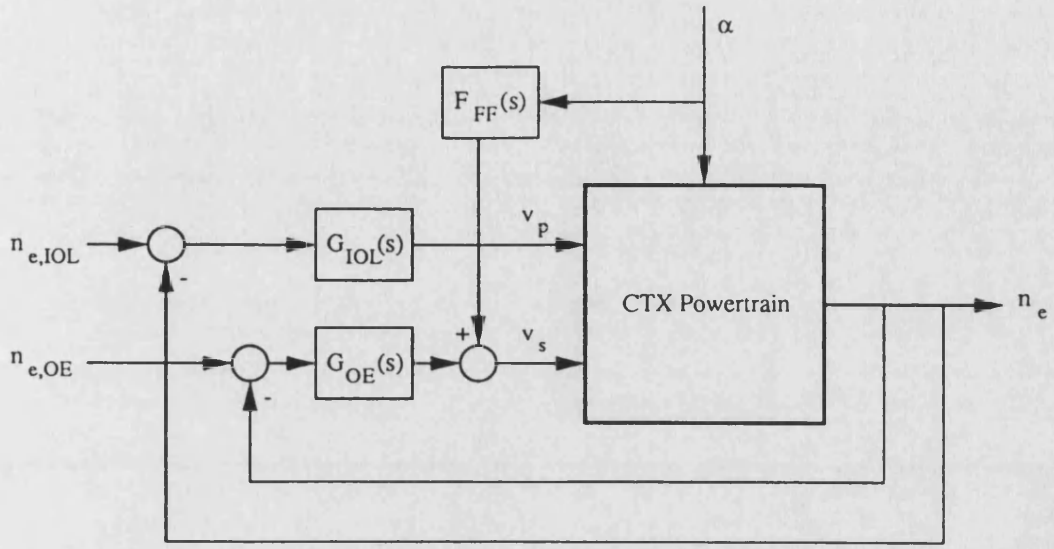

$$G_{IOL}(s) = K_P$$

$$G_{EFF}(s) = \frac{K_I}{s}$$

$$F_{ff}(s) = K_{FF}\frac{a_2 s^2 + a_1 s + a_0}{b_2 s^2 + b_1 s + b_0}$$

Figure 6.21 Implemented independent loop controller

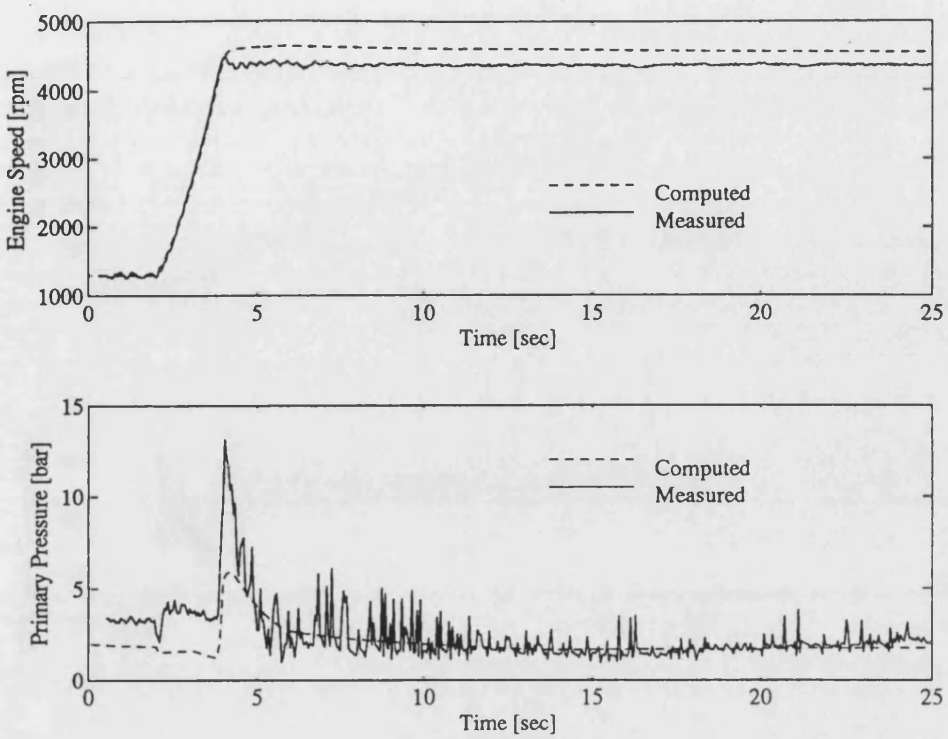

Figure 6.22 Measured and computed throttle step data, n_E and p_p

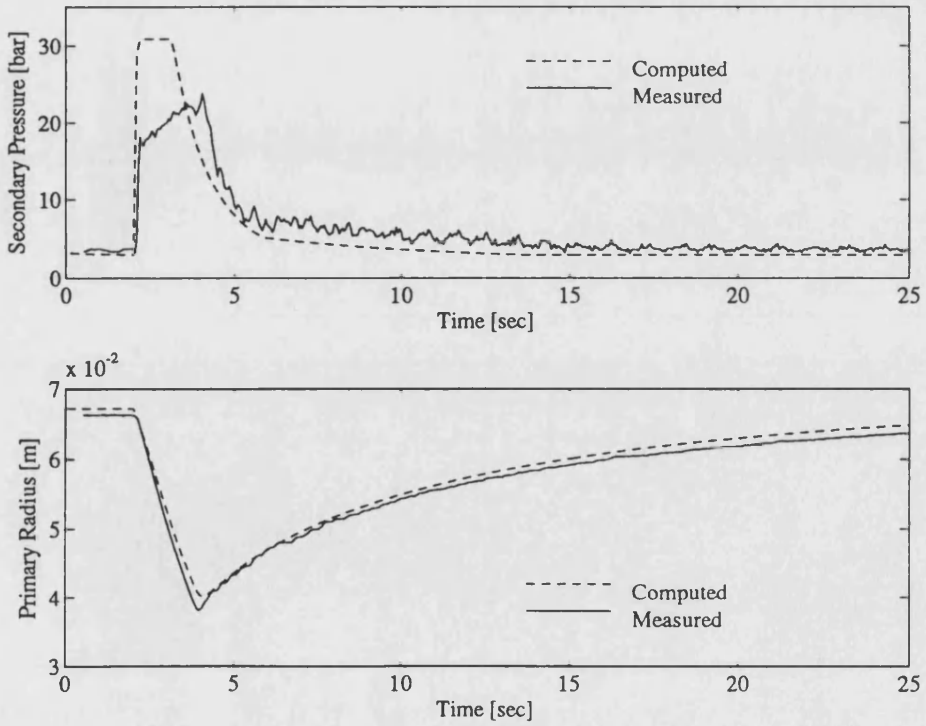

Figure 6.23 Measured and computed throttle step data, p_s and R_p

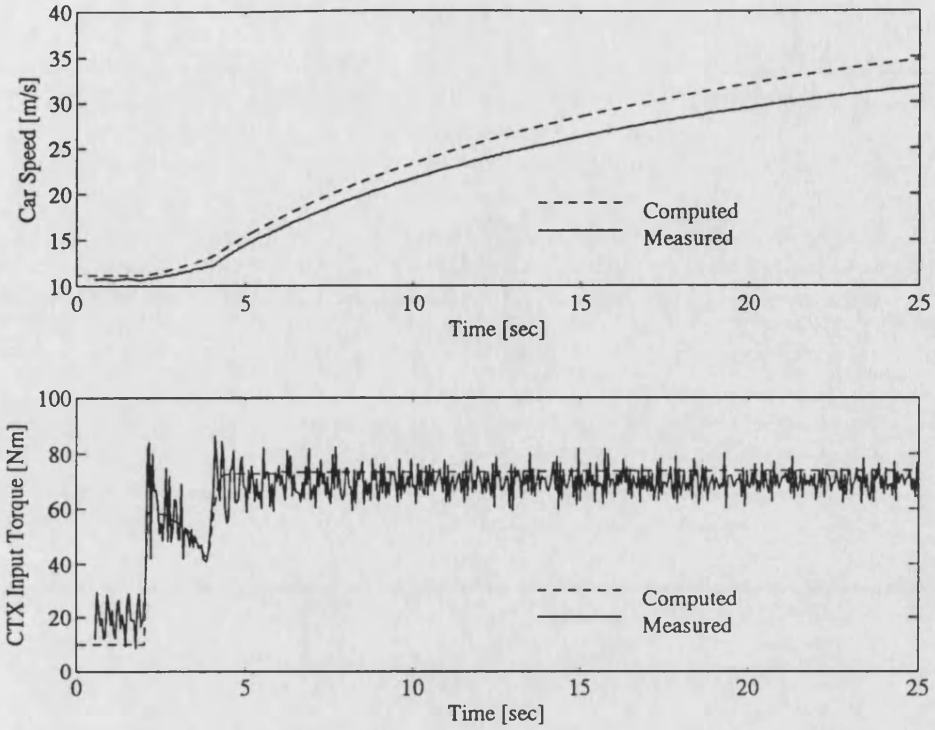

Figure 6.24 Measured and computed throttle step data, v_c and T_t

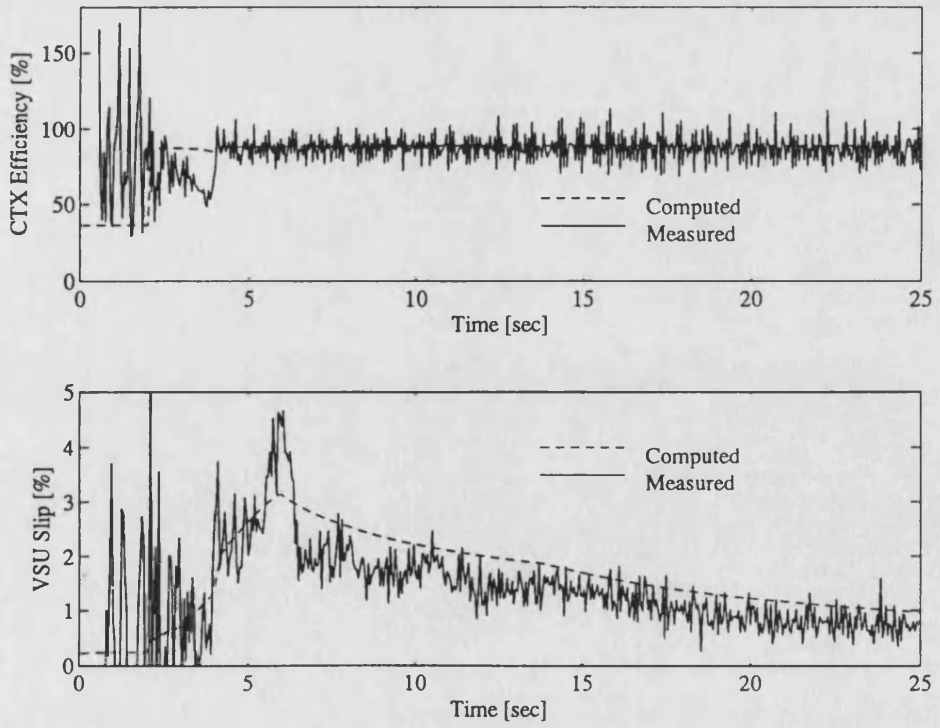

Figure 6.25 Measured and computed throttle step data, CTX efficiency and VSU slip

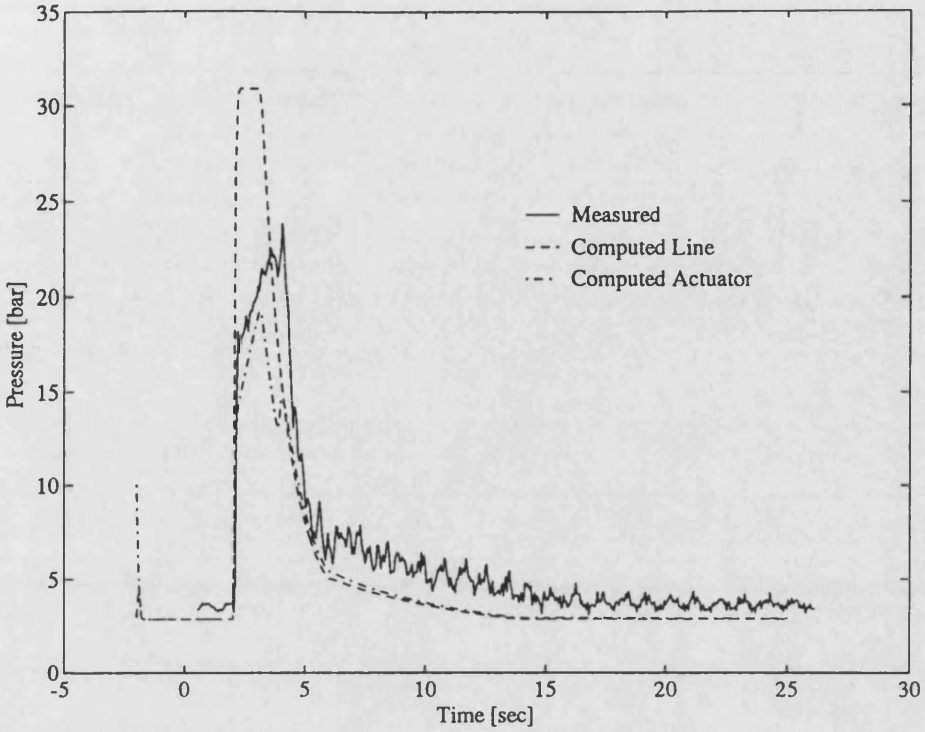

Figure 6.26 Comparison of measured and computed p_s data. The simulation shows that the actuator pressure considerably differs from the line pressure.

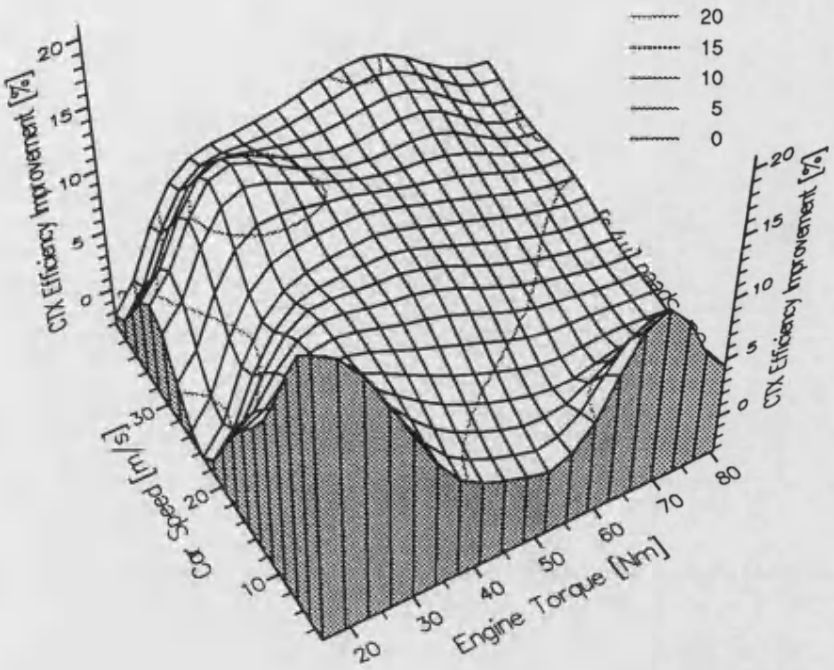

Figure 6.27 Calculated improvement of the CTX overall efficiency in 3D

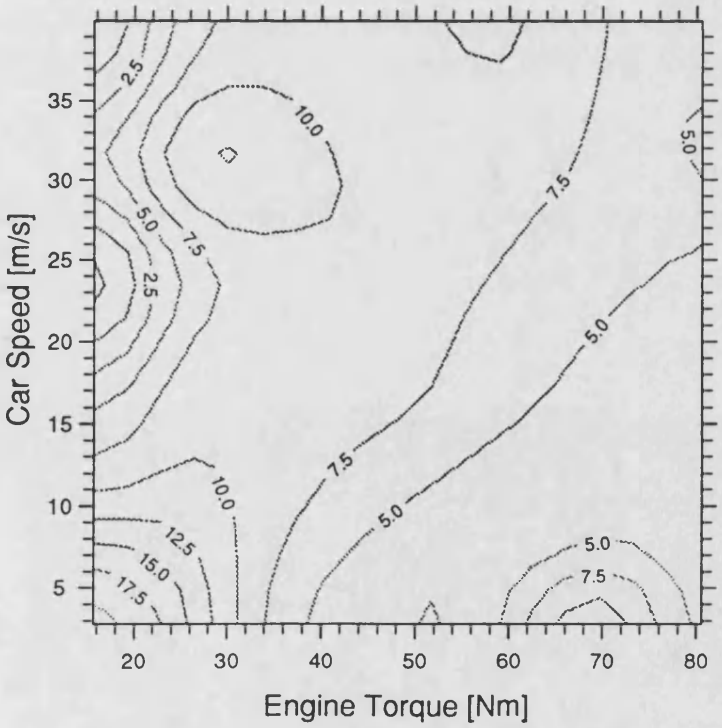

Figure 6.28 Calculated improvement of the CTX overall efficiency in 2D

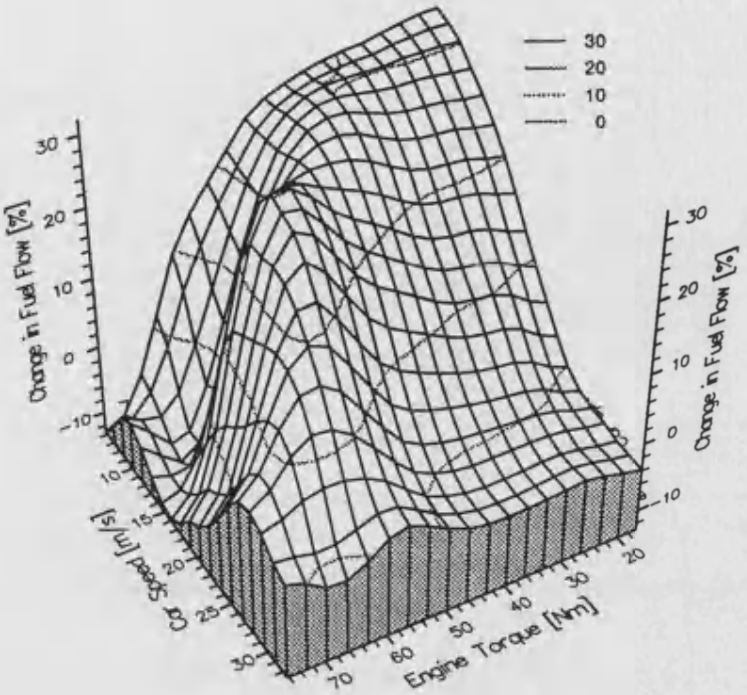

Figure 6.29 Measured Improvement in steady state fuel consumption of the EH controlled CTX in 3D

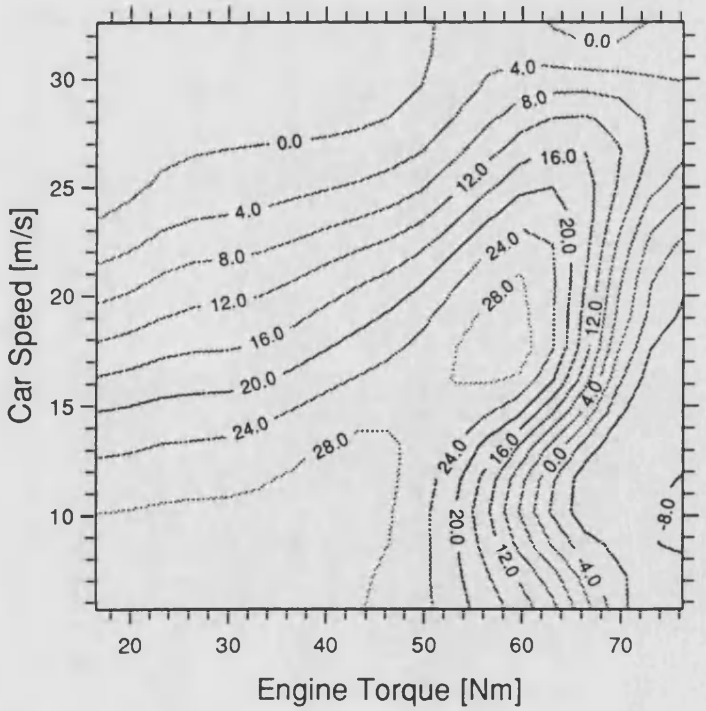

Figure 6.30 Measured Improvement in steady state fuel consumption of the EH controlled CTX in 2D

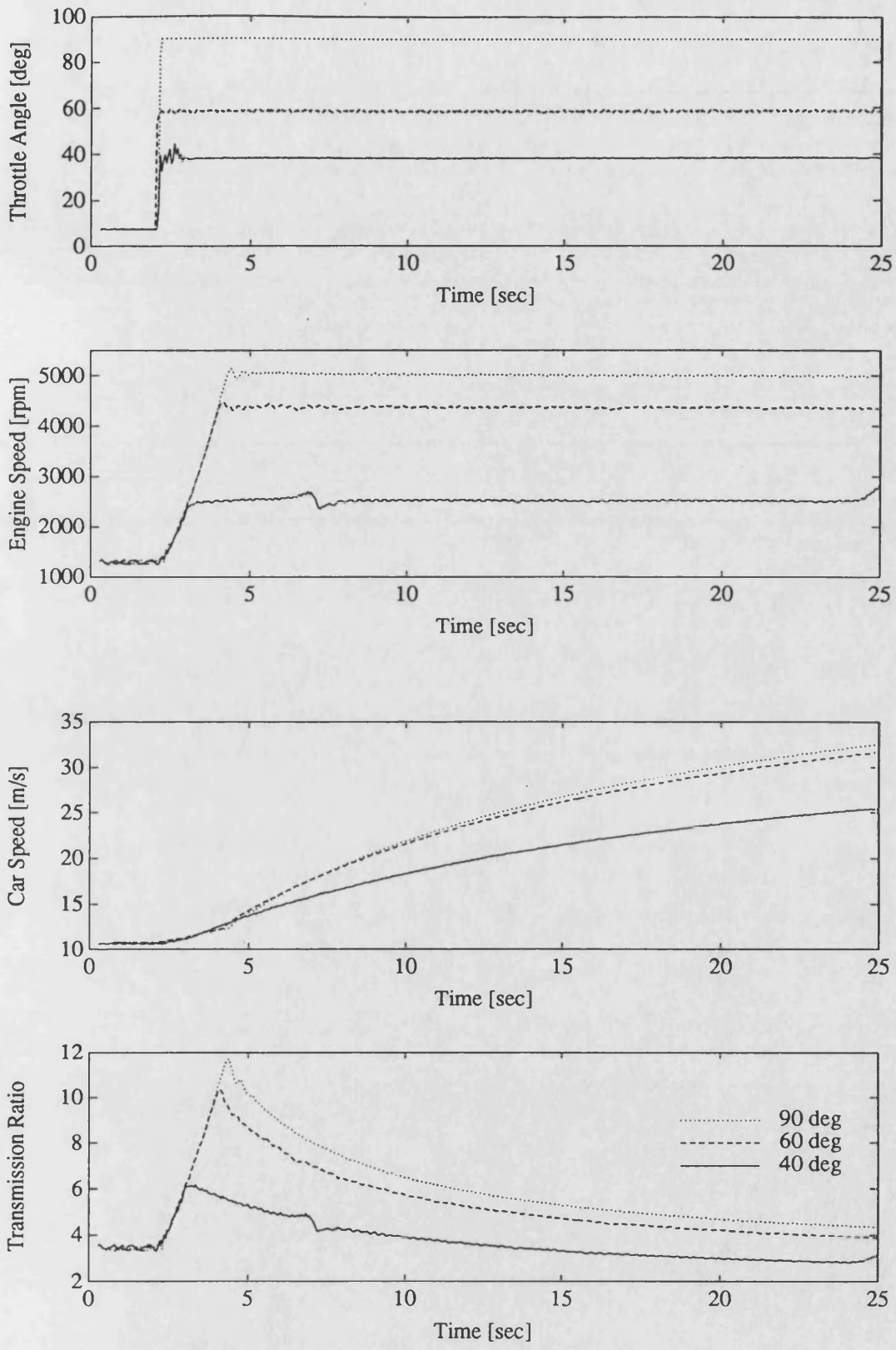

Figure 6.31 Response of the EH controlled CTX powertrain on throttle step demands

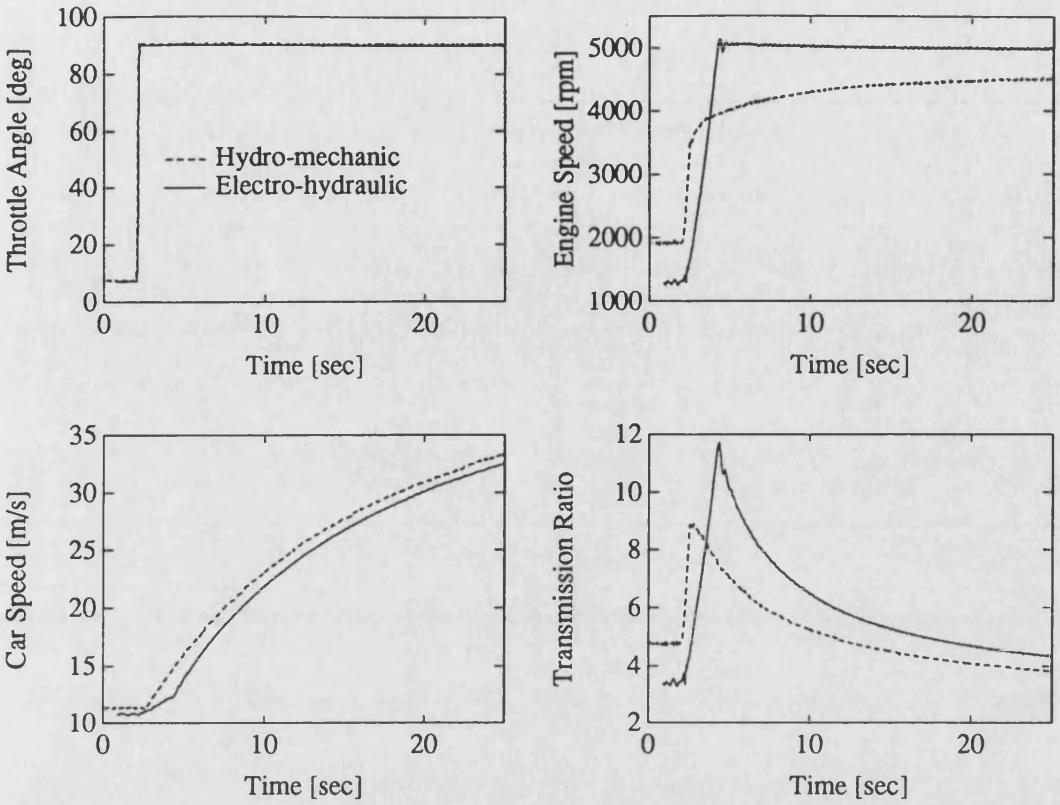

Figure 6.32 Comparison of 90° throttle step demand of the HM controlled and EH controlled CTX powertrain

7. OPTIMUM TRANSIENT CONTROL OF THE CTX POWERTRAIN

The control strategies designed in the previous chapter ensure efficient operation in steady state. From a driveability point of view it is desirable to achieve good transient behaviour and this is investigated in this chapter.

Section 7.1 explains the drawback of the controller designed so far and outlines the objective for this chapter. H-Infinity methods are used to design a robust ratio controller while maintaining optimum efficiency operating conditions for steady state, 7.2. The findings are embedded in an overall powertrain control strategy in 7.3. A discussion, 7.4, relates the findings to previous results.

7.1. Preliminaries

The CVT powertrain system considered in Chapter 6 comprised of the three inputs primary and secondary pressure and the throttle angle. Two objectives formulated in steady state, i.e. the optimum efficiency (OE) and the ideal operating line (IOL) strategy, constrained the degrees of freedom from three to one. The driver is in control of the engine power which is set by means of the throttle angle. This stands against what the driver really wants: tight control over the axle torque while maintaining optimum operating conditions. This is important in the light of *transients* and that issue is addressed.

THE DRAWBACKS OF THE CONTROLLER DESIGNED IN CHAPTER 6

The performance of the closed loop system from Chapter 6 is poor with respect to the transient behaviour. The causes are the restricted, and compared with the standard HM system sluggish, rate of change of transmission ratio (Figure 6.32) and the true implementation of the IOL that makes larger engine speed changes necessary if fast increases in power delivery are demanded. The performance was improved by introducing a feed forward from the throttle angle command. But this is not a satisfactory solution; a differentiation of the throttle signal is carried out. This could

reduce the stability of the system considerably and, thus, is questionable for a real application.

THE AIM OF THIS CHAPTER

The aims of this chapter are to design a *robust* controller that maximises the *transient capabilities* of the VSU while ensuring optimum efficiency in steady state and to assess the robust controller's potential in conjunction with a *strict IOL strategy.*

7.2. Transient OE Ratio Control

A robust multivariable control approach is pursued. This allows to exploration of both *robustness* and *transient response* to its full extent.

7.2.1. Robust Multivariable Control

Robust control describes methods to synthesise a control law which maintains system response and error signals to within pre-specified tolerances in the light of *plant uncertainties.* A quantitative measure for the size of uncertainty is the H_∞ *norm.*

Recent advances in the theory for the design for robust control systems helped to close the gap between the exclusively mathematically based theory and the practice of control design, Dorato, 1990. Commercial software (Chiang, 1992) make the theory available to the process orientated engineer and are thus further evidence for usefulness of the advanced theory. Chiang et al (1993) applied multivariable H_∞ methods to modern fighter planes; Safonov et al (1989) to flexible large scale structures; Doyle et al (1989) to process engineering. Many other successful applications have also been published.

Robust controller design. A theory has been developed and made available through the Robust Control Toolbox (Chiang, 1992) within Matlab which allows the

specification of the desired disturbance attenuation factor and the largest plant perturbations. Frequency dependent functions that limit the *sensitivity S(s)* and the *complementary sensitivity T(s)* are the basis for the design. The *singular value Bode plot* defines the gain in the principal directions of the inputs and is a key indicator for multivariable feedback systems performance. The design process uses *singular value loop shaping*. The H_∞ *method* enables this process by iterating only on one parameter.

7.2.2. Process and Specification

Input-output system. Appendix C shows the Bath*fp* icon representation of the system. The inputs considered are primary and secondary valve commands, v_p and v_s, and the outputs are the engine speed and the slip error. The incorporation of the slip error extended the model to a true 2 input 2 output system. A combination of input signals can control either of the outputs. For optimum efficiency the slip error should always be zero and it may seem, at this stage, superfluous to have control over it. However, the slip error demand can be manipulated to improve the transient rate of change of transmission ratio (7.2.5).

Linear plant. A linear analysis led to the representation of Appendix C (see 6.3.1). Only the availability of an accurate linear model enables LQG controlller design methods, and thus the linearisation process is paramount for a successful application. A model reduction based on a Schur balanced truncation method yielded the 4 state, 2 input, 2 output model listed in Appendix D. The singular value Bode plot of this model and the full state one from Appendix C are compared in Figure 7.1. Differences between the two models only occur at high frequencies.

System specification. Separate specifications for the robustness and the disturbance attenuation can be given. The H_∞ design procedure requires specification of two weighting functions.

1. Robustness. A closed loop bandwidth of about 100 rad/s is the aim. A 20 dB roll-off above this frequency is specified. These two specifications define

$$W_3^{-1} = \frac{100}{s} \tag{7.1}$$

This means that above 100 rad/s multiplicative plant perturbations can grow at 20 dB/decade while stability is still ensured.

2. *Performance*. Zero steady state error is specified. This yields

$$W_1^{-1} = \gamma \frac{s}{10} \tag{7.2}$$

where the maximum γ that leads to a stable plant is sought. The division by a factor of 10 is chosen to give a 0 dB cross over frequency that is sufficiently lower than that of $1/W_3(s)$ for $\gamma = 1$.

7.2.3. Controller Design

The two weighting functions W_1 and W_3 penalise the sensitivity, $S(s)$, and the complementary sensitivity, $T(s)$.

$$\begin{aligned} \bar{\sigma}\left(S(j\omega)\right) &\leq |W_1^{-1}(j\omega)| \\ \bar{\sigma}\left(T(j\omega)\right) &\leq |W_3^{-1}(j\omega)| \end{aligned} \tag{7.3}$$

σ being the maximum singular value. The plant is augmented and subsequently arranged for the *small gain problem* (Chiang, 1992). This enables the formulation of a single infinity norm specification, reducing the controller design to a single dimension iteration of the parameter γ from equation (7.2) (mixed performance and robustness objective, Maciejowski, 1989)

$$\| T_{y1u1} \|_\infty \leq 1 \quad , \quad \text{with} \quad T_{y1u1} \triangleq \begin{bmatrix} W_1 S \\ W_3 T \end{bmatrix} \tag{7.4}$$

A few iterations led quickly to γ = 9.9 maximising the cost function T_{ylul}. The resulting sensitivity and compensated sensitivity functions are compared with the weightings $1/W_1(s)$ and $1/W_3(s)$ in Figure 7.2. The designed controller has a 6 state representation listed in Appendix D.

The H_∞ *Controller* has been implemented in Bath*fp* to investigate the closed loop behaviour of the non-linear system. Figure 7.3 shows the response of the system. The CTX powertrain accelerated the car from 10 m/s with a constant throttle angle of 40°. A step in demanded engine speed at 2 seconds followed by a step in demanded slip error at 5 seconds are initiated. The engine speed and slip error manage to follow the demand, top left and top right plot.

The transient at the very beginning is due to the initial condition of the state vector. This can be interpreted as a disturbance simultaneously affecting both inputs. For both signals there seems to be an initial steady state error. However, due to the produced engine power the car is accelerating rapidly and hence the transmission ratio is changing which means that the system is in fact not in steady state. The "steady state errors" displayed in Figure 7.3 could be reduced by introducing additional integrators in the H_∞ design procedure.

Initially, the engine speed and slip error react very slowly to the disturbance that can be thought of as the initial conditions of the states. The engine speed increases steadily on the step demand but the pressure difference between the primary and secondary pressures limits the rate of change of transmission ratio. The aim to increase this pressure difference is pursued in the next section. This will maximise the transient control over the transmission ratio. During the rapid change in engine speed the primary valve is in saturation and explains the large error in slip error during that phase. Once out of saturation the slip error is controlled satisfactorily.

The simulation showed the robust behaviour of the H_∞ controlled closed loop system. This justifies the whole design process which includes the determination of a linear model from a non-linear simulation.

7.2.4. Comments on the Design Process

The design parameters for the presented H_∞ approach are the two penalising functions $1/W_1(s)$ and $1/W_3(s)$. The choice of these determines the controller and is thus the major part of the design process. Their listing in the specification section follows the logic of presentation; although in practice they were found through many iterations between specification and, often failed, designs. In order to go into the design algorithm the penalising functions must additionally fulfil certain criteria in conjunction with the plant properties. For example the D_{12} matrix of the augmented system must have full rank. This is another constraint when defining the penalising functions.

The chosen penalising functions expressed the specifications and fulfilled all necessary constraints for the design process. However, they are the simplest choice. A controller trading off the bandwidth against the robustness of the plant to a better degree might be found easily. On the other hand, the arbitrarily chosen restriction to a bandwidth of 100 rad/s ensured that plant uncertainties above this frequency did not decrease the stability of the system. This highlights the robust control aspect. Additional stability can be gained at the expense of limited bandwidth. This fundamental design constraint is intuitive like the whole design process that, thanks to the specialised software, makes the otherwise difficult mathematical treatment easy.

7.2.5. Slip Error Warping

Optimum efficiency is achieved by having low secondary pressures which are obtained by making the slip error zero. For a large rate of change of transmission ratio the secondary pressure needs to be as high as possible. This can be achieved by asking for an increased slip error. The intention to change the transmission ratio is directly given by the difference between the demanded and the actual engine speed, i.e. the engine speed error. Introducing a proportional gain leads to the control scheme shown in Figure 7.4. Note that in steady state the speed error disappears and thus a zero slip

error is demanded. This ensures optimum efficiency in steady state.

Independent of the sign of the speed error the demanded slip error has to be made positive to boost the secondary pressure. Thus the absolute value of the speed error is multiplied by k_s. The simulation in Bath*fp* led to $k_s = 0.1$ to give satisfactory response. Strictly speaking the multivariable stability of the system has to be investigated to size k_s correctly. This process might result in the introduction of additional compensators and was not carried out.

Figure 7.5 shows the response of the overall system with the slip warping controller. The same initial conditions and engine speed demand as in the test of Figure 7.3 were applied. The main difference to Figure 7.3 is the much faster change of the engine speed which was the motivation for the slip warp controller. During the ratio change phase between 2 and 3 seconds the secondary pressure is at its upper limit of about 30 bar. The demanded and measured slip error do not correspond during the rapid ratio change but once the speed error is small the correspondence is good.

7.2.6. Practical Implementation

During the simulation it became clear that the controller runs into saturation for steady car speed. For a practical implementation it would be vital to implement a sort of antiwindup feature. For a 6 state, 2 input, 2 output system of the designed H_∞ controller an antiwindup facility is complex and was not developed. This restricted the further experiments to transients only. Being the aim of this chapter this can be justified. However, the standard transient test acceleration from a steady 11 m/s car speed could not be carried out.

7.3. Transient CTX Powertrain Control

The transmission ratio control system designed in 7.2 can be incorporated into a strict IOL overall powertrain system shown in Figure 7.6. The optimum hydraulic control of the CTX ensures optimum efficiency and maximum transient response on demanded engine speed. However, the dynamic limits of this system are governed by the properties of the hydraulic system, i.e. hydraulic resistance of the pipe work and flow limitations of the pump. This is investigated in the light of a strict IOL strategy.

7.3.1. Strict IOL Strategy

The ideal operating line (IOL) determines the relation between the throttle angle and the engine speed (see 6.3). A strict IOL strategy aims to maintain that relation within limits set by the system, i.e. transient capability to change the engine speed by means of adjusting the transmission ratio. This leads to minimum consumption but has disadvantages concerning the transient vehicle response.

7.3.2. Pressure Limitations

Figure 7.7 shows the simulated engine speed response of a strict engine speed implementation for throttle step demands from 20° to 40°, 60° and 90°. The throttle step was initiated at time 0.5 seconds. Two degrees of hydraulic resistance of the pipe work are modelled. The first corresponds to the electro-hydraulic (EH) implementation on the rig, the second to the standard hydro-mechanical (HM) implementation in the CTX. The lower hydraulic resistance of the HM implementation results in rise times twice as fast as compared to the EH system. Figure 7.8 shows the resulting axle torque for the same manoeuvre as in Figure 7.7. The maximum torque point is reached quicker for the HM system. However, from a driveability point of view it is very important *how* the maximum torque point is reached. The negative torques for the 60° and 90° cases of the HM system decelerate the car, although the driver demands an

instant acceleration. This behaviour is not acceptable and demonstrates the need for a *transient scheduling* of the demanded engine speed.

7.3.3. Flow Limitations

Having realised that pressure limitations are the limiting factor for the rate of change of transmission ratio the size of the pump in the light of maximum transients for the transmission ratio can be investigated. The 90° step demand from the above test demonstrates the flow limitations. The step response is evaluated for three different pump sizes, i.e. 9.72 (which is the size of the pump currently built into the CTX), 4.86 and 2.43 cc/rev. The simulation used a pump model described by McCandlish (1984) and thus the volumetric effiency depended on the pressure drop and speed. This ensured a sensible investigation. Additionally, a down step is included in the presentation. Figure 7.9 shows the speed response of the engine. The smaller the pump the slower is the engine speed increase. As expected the engine speed decrease is not affected by the pump size. Figure 7.10 shows the pressure and flow relations in the primary and secondary actuators. The flow limitations can be seen by observing the secondary pressure and flow between 0.5 and 1.5 seconds. Although not plotted the whole delivery from the pump went straight into the secondary cylinder during that interval. The secondary pressure thus builds up more slowly for smaller pumps. The delay of the engine speed increase does not seem serious but this has to be investigated further. For this purpose the CTX output torque is plotted in Figure 7.11. The response for the smallest pump is not satisfactory because the torque curve has sharp negative peak that would be felt by the passengers. This shows that with a smaller pump the transient ratio adjustment is limited but this does not defeat the problem of how the transition is done.

7.4. Discussion

A robust controller for the VSU of the CTX optimising the transient response and the transmission efficiency in steady state has been designed. The controller makes use of the speed feedback scheme developed in 6.2.3. This strategy has been shown to be sensitive to measurement noise. This could be eliminated by adopting the pressure feedback scheme and using the same multivariable techniques to design a controller. The price to pay would be the measurement of the pump pressure and the real time knowledge of the transmitted torque.

The need for a *transient powertrain scheduler* has been demonstrated. Having an optimum transient VSU system is certainly a very good start to tackle this problem. The time history of the CTX output torque is to be optimised because this quantity determines what the driver feels. However, driveability aspects determine the reference for the scheduling and cannot be defined easily.

Surprisingly, it was found that the pump installed in the CTX is far too big. The flow limitations are modest. The rate of change of transmission ratio is much more restricted by the pressure drop caused through the pipe work at high flows. There is a lot of potential in the minimisation of the pressure drop. This result stands against data published by Röper, 1989. He also recognised that the cylinder pressures govern the dynamics; his formula based on the Coulomb phenomenon and not having validated any hydraulic properties might have been reasons for his misleading data.

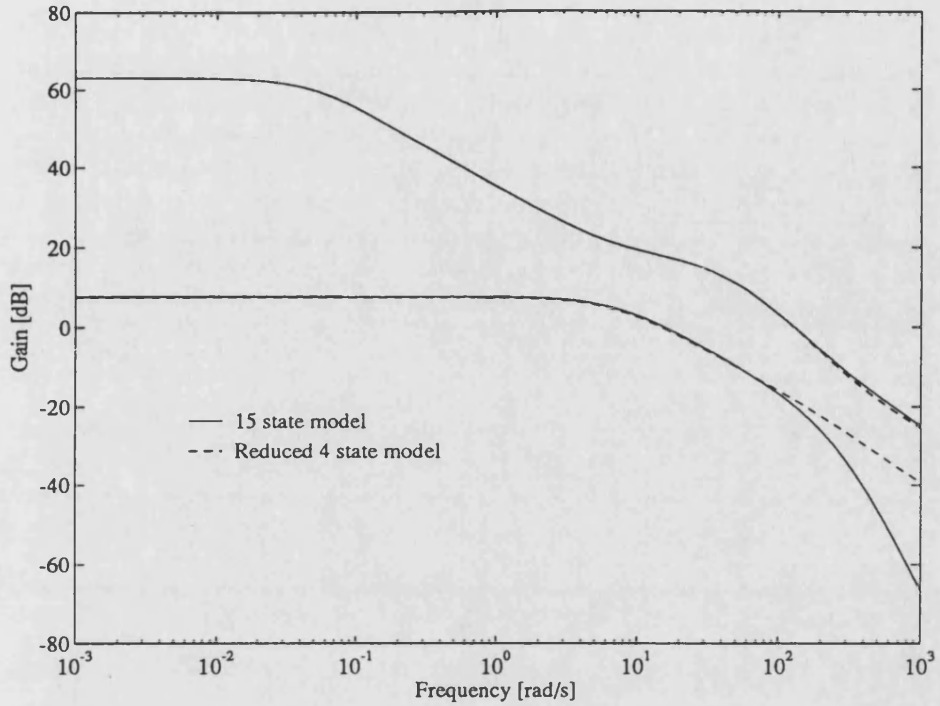

Figure 7.1 Singular value bode plots of initial and reduced plant

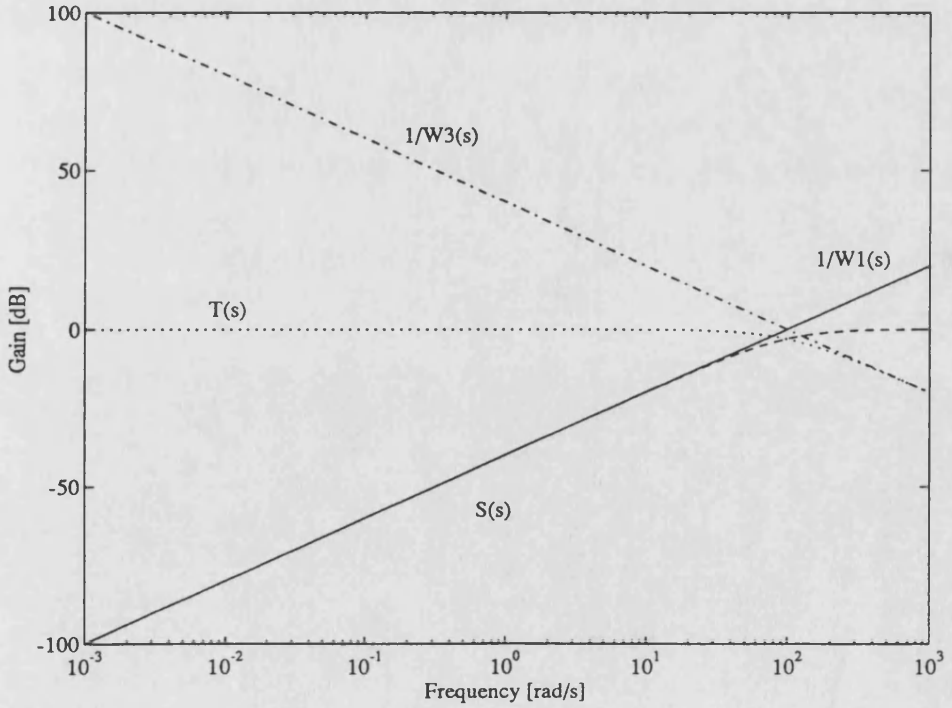

Figure 7.2 Sensitivity *S(s)* and complementary sensitivity *T(s)* and their penalising functions W_1^{-1} and W_3^{-1}, respectively

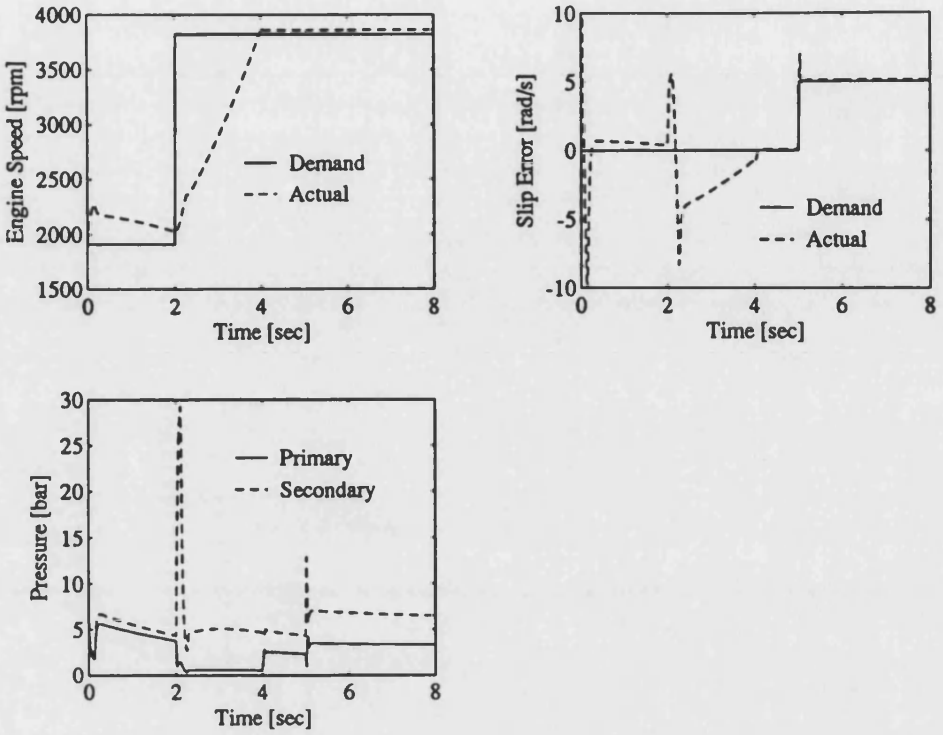

Figure 7.3 Computed step response of the multivariable H_∞ controlled VSU

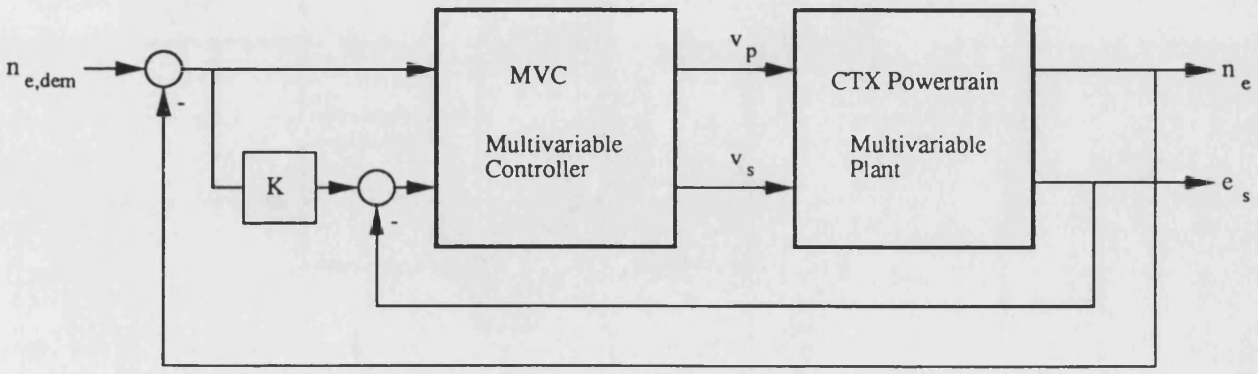

Figure 7.4 Multivariable control scheme for the VSU with slip warp.

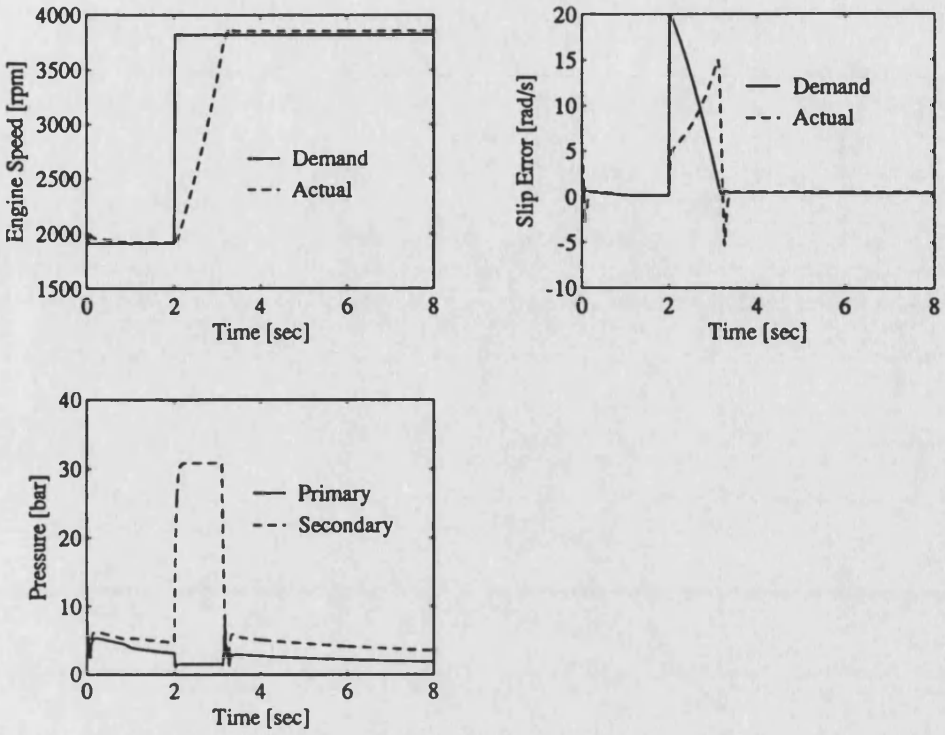

Figure 7.5 Computed step response with slip warp controller

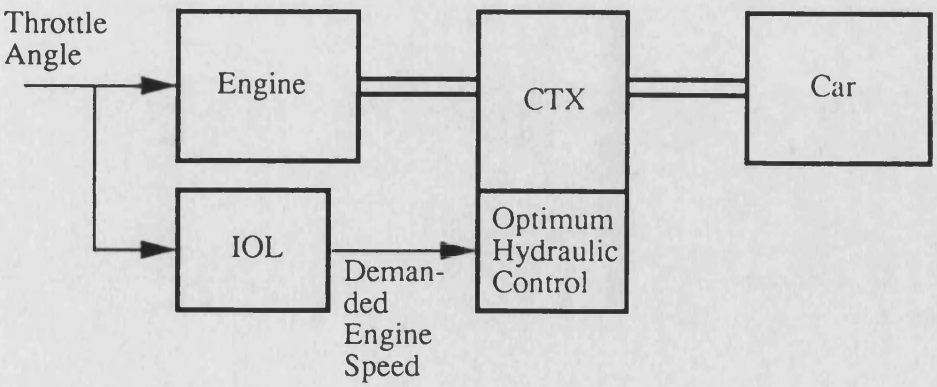

Figure 7.6 Schematic powertrain system incorporating optimum hydraulic control of the CTX

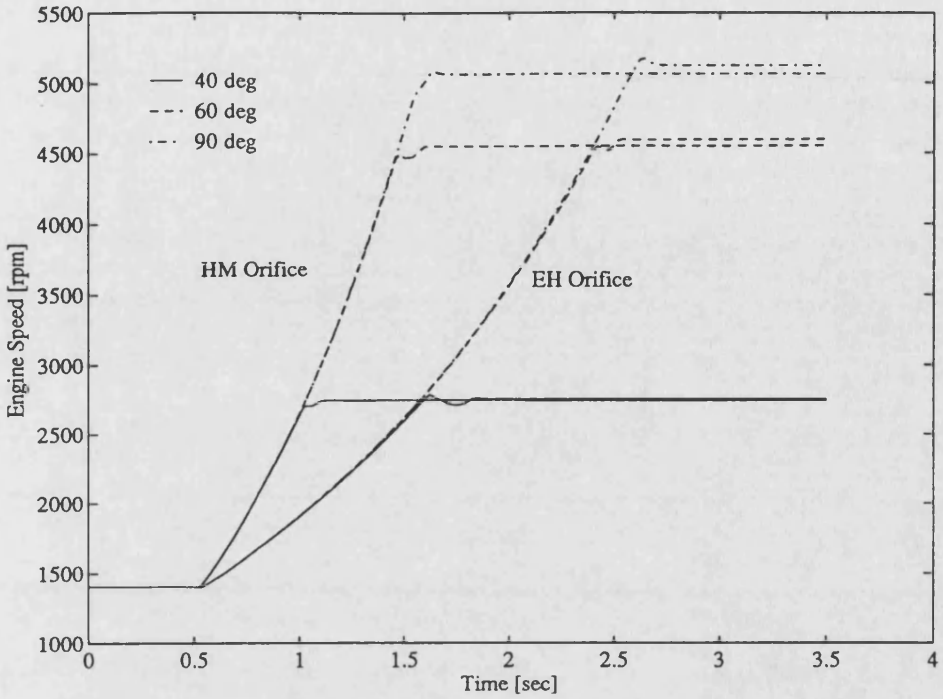

Figure 7.7 Engine speed response on throttle step demands

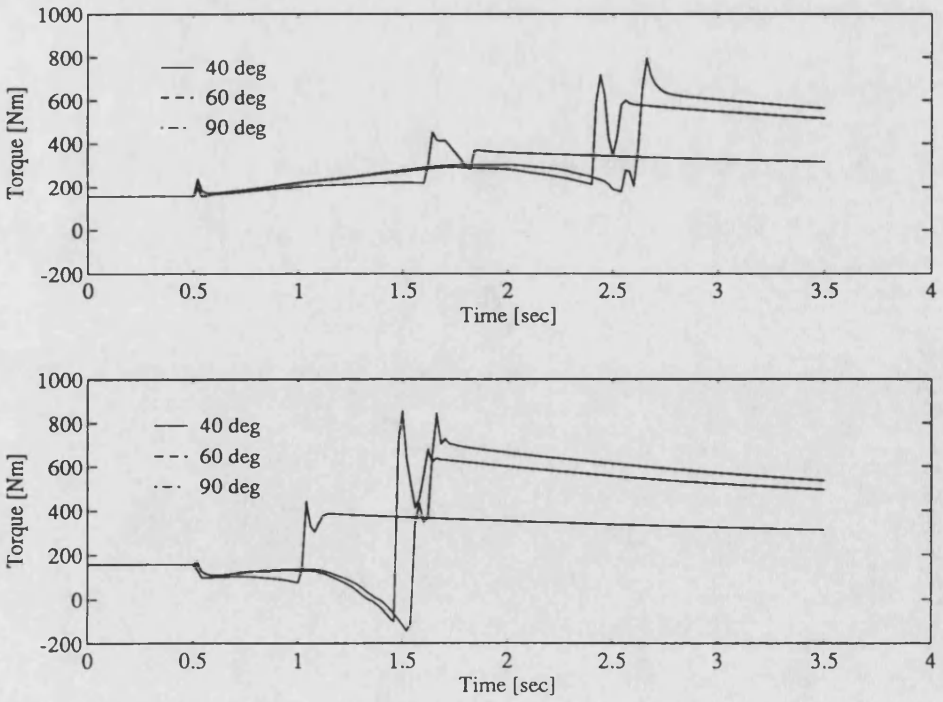

Figure 7.8 CTX output torque for throttle step changes for EH orifice (top) and HM orifice (bottom)

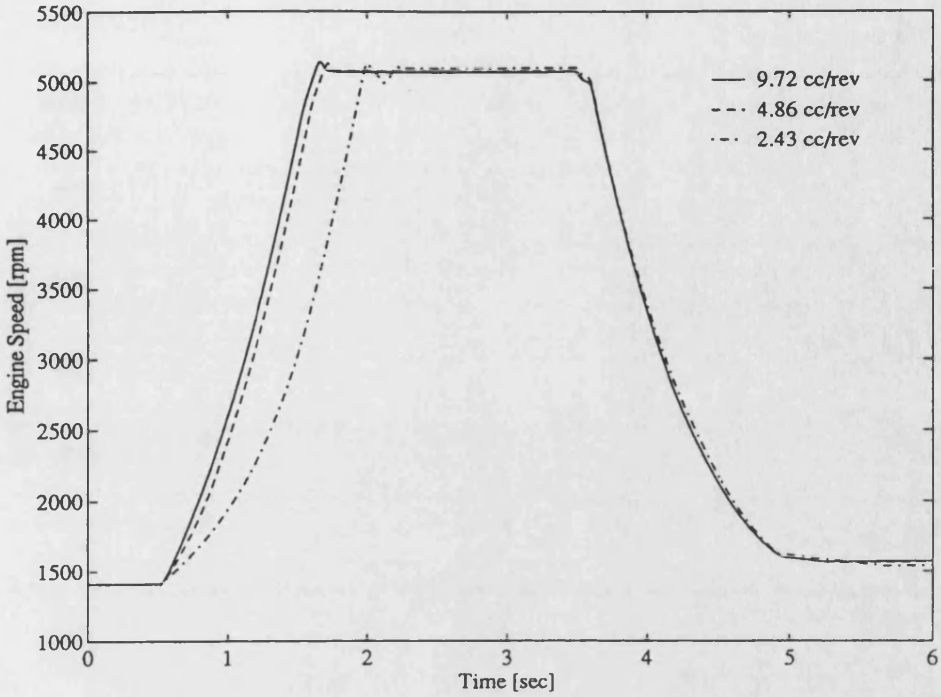

Figure 7.9 Engine speed response with different pump sizes

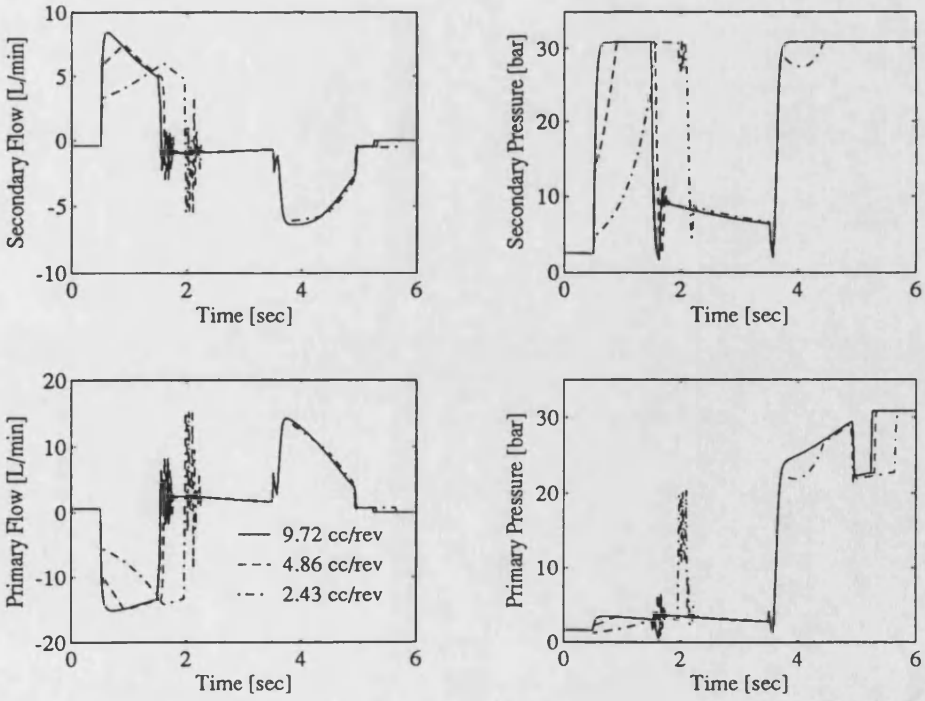

Figure 7.10 Pressure and flow data for the throttle step test for different pump sizes

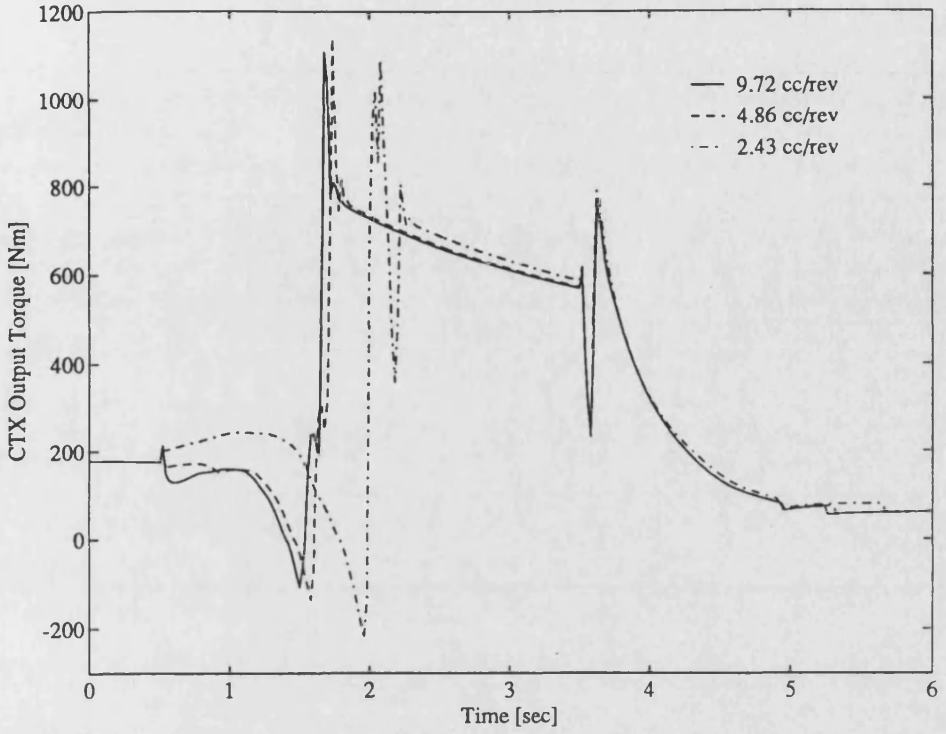

Figure 7.11 CTX Output torque for different pump sizes

8. GENERAL DISCUSSION

8.1. Summary of Results

The results explain the methods that were developed to answer the questions outlined in the objectives in 1.1. The enhanced understanding of the transmission of power through the VSU facilitated the development of a feedback control scheme that *optimises the power transmission efficiency through the VSU.* Dynamic simulation together with measurements from the rig confirmed the *reduction in fuel consumption* and outlined the *dynamic limitations of a strict IOL strategy.* An autonomous controller for the VSU prepared the application of an *overall powertrain controller.*

8.2. Viscous Shear Theory

The extended application of the viscous shear theory (Micklem, 1991) defines the line pressure such that the transmission efficiency through the VSU is optimised. Such a condition could not be formulated when using the Coulomb friction approach that was believed to describe the transmission of power. Becker's work (1986 and 1987, He is the exponent of that theory due to his thorough theoretical treatment.) and most probably early experiences with the Van Doorne VSU have created the erroneous idea of minimum line pressure for "safe operation". It was thought that the power transmission phenomenon between the pulley and belt had always to be stiction, since any sliding would have resulted in instability and, subsequently, in excessive slip and thus catastrophic wear. This work has shown that the "safe operation" aspect can be dropped and replaced by a strategy that sets the line pressure to maximise the power transmission efficiency.

8.3. Potential of the CTX

The presented methods optimise the power transmission efficiency of the Van Doorne VSU that is the most lamentable characteristic of this type of drive. This is expressed by many in the need for electronic line pressure control (Seidel, 1992, Schwab, 1990, Hendriks, 1993, Narumi, 1990). All authors have recognised the connection between line pressure and efficiency. They expressed the need to schedule the line pressure but none of them even suggested a suitable method. This underlines the importance of the optimum efficiency controller that maximises the potential of the Van Doorne VSU.

The analysis has also shown that the potential of the CTX can be improved by re-designing the hydraulic circuit. A dynamic simulation is an essential tool for doing this. Staffel (1984) made a first attempt, that did not seem to be pursued further. Röper (1987) attempted to size the hydraulic pump based on analytical thoughts. He did not recognise the importance of the pressure drop over the pipe work which is the limiting factor for the transient performance. The tools developed in this thesis could be used to design a new hydraulic circuit, i.e. find optimum actuator areas, pump size and match them with the occurring pressure drop over the pipe work. Moreover, the performance can be evaluated in the light of an overall control concept that might trade-off dynamic requirements with driveability aspects.

The optimum efficiency strategy and a new design of the hydraulic circuit can increase the efficiency further. Values exceeding 90% overall efficiency as given by Hendriks (1993) can be achieved. An accurate dynamic simulation, particularly of the hydraulics, is essential to optimise the design.

8.4. Viability of Proposed Controller

Streib (1992) expressed the desire for an hierarchical control strategy for a powertrain. Narumi (1990) forecasts the application of modern control algorithms and the use of fuzzy logic to detect the driver's intention and thus improve the transient performance.

The proposed state space controller goes well in line with these statements. However, the multivariable controller has to include an anitwindup feature.

8.5. Consequences for Overall Powertrain Control

A high dynamic capability of the transmission ratio adjustment was thought to lead to acceptable driveability in conjunction with a strict IOL strategy. This is not true. A *transient powertrain scheduler* that ensures a comfortable development of axle torque has to be designed. The optimum robust controller for the CVT simplifies this task considerably. However, improved transient response can only be achieved by giving up the IOL strategy.

8.6. Future of CVTs

According to Autocar & Motor (1992) 6% of total 1992 Fiesta sales were CTX cars. That figure can be expected to grow if CVTs get more efficient and improve the driver's comfort. However, there are two major obstacles that might prevent unlimited success. A good transient response cannot be achieved if the engine is operated in its most efficient operating point. An intelligent control algorithm might optimise the compromise that has to be struck. Secondly, enhanced electronic control has to be implemented swiftly. Otherwise, the rapidly developing technology of sophisticated automatic control of conventional clutch-stepped-transmission systems (Car Design & Technology, 1992) as seen in Formula 1 will supersede the practical benefits of CVTs.

9. CONCLUSIONS

VARIABLE SPEED UNIT (VSU) MODEL

The application of the *viscous shear theory* led to the exact quantification of the power loss through the VSU of the CTX transmission. The two phenomena *viscous slip* and *torque loss* determine - together with the power consumption of the hydraulic pump - the power transmission efficiency of the VSU.

Viscous slip. Measurements have shown that slip always exists. The slip depends linearly on the *viscous shear power density* that defines the relation between the transmitted torque and the active clamping force. The linear relation is reflected in the empirical assumption that the thickness of the oil film between the pulleys and the belt is the reciprocal of the mean oil film pressure. It has been shown that the model approximates the measurements satisfactory and that the simple empirical formula is valid for the relevant operating range.

Torque loss. The forcing of the belt into and out of the pulley sheaves accounts for the torque loss. The loss depends on the system pressure and the active radii and has been validated using no-load tests.

ELECTRO-HYDRAULIC CONTROL OF THE VSU

An analytical formula to adjust the hydraulic system pressure to *maximise the power transmission efficiency of the VSU* has been derived. The formula has been incorporated in an *autonomous control scheme* that only requires the transmission's input and output speed and the pulley displacement to be measured. This corresponds to the closed loop set point control of the slip. The set point (or demanded) slip is computed such that the efficiency of the transmission is optimum. The optimum efficiency controller has been implemented on the test rig using PI control and successfully adjusted the system for optimum efficiency. The control scheme has been shown to *improve the transmission efficiency by 5%* in the representative operating range.

Numerical simulation using accurate hydraulic components revealed that the transients to adjust the transmission ratio are limited by the restrictions in the pipe work to the actuators. The transient ability can be improved by either minimising the hydraulic restrictions or, alternatively, increasing the pressure levels. *Multivariable control techniques* have been used to pursue the second strategy. The simultaneous consideration of the primary and secondary valve command yielded enhanced control over the robustness-gain compromise. The transient performance has been extended to limits given by the hydraulic circuit.

A comprehensive numerical simulation of the electro-hydraulically controlled CTX powertrain has been developed. The simulation served two purposes. First, it was used to extract linear models that were the basis to design multivariable dynamic controllers. Secondly, the interaction of the linear controller with the non-linear and discontinuous powertrain system was investigated using the simulation. This proved the robust dynamic behaviour and indicated the performance.

CONTROL OF THE CTX POWERTRAIN

A strict ideal operating line (IOL) strategy in conjunction with the optimum efficiency controller has been implemented. Data from the rig *have been predicted to improve the fuel consumption by 20% in steady state driving* in the representative operating range. The implementation did not include driveability aspects and it has been shown that a true IOL strategy has severe disadvantages from a transient point of view.

Results from the computer simulation have shown that the dynamically optimised transmission ratio control (multivariable controller) assists in counteracting the transient disadvantages but, at the same time, makes the employment of a *transient ratio scheduler* necessary.

POTENTIAL OF THE CTX POWERTRAIN

Electronic control has been shown to improve both the dynamic performance and the CTX powertrain economy. Three actions can improve the potential of the CTX powertrain further.

1. The autonomous optimum efficiency scheme maximises the efficiency of the VSU. The transmission efficiency of other power transmitting components in the CTX powertrain (clutch, differential) has to be optimised.

2. The dynamic performance of the transient ratio adjustment depends only partly on the electronic control. The dynamic aspects of the hydraulic circuit and the transient interactions within the engine operating strategy have to be evaluated in order to re-design the hydraulic system. This includes the sizing of the pump and the incorporation of the electro-hydraulic valves.

3. The strict IOL strategy has clearly to be compromised to achieve satisfactory transient performance. The potential of the CTX powertrain can be improved further by applying a sophisticated strategy that intelligently schedules the engine operating point while maintaining favourable consumption (and emission) values.

APPENDICES

Appendix A. Maximum Transmission Efficiency of a Steel Belt CVT

This appendix lists the paper "Maximum transmission efficiency of a steel belt continuously variable transmission" by Gübeli, Micklem and Burrows (1992). It was presented at the 6th International Powertrain and Gearing Conference in Phoenix, USA in September 1992. In the meantime it has been accepted for publication in the *ASME Journal of Mechanical Design.*

The paper substantiates the viscous shear stress approach and introduces the concept of optimum efficiency (see 6.2). It concludes with two important points. Efficiency improvements of about 2% as compared to the standard hydro-mechanical control unit are achieved when operating conditions defined by the optimum formula are imposed. Secondly, the importance of minimising the pump size is stressed. The pump size greatly influences the overall efficiency.

The described model does not take any torque losses into account. This phenomenon was only explored after the paper's publication. However, the negligence of the torque loss has only an effect on the absolute value of the VSU's efficiency, and has hardly an effect on the efficiency improvement. Within this frame it is to understand that the projected peak efficiency of 97% is too optimistic. More realistic values are given in 6.1.

MAXIMUM TRANSMISSION EFFICIENCY OF A STEEL BELT CONTINUOUSLY VARIABLE TRANSMISSION

M Guebeli, J D Micklem, C R Burrows
School of Mechanical Engineering, University of Bath, England

ABSTRACT

A mathematical model of the power transmission through a Van Doorne steel belt continuously variable transmission is developed. The approach is based on a simplified viscous oil shear stress model. This enables the determination of the power transmission loss resulting from shearing the oil film along the traction line. The power to maintain the necessary hydraulic clamping forces is taken into account to optimise the power transmission efficiency. The analytical solution is evaluated numerically and compared with experimental results. Variations in the hydraulic pump displacement that are determined by the required ratio adjustment dynamics show that with a sufficiently small pump, peak efficiencies exceeding 97% are possible.

1. INTRODUCTION

The potential to improve the fuel consumption of a car with a powertrain consisting of a conventional internal combustion engine and a continuously variable transmission (CVT) divides into two aspects. These are, first, the strategy used to control the transmission ratio and the engine operating point and, secondly, the efficiency of the powertrain components. The works by Stubbs (1981), Yang et al (1985) and many others have shown the potential of a CVT powertrain and have given solutions to the first aspect. The efficiency of a CVT powertrain has been more controversial and nearly suppressed from academic discussion. This paper explores the efficiency potential of a Van Doorne steel belt CVT taking into consideration the necessary power consumption to guarantee operation.

Ford Europe currently builds a CVT called the CTX transmission used in the Fiesta and Escort range. This transmission was used for experiments in this paper. The variable speed unit (Figure 1) consists of two axially adjustable V-pulleys and the Van Doorne compression belt (Hendriks et al, 1988). Hydraulic actuation of the pulley halves varies the radius at which the belt acts on each pulley which, in turn, adjusts the transmission ratio. Driving power is transmitted from the primary to the secondary pulley. This terminology is used to designate the variables at either pulley. The metal belt's construction allows

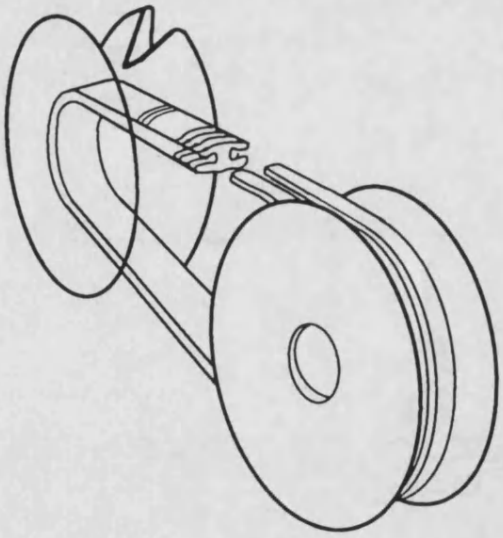

Figure 1 Variable speed unit of the Ford CTX/Van Doorne continuously variable transmission

power to be transmitted by compression rather than tension. The belt consists of approximately 300 metal segments and two packs of thin, endless metal bands, which guide the segments in

circular paths around the two pulleys and on straight lines between them. This separates the tasks of power transmission (compression of the segments) and guidance of the belt (tension of the bands).

There are two major losses associated with this kind of CVT (and all traction type CVTs which use auxiliary hydraulics). The hydraulic power to generate the clamping forces and the power resulting from shearing the oil between the pulleys and the belt (the traction line) are wasted. A minimization of the sum of the two losses corresponds to the optimization of the transmission efficiency.

Nomenclature

1. Dimensions

- Θ Half the pulley wedge angle
- L Belt length
- X Pulley centre distance
- s Segment thickness at rocking edge
- b Segment thickness at most inner part
- c Radial length of segment side
- m Mass of belt per unit length
- D Pump displacement
- A_s Secondary actuator area

2. Variables

- α Angle between the straight belt line and the pulley centre connection
- β Angle of lap on a pulley
- R Active belt radius
- T Pulley torque
- F Pulley clamping force
- C Compressive force in segments
- v_R Radial belt velocity
- v_L Longitudinal belt velocity
- t Oil film thickness between segments and pulley
- U Tension in the bands
- n Pulley speed
- p Hydraulic pump pressure
- Q Hydraulic pump flow

3. Empirical Constants

- η Viscosity of oil between segments and pulley
- k Oil film thickness constant
- υ Oil pump efficiency

4. Geometrical Substitution Variables

- h Uniform radial belt thickness
- A_c Sliding contact area of a segment in radial direction
- r Number of segments engaged
- q Radial allowance for the line of action

5. Subscripts

- s Secondary Pulley
- p Primary Pulley

2. THE POWER TRANSMISSION THROUGH THE BELT-PULLEY SYSTEM

A mathematical model of the power transmission through the belt-pulley system based on a simplified viscous oil shear stress model and a continuous belt description is developed. The analytical approach based on the dynamics of the belt-pulley system is outlined in the Appendix.

2.1 Simplifications

Belt

The segment and band structure of the belt is treated as a uniform continuum. There is no shear connection between the bands and the segments. The only inertia forces included are those due to centripetal accelerations of the belt.

Shear Stress in the Oil Film

The power is transferred between the pulleys and the belt by a means of a viscous shear stress (Micklem et al, 1991)

$$\tau = \eta \frac{v_{rel}}{t} \qquad (1)$$

where v_{rel} is the relative velocity between the two sliding members.

Thickness of the Oil Film

The thickness of the oil film is assumed to be

$$t = \frac{k}{p_{mean}} \qquad (2)$$

where p_{mean} is the mean oil pressure and k is an empirical constant.

2.2 Belt Equations

2.2.1 Radial

The interaction between the two clamping forces tensions the belt and, in turn, determines the radial dynamics of the belt. Substituting (A1) through (A5) in (A8) gives the rate of change of the primary pulley radius.

$$\dot{R}_p = \frac{\tan\Theta A_c k}{h\eta s} \frac{F_p - \frac{\beta_p}{\beta_s}F_s}{F_p + F_s} \quad (3)$$

This equation describes the dynamics of the belt adjustment, and it is essential for the design of the hydraulic control system for the ratio adjustment. However, this issue is not considered here. It is assumed that the change in R_p be sufficiently slow that its effect on the power transmission characteristics is negligible. This leads to a quasi steady state consideration in which equation (3) becomes zero, and thus

$$F_p = \frac{\beta_p}{\beta_s}F_s \quad (4)$$

2.2.2 Longitudinal

The longitudinal belt problem characterizes the relation between the input and output speeds and torques. As shown above, the two clamping forces determine the position of the belt independent of the transmitted torque. Additionally, they play a crucial role in the transmission of power through the belt pulley system. Inserting (A10) applied to both pulleys in (A11) yields the torque relationship

$$T_p = -T_s\frac{R_p}{R_s} \quad (5)$$

This equation neglects any belt torque loss for reasons of simplicity. This loss has been measured and included in other work at Bath. Its effect on the optimisation presented in this paper is negligible.

Equation (A9) can be applied to the primary and secondary pulley. These two equations can be used to eliminate the longitudinal belt speed, v_L. Using (A5) to substitute for the oil film thickness leads to the speed relationship

$$n_p = \frac{R_s}{R_p}n_s - \frac{A_c k}{\eta}\left(\frac{R_s T_s}{R_p q_s F_s} + \frac{R_p T_s}{R_s q_p F_p}\right) \quad (6)$$

(5) and (6) are used to express the power transmission losses through the belt-pulley system. They can be determined as the difference of input and output power. In a physical interpretation, they correspond to the losses due to the shear of the oil film between the belt and the pulleys.

$$P_{Shear} = n_p T_p + n_s T_s \quad (7)$$

The positive sign results from the sign convention mentioned in the Appendix.

2.3 Experimental Results

Experimental data were collected on a dynamic test rig. Real time car emulation enabled the CVT powertrain to be operated as it would be in a car. The test cycle for all presented data in this paper was a full acceleration from standstill. The standard CVT hydraulic control unit was used.

Figure 2 shows details of the test cycle. The engine throttle input and the resulting engine and car speed, respectively, are plotted. The transients of the engine speed between 3 and 5 seconds correspond to the clutch engagement phase which can be observed in Figures 3 and 4. These Figures show a comparison of measured and computed primary pulley speeds and torques. In particular, the speed plot in Figure 3 shows the behaviour of the components on either side of the clutch. The engine speed and the primary pulley speed converge to the same value in the engagement point.

The same data was used to plot the measured and computed transmission efficiency in Figure 5. The power used to drive the hydraulic pump was taken into consideration. The large fluctuation in the measured efficiency curve is due to the high sensitivity of the efficiency computation. This arises because the efficiency is the ratio of two products of noisy quantities of similar magnitudes.

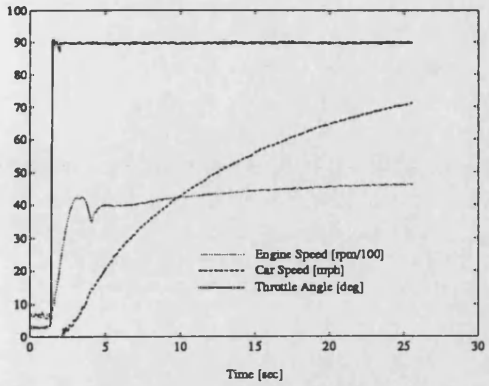

Figure 2 Experiment data from dynamic test bed

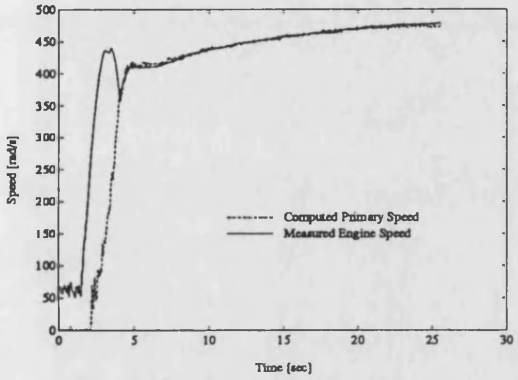

Figure 3 Comparison of measured and computed primary pulley speed

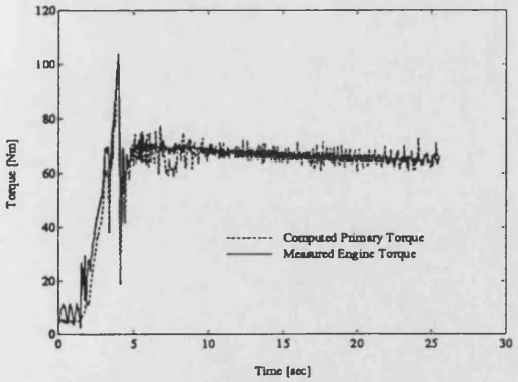

Figure 4 Comparison of measured and computed primary pulley torque

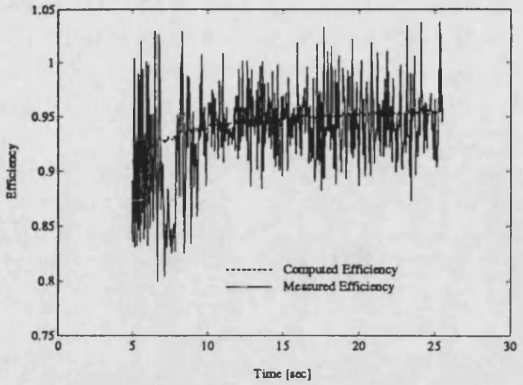

Figure 5 Comparison of measured and computed power transmission efficiency including hydraulic power losses

3. EFFICIENCY OPTIMISATION

The efficiency optimisation of the power transmission through the belt pulley system corresponds to the minimisation of the power losses. These comprise of the shear losses and hydraulic pump losses. The necessary clamping forces influence both loss components because they control the power transmission characteristics between the belt and both pulleys and they are directly proportional to the auxiliary pump discharge pressure. As expressed in equation (3), the difference or alternatively the ratio of the two clamping forces determines the radial position of the belt.

In order to facilitate the hydraulic valve assembly both actuator areas are chosen such that the pump outlet pressure is always equal to the pressure in the secondary actuator. The pump runs on the engine shaft and - with engaged clutch - will run at the primary pulley's speed. Thus the power to drive the hydraulic pump can be expressed as

$$P_{Pump} = \frac{Qp}{\upsilon} = n_p F_s \frac{D}{2\pi A_s \upsilon} \quad (8)$$

The minimisation of the sum of the power losses expressed in terms of the secondary clamping force leads to an optimum F_s ($F_{s,opt}$) that is proportional to the pump discharge pressure. That is we seek to minimise the sum of P_{Shear} and P_{Pump}. This leads to

$$\frac{d\left(P_{Shear}+P_{Pump}\right)}{dF_s} = 0 \qquad (9)$$

Inserting equations (4) trough (8) in (9) yields $F_{s,opt}$, the secondary clamping force at which the power loss through the variable speed unit is minimum

$$F_{s,opt} = T_s \sqrt{\frac{A_c k A_s \upsilon}{\eta D_p} \frac{1}{n_s} \frac{R_p^2}{R_s^2} \left[\frac{R_s}{R_p q_s} + \frac{R_p \beta_s}{R_s q_p \beta_p} \right]} \qquad (10)$$

The computed efficiency of the variable speed unit including the hydraulic pump losses from Figure 5 is compared with the optimum one in Figure 6. This has been computed assuming that the adjusted discharge pressure of the hydraulic pump fulfilled equation (10) at any time. Fluctuations in the optimum efficiency are non-existent because the secondary clamping force has no source of noise. It is computed as a function of secondary speed and power and the belt position. This eliminates the noise component in the quotient of the power ratio. The displacement of the hydraulic pump was 9.72 cc/rev and its overall efficiency was assumed 60%.

The optimum achievable efficiency of the variable speed unit, taking into account the hydraulic power losses, is influenced by the power throughput (T_s, n_s) and the radii at which the belt runs on the pulleys. In the presented results the power throughput did not largely vary with time and was near the maximum of the rated power throughput. The optimum efficiency is between 93% and 97%. The efficiency improvement using the optimised control strategy is around 2%.

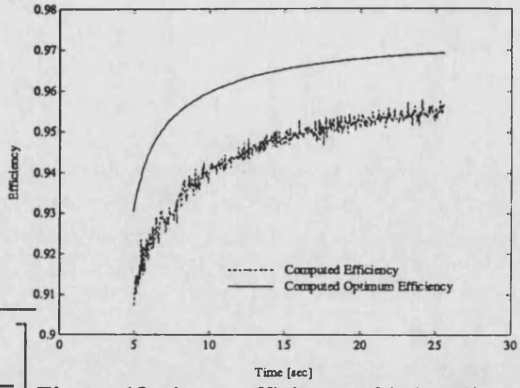

Figure 6 Optimum efficiency of belt-pulley system with respect to the secondary clamping force including hydraulic power losses

4. DISCUSSION

The modest power efficiency of variable speed units, as compared to straight gears, is one of the main reasons why CVTs are not employed more often in vehicles. The presented method to optimise the power efficiency could help to delineate the inherent disadvantage of this and to lead to the reduced consumption predicted by powertrain specialists.

The pump size is determined by the required transients for the ratio adjustment. Figure 7 shows the optimum efficiency for the same test cycle with different pump displacements. Halving and doubling the capacity of the pump leads to remarkable differences. The pump capacity should be as small as possible. This provides a framework for the control engineer to design the ratio control system.

An implementation of the proposed optimum control strategy requires knowledge of the transmitted torque. The model developed in section 2. assists in determining this by measuring the speed difference of the primary and secondary pulley letting the CVT act as a torque calculator. As opposed to the presented test cycle the foremost use on the road consists of mainly part-load power transmission. Especially in this operation the optimised control strategy would lead to improved efficiencies as compared to the tested CVT version, since the hydraulic control unit is designed for maximum throughput torque at any time.

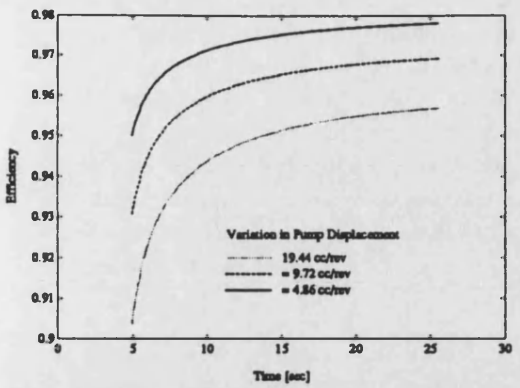

Figure 7 Effect of hydraulic pump displacement on optimum efficiency of the belt-pulley system including hydraulic power losses

5. CONCLUSIONS

The optimum full-load efficiency of a Van Doorne variable speed unit, taking into account the necessary auxiliary hydraulic power, is between 93% and 97%, if an optimised system pressure controller is used. The variation in the efficiency corresponds to the active transmission ratio and compares to 98% efficiency of a straight gear transmission. The optimum controller adjusts the pump discharge pressure such that the power losses comprising of shear losses and hydraulic pump losses are minimum.

The pump capacity is determined by the required dynamic capabilities of the ratio adjustment and influences the efficiency considerably. Research into lowering the dynamic ratio requirements such as by means of controlling the engine torque actively (Drive-By-Wire) could improve the efficiency further.

APPENDIX

The following equations describe the power transmission through the belt pulley system. They are based on the assumptions of Micklem (1990) which postulate a viscous shear relation between two sliding members. The simplifications in section 2 ease the mathematical interpretation of the belt.

The two clamping forces control the operation of the CVT, enabling the transmission of power as well as the adjustment of the transmission ratio. The latter is primarily done by adjusting the belt position and described in section 2.2.1 (*Radial Belt Equation*). The clamping forces influence the transmission of power in that they determine the viscous slip between the pulleys and the belt. Thus they affect the power wasted by shearing the oil and, to a certain amount, the transmission ratio. This effect is addressed in 2.2.2 (*Longitudinal Belt Equations*)

The sign convention is that positive power, and positive torque, flows into the variable speed unit. The equations are formulated to compute the primary power and transmission ratio when the secondary power and the clamping forces are known.

Belt Kinematics

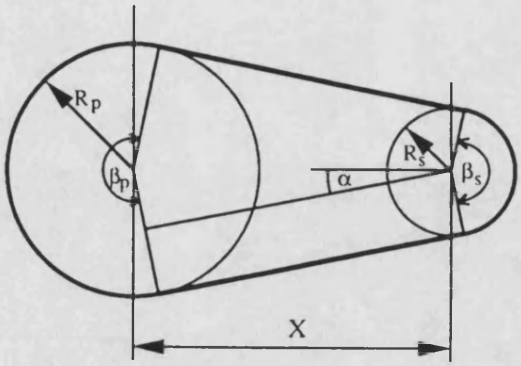

Figure 8 Belt geometry

The belt geometry (Figure 8) is given by

$$L = R_p\beta_p + R_s\beta_s + 2\sqrt{X^2 - (R_s - R_p)^2} \quad \text{(A1)}$$

$$\beta_p = \pi - 2\alpha\,, \quad \beta_s = \pi + 2\alpha$$
$$\sin\alpha = \frac{R_s - R_p}{X} \quad \text{(A2)}$$

For v_{Rp} and v_{Rs} holds

$$v_{Rs} = -v_{Rp}\frac{\beta_p}{\beta_s} \quad \text{with:} \quad v_{Rs} = \dot{R}_s \quad \text{(A3)}$$
$$v_{Rp} = \dot{R}_p$$

Empirical Relationship

The mean pressure in the oil film is

$$p_{mean} = \frac{\frac{F}{\cos\Theta}}{\frac{c(s+b)}{2}\frac{R\beta}{s}} \quad \text{(A4)}$$

The numerator is the perpendicular force component, whereas the denominator is the contact area between the pulley and the belt consisting of the number of engaged individual segment areas. The effect of the radial viscous shear force is neglected. Inserting (A4) in equation (2) (2.1 Simplifications, Thickness of the Oil Film; Micklem, 1991) gives

$$t = rA_c\frac{k}{F} \quad \text{(A5)}$$

where r and A_c are defined below.

Note: Variables t, r and F can take on subscripts p or s denoting primary and secondary pulley. This yields two equations.

Geometrical Substitutions

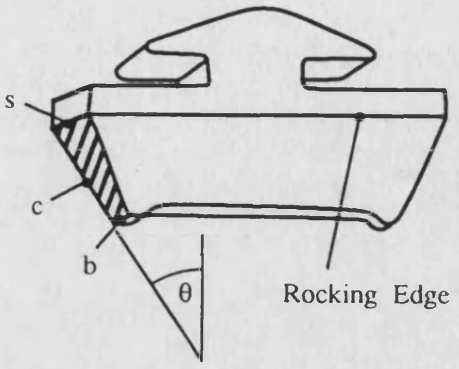

Figure 9 The surface of a segment in contact with a pulley

The following abbreviations are used. The first two only depend on the geometry of a segment and the pulley wedge angle (Figure 9) whereas the third and the fourth are functions of the active primary or secondary radii.

$$h = \frac{(s+b)c}{2s\cos^2\theta}$$
$$A_c = \frac{1}{2}c\cos\theta(s+b)$$
$$r = \frac{R\beta}{s} \quad \text{(A6)}$$
$$q = (s+b)cR^2 - \frac{2}{3}c^2\cos\theta(s+2b)R + \frac{1}{6}c^3\cos^2\theta(s+3b)$$

q is the radial allowance factor and originates from the radial variation of the slip speed over the contact surface of a segment. It results from the solved integral over this surface and relates the tangential shear force component to a slip speed between the pulley and the segment at a given radius R. s, b and c are defined in Figure 9.

Radial Belt Equation

The evaluation of the radial equation of motion integrated around the pulley gives

$$U = \frac{2\tan\Theta F}{\beta} + \frac{\Sigma C}{2} - \frac{2h\eta R v_R}{t} + v_L^2 m \quad \text{(A7)}$$

where U is the band tension and the terms on the right correspond to the radial component of the

clamping force, the radial component of the segment compressions, the radial shear force and the centrifugal force, respectively.

As was stated in 2.1 Simplifications, the change in compression along the straight belt paths is zero. This results in equal radial compression for both pulleys. Also, the tension in the band is uniform. Introducing these constraints into the equation for the primary and secondary pulley gives

$$\frac{2\tan\Theta F_p}{\beta_p} - \frac{2h\eta R_p v_{Rp}}{t_p} = \frac{2\tan\Theta F_s}{\beta_s} - \frac{2h\eta R_s v_{Rs}}{t_s} \qquad \text{(A8)}$$

Longitudinal Belt Equations

The viscous shear transfer along the length of the part of the belt around the pulley is

$$T = \frac{\eta}{t}\left(n - \frac{v_L}{R}\right) q\, r \qquad \text{(A9)}$$

where the second factor on the right corresponds to the relative speed between the sliding members, i.e. the pulley and the belt.

Note: Variables T, n and q can take on subscripts p or s, yielding two equations.

Because the longitudinal inertia of the belt is neglected the tangential equilibrium condition applied to a single segment multiplied by the number of segments is

$$\Delta C = \frac{T}{R} \qquad \text{(A10)}$$

where ΔC is the change in compression over a pulley.

Note that C can take on subscripts p or s. Additionally, the sum of the longitudinal change in compression over both pulleys must be the same. This yields

$$\Delta C_p = -\Delta C_s \qquad \text{(A11)}$$

REFERENCES

Hendriks E., ter Heegde P., van Prooijen T., 1988, "Aspects of a metal Pushing V-Belt for Automotive Cut Application", SAE paper 881734, 1988, Passenger Car Meeting and Exposition Dearborn, Michigan, 31 Oct. - 3 Nov.

Micklem J.D., 1990, "Research Project on the Modelling of the Ford CTX/Van Doorne Continuously Variable Transmission System", Fluid Power Centre report nr. 2184, Bath University,

Micklem J.D., Longmore D.K., Burrows C.R., 1991, "Modelling of the Van Doorne, Metal V-Belt, Continuously Variable Transmission System", International Conference on Motion and Power Transmissions, Hiroshima, Japan, 23-26 Nov. 1991

Stubbs P.W.R., 1981, "The Development of a Perbury Traction Transmission for Motor Car Applications", Journal of Mechanical Design, Vol. 103, Jan. 1981, pp. 29-40

Yang D., Frank A.A., 1985, "An optimization technique for the design of a continuously variable transmission control system for automobiles", Int. J. of Vehicle Design, vol. 6, no. 1, pp. 41-54

Appendix B. Engine Steady State Data

This appendix lists the steady state engine data that was used throughout the thesis. The data resulted from a test of a Ford Fiesta 1.1l "Valencia" engine and were recorded in February 1988.

APPENDIX B. Engine Steady State Data

Speed [rpm]	Torque [Nm]	Manifold Pressure [kPa]	Fuel Flow [kg/h]	Specificic Consumption [g/kWh]	Volumetric Efficiency [%]	Throttle Angle [deg]
1000	71.0	99.0	2.49	350	76.6	86.2
1500	77.6	98.6	4.06	348	80.2	86.2
2000	87.1	98.0	5.31	304	83.3	86.2
2500	89.2	97.5	6.19	278	84.6	86.1
3000	88.4	96.9	7.40	280	84.4	86.0
3500	87.0	96.4	8.57	282	84.6	86.0
4000	86.2	95.7	9.77	283	82.9	86.0
4500	81.7	94.9	10.94	297	79.9	86.0
5000	76.2	94.7	11.74	308	76.7	86.0
5500	69.5	94.0	12.17	318	73.7	85.8
1000	61.0	88.0	1.80	281	69.4	24.9
1500	66.8	88.7	2.75	262	72.2	32.8
2000	74.9	95.2	4.03	257	80.6	55.5
2500	76.5	93.9	5.10	255	80.6	56.7
3000	75.8	91.7	6.03	253	78.4	56.2
3500	74.8	91.1	7.17	262	77.4	58.6
4000	74.0	91.0	8.40	271	77.1	61.1
4500	70.4	89.6	9.18	277	74.9	61.5
5000	65.5	89.0	9.68	282	70.8	61.0
5500	59.8	88.2	10.36	301	68.6	61.3
1000	54.4	78.9	1.61	282	60.1	19.4
1500	59.3	79.1	2.48	266	62.5	25.2
2000	66.6	84.0	3.59	257	68.4	33.7
2500	68.1	85.9	4.56	256	71.5	40.8
3000	67.3	86.2	5.41	256	72.2	46.1
3500	66.5	88.6	6.26	257	73.9	53.8
4000	65.8	87.3	7.20	261	72.5	55.3
4500	62.4	85.6	7.85	267	69.6	55.7
5000	58.3	83.7	8.47	278	66.3	55.4
5500	53.1	82.2	8.94	292	63.0	55.7
1000	47.5	75.0	1.40	282	57.1	18.0
1500	51.9	74.6	2.17	266	59.1	23.3
2000	58.3	76.5	3.16	259	61.4	28.9
2500	59.6	77.0	4.05	260	62.8	33.4
3000	58.9	76.7	4.85	262	63.1	37.1
3500	58.1	77.7	5.60	263	63.3	41.1
4000	57.6	79.6	6.43	266	64.6	46.1
4500	54.7	79.0	7.03	273	63.1	48.8
5000	51.0	78.5	7.59	284	61.2	50.9
5500	46.5	77.2	7.98	298	58.4	51.6
1000	40.6	67.8	1.22	286	51.3	15.8
1500	44.5	68.7	1.92	274	54.3	21.1
2000	50.1	69.2	2.83	270	55.1	25.4
2500	51.0	69.2	3.62	271	55.7	29.1
3000	50.6	69.9	4.34	273	56.4	32.8
3500	49.9	70.0	5.03	275	56.1	35.9
4000	49.3	72.2	5.74	278	57.2	39.9
4500	46.8	71.9	6.27	284	56.1	42.4
5000	43.8	72.0	6.78	296	54.8	44.4
5500	39.8	70.8	7.16	312	52.5	45.5

APPENDIX B. Engine Steady State Data

Speed [rpm]	Torque [Nm]	Manifold Pressure [kPa]	Fuel Flow [kg/h]	Specificic Consumption [g/kWh]	Volumetric Efficiency [%]	Throttle Angle [deg]
1000	33.8	58.8	1.13	318	43.4	13.2
1500	37.1	59.1	1.72	296	45.7	18.1
2000	41.5	62.8	2.46	283	50.0	23.1
2500	42.4	62.4	3.17	286	49.2	26.2
3000	42.2	62.9	3.82	288	49.2	29.2
3500	41.5	63.0	4.43	291	49.2	32.0
4000	41.2	65.0	5.09	295	50.1	35.3
4500	38.9	64.6	5.59	304	49.4	37.5
5000	36.5	64.4	6.03	316	48.2	39.3
5500	33.2	64.5	6.50	340	47.5	41.0
1000	27.3	54.6	0.94	329	40.5	12.4
1500	29.7	56.9	1.42	303	44.1	17.5
2000	33.4	59.3	2.15	308	47.2	21.8
2500	33.9	59.0	2.63	296	46.7	25.0
3000	33.7	58.8	3.14	297	45.9	27.5
3500	33.3	58.7	3.65	299	44.8	29.9
4000	32.8	59.3	4.38	318	45.2	32.3
4500	31.2	59.3	4.78	324	44.6	34.3
5000	29.2	59.7	5.20	341	44.0	36.3
5500	26.4	59.8	5.66	372	43.4	37.9
1000	20.4	47.3	0.77	358	33.4	10.4
1500	22.2	47.3	1.17	338	34.7	14.6
2000	25.1	51.3	1.72	327	39.9	19.1
2500	25.5	51.4	2.19	329	40.7	22.1
3000	25.2	49.2	2.70	341	37.2	23.6
3500	24.9	50.0	3.10	339	37.2	26.1
4000	24.7	52.5	3.54	342	39.6	29.2
4500	23.4	53.7	3.95	358	40.7	31.8
5000	21.9	55.0	4.39	382	41.4	34.3
5500	19.8	56.2	4.70	413	40.5	36.2
1000	13.5	38.5	0.66	464	27.6	8.4
1500	14.8	38.8	0.96	412	28.6	12.3
2000	16.7	41.5	1.36	390	31.5	16.3
2500	17.0	42.6	1.73	389	32.9	19.3
3000	16.9	41.2	2.18	411	30.5	20.7
3500	16.8	42.2	2.56	417	31.0	22.9
4000	16.5	44.2	2.91	420	32.4	25.4
4500	15.6	46.1	3.26	444	33.5	27.9
5000	14.5	46.8	3.62	479	33.9	29.9
5500	13.4	48.7	3.98	517	34.0	32.0
1000	6.9	31.9	0.54	752	21.7	6.4
1500	7.3	30.5	0.73	636	21.4	9.5
2000	8.3	31.7	1.03	590	23.0	12.7
2500	8.5	33.2	1.29	578	23.9	15.5
3000	8.4	34.8	1.58	599	25.2	18.1
3500	8.2	33.4	1.93	643	23.2	19.0
4000	8.2	35.5	2.24	653	24.4	21.3
4500	7.7	37.1	2.53	695	25.5	23.6
5000	7.2	39.1	2.96	781	27.2	26.1
5500	6.5	41.5	3.35	894	28.2	28.1

Appendix C. Linearised Model of CTX Powertrain

The linearised model of the CTX powertrain with EH control is presented. The model is used to design the controllers in Chapters 6 and 7. It was obtained through a computation of the Jacobian in a Bath*fp* simulation process and is presented in state space form.

1. INPUT-OUTPUT SYSTEM

Figure C.1 shows the icon representation of the Bath*fp* simulation of the EH controlled CTX powertrain. Inputs 1 through 3 are the secondary valve voltage demand (v_s), the primary valve voltage demand (v_p) and the throttle angle (α). The outputs are the engine speed and the slip error.

2. LINEARISATION POINT: U_0, Y_0, X_0

Inputs: $\mathbf{U_0} = [u_1\ u_2\ u_3]'$

Secondary voltage (v_s)	$u_1 =$	7.00e-01	[V]
Primary voltage (v_p)	$u_2 =$	2.00e+00	[V]
Throttle Angle (α)	$u_3 =$	4.00e+01	[°]

Outputs: $\mathbf{Y_0} = [y_1\ y_2]'$

Engine speed (n_e)	$y_1 =$	3.35e+02	[rad/s]
Slip error (e_s)	$y_2 =$	5.61e+00	[rad/s]

States: $\mathbf{X_0} = [x_1\ x_2\ \ldots\ x_{15}]'$

Manifold pressure (p_m)	x_1 =	8.40e+04	[kPa]
Manifold temperature (T_m)	x_2 =	3.00e+02	[K]
Engine speed (n_E)	x_3 =	3.35e+02	[rad/s]
Differential speed (n_D)	x_4 =	5.67e+01	[rad/s]
Primary radius (R_p)	x_5 =	5.31e-02	[m]
Primary actuator pressure (p_p)	x_6 =	5.29e+00	[bar]
Secondary actuator pressure (p_s)	x_7 =	1.07e+01	[bar]
Driveline deflection	x_8 =	5.51e-02	[rad]
Covered car distance	x_9 =	2.77e+01	[m]
Wheel Speed (n_T)	x_{10} =	5.67e+01	[rad/s]
Primary valve spool velocity	x_{11} =	2.70e-09	[%/s]
Primary valve spool demand	x_{12} =	3.80e+01	[%]
Secondary valve cracking pressure	x_{13} =	9.80e+00	[bar]
Pressure in secondary pipe	x_{14} =	9.87e+00	[bar]
Pressure in primary pipe	x_{15} =	5.78e+00	[bar]

3. SYSTEM MATRICES A, B, C, D

A = [

-2.51e+01 -2.04e+03 -1.69e+03 0.00e+00 0.00e+00 0.00e+00 0.00e+00 0.00e+00 0.00e+00 0.00e+00 0.00e+00 0.00e+00 0.00e+00 0.00e+00 0.00e+00

-2.51e-02 -7.30e+00 -1.70e+00 0.00e+00 0.00e+00 0.00e+00 0.00e+00 0.00e+00 0.00e+00 0.00e+00 0.00e+00 0.00e+00 0.00e+00 0.00e+00 0.00e+00

6.98e-03 0.00e+00 -9.91e+01 5.76e+02 -1.24e+06 -3.98e+01 -1.89e+01 0.00e+00 0.00e+00 0.00e+00 0.00e+00 0.00e+00 0.00e+00 0.00e+00 0.00e+00

0.00e+00 0.00e+00 1.79e+02 -3.44e+03 2.22e+06 6.83e+01 3.43e+01 -1.33e+04 0.00e+00 2.40e+03 0.00e+00 0.00e+00 0.00e+00 0.00e+00 0.00e+00

0.00e+00 0.00e+00 0.00e+00 0.00e+00 -2.75e+00 3.02e-02 -1.50e-02 0.00e+00 0.00e+00 0.00e+00 0.00e+00 0.00e+00 0.00e+00 0.00e+00 0.00e+00

0.00e+00 0.00e+00 0.00e+00 0.00e+00 2.39e+07 -2.95e+05 1.30e+05 0.00e+00 0.00e+00 0.00e+00 0.00e+00 0.00e+00 0.00e+00 0.00e+00 3.39e+04

0.00e+00 0.00e+00 0.00e+00 0.00e+00 -1.45e+07 1.63e+05 -9.43e+04 0.00e+00 0.00e+00 0.00e+00 0.00e+00 0.00e+00 0.00e+00 1.32e+04 0.00e+00

0.00e+00 0.00e+00 0.00e+00 1.00e+00 0.00e+00 0.00e+00 0.00e+00 0.00e+00 0.00e+00 0.00e+00 -1.00e+00 0.00e+00 0.00e+00 0.00e+00 0.00e+00 0.00e+00

0.00e+00 0.00e+00 0.00e+00 0.00e+00 0.00e+00 0.00e+00 0.00e+00 0.00e+00 0.00e+00 0.00e+00 2.70e-01 0.00e+00 0.00e+00 0.00e+00 0.00e+00 0.00e+00

0.00e+00 0.00e+00 0.00e+00 1.80e+01 0.00e+00 0.00e+00 0.00e+00 1.00e+02 0.00e+00 -1.80e+01 0.00e+00 0.00e+00 0.00e+00 0.00e+00 0.00e+00 0.00e+00

0.00e+00 0.00e+00 0.00e+00 0.00e+00 0.00e+00 0.00e+00 0.00e+00 0.00e+00 0.00e+00 0.00e+00 0.00e+00 -6.28e+02 -9.87e+04 0.00e+00 0.00e+00 0.00e+00

0.00e+00 0.00e+00 0.00e+00 0.00e+00 0.00e+00 0.00e+00 0.00e+00 0.00e+00 0.00e+00 0.00e+00 0.00e+00 1.00e+00 0.00e+00 0.00e+00 0.00e+00 0.00e+00

0.00e+00 0.00e+00 0.00e+00 0.00e+00 0.00e+00 0.00e+00 0.00e+00 0.00e+00 0.00e+00 0.00e+00 0.00e+00 0.00e+00 0.00e+00 -2.94e+01 0.00e+00 0.00e+00

0.00e+00 0.00e+00 0.00e+00 0.00e+00 0.00e+00 0.00e+00 9.59e+02 0.00e+00 0.00e+00 0.00e+00 0.00e+00 0.00e+00 -2.45e+02 1.05e+06 -1.05e+06 7.17e+02

0.00e+00 0.00e+00 0.00e+00 0.00e+00 0.00e+00 3.17e+03 0.00e+00 0.00e+00 0.00e+00 0.00e+00 0.00e+00 2.45e+02 0.00e+00 7.17e+02 -3.88e+03

]

B = [

0.00e+00 0.00e+00 2.70e+04
0.00e+00 0.00e+00 2.70e+01
0.00e+00 0.00e+00 0.00e+00
0.00e+00 0.00e+00 0.00e+00
0.00e+00 0.00e+00 0.00e+00
0.00e+00 0.00e+00 0.00e+00
0.00e+00 0.00e+00 0.00e+00
0.00e+00 0.00e+00 0.00e+00
0.00e+00 0.00e+00 0.00e+00
0.00e+00 0.00e+00 0.00e+00
0.00e+00 9.87e+05 0.00e+00
0.00e+00 0.00e+00 0.00e+00
4.12e+02 0.00e+00 0.00e+00
0.00e+00 0.00e+00 0.00e+00
0.00e+00 0.00e+00 0.00e+00

]

C = [

0.00e+00 0.00e+00 1.00e+00 0.00e+00 0.00e+00 0.00e+00 0.00e+00 0.00e+00 0.00e+00 0.00e+00 0.00e+00 0.00e+00 0.00e+00 0.00e+00 0.00e+00 0.00e+00
0.00e+00 0.00e+00 -1.0e+00 5.92e+00 -1.28e+04 0.00e+00 0.00e+00 0.00e+00 0.00e+00 0.00e+00 0.00e+00 0.00e+00 0.00e+00 0.00e+00 0.00e+00 0.00e+00

]

D = [

0.00e+00 0.00e+00 0.00e+00
0.00e+00 0.00e+00 0.00e+00

]

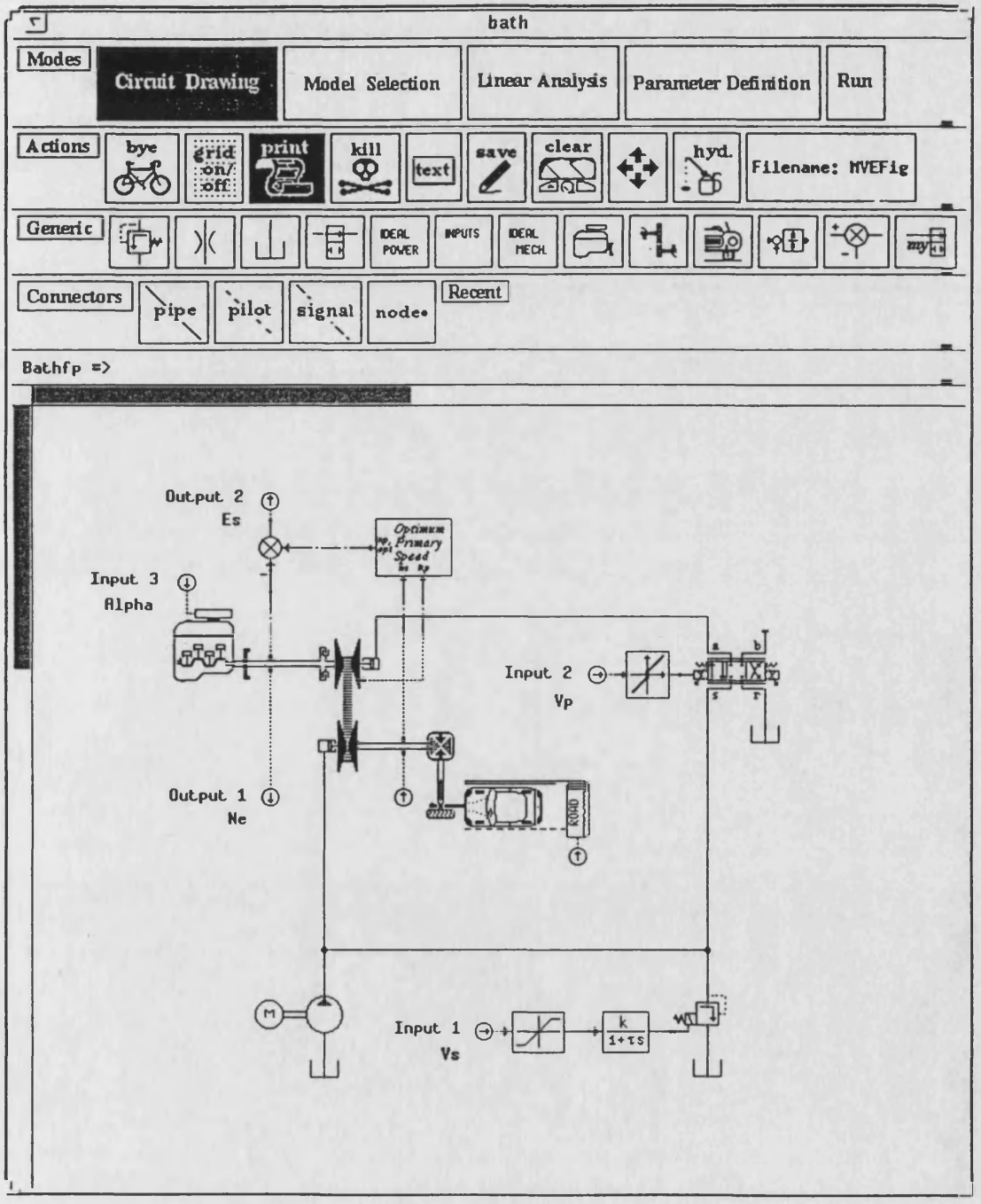

Figure C.1 Bath*fp* icon representation of the open loop simulation

Appendix D. System Matrices for H_∞ Analysis

1. REDUCED MODEL

A = [

-5.82e-01	-5.58e+00	6.13e+00	1.19e-01
-4.01e-01	-3.34e+01	3.04e+00	-1.93e+00
6.29e+00	6.39e+01	-7.15e+01	-1.18e+00
2.20e-01	2.06e+00	-2.79e+00	-1.64e-01

]

B = [

-7.48e+00	-3.49e+00	5.77e-02
-1.41e+01	-7.04e-01	1.77e-01
3.98e+00	1.02e+00	-4.05e-02
-1.97e+00	-9.45e-01	-5.64e-02

]

C = [

6.92e+00	-6.44e-01	1.14e+01	-1.40e+00
8.56e-01	-6.21e+00	-8.34e+00	-1.06e+00

]

D = [

0.00e+00	0.00e+00	0.00e+00
0.00e+00	0.00e+00	0.00e+00

]

2. H_∞-CONTROLLER

A = [

-2.92e+02	3.49e+02	-7.12e+01	6.61e+00	-2.77e+03	3.08e+03
2.42e+02	-2.90e+02	7.13e+01	1.26e-01	1.53e+03	-2.73e+03
-1.06e+01	1.48e+01	-5.28e+01	-3.04e+01	3.03e+03	1.19e+03
1.20e+00	-1.93e+00	9.37e+00	-4.91e+01	-3.91e+02	2.34e+03
-3.44e+00	-3.00e+00	1.59e+02	2.60e+01	-9.95e+03	2.50e+01
-1.89e+00	3.16e+00	-1.16e+01	2.09e+02	-1.07e+01	-9.95e+03

]

B = [

9.15e-04	5.24e-04
-8.02e-05	-1.40e-05
-1.69e-01	-1.11e-01
5.36e-01	-4.37e-01
-8.75e+01	-4.29e+01
5.75e+01	-1.20e+02

]

C = [

1.20e+01	-1.44e+01	4.12e+00	7.78e-01	1.81e+01	-1.83e+02
5.11e+01	-6.07e+01	7.02e+00	-4.28e+00	8.61e+02	-3.98e+02

]

D = [

0.00e+00	0.00e+00
0.00e+00	0.00e+00

]

GLOSSARY

CTX. Stands for *C*ontinuously variable *T*ransa*X*le. This is the name of Ford's CVT transmission.

CVT. CONTINUOUSLY VARIABLE TRANSMISSION. A transmission that allows the transmission of power at continuously variable ratio, within some limits. This adjustable transmission ratio is largely independent of the transmitted torque.

DBW. DRIVE-BY-WIRE. Control scheme in which the powertrain controller governs the actuation of engine throttle valve. There is no direct link between the driver's accelerator and the throttle valve any more.

EH. ELECTRO-HYDRAULIC. Referes to the electronically controlled hydraulic circuit for adjusting the clamping pressures of the VSU.

EHD. ELASTO HYDRO DYANIMICS. Theory that explaines the behaviour of the oil film typically present when shearing two surfaces under high clamping pressures.

HM. HYDRO-MECHANIC. Referes to the mechanically controlled hydraulic circuit for adjusting the clamping pressures of the VSU.

IOL. IDEAL OPERATING LINE. Defines the operating conditions of the engine such that, for a demanded power, the consumption is minimum. It relates engine speed to demanded power.

MVC. MULTIVARIABLE CONTROL. Controller design technique for pants with multiple inputs and outputs. The interactions between all inputs and outputs are taken into account for the design procedure.

OE. OPTIMUM EFFICIENCY. Philosphy to control the VSU operating point to achieve optimum efficiency.

VSU. VARIABLE SPEED UNIT. The device that matches the input to the output speed at variable ratio. The transmitted torque does hardly influence the ratio.

REFERENCES

Abromeit, G. and Wilkinson, A.C.N. (1984). An electronic control concept for a continuously variable transmisison. ISATA 1984, Milan

Adler, U. ed. (1986), Bosch Automobile Handbook, Stuttgart: Robert Bosch GmbH

Autocar & Motor (1992). CVT. 8 January 1992, 44

Beachley, N.H. and Frank, A.A. (1980). Principles an definitions for continuously variable transmissions, with emphasis on automotive applications. ASME 80-C2/DET-95

Becker, H.J. (1986) Mechanik des Van-Doorne-Schubglierderbandes. *Antriebstechnik*, 25, no. 8

Becker, H.J. (1987). Berechnung des Van Doorne CVT-Schubgliederbandes. 1. Aachener Kolloquium Fahrzeug- und Motorentechnik '87, pp. 457

Bonthron, A. (1985). CVT-efficiency measured under dynamic running conditions. SAE 850569

Chiang, R.Y. and Safonov, M.G. (1992). Robust Control Toolbox User's Guide. Natick, Mass.: The MathWorks, Inc.

Chiang, R.Y., Safonov, M.G., Haiges, K., Madden, K. and Tekawy, J. (1993). A fixed H_∞ controller for a supermaneuvrable fighter performing the Herbst Maneuver. *Automatica Special Issue on Robust Control*, January 1993

Dittrich, O. and Simon, H. (1988). The Continuously Variable Transmission in Motor-Cars. SAE 885064

Dongen, van L.A.M. (1982). Efficiency characteristics on manual and automatic passenger car transmissions. SAE 820741

Dorato, P. and Yedavalli, R.K. eds. (1990). Recent Advances in Robust Control, A volume of selected conference papers, prepared under the sponsorship of the IEEE Control Systems Society. New York: IEEE Press

Doyle, F.J., Packard, A.K. and Morari, M. (1989). Robust controller design for a nonlinear CSTR. In: Proceedings of the 1989 American Control Conference, June 1989

Eggert, U. and Schneider, H.D. (1984). Control Strategies for a Chain Drive CVT.

IMechE C447/84, SAE 841302

Engels, H.R. and Main, J.J. (1985). Neue Entwicklungen auf dem Gebiet der Antriebsregelung für Personenwagen. *MTZ Motorentechnische Zeitschrift*, 46, 12, 481-487

Finlay, I.C., Boam, D.J., Martins, J.J.G., Gilchrist, A. and Lee, C.K. (1987). Models for predicting engine torque response during rapid throttle transients in spark ignition engines. In: Murthy T.K.S., Brebbia, C.A. ed. (1987). *Computers in Design, Construction and Operation of Automobiles*, 47-71, Computational Mechanics Publications

Gerbert, G. (1984). Metal V-belt mechanics. ASME 84-DET-227

Gieles, W.T.M. (1989). Electronic control of continuously variable transmission and its extension to engine transmission management. IMechE C382/048

Guebeli, M. (1989). Frequency to voltage converter. Bath University Report 082/92

Guebeli, M., Dorey R.E. (1990). Real time power train simulation for dynamic engine testing using a hydrostatic dynamometer. IEE Colloquium on Power Train Control. 16 May 1990

Guebeli, M. (1990). A hydrostatic dynamometer for real-tim engine testing. Bath University Report 083/92

Guebeli, M. (1992). Optimum control of the CTX transmission. Bath University Report 084/92

Guebeli, M., Micklem, J.D. and Burrows, C.R. (1992). Maximum transmission efficiency of a steel belt continuously variable transmission. 6th International Power Transmission and Gearing Conference (PTG 92), Phoenix, Arizona, 13-16 September 1992, organised by ASME

Guo, Z.Y, Yang, X.C., Yang, D. and Frank, A.A. (1988). On obtaining the best fuel economy and performance for vehicles with engine-CVT transmissions. SAE 881735

Hahne, D. (1984). A Continuously Variable Automatic Transmission for Small Front Wheel Drive Cars. IMechE C2/84

Harrington, D.L. (1970). Analysis and digital simulation of carburettor metering. SAE 700082

Hendriks, E., Heegde, ter P. and Prooijen, van T. (1988). Aspects of a metal Pushing V-Belt for Automotive Cut Application. SAE paper 881734. 1988, Passenger Car Meeting and Exposition Dearborn, Michigan, 31 Oct. - 3 Nov.

Hendriks, E. (1993). Qualitative and quantitative influence of fully electronically controlled CVT on fuel economy and vehicle performance. SAE 930668

Heywood, J.B. (1988). Internal combustion engine fundamentals, New York, London: McGraw-Hill

Hong, C.W. (1991). A PC-based computer simulation package for spark ignition engine system design. IMechE C430/069

Horowitz, A. (1980). Evaluation of novel and powerful continuously variable V-band transmissions in comparison with current variable and fixed drives. ASME 80-C2/DET-121

Howard, G. (1992). The doubtful future of the CVT. *Car Design & Technology*, April 1992, 44-48

Kalkert, W. and Eggert, U. (1988). Field Experience and Further Developments of Control Systems for CVTs in Passenger Cars. SAE 885061. FISITA '88, Dearborn, Michigan, September 25-30, 1988

Lambert, D.R. (1988). Development of a continuously variable transmission (CVT) for commercial vehicles. *Electric Vehicle Design*, vol. 7, no. 2 (April 1988), 69-70

Lees, H. (1992). Double de-clutching. *Car Design & Technology*, October 1992, 24-26

Liebrand, N.J. (1992). Future developments in push belts for CVT application. IMechE C389/212, SAE 925063

Machida, H. and Kurachi, N. (1990). Prototype design and testing of the half toroidal CVT. SAE 900552

Maciejowski, J.M. (1989). Multivariable feedback design. Addison-Wesley

McCandlish, D. and Dorey, R.E. (1984). The mathematical modelling of hydrostatic pumps and motors. *Proc IMechE*, vol. 198B, no. 10

Micklem, J.D. (1990). Research project on the modelling of the Ford CTX/Van Doorne continuously variable transmission system. Bath University Report 2184

Micklem, J.D., Longmore, D.K. and Burrows, C.R. (1991). Modelling of the Van Doorne, metal V-belt, continuously variable transmission system. International Conference on Motion and Power Transmissions, Hiroshima, Japan, 23-26 Nov. 1991

Micklem, J.D. (1993). Modelling of the Van Doorne CVT, to be published in two parts in the Proceedings of the IMechE, part C in 1994

Nakano, M. and Hibi, T. (1990). Dynamic characteristics of speed ratio control of the half toroidal CVT of passenger cars. SAE 901761

Narumi, N., Suzuki, H. and Sakakiyama, R. (1990). Trands of powertrain control. SAE 901154

Rogers, G.F.C. and Mayhew, Y.R. (1967). Engineering thermodynamics work and heat transfer. Longman

Röper, H. (1987). Anforderungen an die Druckölversorgungseinheit hydraulisch gesteuerter CVT-Getriebe. *Antriebstechnik*, 26, no. 8

Röper, H. and Simon, E. (1987). Die Steuerung des CTX-Getriebes. *Automobiltechnische Zeitschrift*, 9/1987

Safononv, M.G. and Flachner, H. (1989). Modeling and robustness issues in control design of flexible structures. In: Proceedings of the 1989 American Control Conference, June 1989

Sakai, Y. (1988). The "ECVT" Electro Continuously Variable Transmission. SAE 880481

Schwab, M. (1990). Electronically controlled transmission systems - current position and future developements. SAE 901156

Seidel, W., Petersmann, J., Hickmann U. and Möllers W. (1992). Adaptive control system for continuously variable transmission (CVT). IMechE C389/328, SAE 925062

Sogawa, Y., Kameoka, T. and Matsui, F. (1989). Improvement of engine transient characteristics using an induction chamber model. *Int. J. of Vehicle Design*, vol. 10, no. 5, 581-591

Staffel, H. (1984). Digital simulation of a CVT hydraulic control system. ISATA 1984, Milan

Steib, H.M. and Leonhard, R. (1992). Hierarchical control strategy for powertrain functions. IMechE C389/342, SAE 925052

Stockton, T.R. (1984a). The Ford Research Dual Mode Continuously Variable Transmission. IMechE C445/84, SAE 841305

Stockton, T.R. (1984b). Powertrain matching and fuel economy projection methods. In: Hilliard John C. ed. (1984). *Fuel Economy in road vehicles powered by spark ignition engines.* Chapter 11, New York and London: Plenum Press

Stubbs, P.W.R. (1980). The development of a Perbury traction transmission for motor car applications. ASME 80-C2/DET-59

Sun, D.C. (1988). Performance analysis of a variable speed-ratio metal V-belt drive. *Transmissions and Automation in Design*, vol. 110, 472-481

Wilson, W.E. (1948). Performance criterea for positive-displacement pump and fluid motors. ASME Semi-Annual Meeting, May 30 - June 5 1948, 48-SA-14